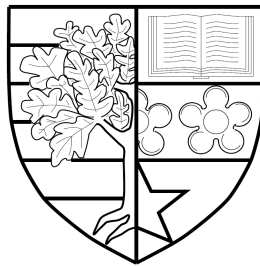# ROTATING POTENTIAL OF A STOCHASTIC PARAMETRIC PENDULUM

by

Panagiotis Alevras

Submitted for the degree of
Doctor of Philosophy

HERIOT-WATT UNIVERSITY

SCHOOL OF ENGINEERING AND PHYSICAL SCIENCES
INSTITUTE OF MECHANICAL PROCESS & ENERGY ENGINEERING

January 2015

Abstract

The parametric pendulum is a fruitful dynamical system manifesting some of the most interesting phenomena of nonlinear dynamics, well-known to exhibit rather complex motion including period doubling, fold and pitchfork bifurcations, let alone the global bifurcations leading to chaotic or rotational motion. In this thesis, the potential of establishing rotational motion is studied considering the bobbing motion of ocean waves as the source of excitation of a floating pendulum. The challenge within this investigation lies on the fact that waves are random, as well as their observed low frequency, characteristics which pose a broader significance within the study of vibrating systems. Thus, a generic study is conducted with the parametric pendulum being excited by a narrow-band stochastic process and particularly, the random phase modulation is utilized. In order to explore the dynamics of the stochastic system, Markov-chain Monte-Calro simulations are performed to acquire a view on the influence of randomness onto the parameter regions leading to rotational response. Furthermore, the Probability Density Function of the response is calculated, applying a numerical iterative scheme to solve the total probability law, exploiting the Chapman-Kolmogorov equation inherent to Markov processes. A special case of the studied structure undergoing impacts is considered to account for extreme weather conditions and finally, a novel design is investigated experimentally, aiming to set the ground for future development.

Acknowledgments

Research Thesis Submission Form

Insert the declaration here

Contents

List of Figures

List of Tables

Nomenclature

Chapter 2

H	–	wave height
T	–	wave period
λ	–	ocean water waves' wavelength
θ	–	inclination angle
δ, ϵ	–	parameters of Mathieu equation
ω	–	excitation frequency
Ω	–	natural frequency of a simple pendulum

Chapter 3

$\mathcal{J}$	–	σ-algebra
Ω	–	sample space
ω	–	sample point
P	–	measure of probability
A_i	–	an event of the sample space Ω
X	–	random variable
F	–	probability function on events
p_X	–	probability density function of a random variable X
$p_{x_1 \cdots x_m}$	–	joint probability density function of the random variables $x_1 \cdots x_m$
σ_X	–	standard deviation of a random variable X
Φ_{XX}	–	power spectral density of the random variable X

R_{XX}	–	autocorrelation function of a stationary process $X(t)$
$\zeta(t)$	–	Gaussian white noise
W	–	the Wiener process
$\alpha(\mathbf{X}, t)$	–	the drift term of an Ito stochastic differential equation
$b(\mathbf{X}, t)$	–	the diffusion term of an Ito stochastic differential equation
H	–	wave height
T	–	wave period
λ	–	ocean water waves' wavelength
k	–	wave number of the Stoke's wave
H_s	–	significant wave height
$S(f)$	–	power spectrum of ocean waves
q	–	phase of water particle displacement
D	–	intensity of a stochastic process
ω_m	–	mean excitation angular frequency
λ_D	–	nonlinearity parameter of the Duffing equation
α	–	damping coefficient of the Duffing equation
A	–	amplitude of vibrations
ϕ	–	phase of vibratory response
$B_{i,j}$	–	i-th basis function of j-th order B-splines
ϵ	–	a small parameter
D_{ij}	–	joint moment of x_i with x_j
Λ	–	largest Lyapunov exponent

Chapter 4

M	–	lumped mass of a simple pendulum
L	–	length of a simple pendulum
$f(t)$	–	displacement of a pendulum's pivot
θ	–	inclination angle

$\mathcal{L}$	–	the Lagrangian function
Ω	–	natural frequency of a simple pendulum
c	–	viscous damping coefficient
γ	–	non-dimensional damping coefficient
ω_m	–	mean excitation frequency
ν	–	ratio of excitation frequency over the natural frequency
λ	–	non-dimensional excitation amplitude
$\zeta(t)$	–	Gaussian white noise
D	–	variance of a stochastic process
p	–	probability density function
p_{E^*}	–	probability density function of a simple pendulum's normalized energy
R	–	dry friction parameter
A_h	–	horizontal excitation amplitude
A_v	–	vertical excitation amplitude
λ_h	–	non-dimensional horizontal excitation amplitude
λ_v	–	non-dimensional vertical excitation amplitude
ρ	–	ratio of the horizontal over the vertical excitation amplitude
ψ	–	the inverse tangent of ρ

Chapter 5

θ_i	–	i-th pendulum's inclination angle
c_i	–	i-th pendulum's damping coefficient
Ω_i	–	i-th pendulum's natural frequency
l_i	–	i-th pendulum's length
x	–	displacement of the platform
α	–	platform's damping coefficient
η	–	platform's natural frequency
$f(t)$	–	base excitation of the platform

m_i	–	i-th pendulum's mass
M	–	mass of the platform
ψ_i	–	ratio of the i-th pendulum's mass over the mass of the platform
m_i^r	–	ratio of the i-th pendulum's mass over the total mass of the system
A	–	excitation amplitude
ω_m	–	mean excitation frequency
$\tilde{\sigma}^2$	–	variance of the stochastic excitation's phase
$\zeta(t)$	–	Gaussian white noise
$\tilde{\sigma}^2$	–	variance of the stochastic excitation's phase
γ_i	–	non-dimensional damping coefficient of the i-th pendulum
κ	–	ratio between the natural frequency of the pendulums
ν	–	ratio of the excitation frequency over the natural frequency of the tuned pendulum
λ	–	non-dimensional excitation amplitude
σ^2	–	normalized variance of the stochastic excitation's phase
β	–	normalized damping coefficient of the platform
e	–	normalized natural frequency of the platform
y	–	normalized displacement of the platform
ρ	–	cross-correlation coefficient

Chapter 6

x	–	displacement of the platform
α	–	platform's damping coefficient
Ω_M	–	platform's natural frequency
Ω_P	–	pendulum's natural frequency
L	–	length of a simple pendulum

λ	–	non-dimensional excitation amplitude
ω_m	–	mean excitation frequency
m	–	mass of a simple pendulum
M	–	mass of the platform
γ	–	ratio of the pendulum's mass over the mass of the platform
β	–	damping coefficient of the pendulum
z	–	normalized displacement of the platform
h	–	distance of the platform's equilibrium to the barrier
h^*	–	proportion of the distance to the barrier of the non-dimensional excitation amplitude
r	–	restitution coefficient of the impacts
y	–	transformed displacement of the platform
A_i	–	amplitude of the response of the $i$ith DOF
ϕ_i	–	phase of the response of the $i$ith DOF
χ	–	difference between the phase of the excitation and the double phase of the platform's response
ψ	–	phase difference between the response of the DOFs
u, v	–	transformed averaged response of the 2-DOF system
Δ	–	detuning between the excitation and the double natural frequency of the platform
δ	–	detuning between the DOFs of the system
$\lambda_{L,R}$	–	excitation amplitude defining the boundaries of the stable response
$\sigma\tau$	–	superscript denoting stochastic response
λ_{init}	–	amplitude of the initiation point of the stability boundaries
λ_{low}	–	amplitude of the lowest point with unstable response
m_u, m_v	–	mean values of the transformed averaged response
A_1^*	–	mean amplitude of the platform's response

D_{ij}	–	second moment of the i, j random processes
σ^2	–	noise intensity
${\sigma_{crit}}^2$	–	critical noise intensity
Λ	–	largest Lyapunov exponent

Chapter 7

Ω	–	natural frequency of a simple pendulum
Ω_{eq}	–	natural frequency of a compound pendulum
l_{eq}	–	length of a simple pendulum equivalent to a natural frequency Ω_{eq}
M_i	–	mass carried by the i-th arm of the N-pendulum
L_i	–	distance from the pivot to the centre of gravity of M_i
m	–	mass of each arm
θ	–	inclination angle of a pendulum
ψ	–	ratio of the moment of inertia of one arm over the moment of inertia of the shortest arm
γ_i	–	ratio of the distance L_i over a non-equal distance L_j
n	–	ratio of the mass M_i over the non-equal mass M_j
N	–	number of arms of the N-pendulum
I_c	–	constant moment of inertia of a compound pendulum
I_v	–	configurable moment of inertia of a compound pendulum
$f(t)$	–	excitation of the pendulum's pivot
ω	–	angular frequency of the excitation
ν	–	ratio of the excitation frequency over the pendulum's natural frequency
λ	–	non-dimensional excitation amplitude
x	–	displacement of the pivot

l	–	length of the connecting rod
r	–	length of the crank
j	–	ratio of the crank's length over the connecting rod's
c	–	damping coefficient of the pendulum
β	–	normalized damping coefficient of the pendulum

List of Publications

[1] P. Alevras, R. Bobryk and D. Yurchenko. *Stability of an autoparametic pendulum system with impacts.* J Sound Vib, **333**(26), 7233–7247 (2014).

[2] P. Alevras and D. Yurchenko. *Stochastic rotational response of a parametric pendulum coupled with an SDOF system.* Probabilist Eng Mech, **37**, 124–131 (2014).

[3] P. Alevras, D. Yurchenko and A. Naess. *Stochastic synchronization of rotating parametric pendulums.* Meccanica, **49**(8), 1945–1954 (2014).

[4] D. Yurchenko and P. Alevras. *Dynamics of the N-pendulum and its application to a wave energy converter concept.* International Journal of Dynamics and Control, **1**(4), 290–299 (2013).

[5] D. Yurchenko and P. Alevras. *Stochastic dynamics of a parametrically base excited rotating pendulum.* Procedia IUTAM, **6**, 160–168 (2013).

[6] D. Yurchenko, A. Naess and P. Alevras. *Pendulum's rotational motion governed by a stochastic Mathieu equation.* Probabilist Eng Mech, **31**, 12–18 (2013).

[7] P. Alevras, I. Brown and D. Yurchenko. *Experimental investigation of a rotating parametric pendulum.* Nonlin Dyn. Under review.

and over 15 international conference abstracts and proceedings papers

Chapter 1

Introduction

The present thesis is concerned with the development of a Wave Energy Converter (WEC), generically defined as a device that transforms the energy carried by ocean surface waves to an exploitable form of energy. This is a subject which could be viewed from numerous and diverse, often contradicting, standpoints including economical, environmental and social aspects closely related to centrally applied policies from governments and international institutions as well as decentralized socio-economical procedures in the markets level. A peculiar challenge concerning this class of projects, and particularly innovative Renewable Energy (RE) technologies, lies within incorporating through composition and optimization, certain *a priori* requirements stemming from the previous considerations with the engineering science, that one would think to be the backbone of suchlike efforts.

Hereinafter, the issues arising from an engineering point of view, and especially from a dynamics one, such as the nature of the resource are considered. The device is understood as a mechanical system under a quite special environmental excitation and the dynamic response of this system is evaluated with respect to the working principle of the discussed WEC. The influence of the particular conditions imposed by the ocean onto this working principle is investigated, with the study placed on the level of proof-of-concept. Hence, the main target is to extend the study to a more realistic frame, explore the natural limitations and seek solutions to overcome them. Questions that have not been previously addressed in the literature reasonably

become of high importance towards the realization of this device and thus, a major part of the present work is devoted to them.

1.1   Motivation

In the past few decades, energy has been emerging as a key pivotal element of the global economy with accelerating demands. Currently, the world energy consumption for 2010 is estimated around 12765 Mtoe[1] according to the European Union (EU) latest figures [1], or close to 524 quad[2] on the other side of the Atlantic [2]. Yet, the full extent of the energy dependency is revealed by considering that just 15 years ago the same figure is estimated to have been at 9235 Mtoe [1], i.e. an increase of more than 38% has occurred. All the major international institutions estimate that this trend will be sustained with the US Energy Information Administration foreseeing an average 1.5% [2] annual increase up until 2040.

Within this context, the impact on the environment has been a growing concern. The increasing energy consumption leads to excessive CO_2 emissions since more than 70% of the energy production is related to fuel combustion in one way or another. Climate change, the greenhouse effect and their repercussions are as of now part of the everyday concerns and subject of central political actions. Let alone the economical impact of the current state in energy production, especially for large consumers with disproportional fuel resources such as the EU. The development of RE technologies and a much more confident reliance on them are in the front line of the counteractions. Latest estimates seen in Fig. 1.1(a), place the share of RE around 10% for the EU, which however has adopted an encouraging goal to produce 20% of the energy it needs through RE resources by 2020[3].

Inside the EU, RE is used mostly to produce electricity with hydroelectric power dominating the field (see Fig. 1.1(b)). The rest of the sources contribute significantly with especially wind and solar power conversion growing fast in the last few years.

---

[1]megatonne of oil equivalent. 1 Mtoe = 4.1868×10^{16} J (www.aps.org).
[2]quadrillion Btu. 1 quad = 10^{15} Btu (www.aps.org).
[3]Europe 2020 Strategy (ec.europa.eu/europe2020)
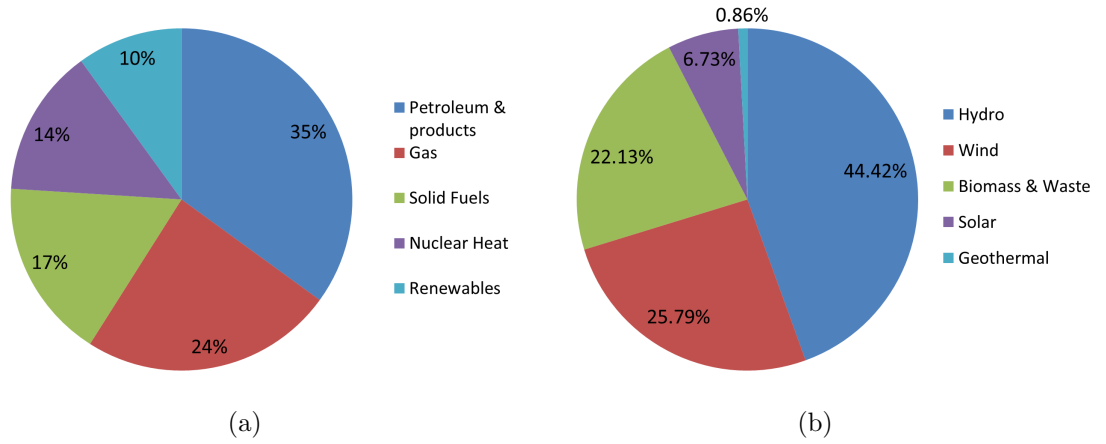
Figure 1.1: Statistics for the EU-27 for 2011; (a) Gross inland energy production classified by fuel source [1]; (b) Contribution of RE sources to electricity production [3].

These statistics also reveal the lack of exploitation of ocean energy, for which the installed capacity is just over 10 MW [4], when at the same time the global resource is evaluated at more than 2 TW [5]. However, this capacity has been tripled since 2009 and the predictions for future development are very optimistic. This confidence in ocean energy and especially wave energy is based on the competitive properties of the resource, reaching up to the highest theoretical extraction potential [6] among REs.

Upon this mismatch with the actual potential, a WEC is put under the microscope. The underlying physics of this concept are based on the response of a pendulum to parametric excitation. The latter is a widely known phenomenon in the study of dynamical systems which has found numerous applications through the years. A common example of a parametrically excited system is indeed a pendulum having its pivot point vibrating. Within the context of ocean energy conversion, waves have been seen as a possible source for those vibrations (see Fig. 1.2), thus forcing a pendulum suspended on a floating structure to parametric excitation [7].

Yet, exploitation of the waves' bobbing motion is not a newly introduced concept. Several designs take advantage of the kinetic energy of waves transforming it to electricity by means of another oscillating body and a connection to a generator. The innovation within the discussed WEC is attached to the well-known potential of rotational motion of the pendulum due to exposure to periodic parametric excitation
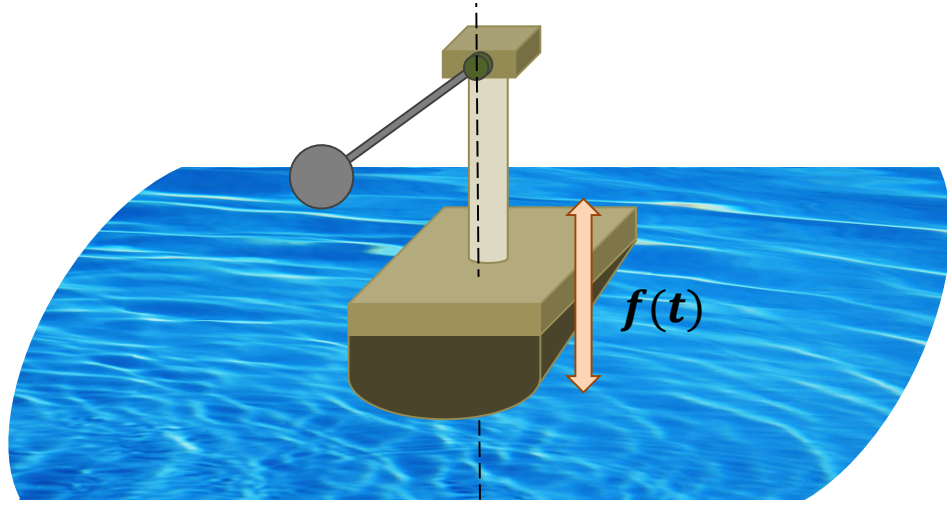
Figure 1.2: The WEC concept discussed in this thesis. The vertical motion of ocean waves provide the forcing action onto a floating structrure upon which a pendulum is suspended. Parametric excitation of the pendulum is sought to result in the latter's rotational response to be thereafter utilized for electricity production by coupling with a generator.

[8, 9]. From an energy production standpoint, a significantly larger amount of energy could be taken off waves by a rotating pendulum rather than an oscillating body, thus promising much better conditions for wave energy extraction.

Even though, at first sight a quite encouraging picture is drawn, this concept comes with some issues and drawbacks that have not yet been dealt with. A major issue is related to the nature of the resource. Ocean waves are characterized by a particularly low frequency. In order for parametric resonance to occur under the excitation of waves, one would need to deploy a nearly 100m long pendulum. Such a bulky device could only mean trouble, if feasible at all.

Furthermore, apart from the numerous studies concerned with characterizing ocean waves in the context of Ocean and Marine Engineering, even an untrained eye would recognize that waves are not perfectly periodic, but rather a random process. Also, the motion of water particles is not one-dimensional but planar and particularly elliptical with a trajectory influenced by the depth of the seabed. These issues bring up some important questions that have not been addressed satisfactorily so far and are generally related to the kinematics of waves as a forcing feature of the WEC system. To what extent are the observations made on the deterministic system reliable for the stochastic one as well? How could the noise intensity influence the response

of the pendulum in view of the effects on linear stochastic parametric systems? Could rotations of the pendulum arise and be sustained in a noisy environment and what would be the necessary parameters then? Extreme conditions that could be described in terms of stochastic processes, may be met quite often in the oceans and could render the device nonfunctional or even destroy it.

1.2 Outline

The present thesis aims to address two main objectives. The primary one is concerned with studying the response of a pendulum to stochastic parametric excitation with regard to the potential of establishing rotational motion. Within the scope of this objective, the following are aimed:

A1. Construct Parameter Space Plots (PSPs) to characterize the stochastic response of the parametric pendulum with purely vertical stochastic excitation directly applied at its pivot.

A2. Investigate the influence of the noise intensity magnitude onto the extent and intensity of the parameter regions leading to rotational response.

A3. Derive the Probability Density Function (PDF) of the response for selected characteristic cases to calculate the probability of rotational motion in order to verify the PSPs.

A4. Investigate the evolution of rotational parameter regions when the excitation is planar and particularly, titled from the purely vertical direction.

A5. Construct PSPs of the stochastic response for an autoparametric system with a single pendulum receiving the stochastic excitation as a base excitation.

A6. Evaluate the influence of the properties of the base platform in conjunction with increasing noise intensity magnitude.

A7. Consider the possibility of multiple pendulums mounted on a common plat-

form and study the interaction between them with regard to establishment of rotational motion.

A8. Introduce impacting motion of the platform and derive analytical approximate expressions of the instability boundaries of the pendulum's bottom equilibrium position.

A9. Conduct a numerical study to evaluate the analytical expressions and extend these results to further, more complicated cases.

The secondary objective falls within the development of a WEC attempting to propose a novel solution to the technological limitation of this device at its current state. The second objective comprises of the following sub-objectives:

B1. Present the design aimed to tackle the technological limitations imposed by the natural resource of ocean waves.

B2. Conduct a broad theoretical study to identify the capabilities of this design with respect to its natural frequency and some available modifications.

B3. Develop an experimental rig aiming to model the ocean wave excitation and describe the setup and operation.

B4. Present the experimental results aiming to demonstrate the flexibility and configurable properties of the novel design.

Chapter 1 attempts to concisely present the topic of this thesis, stating the motivation of the herein study. The main challenges and objectives are identified and an outline of the following chapters is listed.

Chapter 2 presents a literature review in two parts. First, the technological advances in Wave Energy Conversion are reviewed and, second, parametric excitation of dynamical systems is discussed with the focus on pendulum systems.

Chapter 3 contains the sum of the methods used to model the stochastic excitation, as well as the main tools used to analyze the stochastic response.

Chapter 4 deals with the stochastic parametric excitation of a pendulum applied directly at its pivot. The aim is to investigate the potential of rotational motion of this SDOF system and the influence of the noise intensity magnitude on the parameter regions leading to rotary response. Extensive simulations are presented and pinpointed cases are examined in a probabilistic context with the focus on the influence of the noise intensity. It is found that under a realistic noise intensity range, rotational motion is still achievable; yet, the design parameters that could lead to such a response change rapidly under increasing randomness, as does the robustness of these parameter regions, drifting away from the picture drawn by a deterministic model.

Chapter 5 follows up to the previous chapter, considering a more complicated system. Particularly, multi-Degree-of-Freedom (DOF) systems are discussed, with multiple pendulums mounted on a common platform. The stochastic excitation is forming a type of base excitation, classifying these systems in the autoparametric ones. The introduction of the platform in the model will be shown to have a beneficiary effect onto both the robustness of the rotational response and the favourable design parameters which are shifted to a more feasible range. However, the interaction between the pendulum and the platform is found to counteract this advantage, setting a requirement for a pendulum mass considerably lower than the platform's.

Chapter 6 increases the complexity of the concerned dynamics through introducing the possibility of impacts of the mounting platform onto a rigid barrier. The aim is to study the development of the instability boundaries of the pendulum, with regard to the escape of the pendulum from the bottom equilibrium point. The analytical and numerical analysis reveals a striking switch of the instability domains from being symmetrical around the resonance frequency to being contained only on the half-plane of positive detuning. The critical noise intensity that forces these domains to cross to the negative detuning half-plane is evaluated along with the threshold excitation amplitude that could lead to instability in a random environment.

Chapter 7 is concerned with the secondary objective of this thesis dealing with the technological limitations present in the current development of a WEC application. An experimental study is presented to demonstrate the functionality of the proposed novel design. The construction of this novel design and the development of an experimental rig are described. The results of the experimental tests verify the capability of this design to experience primary parametric resonance under low excitation frequencies, overcoming the so far technological constraints. Moreover, a second set of experiments reveal the flexibility that this design offers, leading to identical response of the system under different configuration options.

Chapter 8 extracts and lists the main conclusions of the present study delineating the importance of the herein results with direct correspondence to the questions placed in Chapter 1.

Chapter 2

Literature review

2.1 Wave energy conversion

The first patent for a device designed to capture wave energy dates back to 1799. Monsieur Girard and his son proposed harnessing mechanically wave energy to drive pumps and sawmills through a shore-attached lever following the oscillatory motion of a buoy. However, history is known, fossil fuels were the ones to motor industrialization and despite the fact that Girards' heaving buoy never got to be built and tested, it engaged to a series, over 340, of WEC patents until the 1970s [10].

In 1973, wave energy extraction has not been on the forefront. But then, the major oil crisis gave rise to the interest on wave energy. In 1976, Professor Stephen Salter's work of the University of Edinburgh became the landmark of WECs. His proposed device first published in his famous *Nature* article [11], known from then on as Salter's Duck, was an offshore device bobbing up and down on the waves. The oscillatory motion of the cam it consisted of, would drive hydraulic cylinders which in turn would result in electricity through hydraulic generators. The theoretical efficiency was calculated up to 100% for linear waves [12], with the optimum value dropping to around 85% if random waves are considered [13]. Even though Salter's Duck is considered a pioneering device in recent wave energy history and performed in lab with over 80% efficiency for a wide band of wave frequency [12, 14], it was never deployed in the ocean due to the disadvantage of long wavelengths in sea and

a general redirection at that time of public efforts towards nuclear energy [15]. One should not forget to mention the pioneering work of Yoshio Masuda in Japan in the 1960s which resulted in the Kamei device [16].

From then on, Europe rose up to the forefront of research on wave energy conversion. Earlier government-funded programmes started in the United Kingdom until 1983 when power devices with large energy production (i.e. nuclear energy) were promoted. At the same time, Norway, Portugal and Sweden turned to wave energy mostly due to their physical advantage of relatively high wave resources compared to other countries in Central or Southern Europe. In 1991, the European Commission included wave energy in its renewable energy programmes, thus re-igniting the interest in wave energy conversion technologies with the leading countries staying at the frontier of research. This coincided with the first deployment of a 75kW shoreline converter (the LIMPET) in the Islay Island which was to be the first commercial converter integrated in the National Grid. An important development is the Kyoto Protocol (1997), which stated the need to reduce CO_2 emissions thus promoting RE generation, among which wave energy too. Last, the Europe 2020 strategy set the goal for RE production at 20% of the energy consumed in EU.

In industry though, WECs represent an insignificant portion of the renewable technologies. It is evident, that the first commercialization took place with LIMPET which was upgraded in 2000, just over a decade ago. In academia however, confidence over wave energy is constantly rising after 1973. This could be implied by a number of conferences supported by the EU and government R&D programmes. The first conferences were the *International Symposium on Wave and Tidal Energy* held in Canterbury (1976) and the *Wave Energy Conference* in Heathrow (1978). A step up was made with the *Symposia on Wave Energy Utilization* in Gothenburgh (1979) and Trondheim (1982) and the IUTAM Symposium on Hydrodynamics of Ocean Wave-Energy Utilization (Lisbon, 1985). After 1991, the European Commission supported more effectively wave power holding the *European Wave and Tidal Energy Conferences* from 1993 in Edinburgh until the 10th symposium in Aalborg (2013). Moreover, wave energy has been of the interest of more generic conferences such as the *World Renewable Energy Congresses*. At the moment, several organi-

zations support the research on wave energy conversion. Indicatively, the European Commission over the last years supported 18 programmes concerning ocean energy [17]. Other important organizations include the European Ocean Energy Association, the European Marine Energy Centre (EMEC), the Wave Energy Centre in Portugal, the Ocean Wave Energy Project in Norway, the Ocean Energy Council in USA, the Japan Agency for Marine-Earth Science and Technology (JAMSTEC) and others whose purpose is to promote wave energy conversion and also provide researchers with testing sites etc.

2.1.1 The resource

It has been estimated that the total world's wave energy capacity is over 2TW [18] from which the efficient electricity production could be around 2000 TWh per year [19]. A more recent study verified the worldwide wave energy capacity to be around 2.11 TW [5] In other words, more than 10% of the available resources could be converted to electricity. This is quite uncertain for now since the wave harnessing technologies have merely been employed and depends on grid losses, harnessing efficiency, other conflicting sea activities etc. The above estimations become more interesting when compared to the current electricity needs. The global electricity capacity was around 5085 GW [3] in 2010 while the annual consumption for the same year was around 20000 TWh [2].

Especially for the UK which is considered to be fortunately placed next to the Atlantic Ocean, it is estimated that on an average day around 1 TWh of wave energy is welcome in the British Isles [15], comparable to the average daily electricity consumption in the UK. Other studies estimate the wave power entering the UK from 30 GW to 80 GW [21–23] depending on the distance from the shoreline, from which 7-10 GW could be obtained as electricity [24] compensating 8.1-11.6% of the UK electricity capacity ($\sim$86.4 GW, 2010) [1]. Undoubtedly, these figures describe a great potential for wave energy extraction currently unexploited, encouraging the UK Department of Energy and Climate Change to estimate that the installed capacity of marine energy will rise to 300 MW by 2020 [25].
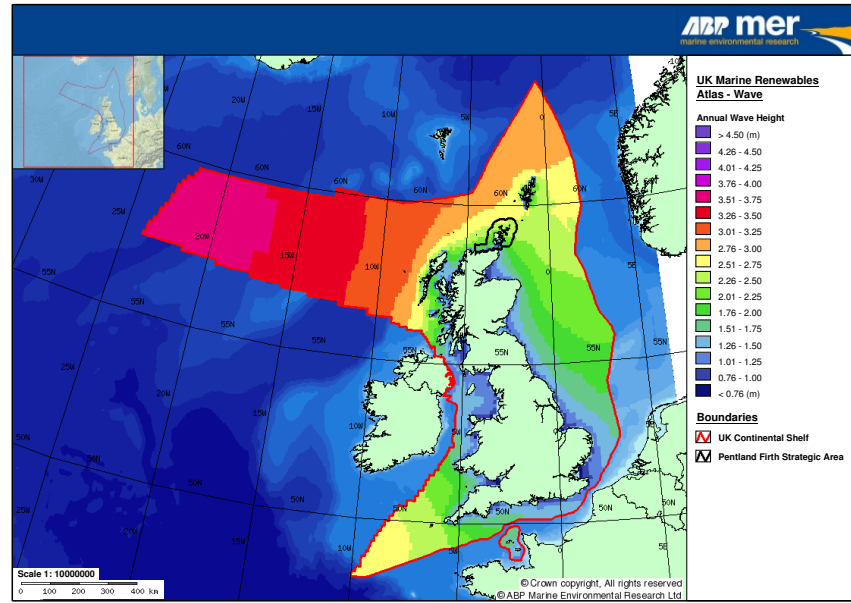
Figure 2.1: The Atlas of UK Marine Renewable Recources has been developed by ABP Marine Environmental Research Ltd in collaboration with the Met Office and Proudman Oceanographic Laborator. It provides a detailed regional map of wave, tidal and wind resources around the UK. Here the average wave height around the UK is shown [20].

Surface waves are an ocean energy form created by the interaction of the sea surface with winds blowing over it. Generically, sea waves stem from solar energy which creates temperature differences along the globe causing winds to blow [26]. Ocean waves could be separated to wind seas, referring to waves grown by a local wind, and to swells, which are waves that travel away from their creation area such as storms. Swells are capable of carrying energy with minimal losses except for when approaching the shoreline when they lose a considerable amount of energy through shoaling, breaking, friction with the seabed, etc. [19, 21]. The advantage of wave energy compared to solar and wind energy is the much higher power density observed in waves. Typically, waves present a power density of 8.42 kW/m^2 on average, while wind and solar 0.58 kW/m^2, 0.17 kW/m^2 [27] respectively, with these data slightly varying among other studies [15, 19, 24, 28]. Note that sometimes, the wave energy density is measured over a unit of the wave' s crest length, eg kW/m.

The amount of energy transported by ocean waves depends on many factors where dominant role play the wind's velocity blowing over the sea surface, the distance over which the wind blows (fetch), the amount of time for which this happens, the depth of the seabed [19]. The resulting waves are characterized by their height H

No	Location	Latitude	Longitude	Annual Average Power (kW/m)
1	Faeroes	62.08 N	8.43 W	80.9
2	Bergen	60.88 N	4.32 E	38.9
3	Shetlands (DB3)	60.50 N	2.60 W	66.9
4	NW (DB2 new)	58.90 N	7.06 W	75.8
5	South Uist	57.39 N	8.06 W	71.6
6	Lima	56.96 N	19.96 W	119.9
7	Malin Head	55.78 N	7.72 W	53.1
8	Islay	55.66 N	6.48 W	29.3
9	Belmullet	54.56 N	10.49 W	89.3
10	Porcupine	52.71 N	12.66 W	95.3
11	Fastnet	50.54 N	9.96 W	73.1
12	Valentia	49.86 N	10.97 W	83.4
13	Scillies	49.86 N	7.09 W	52.4
14	SW (DB2 old)	49.10 N	8.43 W	65.5
15	Ouessant	48.49 N	5.98 W	44.9

(a) (b)

Figure 2.2: (a) Locations for offshore wave power levels assessment; (b) the power levels corresponding to these locations [22].

which is the distance between the upper and lower point that the wave displaces water particles, their period T and their wavelength λ which are the time and distance between successive crests respectively. Swells could travel long distances in deep water maintaining their energy and characteristics (sea state). However, when approaching the shoreline and traveling over shallow waters their height becomes bigger which in turn results in breaking and actually losing a significant amount of energy. Shallow waters are defined by some researchers based on the depth of the seabed being smaller than half of the wavelength, and others smaller than one third of it. Moreover, near-shore and shoreline waves tend to change their direction according to the shore's and seabed' s profiles causing another source of energy loss (reflection, refraction, bending).

In 1992, the Queen's University of Belfast in association with Kirk McClure Morton and Heriot-Watt University conducted a study to evaluate the shoreline and near-shore wave energy resources in the UK on behalf of the Department of Energy [22]. In this report, the authors applied the Meteorological Office's model to calculate the offshore wave characteristics [23], using data from 15 locations around the Western coastline of the British Isles taken from 1983 to 1986. Then, they used the model
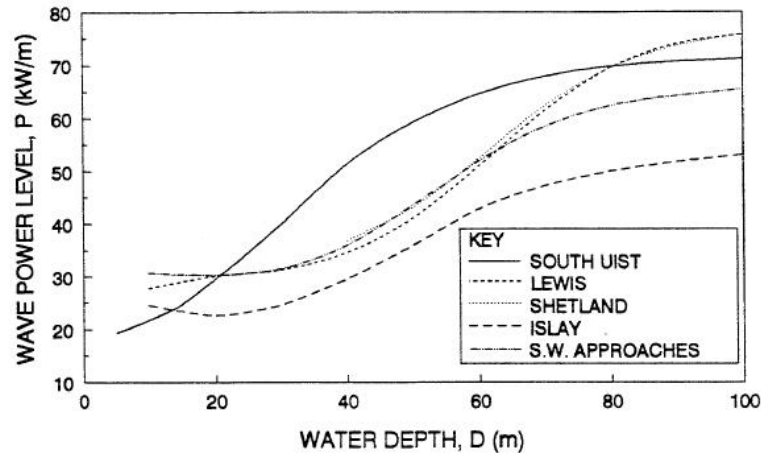
Figure 2.3: Averaged power levels for 5 locations around the UK presented against the seabed depth [21], attempting to demonstrate the wave power losses attributed to the interaction of surface waves with the seabed. Particularly important feature for the available power with respect to the distance from the shoreline.

proposed by Southgate in 1987 to estimate the near-shore and shoreline resources. The data used for the offshore resource assessment were taken from the locations shown in Fig. 2.2(a), while the corresponding power levels in Fig. 2.2(b). The results of this study, which practically started from offshore moving closer to the shoreline showed the resource power levels of Western British waters with respect to the seabed's depth as shown in Fig. 2.3

2.1.2   WEC classification

Over the decades, more than 1000 WECs [10] have been patented worldwide. Though extremely diverse, the classification usually made is regarding their location, orientation, operating principle and power take-off system [10, 19, 21, 24, 28–30]. Note that some of the above classes constrain others meaning that not all of the classifying options are available for all the types of converters.

Location

The characteristic that classifies the device concerning location is the distance from the shoreline. First, there are the shoreline devices. These concepts have the advantage of being placed at the shoreline and thus the transfer of electricity is almost trivial and with losses comparable to ground-based generation plants. Moreover,

maintenance is much an easier task since the devices are approachable through soil. However, their great disadvantage is the available power levels for extraction. As stated before, the power levels at the shoreline drop around 35% of the offshore levels. Additionally, there are some environmental concerns regarding nearby ecosystems and since the shoreline is much more limited compared to offshore deployment options the extractable power reduces even more.

Next, near-shore devices are considered those that are functioning in relatively shallow waters. Most researchers consider shallow waters to be those with depth less than 1/3 of the wavelength. They can be attached to the seabed but still the available power levels are low.

Last, there are the offshore devices which are most often considered. Their great advantage is the high power levels. Indicatively, western offshore waters in the UK carry power of 80kW/m while near-shore 30kW/m. Also, their environmental impacts and generally their impact on ecosystems or human activities is negligible. The main challenges here concern maintenance and power transfer. Moreover, there is the requirement to withstand extremely heavy, even rare, weather conditions such as 10 times fiercer waves than those designed to extract energy from.

Orientation

Here, the classification is made based on the relative direction of the devices' main axis with respect to the main wave propagation direction. An Attenuator lies on the surface with its main axis, i.e. its largest dimension, being parallel to the waves' direction. These devices practically ride the waves and the energy extraction is employed with relative movements of its partially constrained parts due to wave oscillation. Secondly, a Terminator is placed with its primary axis perpendicular to the main wave direction. Both types of devices are very large in length to achieve larger power generation. Last, there are Point-absorbers, of which all dimensions are very small compared to the waves' wavelength. Their main advantage is that they can function irrespectively of the wave direction.

Figure 2.4: Artistic overview of the OWC type of WEC. The incoming waves force the surface level of the water trapped in the capture chamber to rise. Consequently, the contained air is compressed and escapes through the attached Wells turbine, resulting in electricity production. This figure illustrates the LIMPET, an OWC WEC developed by Wavegen. (courtesy of Voith Hydro Wavegen).

Operating Principle

In this part of the classification, WECs are listed in the available categories according to the physical principle employed for the energy extraction. Even though there is significant diversity in the principles, one could narrow down the different concepts to three generic categories.

The *Oscillating Water Column (OWC)* is a device usually deployed at the shoreline or near-shore. Most of the devices listed under this section are mounted on the seabed or on shore-by cliff. A barrier perpendicular to the wave direction blocks the surface waters, while allowing the water at the bottom of the sea to move past the barrier. In that way, a chamber is formed where water and air co-exist. The ways for this chamber to communicate with the outer environment is first, the barrier opening from which water comes in and out depending on whether a crest or trough hits the barrier thus forcing the water column inside the chamber to oscillate vertically. Second, an opening on the top through which air flows in and out forced by the water column. In this opening, an air turbine drives an electrical generator. Most frequently this turbine is a Wells type which functions in both air flow directions. Fig. 2.4, shows a general overview of LIMPET, an OWC converter which has been

(a)   (b)   (c)
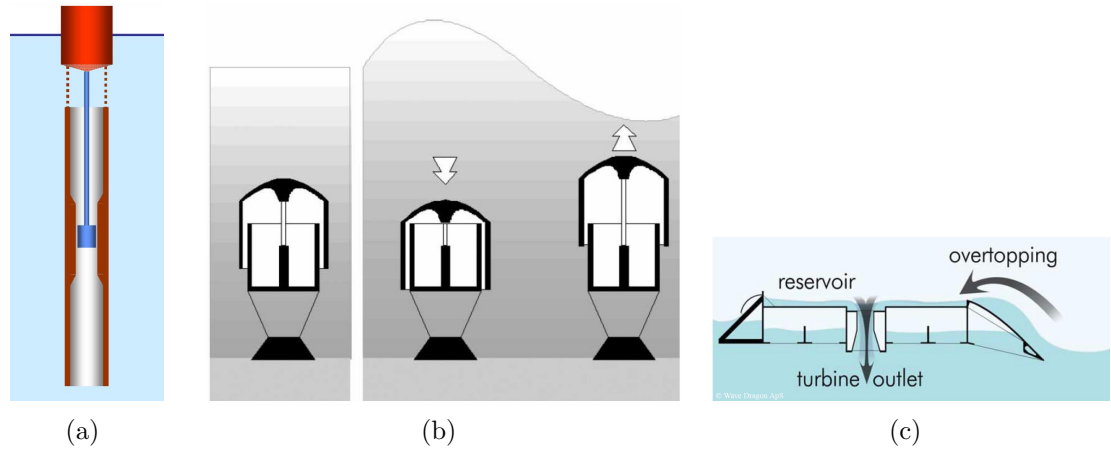
Figure 2.5: (a) The IPS buoy is an OB WEC [29]. The floating buoy follows the wave motion and which is transmitted to the submerged power take-off system. This is usually comprised of hydraulic cylinders which drive an electric generator; (b) The Archimedes Wave Swing. An OB WEC with similar power take-off system. The operational difference is the absence of a buoy, the action of which is replaced by the pressure differential created with the periodic alteration of crests with troughs. [31]; (c) An overtopping device operational principle [32]. A wave tank raised from the average sea level receives incoming waves which fall back into the sea through electricity producing turbines.

deployed at the Islay Island and connected to the UK National Grid.

Another application is to take advantage of the surface waves oscillating movement to force a body to oscillate through either a heaving buoy (Fig. 2.5(a)) or through hydraulic pressure differential formed under wave crests and troughs (Fig. 2.5(b)). These devices are usually designed for offshore deployment where the average power levels are much higher. Here, there are many different ways to achieve energy extraction. The *Oscillating Body (OB)* system might be a single body or multiple, over the surface or submerged, mounted on the seabed or moored and the direction of oscillation could be vertical or parallel to the wave propagation. Also, it could be a pitching device which is at the moment considered to be the most promising concept through the Pelamis application. The corresponding electricity generation also differs from one application to another, but this will be discussed in the power take-off system classification.

Last, *Overtopping* devices (Fig. 2.5(c)) are terminators which create a water tank over the average free-surface level. The water of the crests is driven inside the tank or reservoir and kept there by a surrounding ramp. Then, due to the potential energy of the tank water, this tends to fall down under the influence of gravity and

the device is designed to return the water to the sea through hydraulic turbines thus generating electricity.

Recently, the classification of the operating principle is expanding considering new subclasses such as the pressure differential, the surge converter, the bulge wave, rotating mass and others [30].

Power Take-off System

The power take-off systems are designated to generate electricity by the wave energy which has already been transformed into some form of useful mechanical energy. The kind of systems used depends mostly on the operating principle. Air turbines are used mostly at OWC where the compressed and decompressed air flows through the turbine. The turbine in turn, drives an electrical generator to produce electricity. The most widely used air turbine is the Wells turbine which is self-rectifying, meaning that it functions for both air flow directions. In other WECs, such as overtopping or OB devices, hydraulic turbines are used correspondingly to the air turbine to generate electricity. Moreover, some OB systems, use hydraulic cylinders which are driven by them and act on high-pressure oil. Hydraulic motors then drive their attached generators to produce electricity. Some OB systems use linear electrical generators directly driven by the acting bodies.

2.1.3   Technological advances

As mentioned before, there is a vast number of WECs proposed over the years especially in the last decades. Many of them have been prototyped and tested in laboratory and some in real sea conditions. Here, a brief presentation of the most promising attempts will be conducted to help recognize the current state of the technological achievement.

The *LIMPET*, Fig. 2.4, is a WEC developed by the Queen's University of Belfast and Wavegen. A first 75kW prototype was deployed in the Islay Island at 1991 and was tested for 8 years. After that, an upgrade was decided and a total 500kW

capacity device was constructed and connected to the national grid and was used as a demonstrative example. The LIMPET is a classic oscillating wave column device which uses a Wells turbine to drive the electrical generators. It comprises of a pair of generators of 250kW capacity. The total width of the device required to achieve the 500kW was 21m. The data gathered and published [33] were below predictions. The annual average estimation was 150kW but the actual generation was less than one third of this, charged to the site deficiencies. This application showed an output of around 2.5kW/m [33]. Moreover, shoreline sites suitable for wave energy extraction are limited compared to offshore applications. Voith Hydro Wavegen had announced in November, 2011 that the first commercial action kicked off for a 300kW LIMPET device with the Basque Energy Board in the North of Spain, at the port of Mutriku, expected to be delivering 600 MWh/yr [34].

The second WEC in time to have risen hopes is *Pelamis* (Fig. 2.6), also being the most promising design at the moment. Pelamis belongs to the Attenuator class and its operating principle is pitching - OB. Developed by Pelamis Wave Power and Richard Yemm from 1998 [37], it was the first offshore commercial WEC. This articulated device consists of five semi-submerged cylindrical components linked by hinged joints. The wave excitation forces these components to move relative to one another and this motion is resisted by hydraulic rams. These rams in turn, act on high pressure oil driving hydraulic motors. Electric generators are driven by these motors to produce electricity. Each device is 130m in length and 3.5m in diameter [38] and is designed to function at over 40m deep waters. The first full-scale 750kW prototype was deployed at the EMEC testing site at Orkney in August,
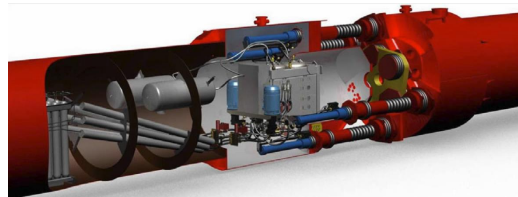
| (a) | (b) |

Figure 2.6: (a) P2 Pelamis working in Orkney [35]. The articulated OB device exploits the relative motion of its parts induced by waves. This motion is received by hydraulic cylinders which act on pressurized oil; (b) An inside look at the Pelamis device [36];

2004. However, the achieved and reported output from these sets of experiments was on average 150kW on a 30 mins basis from a 2007 measurement [36]. After that, the first wave harnessing farm was installed offshore Portugal with 3 Pelamis WECs rated in total at 2.25MW in September, 2008 but only worked for a couple of months.These were known as P1 Pelamis devices since the introduction of an updated design, P2. Two of these new machines have been deployed at Orkney, EMEC for testing in 2010 and 2011 and later updates on the P2 performance show that around 70% [39] of the available energy was exploited and average power output of 100 kW but final reports are awaited. Note that the P2 Pelamis is 180m long.

Another design is the *Oyster* developed by Trevor Whittaker and his team in Queen's University of Belfast from 2002 [40, 41]. In 2005 the design was ready to be prototyped and Aquamarine Power was formed to develop this device. Oyster is a near-shore, mounted at the seabed, submerged OB comprising of a wide buoyant flap hinged at its bottom oscillating under the wave surge action. This motion is translated through hydraulic cylinders acting on high pressure water. This hydraulic system drives a Pelton wheel turbine located onshore to generate electricity (Fig. 2.7). It is quite uncertain if the device can be regarded as a terminator since the flap's main surface lies perpendicular to wave direction but it is much less wide than other terminator devices. In 2009 Oyster 1, as the project was named, was deployed at EMEC's testing site in Orkney rated at 315kW. The flap was 18m

<div align="center">(a)   (b)</div>
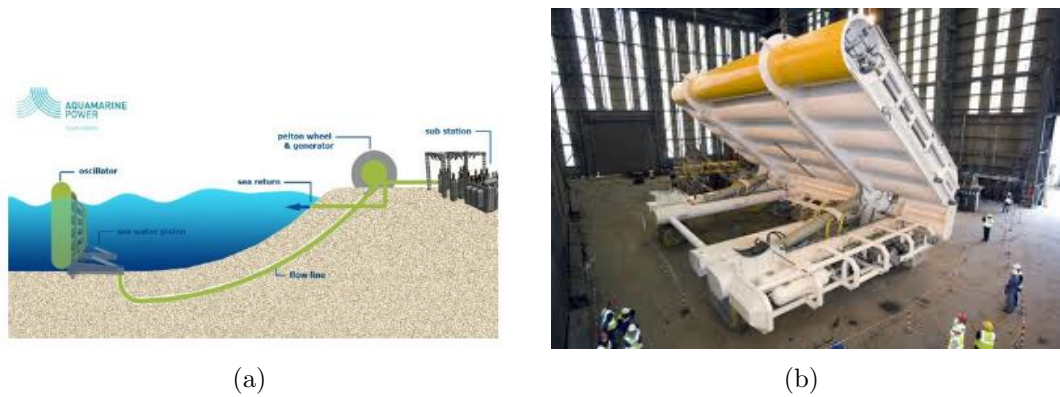
Figure 2.7: (a) A general overview of the Oyster WEC and its power take-off system [40]. The surge motion of waves force the flap to oscillate, a motion which is transferred to hydraulic cylinders. An onshore Pelton turbine converts the energy stored in the medium (sea water) to electricity; (b) The Oyster at the construction site before deployment [41];
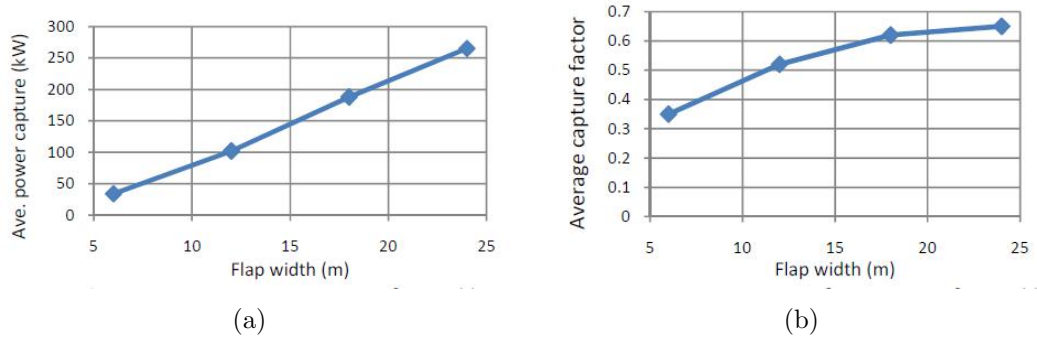
Figure 2.8: Data of the laboratory tests performed on the Oyster in a wave tank [42]; (a) Average tapped power during the tests against the flap width; (b) Efficiency (capture factor) of the prototype for different flap width trials;

wide and 11m high and was deployed at 12m deep waters. Even though this was a small scale proof-of-concept project, earlier wave tank tests [42] showed performance against flap width as in Fig. 2.8(a) and efficiency as in Fig. 2.8(b). A next generation Oyster 800 [43] was installed in Orkney and another two will be installed to achieve total capacity of 2.4MW. The new design flap has 26m width and 12m height and operated generating 1 MWh in 5 hours [44].

Moving to the overtopping class, the *Wave Dragon* was originally developed from the late 1980s. In 2003 a prototype was delpoyed in Nissum Bredning, Denmark until January 2005 [32]. The Wave Dragon is an offshore WEC which uses two reflectors to concentrate waves before overtopping the ramp and driven to the reservoir. The potential energy of the gathered waters is harnessed through low-head turbines,
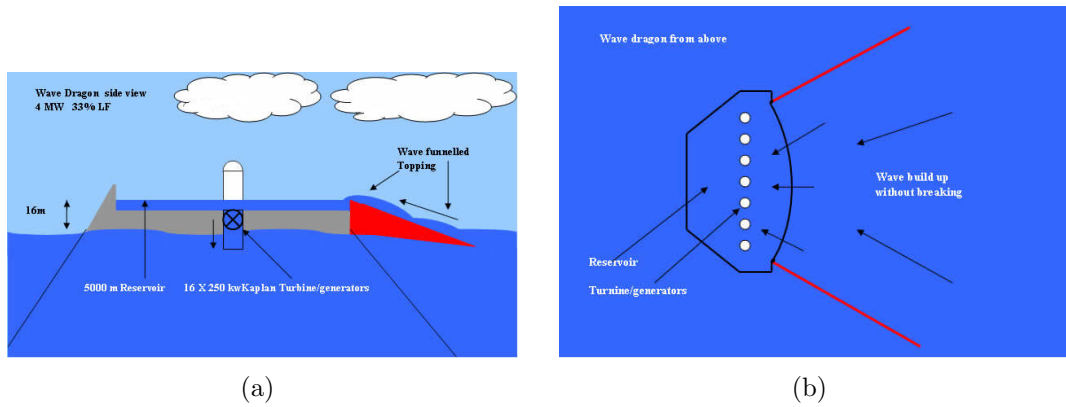
Figure 2.9: Views of the Wave Dragon overtopping device; (a) Side view. Waves build up so that to be directed into the lifted reservoir. The collected water returns in the ocean through Kaplan turbines generating electricity; (b) Top view. The characteristic reflectors could be seen, used to collect waves without causing them to break. [45]

<p style="text-align:center">(a)   (b)</p>
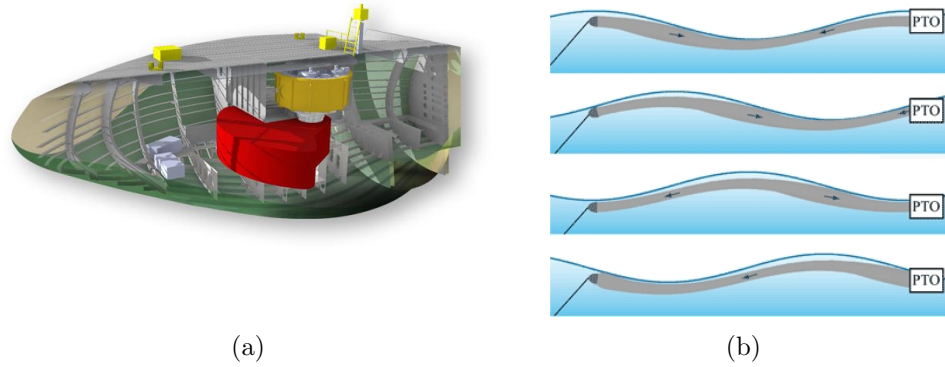
Figure 2.10: (a) The Wello Penguin device is a point absorber OB or rotating mass device with the newest classification [47]. An inner eccentric mass exploits the roll and yaw motion of the floating device to rotate and drive a generator; (b) The Anaconda attenuator [48]. Bulge waves are excited within a destensible tube filled with water, at the one end of which, a generator is attached relieving the bugle pressure in favour of electricity.

before the waters are returned to the sea. The device is moored in relatively deep waters (>25m). Figure 2.9 presents a sketch of the full-scale device of 4 MW and 260m width to be deployed at Ekofisk, North Sea, Denmark. However, until now the only available experimental data concern the 1:4.5 prototype deployed at Nissum Bredning rated at 20 kW with a 58m total width [46] and a 1:1.5 at Hanstholm rated at 1.5 MW and producing 640 MWh/yr out of a 6 kW/m sea.

There are a lot of WECs that have been developed at different stages such as Bolt 2, Penguin, SSG, SEAREV, Seatricity, Waveroller, Archimedes Wave Swing, Aquabuoy, Anaconda, etc. Some of them are actually utilizing a pendulum-like mechanism (SEAREV, Salter's Duck, Penguin). Next, Table 2.1 concentrates some of the WECs developed so far classifying them by their operating principle and listed along with their power output density, with R denoting rated power output. It must be noted that these reported numbers reflect the performance of the corresponding devices under versatile conditions, ranging from laboratory tests up to full-scale sea deployments. Of course, if a comparison is attempted, it can my no means lead to final conclusions, which also reflects the current unsettled state of the field.

Yet, there is a striking observation with a deeper impact on the development of wave energy. The performance of OBs overtakes the power output of OWCs and large overtopping terminators. This is emphasized by Salter's Duck and the Oyster when

Device	Type	Power Output (kW/m)
LIMPET	OWC	2.5
Pelamis	OB Attenuator	1.5
Oyster	OB	10.0
Wave Dragon	Overtopping	0.34
SSG	Overtopping	1.7
AWS-III	Other	41.6(R)
Bolt 2	OB Point absorber	14.0 (R)
Penguin	OB	16.6(R)
Wave Roller	OB	2.2
AquaBuoy	OB Point absorber	5.4
Anaconda	Attenuator	6.6 (R)
Pico	OWC	2.6
OSPREY	OWC	2.0
McCabe Wave Pump	Attenuator	6.4
Salter's Duck	OB	29.7
Mighty Whale	OWC	0.2

Table 2.1: List of the more important WECs shortlisted against their operating principle and presented along with with their power output density in kW/m.

compared with LIMPET and the Wave Dragon. A confusion should be avoided here with attenuators (Pelamis, Anaconda), whose power output is based on their length and not the wave front they take up, which is much smaller than their length. This lead of OBs points the way towards a slightly different path than the current one. The competition with other applied RE technologies, e.g. nuclear power in the 1980s, has driven the development of WECs to aim at large power production units, such as the large structures consisting the OWCs. On the other hand, OBs are smaller, less complex devices with lower nominal power output, but overall, with a higher power output density, as Table 2.1 shows. This means that wave energy conversion would be more efficient in remote applications where the high power density of point absorbers and other OBs could cover the limited power needs of offshore platforms, meteorological stations, offshore field research, maintenance of offshore wind turbines etc. with the advantages of possible relocation of the devices and flexibility in the size of the deployed array to meet specific needs.

Nevertheless, there is a significant drawback with WECs which blocks the way forward, with the case of Salter's Duck being indicative of the challenge. This device is by far the most efficient WEC to date with a power output of 29.6 kW/m. Even
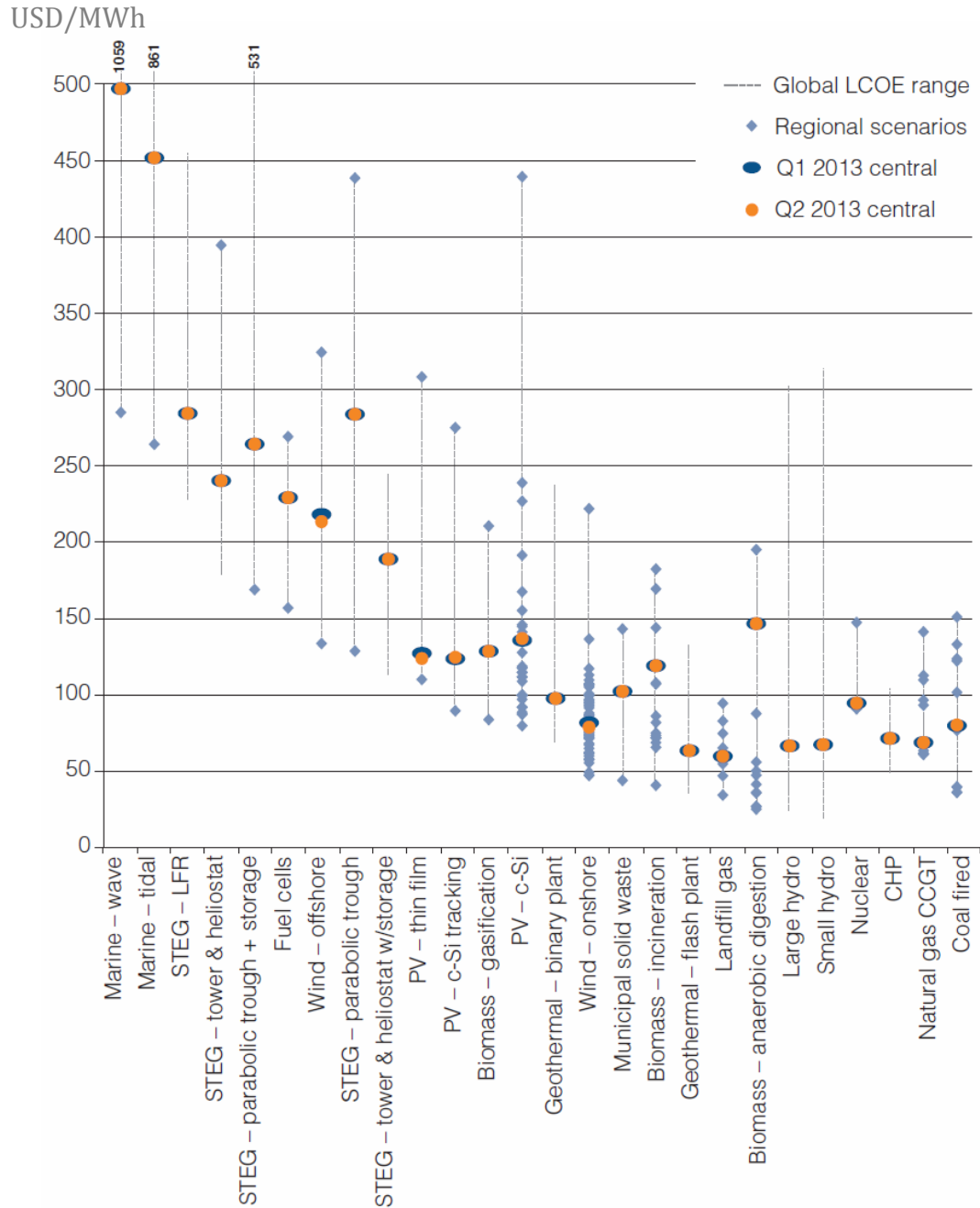
Figure 2.11: Chart containing the LCOE in USD/MWh for the first (Q1) and second (Q2) quarters in 2013. It was published within a report of the World Energy Council on the cost of electricity production [49]. The costs demonstrate the state of the industry for each of the conventional and non-conventional energy sources.

though this number comes from laboratory tests and it is reasonable to expect it to drop in real sea operation, one could recognize the strong potential. However, the cost of construction per kW and the high dependence of its performance on the sea state were the main reasons for which nuclear power was preferred in the 1980s. Ever since, the main challenge in the field of wave energy is cost reduction.

Despite the abundance of WEC technologies, the share in the global energy production is insignificant mainly because of the uncompetitive cost. Currently, wave energy is considered to be the most expensive source of producing electricity. (Fig. 2.11). Example given, a study from 2005 on the OWC devices rated the energy cost of shoreline devices at 17.5p/kWh (LIMPET project in Orkney) while the cost reduces at 9.6p/kWh for a near-shore 22.5MW OWC device [50]. The Carbon Trust in a recent study estimated the cost of wave energy at 38-48 p/kWh [51] with the 2011 state of the industry. Currently, the World Energy Council placed this range at 28-49 cUSD/kWh, when at the same time as Fig. 2.11 shows, conventional sources and mainstream REs provide electricity with just over 5 cUSD/kWh [49]. Furthermore, wave energy is considered a capital intensive industry requiring significant initial investments of 6450-13500 € /kW [52].

Even though the current cost is beyond comparison with that of conventional energy production, one should take into account that most WECs are in the R&D stage with only a handful of devices at the commercialization stage. Nevertheless, there is grounds for belief that areas such as power take-off systems, installation, operation and maintenance, station keeping, grid connectivity as well as a new generation of concept designs are offered for cost reduction through earned experience and optimization [51].

2.2 Parametric pendulum

One of the most interesting phenomena in dynamical systems, known as parametric vibrations, is the vibrating response of a system to time-dependent variations of one or some of its parameters, such as the inertia, the damping and the stiffness [53–57]. The externally applied forces that cause these variations are referred to as parametric excitation. This is the notation that will be used hereafter to distinguish from external excitations, "which lead to inhomogeneous differential equations with constant or slowly varying coefficients" [53], such as the weight of a mass suspended by a spring. The most characteristic feature of these systems is that a resonance occurs at twice their natural frequency (principal parametric resonance), while one

is likely to come across other interesting phenomena, such as chaotic response [54].

This class of dynamical systems could be met in a wide range of engineering applications [53, 54, 56]. Several mechanical systems and large structures could experience parametric resonance. A cantilever beam undergoing axial forcing experiences parametric vibrations [53, 54, 58] shown in Fig. 2.12(a), the surface waves in a vertically excited cylinder filled with water [59], the roll motion of ships and offshore structures [56] and even more complicated mechanical structures such as the turbine engines of a plane that are elastically suspended by its wings [54], large structures and bridges [60, 61] and energy harvesting applications [55, 62] all could experience vibrations falling in the broad class of systems undergoing parametric vibrations. Furthermore, electrical systems e.g. a circuit with constant impedance and varying capacitance (Fig. 2.12(c)), micro-electromechanical systems used in actuators and sensors [63], can undergo parametric vibrations.

    (a)   (b)   (c)
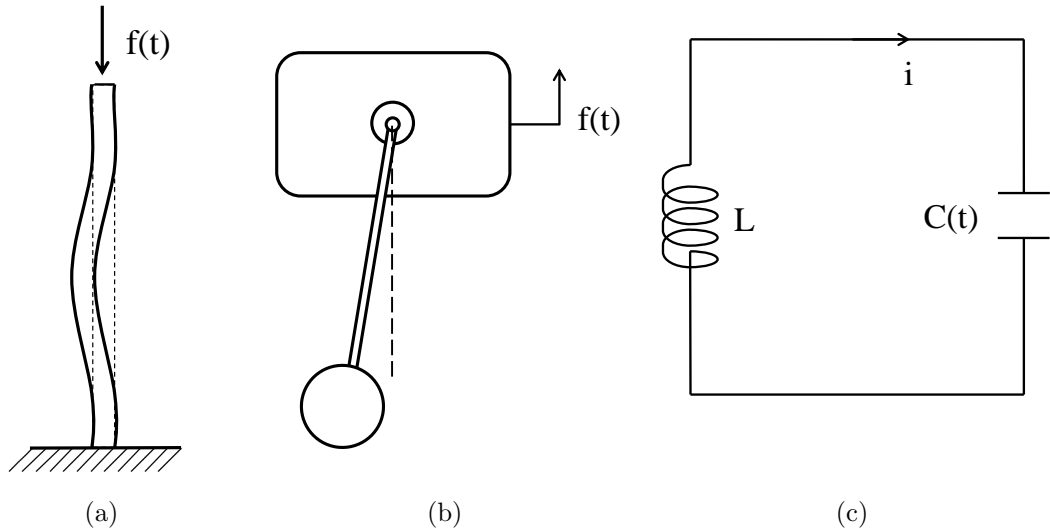
Figure 2.12: Examples of systems undergoing parametric vibrations; (a) axial loading of a cantilever beam; (b) vertical excitation of a pendulum's pivot point; (c) time-dependent capacity in simple electric circuit.

However, a pendulum having its pivot point displaced by a time-dependent force is the most representative of these examples (Fig. 2.12(b)). The parametric pendulum is used throughout the literature to demonstrate the dynamical properties of this class of vibrations, including the instability of the response, the structure of the resonance curves, the rich bifurcations that can be observed, the resulting chaotic response.

2.2.1   Linear stability

A fundamental system in the study of parametric vibrations is described by the Mathieu equation, a special case of the Hill equation with periodic forcing [53, 64, 65], which describes linear systems with time-varying stiffness. In the context of the parametrically excited pendulum, the Mathieu equation corresponds to the linearization of the equation of motion assuming a very small angular motion of the pendulum $(\sin(\theta) \approx \theta)$ and essentially describes the dynamics of the equilibrium point. The general mathematical expression of this class of systems is:

$$\ddot{\theta} + (\delta + 2\epsilon \cos 2t)\,\theta = 0 \tag{2.1}$$

Mathieu [66] introduced this equation while studying the vibrations of an elliptical membrane. Floquet's theory [53, 54] developed as early as 1883 to provide an analytical solution to the problem and proved that the normal solutions of Eq. (2.1) are the product of a periodic, thus bounded, function with an exponential one. The latter's argument is the product of the *characteristic exponent* with time [53]. Depending on the sign of the characteristic exponent, these solutions are bounded (negative sign), periodic (equal to zero) and unbounded (positive sign) as $t \to \infty$.
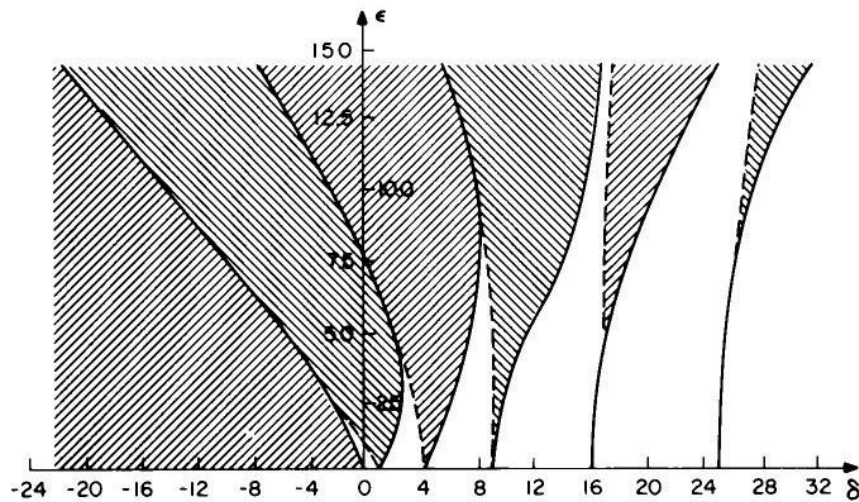
Figure 2.13: The Strutt diagram [53]. Illustrative separation of the stable solutions of the Mathieu equation - Eq. (2.1), from the unstable ones (shaded area) with respect to the parameters of the system.

On this basis, the so-called Strutt diagram has been produced [53, 67], illustrating the dependence of the stability of the solution of Eq. (2.1) on the parameters δ and ϵ. In Fig. 2.13, the regions of stable solutions are separated from the unstable ones in the shaded area.

There are several analytical techniques for deriving the stability-instability boundaries including Hill's infinite determinants, perturbation methods, Lyapunov stability theory [53, 64, 65]. The structure of the stability-instability boundaries contains the so-called resonance tongues, which are the zones at which unstable solutions arise for low ϵ. In terms of frequencies, these tongues initiate at particular frequency ratios and specifically, for $\omega/\Omega = 2/n$, $n = 1, 2, 3, \ldots$ with ω the exciting frequency and Ω the system's natural one. Note that $n = 1$ leads to the double frequency ratio and the principal parametric resonance. Another known effect is connected to viscous damping, which has been found to displace the whole diagram towards higher values of ϵ, or in other words, increasing energy dissipation requires higher input energy from the excitation to achieve the same response [53].

In view of the response of a pendulum to parametric excitation, Eq. (2.1) is an expression of the linearized equation of motion. It is well-known in the stability theory of nonlinear systems [65, 68], that the stability of the trivial solution could be extracted from the linearization of the equation of motion around the neighborhood of the equilibrium point. Unstable solution of Eq. (2.1), means that the pendulum escapes from the potential well of the equilibrium and starts swinging, even though this expression cannot describe this motion and one needs to resort to the pendulum's full dynamics.

2.2.2   Stochastic excitation of the linear system

The influence of randomness on dynamical systems has been a major front in the past decades. A broad subject arises by the time that the parametric excitation of the linear system in Sec. 2.2.1 cannot be considered periodic and has to be treated as a stochastic process. There are many textbooks on stochastic excitation of dynamical systems and some are concerned with random parametric vibrations [57, 69, 70].

Ibrahim [57] concentrated and presented numerous works on random linear systems with time-varying coefficients. Linear systems with coefficients perturbed by wide-band stochastic processes were discussed. Ariaratnam and Tam [71] extended the stochastic averaging of Stratonovich [72] who studied the system with random wide-band stiffness, to include a periodic term added to the perturbation of the stiffness coefficient around the region of the principal parametric resonance. Extensive review on averaging techniques of stochastic systems can be found in [57, 73]. The stability of the linear system is reflected onto the stability of the first and second moments, shown in Fig. 2.14.
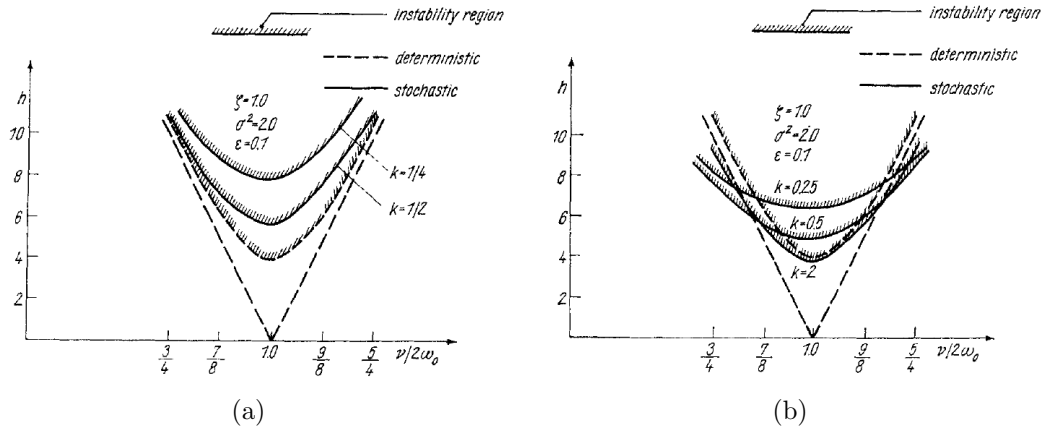
Figure 2.14: Stability curves computed by Ariaratnam and Tam [71] through stochastic averaging around the principal parametric resonance ($\nu/2\omega_0 = 1$) and the method of moments [57, 69], for exponentially correlated random excitation; (a) the stability diagram for the first moment; (b) the stability diagram for the second moment where k controls the damping coefficient, σ^2 the noise intensity and ϵ is a small parameter.

Dimentberg [69] conducted a comprehensive study on random systems with parametric excitation. Among numerous others, linear systems with disordered periodic parametric excitation were considered. First, nonlinear damping was added to the system studied in [71] and the influence of the stationary broadband random fluctuation of the periodic variations of the stiffness were considered through stochastic averaging. The critical value of damping for instability and an expression for the variance of the response amplitude were derived and it was shown that noise can have a stabilizing effect due to the induced fluctuations of the phase of the response process and a destabilizing one through the influence on the amplitude equation.

Furthermore, the linear stiffness fluctuated by imperfect periodic variations has also

been considered in [69]. This model assumes random frequency of the sinusoidal variations in Eq. (2.1) by a broadband process. The resulting excitation is similar to the output of a linear filter, with the main feature being the narrow-band spectral density [74, 75]. This type of excitation is commonly referred to in the literature as narrow-band random excitation [74–83] and this term will be adopted here as well.

The stability of the response of the linear system to parametric narrow-band excitation has been the subject of a plethora of studies. Dimentberg [69] applied stochastic averaging to calculate the PDF of the phase process through the Fokker-Planck-Kolmogorov (FPK) equation. The expression for the critical damping that was derived allowed for quantification of the stabilization effect – Fig. 2.15(a) – in terms of the increase of the minimum excitation amplitude needed to cross the critical value and its relation to the noise intensity. The same system has been investigated by Wedig [74] with a different approach. The Lyapunov exponent of the amplitude process has been numerically calculated to arrive at similar conclusions regarding the stability of the response (see Fig. 2.15(b)). Moreover, Rong et al. [78] used the multiple scales method [84, 85] to derive the equations with respect to the amplitude and phase of the response. The FPK equation was solved for the phase process and the Lyapunov exponent was used as an instability indicator. The multiple scales method obtained results similar to Dimentberg [86] and Dimentberg et al. [87] who followed up on previous work and elaborated on the formulas for the critical damping. The mean-square stability and the corresponding boundary formulas have been derived through the method of moments [57, 69] as well. A comparative analysis was performed between mean-square stability and stability in probability against the excitation's and system's bandwidth by Dimentberg et al. [87]. Much lower excitation bandwidth was found to eliminate the differences between the two approaches while increasing this ratio would converge to a maximum ratio given constant system parameters. The mean-square stability of the Mathieu equation with parametric narrow-band excitation was also investigated in [79], where a truncated infinite hierarchy of linear differential equations for the mean response was developed. The eigenvalues of this system were used to determine the mean-square stability, overcoming the requirement for small excitation parameters inherent to

(a) (b)
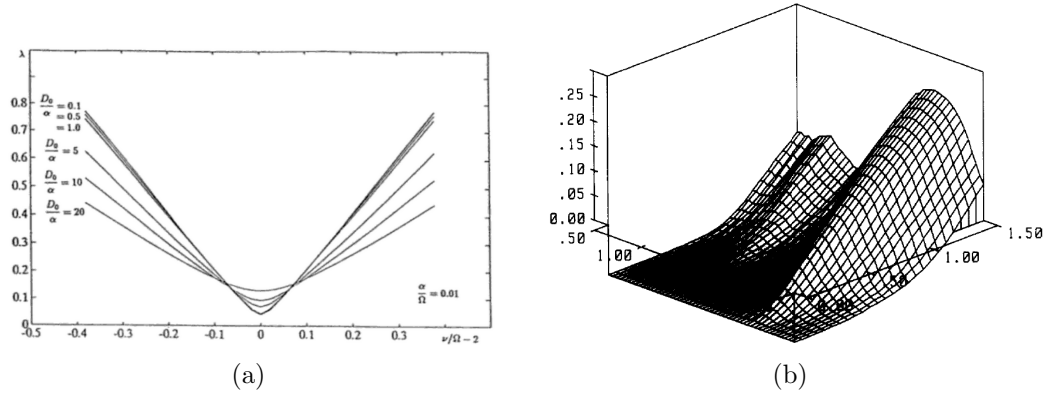
Figure 2.15: (a) Instability boundaries for the principal parametric resonance of the linear system calculated based on a stochastic averaging approach jointly with solving the FPK equation for the phase process with λ being the excitation amplitude, ν – the excitation frequency and Ω – the system's natural frequency. According to the notation used by the authors, the damping coefficient was defined as $c = 2\alpha m$, which reflects that $\alpha/\Omega = c/2m\Omega = c/c_c = \zeta$. Thus, the boundaries presented here were computed for a constant damping ratio $\zeta = 0.01$. Increase of the noise intensity D_0 leads to the boundaries being pushed upwards close to the resonance and become wider [87]; (b) Lyapunov exponents calculated numerically for the same linear system undergoing the same type of excitation. The numerical analysis includes the total of the parametric resonances [74].

previous studies based on stochastic averaging. The almost sure stability of the pth moment was discussed in [82, 88], where a perturbation technique was utilized to derive approximate analytical results and compare them against numerical ones.

In addition, parametric narrow-band excitation has been considered in conjunction with deterministic excitations. Sri Namachchivaya [89] applied a stochastic averaging method and solved the FPK equation for the phase PDF for a linear system with narrow-band parametric and external harmonic excitation. The almost sure stability of the MDOF system was evaluated by means of the Largest Lyapunov Exponent (LLE). Dimentberg et al. [77] derived the mean-square stability of the same system using the method of moments, with the difference that they considered a narrow-band density for the external excitation too. Also, a combination of a harmonic and narrow-band excitation, both parametric, was investigated in [76] using the multiple scales method and Lyapunov exponent analysis. Other studies [80, 81, 90] have considered a similar excitation for Duffing-type oscillators as well, even with combined external and parametric excitation [90].

A common conclusion throughout the aforementioned literature is the fundamental feature of the randomness of the excitation to simultaneously stabilize the response

to lower amplitudes close to the resonance and destabilize it for higher amplitudes and more detuned excitations. Intuitively, looking at Fig. 2.15(a), the instability boundaries move upwards and get wider with increasing noise intensity. This is an important characteristic which will be considered hereinafter.

2.2.3 Nonlinear dynamics of the pendulum

Considering a nonlinear restoring force, and particularly a sinusoidal dependence of the stiffness on the displacement, one is led to the original equation of motion of a pendulum. The pendulum is a classical system widely used for demonstrating fundamental properties of nonlinear dynamical systems [53, 65, 68]. Within the context of parametric vibrations, pendulum systems enjoy a respectable attention primarily through a time-varying stiffness and secondarily through nonlinear damping.

The response of a pendulum to parametric excitation by a harmonic force is characterized by a rich dynamics. The counterintuitive outcome of the stabilization of the up standing position has been shown as early as in 1908 by Stephenson [91], as Clifford and Bishop [92] report. A rich variety of homoclinic, saddle-node, pitchfork bifurcations and period-doubling cascades (Fig. 2.16) could also be observed modifying the motion of the pendulum among oscillatory, rotary and even chaotic response.

Koch and Leven [9] used the Melnikov method to identify homoclinic bifurcations in the response of a vertically perturbed pendulum. Applying a second order averaging on the Melnikov functions, the authors identified that increasing excitation amplitude gives rise to a series of period-doubling bifurcations leading to homoclinic orbits. The analytical results were confirmed against numerical investigation. The homoclinic bifurcation is a known indication for the route to chaos, a behaviour that has been reported for the parametric pendulum by Leven and Koch [93]. The period-doubling route to chaos has also been experimentally found [8], side by side with subharmonic periodic motions arising from a saddle-node bifurcation. The authors also reported that the difficulty of recording periodic orbits would increase with higher periods due to small size of their attractors which nevertheless were
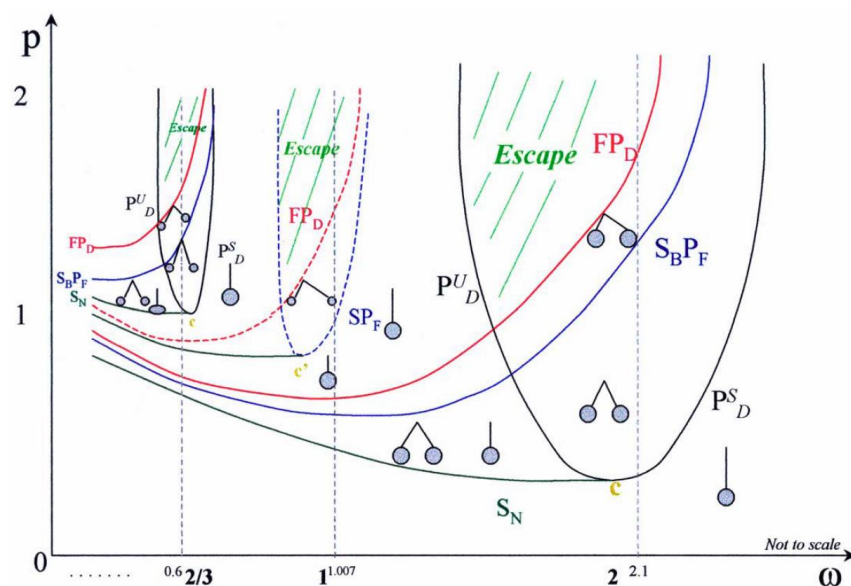
Figure 2.16: Schematic representation of the bifurcation curves in the parameter space with ω being the ratio of the exciting frequency over the natural one and p the non-dimensional excitation amplitude. P_D^S is a period doubling bifurcation giving rise to oscillations around the equilibrium. $S_B P_F$ is a symmetry-breaking, pitchfork bifurcation and FP_D represents the first bifurcation in a sequence of period doubling cascade that then leads to loss of stability. SN is a saddle-node (fold) bifurcations and the Escape zone denotes the parameter region where no major stable non-rotating solution exists. The symmetric and asymmetric oscillations are also denoted [97].

found to coexist. Symbolic dynamics have been applied in [94, 95] to analyze the oscillatory response with a view on the escape from the potential well. For the latter in particular, Clifford and Bishop [96] employed a harmonic balance method in conjunction with the critical velocity criterion targeting the zone where no stable non-rotating orbits exist.

Bishop et al. [97] studied the symmetry-breaking pitchfork bifurcations experienced in the response of the parametric pendulum. The authors numerically constructed bifurcation diagrams in which they also reported the period-doubling bifurcations of the first three resonance zones. The pitchfork bifurcation boundary was found to break the symmetry of the period-2 oscillations before the period-doubling cascade unfolds the route to chaos. This bifurcation was connected to a counter-intuitive possibility of reduced response amplitude with increasing excitation amplitude. It was emphasized that this reduction might as well indicate the forthcoming cascade and the symmetry-breaking was in general understood as a sign of escape from the potential well of the downwards hanging equilibrium. In a subsequent work, Sofroniou and Bishop [98] studied a perturbed asymmetric model by means of a harmonic

balance method. The induced asymmetry eliminated the symmetry-breaking pitch-fork bifurcation with the period-doubling cascade leading to escape from the bottom well.

The global bifurcations that lead to the escape zone have also been studied in [99]. The boundaries of the coexisting rotating and oscillatory attractors have been found to be fractal-based, an indicator of the existence of chaos in the system. The role of the oscillation-rotation attractors in the occurrence of chaos but for an externally excited pendulum were also studied in [100]. Moreover, the chaotic response has been reported in [101] where chaos was found to occupy a significant portion of the parameter space as opposed to rotating and oscillating chaos which were found in narrow regions. Though interesting enough, chaos is mainly avoided in engineering applications with control strategies designed towards that, such as in De Paula et al. [102], where the extended time-delayed feedback was applied to control the development of the bifurcations and steer the response away from chaos. Lenci and Rega [103] on the other hand, examined the properties of the oscillatory and rotary attractors in the parametric pendulum testing their dynamical integrity. Two measures were employed towards that, the global integrity measure and the integrity factor. Their analysis measured the robustness and the "safe region" of each attractor and unveiled the mechanism with which rotary attractors lead to erosion of the oscillatory ones.

However, as interesting as the oscillatory response of the parametric pendulum and the associated bifurcations might be, many researchers have been concerned with the rotational response by applying analytical [9, 104–107] and numerical [7, 108–110] techniques.

In an extensive numerical study, Xu et al. [7] built the full structure of the resonance curves calculating the Lyapunov exponents for varying excitation frequency and amplitude. In that way, PSPs – Fig. 2.17 – were constructed for different initial conditions and damping values denoting the type of the response in each point of the grid. Asymptotically stable response (F), period-1 and period-2 oscillations (O1 and O2 respectively), period-1 (R1) and period-2 (R2) rotations, chaos (C) and
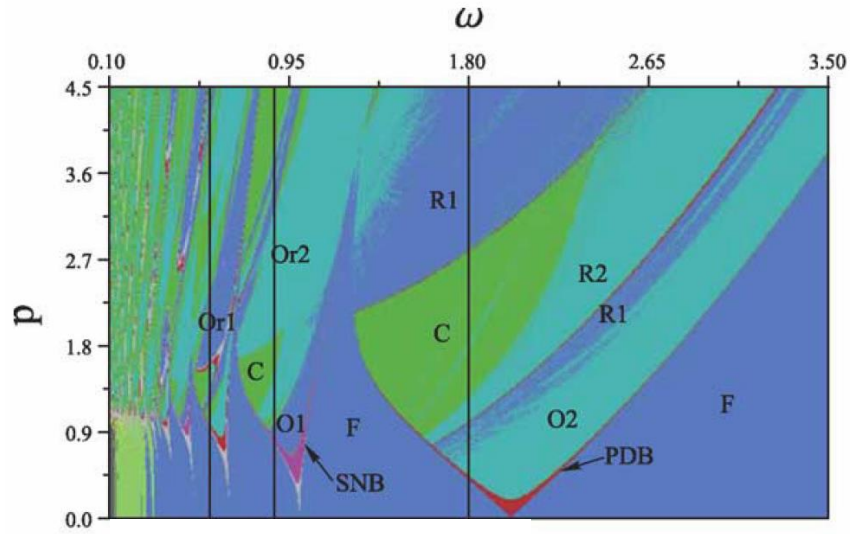
Figure 2.17: Numerically constructed PSP differentiating the different types of responses of the parametrically excited pendulum within the parameter space of the non-dimensional excitation frequency ω and amplitude p. F denotes a stable equilibrium, $O1$ period-1 oscillations, $O2$ period-2 oscillations, $R1$ and $R2$ period-1 and period-2 rotations respectively, C denotes chaos, $Or1$ period-1 oscillations-rotations and $Or2$ period-2. The saddle-node bifurcation is also marked by SNB and the period-doubling by PDB [7].

mixed periodic oscillatory-rotary response of period-1 and period-2 were reported. Pure rotations have only been found for the principal parametric resonance zone. From a design point of view, the approach of PSPs offers the advantage of joint variation of the frequency and the amplitude of the excitation as opposed to bifurcation diagrams, functioning as a more complete tool in the search of rotational response. This important study has been done on the groundwork offered by previous numerical studies [108, 109] as well as the bifurcation analyses presented before. Clifford and Bishop [108] were too concerned with mapping the rotational response of the parametric pendulum. Their view was highly attached to the escape from the potential well problem and they concluded the ambiguity of the non-existence of a certain boundary separating rotations from oscillations, meaning that such a boundary would not exclude the occurrence of a rotational solution below it. Rotations were treated with respect to their period n and the number of full revolutions r within each period and were denoted as (n, r). A saddle-node bifurcation was recorded giving rise to (1,1) rotations followed by a period-doubling leading to (2,2) rotations and initiating a cascade to chaos. This devolves to (1,1) rotations through a reverse period-doubling cascade. This work [108] is the first to have purely considered the rotational solutions and their classification after the early work by Koch and
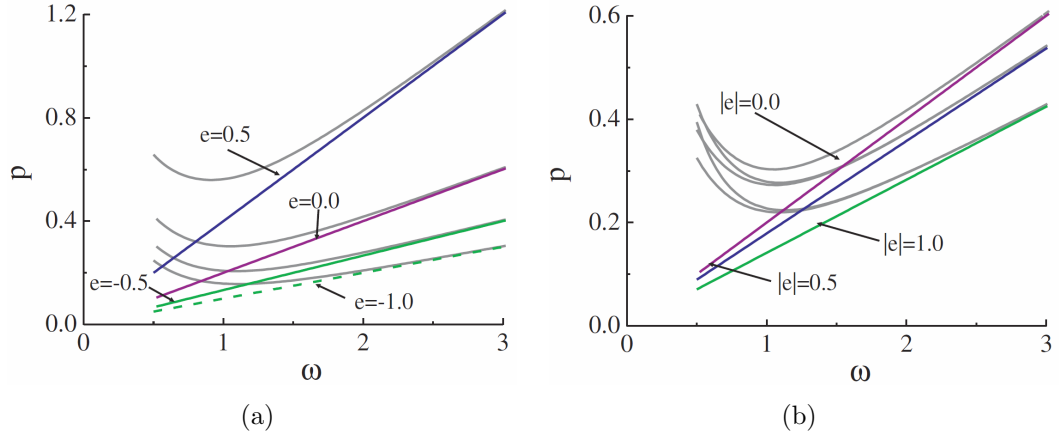
Figure 2.18: Boundaries of the saddle-node bifurcation occurring in (a) the elliptical excitation of the pendulum's pivot and (b) the tilted excitation within the parameter space with ω being the ratio of the exciting frequency over the natural one and p the non-dimensional excitation amplitude. Solid gray lines denote numerical calculation of the bifurcation boundaries and colored lines the approximate analytical evaluation through asymptotic method. The parameter e controls the ratio of the excitation's horizontal amplitude over the vertical. Analytical estimations of the boundaries hold good agreement with the numerical results in the high frequency range [106].

Leven [9]. Garira and Bishop [109] attempted to further standardize the rotational solutions distinguishing different types of rotational motion.

Along with the numerical studies, one would have to pay attention to the analytical work carried out to seek rotational solutions. Regarding the vertically excited parametric pendulum, Xu and Wiercigroch [105] employed the multiple scales method to analyze the pendulum when its response angle is small (the linear system in Sec. 2.2.1) and large as well. The approximate analytical solution of period-1 rotations were obtained and the analytical boundaries were benchmarked against numerical results. Further analytical treatment was performed by Lenci et al. [104], who employed a perturbation method which considered the trajectory of the solution thus incorporating the initial conditions. An explicit formula for the first-order terms of the system's map was obtained while higher order ones involved numerical calculation of the associated integrals. The stability of the rotating solutions was extracted through the Jacobian of the map. The authors reported an excellent agreement with numerical results of the trajectories and effective prediction of the saddle-node bifurcations. This method has also been extended to the case of combined vertical and horizontal excitation [111].

Besides these studies, several modifications of the governing equation of a simple pendulum have also been considered, mainly related to the direction of the excitation. Schmitt and Bayly [112] considered the horizontal harmonic perturbation of the pivot point. The method of multiple scales was employed to predict the mean angle bifurcations, later to be tested against numerical and experimental results. A rather interesting finding was that the experimental imperfections which could be thought of as a bias external torque in the system, destroys the pitchfork bifurcation and replaces it with a saddle-node. This is analogous to the effects of an asymmetric model reported by Sofroniou and Bishop [98] for the vertically driven pendulum. A planar pendulum was considered by Mann and Koplow [113] having a tilted direction of its pivot's motion. Again, the system was treated by the multiple scales method up to the second order and the mean angle bifurcations revealed a symmetry-breaking for the tilted excitation as well. Experimental verification followed the analytical predictions. Morrison and Wiercigroch [114] used the Melnikov function to identify the homoclinic bifurcation in an elliptically excited pendulum. The lower bounds for the escape to rotations was connected to the occurrence of the homoclinic bifurcation as in [9] for the vertically driven pendulum, and a small but quantifiable reduction of this boundary was found for increasing ellipticity of the excitation. The rotational solutions of the planar pendulum have been sought by analytical means. Pavlovskaia et al. [106] used an asymptotic perturbation method to track rotational solutions for both the elliptical and tilted pendulum. Numerically constructed basins of attractions and phase plots were used to verify the derived formulas. The comparison with previously [110] extracted parameter boundaries via numerical means showed that the analytical approximation, shown in Fig. 2.18, could predict correctly the boundaries for higher frequencies, while in the range of lower frequencies the analytics were not able to spot the upwards shift of the saddle-node bifurcation. Yet, the qualitative difference between the tilted and elliptical excitation was visible with the former incurring a less abrupt shift. Belyakov [107] used the multiple scales method to derive approximate rotational solutions for a pendulum excited by an ellipse, close to a circle for high frequencies.

Horton et al. [110] conducted an exhaustive numerical study concentrating on the

bifurcations experienced by the elliptically excited pendulum in a large area of the parameter space. Their analysis was separated into presenting the oscillatory response with the corresponding fold, pitchfork and period-doubling bifurcations. On another level, the bifurcation curves associated with the rotational response were presented in the 2D parameter space and compared against the purely vertical excitation case. An important observation is that the bifurcation bounds are differentiated for each direction of the rotations. It was found that lower amplitudes are required for rotating unidirectionally with the elliptical excitation. More significantly, the distinct principal and secondary resonance tongues merged into one confined by a period-doubling and a fold bifurcation.

Moreover, the nonlinear pendulum equation has been a subject of stochastic analysis as well. Yet, most studies considered an external Gaussian white noise excitation (see for example [69, 115–118, and references therein]), modelling randomly fluctuating torque applied at the pivot. In these cases the usual track of action is attempting to solve the FPK equation to extract the PDF of the response using different methods such as early path integrals [115], Monte-Calro (MC) methods [116, 117], finite element based discontinuous Galerkin method [118].

As long as parametric stochastic excitation of this nonlinear system is considered, the FPK equation is much more difficult to solve, especially when the white noise excitation is filtered. A direct white noise parametric excitation of the nonlinear pendulum was considered in [119–122]. Landa and Zaikin [119] and Landa and Zaikin [120] considered the randomly fluctuating stiffness of the pendulum under nonlinear damping. The nonlinearity was expanded in the Taylor series and an asymptotic expansion of the solution was used to attain a solution to the FPK equation. The adopted approach was benchmarked against numerical realizations of the stochastic system addressing the problem of distinguishing deterministic chaos from stochastic oscillations. Following on that, a harmonic control force was proposed in [121] and the intensification or the suppression of noisy oscillations was investigated. It was found that noise induced phase transitions result in the appearance of a stable attractor around the upper equilibrium. A similar system was considered by Perkins and Balachandran [122], linearly damped with parametric excitation consisting of

a harmonic part and a white-noise Gaussian process. The bifurcation stabilizing the saddle fixed point was considered in the stochastic frame. Noise was found to stabilize the saddle for forcing parameters that in the deterministic frame lead to unstable behaviour of the upper equilibrium. Thus, one could understand this as a noise-induced bifurcation and based on that a controlling scheme depending only on the noise intensity was proposed allowing to switch between the two stable equilibria.

The manipulation of a Gaussian white noise, though, becomes more difficult when it is filtered to a narrow-band process. Liu and Zhu [123] were concerned with the homoclinic bifurcation triggering the onset to chaotic response of the pendulum to periodic excitation. They considered the so-called disordered periodic excitation or sinusoidal excitation with random phase modulation. The random Melnikov process was utilized to derive threshold for the homoclinic bifurcation adjoint with numerical calculation of the LLE as a comparison frame for the former. A similar model was considered in [124, 125] of external and parametric excitation with randomly fluctuating frequency by a Gaussian white noise. This work followed the question of the stabilizing effect of noise on chaotic attractors. MC simulations were conducted and the LLE was calculated for several forcing cases to demonstrate this effect.

Further on, a handful of studies were focused on the rotational response of the pendulum under stochastic parametric excitation. Litak et al. [126] conducted MC simulations for a limited number of forcing conditions and constructed bifurcation diagrams with respect to the standard deviation of the random process perturbing the frequency of the excitation. The rotational number, being the ratio of the mean response velocity over the mean excitation frequency, was used to indicate the type of the response and based on that, it was found that rotational motion eventually degenerates to chaos. A similar procedure of bifurcations of the rotational number was employed by Horton and Wiercigroch [127] with the difference in the model of the noise. Specifically, a second order linear filter was used with a Gaussian white noise as an input. The output of this filter is a narrow-band process with a spectrum equal to the previous model. Also, the realization of the stochastic process was performed according to the spectral representation found in [128]. This
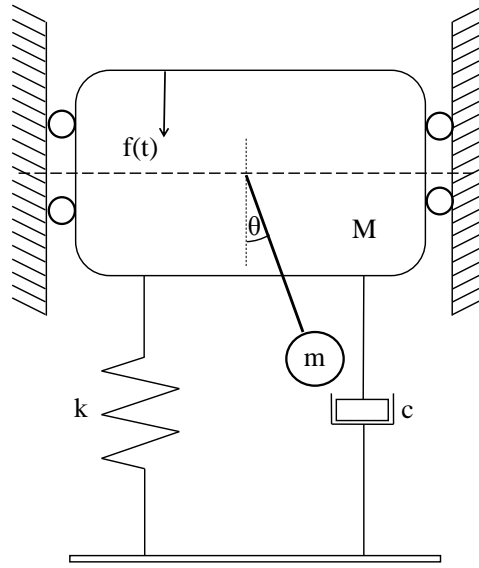
Figure 2.19: Sketch of a pendulum autoparametric system. Vibrations of an elastically suspended mass M parametrically excite a pendulum hinged on it.

study also reported a transition to chaos with increasing noise intensity for a limited however number of parameter pairs.

2.2.4 Autoparametric system

Autoparametric systems is a class of dynamical systems which have at least two DOFs, one of which is called the primary system and the other secondary. Tondl et al. [55] define these systems by stating "the vibrations of the primary system act as parametric excitation of the secondary system, which will no longer remain at rest". A typical example of this class is a pendulum attached on a mass which is suspended on a spring (Fig. 2.19). The study of these systems mainly originates from the development of vibration absorbers [54, 55, 129–132] but have been used to model other dynamical structures such as the effect of heave and pitch motion on the roll of a vessel [55, 133, 134] and flow induced vibrations of self-excited systems [135, 136]. A broad review of the characteristics and applications of such systems can be found in [54, 55, 133, 137].

Haxton and Barr [129] introduced the study of a typical autoparametric system in the context of a vibration absorber aiming to reduce the amplitude of the vibrations of the primary mass through the parametric vibrations of an attached cantilever.

Theoretical and experimental response curves of the amplitude of the primary mass suggested the efficiency of the concept for low excitation amplitudes. For higher amplitudes, the harmonic balance method was employed [138, 139] to obtain stable harmonic solutions. It was found that increasing excitation amplitude leads to amplitude modulated solutions and further increase to chaotic response. Bajaj et al. [130] considered the averaged equations of the first order and the response amplitudes were sought for a system with a pendulum instead of the cantilever. Hopf bifurcations were detected resulting in limit cycles and then to chaos after a period-doubling cascade. The second order averaging was considered by Banerjee et al. [140]. Cartmell and Lawson [131] used the multiple scales method to model the response of an experimental setup of this vibration absorber design. A control method based on the detuning was applied to optimize the absorber's performance. Song et al. [132] used the harmonic balance method and a third order approximation to analyze the response characteristics of a pendulum-mass autoparametric system. The amplitude range of the pendulum for which the approximation was found to be reliable was evaluated with respect to the corresponding suppression the primary amplitude. More complicated layouts have also been studied, considering nonlinearities in the primary system [141–144] or multiple pendulums [145]. One should not neglect to mention the studies considering random excitation of autoparametric systems. The classical cantilever vibration absorber has been considered by Ibrahim and Roberts [146, 147] excited by a broad-band stochastic process, and was analyzed by means of a Markov vector approach and an assumption of Gaussian closure of the dynamic moments equation. Roberts [148] extended the previous work applying a perturbation analysis to extract the mean-square stability boundaries, followed by experimental confirmation. Recently, Onu et al. [149] applied stochastic averaging of the autoparametric system with linear primary subsystem and a pendulum as the secondary one.

Within the frame of the autoparametric pendulum structure, one might consider an additional pendulum with an independent DOF hinged to the primary mass in Fig. 2.19, similar to the general model in [145]. This brings up another interesting phenomenon besides the suppression of the vibrations of the primary system, namely

the synchronizing effect. Huygens was the first to observe the phenomenon of synchronization in his famous two pendulum clocks and since then it has found several applications [150, 151]. Apart from the small amplitude oscillations, synchronous rotational motion of multiple pendulums has been considered in the literature. In particular, an extensive review of the studies concerned with n pendulums mounted on a beam can be found in [152]. Czolzynski et al. [153] considered n identical pendulums hinged from a horizontally excited beam, rotating in the same direction as a result of an external torque excitation. Complete and phase synchronization was identified through numerical solution of the case of $n = 2$ and $n = 3$. The conditions for synchronization and the average phase shift between the pendulums in the synchronized state were also approximated analytically by assuming harmonic motion of the pendulums. The same procedure of the synchronization momentums supported by numerical solutions has been followed in [154] where one of the n pendulums was rotating in the opposite direction. A richness of different types of synchronization states was reported despite the opposite direction of rotations. Lazarek et al. [155] considered two pendulums driven by different torques. Among the synchronized states that have been found numerically, the authors reported the case of a rotating pendulum attracting the second one, initially at rest, to a rotating regime with synchronized mean velocity. Extending their previous approach, Czolczynski et al. [156] considered a number of self-excited pendulums dissipated by van der Pol damping and hinged by a beam with a vertical DOF. Several types of synchronization were observed in the numerically calculated oscillatory response depending on the number of the considered pendulums including complete, anitphase, quarter-phase, 60°, 120°, 90°+90°. The beam free to vibrate in the vertical direction has been considered when carrying elastic planar pendulums as well [157], where synchronized rotations where detected. Besides numerical and approximate analytical approaches, there has been experimental proof of the synchronized rotational motion of pendulums with autoparametric excitation. Strzalko et al. [158] studied the response of two sets of pendulums mounted on a vertically vibrating platform and identified through a custom experimental rig 1:1 and 1:2 synchronized rotations to the oscillations of the platform. Experiments showed a severe sensitivity of the synchronized states to the parameters and the initial conditions of the system.

The time delayed feedback control method was applied to initiate and maintain the synchronization of two pendulums parametrically excited by a shaker in an experimental rig [159, 160]. Complete and antiphase synchronization was reported under the influence of the control.

2.2.5 Experimental efforts

Several experimental studies have been devoted to demonstrate the rich properties and features of the response of a pendulum to parametric excitation, mostly focusing on the stability of the upper equilibrium, or the so-called inverted pendulum [161, and references therein], as well as more complicated pendulum designs [162, and references therein]. The horizontally shaken pendulum has been studied by Schmitt and Bayly [112] who applied the multiple scales method along with experimental excursions of the studied cases. Non-zero mean angle of the response has been reported along with deviations from the theoretical results. This misagreement motivated the study by Mann and Koplow [113], who reported experiments on the planar parametric pendulum, a work aiming to explain these discrepancies between experimental observations and theoretical predictions of the response of this system. It was shown experimentally that small deviations from the purely vertical or horizontal direction of the excitation result in symmetry-breaking bifurcations and relocation of the mean-angle bifurcation point of the equilibrium.

With respect to wave energy harvesting, Xu et al. [163] have studied the response of a simple pendulum to the periodic excitation provided by an electromechanical shaker. The 4-DOF mechanical model describing the dynamics of this complex system were investigated and compared against experimental results. Previous numerical studies attempting to map down the criteria for the excitation parameters that lead to rotational response of the pendulum were evaluated. The study tracked down and reported rotational response of the experimental rig which was also aligned to the theoretical and numerical predictions. Further on, another step was taken towards more realistic excitation supporting the proof-of-concept for this device. Lenci et al. [164], Lenci and Rega [165], Lenci [166] launched and reported a series of experiments where a simple pendulum attached onto a buoy was let to float on water

waves generated in a laboratory wave flume. An unambiguously vast number of excitation parameter pairs were tested and different types of motion were recorded, namely oscillatory, rotary and period-doubled rotations. Electricity generation was demonstrated through powering a LED by the rotating motion of the pendulum.

2.2.6 Summary

The review of the studies on the parametric pendulum clearly reveals the importance of this dynamical system and the interest it has attracted over the years. The richness of bifurcations motivated numerous authors to explore the dynamics of this system, aiming to rigorously deduce the bifurcation diagrams that would allow one to confidently predict the response of the pendulum in a deterministic framework under a harmonic excitation. Intensive efforts were also devoted to the stabilization of the upright position, as well as to the boundaries of the chaotic attractors. With a view to the rotating potential of the parametric pendulum, the work by Xu et al. [7] condenses the advances in the study of the rotating orbits down to a comprehensive construction of PSPs identifying the regions leading to rotary response. This numerical study is a rather substantial one from an engineering design point of view, offering the option to deliberately manipulate the length of a pendulum, such that a rotary response would arise under a given harmonic excitation. Subsequent studies considered systems of increased complexity, utilizing even analytical tools within the same framework, while others provided experimental verification of the numerical results.

However, an environmental excitation can hardly be treated as a deterministic one. The vast majority of the previous studies considered a perfectly harmonic excitation of the pendulum's pivot, which is rather unrealistic especially when the pendulum is driven by the bobbing motion of ocean waves. The handful of studies that considered a random narrow-band excitation were limited with respect to the forcing conditions that were considered and the completeness of the applied methods. Thus, this thesis is mainly concerned with identifying the evolution of the rotational regions of the PSPs under randomness, allied by the computation of the firmly reliable PDF of the response of selected cases. It is attempted to investigate the influence of

increasing magnitude of randomness onto both the parameter regions of the map that rotary response could be located and the intensity of the desired response. This course of action is followed for the basic SDOF system, as well as for more complicated autoparametric systems. A particularly interesting case of the latter, previously unexplored, is considered, addressing the issue of the destabilization of the hanging-down position when the primary system undergoes impacts against a rigid barrier, modelling in such a way the response of the pendulum under extreme weather conditions.

Chapter 3

Modelling and methods

Any attempt to develop a model that would sufficiently describe the dynamics of a system excited by ocean waves, has no alternative but to consider the natural randomness inherent in the ocean. In this chapter, first some of the basic background concepts of Probability Theory are outlined in Sec. 3.1 to support later considerations. Then, the nature of ocean waves is considered in Sec. 3.2 and the up-to-date understanding of the dynamics observed in the ocean is delineated. Finally, Sec. 3.3 concentrates the methods of stochastic dynamical analysis that are being used in the present thesis, discussing the fundamental theory behind them and their application.

3.1 Probability theory preliminaries

The mathematical background necessary for the presentation of the methods and the models that are being used in this thesis are summarized hereinafter. The well-established Probability Theory and the accompanying measure of probability over a sample space are utilized, a thorough discussion of which could be found in many engineering and mathematical textbooks by Stratonovich [72], Lin [167], Lin and Cai [168], Øksendal [169], Arnold [170]. Additional references with respect to topics of particular interest for the purpose of this thesis are spread within the text.

3.1.1   Basic concepts

Let $X : \Omega \to \mathbb{R}$ denote a random variable with Ω its sample space. The probability of X to take on some values, say $X \leq x$, is denoted as $P[\omega : X(\omega) \leq x]$, or abbreviating $P(X \leq x)$, based on which the probability function F is defined as $F(\mathbf{x}) = F(x_1, \ldots, x_n) = P([X_1 \leq x_1] \cup [X_2 \leq x_2] \cdots)$ if X is vector-valued. Further, if F is differentiable, then the PDF is defined as:

$$p_X(x) = \frac{dF(x)}{dx} \ \text{ or } \ p_{X_1 \cdots X_n}(\mathbf{x}) = p_{X_1 \cdots X_n}(x_1, \ldots, x_n) = \frac{\partial^n F(x_1, \ldots, x_n)}{\partial x_1 \ldots \partial x_n} \quad (3.1)$$

where the Right-Hand-Side (RHS) in Eq. (3.1) is called the joint PDF of $X_1, \ldots, X_n$. The exact opposite of equation Eq. (3.1) suggests that:

$$P(X \leq x) = \int_{-\infty}^{x} p_X(x) dx \quad (3.2)$$

indicating that if we integrate the PDF over the whole sample space $(x \to \infty)$ then the result should be equal to 1. Given the multivariate PDF of Eq. (3.1), one could extract the lower dimension joint PDF of m variables as:

$$p_{X_1 \cdots X_m}(x_1, \cdots, x_m) = \int_{-\infty}^{\infty} p_{X_1 \cdots X_n}(x_1, \ldots, x_n) dx_{m+1} \cdots x_n \quad (3.3)$$

Let us moreover assume that a vector of random variables is the function of other random variables, i.e. $\mathbf{Z} = g(\mathbf{X})$ and that $p_{\mathbf{X}}(\mathbf{x})$ is known, then one can express the PDF of $\mathbf{Z}$ in terms of:

$$p_{Z_1 Z_2 \cdots Z_m}(z_1, z_2, \cdots, z_m) = p_{X_1 X_2 \cdots X_m}(x_1, x_2, \cdots, x_n) \begin{vmatrix} \dfrac{\partial x_1}{\partial z_1} & \dfrac{\partial x_1}{\partial z_2} & \cdots & \dfrac{\partial x_1}{\partial z_m} \\ \dfrac{\partial x_2}{\partial z_1} & \dfrac{\partial x_2}{\partial z_2} & \cdots & \dfrac{\partial x_2}{\partial z_m} \\ \vdots & \vdots & \ddots & \vdots \\ \dfrac{\partial x_n}{\partial z_1} & \dfrac{\partial x_n}{\partial z_2} & \cdots & \dfrac{\partial x_n}{\partial z_m} \end{vmatrix} \quad (3.4)$$

with the above matrix being the Jacobian of $\mathbf{x}$ with respect to $\mathbf{z}$.

A widely used definition in stochastic analysis is the expectation operator which is an integral over the probability space reading:

$$E[X] = \int_\Omega x p_X(x) dx \tag{3.5}$$

or for a function g($\mathbf{X}$) of n random variables

$$E[g(\mathbf{X})] = \int_\Omega g(x_1, \cdots, x_n) p_{\mathbf{X}}(x_1, \cdots, x_n) dx_1 \cdots dx_n \tag{3.6}$$

Based on the definition of the expectation operator the *moments* of a random variable X are defined. The 1st order moment is $E[X]$, the 2nd $E[X^2]$, the n-th is $E[X^n]$ etc, also denoted by $<X^n>$. Moreover, the m-th order joint moments of n random variables are defined as $E[X_1^{a_1} \cdots X_n^{a_n}]$ for $a_1 \cdots a_n = m$. Some characteristic moments, widely used for describing the stochastic properties of random variables, say X, are:

- *mean*: the 1st order moment of X denoted by m_X

- *variance*: the 2nd central moment of X written $E[(X - m_x)^2]$

- *covariance*: $E[(X_1 - m_{x_1})(X_2 - m_{x_2})]$

Note that the positive square root of the covariance is called *standard deviation* denoted by σ_X. Following the definition of random variables and their most common attributes we define the *stochastic processes* $X(t)$, which are families of random variables at different times, so that for $t = t_0$, $X(t_0)$ is a random variable. The process $X(t)$ will be often referred to as X_t. All the attributes discussed previously for random variables are generalized for stochastic processes. However, there are some new arising measures which will be listed onwards.

A *homogeneous* or *stationary* process *in the strong sense* is said to be one that

satisfies the following:

$$p(x_1, t_1) = p(x_1, t_1 + t_{sh})$$

$$p(x_1, t_1; x_2, t_2) = p(x_1, t_1 + t_{sh}; x_2, t_2 + t_{sh}) \tag{3.7}$$

$$\vdots$$

$$p(x_1, t_1; x_2, t_2; \cdots x_n, t_n) = p(x_1, t_1 + t_{sh}; x_2, t_2 + t_{sh}; \cdots x_n, t_n + t_{sh})$$

for any forward time shift t_{sh}.

If only the first two of the above equations are satisfied the process is said to be *stationary in the weak sense*. One could think of stationarity as the response of an asymptotically stable deterministic system, only that now we are not talking about a fixed point but a PDF. A very important feature of stationary processes is invoked when a general concept is introduced. Since at different single time instances, the process could be seen as random variables we can apply the 2nd moment $\mathrm{E}[X(t_1)X(t_2)]$ which is now called *autocorrelation* denoted by ϕ_{XX}. For a stationary process, it is proven [167] that the autocorrelation depends only on the difference $\tau = t_1 - t_2$ and it is $\phi_{XX}(\tau) = R_{XX}(\tau)$. Furthermore, if the autocorrelation function has an existing Fourier transform, i.e.,

$$\Phi_{XX}(\omega) = \frac{1}{2\pi} \int\limits_{-\infty}^{\infty} R_{XX}(\tau) exp(-i\omega\tau) d\tau \geq 0 \tag{3.8}$$

it is called the Power Spectral Density (PSD) function and characterizes the distribution of energy along the frequency ω axis.

3.1.2 *White noise and Wiener process*

A weakly stationary noise having a constant spectral density is characterized as *white noise*. Therefore, whenever referring to a white noise it will be automatically considered that:

$$\Phi_{XX}(\omega) = R_{XX}/2\pi \tag{3.9}$$

The spectral density describes the energy distribution along the frequency spectrum and not the distribution the stochastic process follows. Thus, we may as well have a white noise following the Poisson or the Gaussian distribution. A very important process, widely used in engineering, associated with the Gaussian white noise is the Wiener process. The Wiener process is the mathematical modeling of the Brownian motion noticed in the motion of particles inside fluid. This process has the next properties:

- $W(0) = W_0 = 0$

- for $0 < t_1 < t_2$ then $W_{t_2} - W_{t_1} = N(0, t_2 - t_1)$

- for $0 < t_1 < t_2 < t_3 < t_4$, $W_{t_4} - W_{t_3}$ and $W_{t_2} - W_{t_1}$ are independent random variables

- $\mathrm{E}[W_t] = 0$ and $\mathrm{E}[W_{t_1} W_{t_2}] = min(t_1, t_2)$

The Wiener process is sample-path continuous, yet nowhere differentiable. However, attempts to formulate the Brownian motion showed that a Gaussian white noise, say ζ_t, should be the derivative of the Wiener process. Thus, it is defined that $dW_t = \zeta_t dt$. In the above, $N(m, \sigma^2)$ is the normal distribution with m mean and σ^2 covariance.

After that, the stochastic integral can be discussed. Assuming a sequence $t_1 = \tau_1 < \tau_2 \ldots < \tau_n = t_2$ with $\Delta = \tau_{j+1} - \tau_j$, $j = 1, \ldots, M - 1$, there are two ways to define this:

$$\text{Ito} : \int_{t_1}^{t_2} X_t dW_t = \lim_{M \to \infty, \Delta \to 0} \sum_{j=1}^{M-1} X(\tau_j)(W_{t_{j+1}} - W_{t_j}), \tag{3.10}$$

$$\text{Stratonovich} : \int_{t_1}^{t_2} X_t \circ dW_t = \lim_{M \to \infty, \Delta \to 0} \sum_{j=1}^{M-1} X\left(\frac{\tau_{j+1} - \tau_j}{2}\right)(W_{t_{j+1}} - W_{t_j}) \tag{3.11}$$

from which the equivalent expressions for the *Stochastic Differential Equations (SDEs)* are derived. Note that from here on, the SDEs discussed will need to be interpreted into the Ito sense.

3.1.3   Markov Processes

A stochastic process is said to be Markovian if the conditional probability function at t_n depends only on the previously known value at t_{n-1}.

$$p(x_n, t_n | x_{n-1}, t_{n-1} \cdots x_1, t_1) = p(x_n, t_n | x_{n-1}, t_{n-1}) \tag{3.12}$$

Often, these processes are called one-step memory, since they practically "remember" only their adjacently previous state. The Markovian property is crucial for the implementation of the Path Integration (PI) method (see Sec. 3.3.3). A useful implication of Eq. (3.12) concerns the total probability law, which in the general case reads [167]:

$$p(\mathbf{x}_k, t_k) = \int_{-\infty}^{\infty} p(\mathbf{x}_k, t_k; \mathbf{x}_{k-1}, t_{k-1}; \cdots ; \mathbf{x}_1, t_1) d\mathbf{x}_1 \cdots d\mathbf{x}_{k-1}. \tag{3.13}$$

Yet, the joint PDF at times $t_1, \cdots, t_k$ in the integrand can be expressed through the conditional PDFs as:

$$\begin{aligned} p(\mathbf{x}_k, t_k; \mathbf{x}_{k-1}, t_{k-1}; \cdots ; \mathbf{x}_1, t_1) = p(\mathbf{x}_k, t_k | \mathbf{x}_{k-1}, t_{k-1}; \cdots ; \mathbf{x}_1, t_1) \cdot \\ p(\mathbf{x}_{k-1}, t_{k-1} | \mathbf{x}_{k-2}, t_{k-2}; \cdots ; \mathbf{x}_1, t_1) \cdots p(\mathbf{x}_2, t_2 | \mathbf{x}_1, t_1) p(\mathbf{x}_1, t_1) \end{aligned} \tag{3.14}$$

However, taking into account the Chapman-Kolmogorov equation:

$$p(\mathbf{x}_k, t_k | \mathbf{x}_{n-1}, t_{n-1}) = \int_{-\infty}^{\infty} p(\mathbf{x}_k, t_k | \mathbf{x}, t) p(\mathbf{x}, t | \mathbf{x}_{k-1}, t_{k-1}) d\mathbf{x}. \tag{3.15}$$

then Eq. (3.13), reduces to:

$$p(\mathbf{x}_k, t_k) = \int\limits_{-\infty}^{\infty} p(\mathbf{x}_k, t_k | \mathbf{x}_{k-1}, t_{k-1}) p(\mathbf{x}_{k-1}, t_{k-1} | \mathbf{x}_{k-2}, t_{k-2}) \cdots p(\mathbf{x}_2, t_2 | \mathbf{x}_1, t_1) \cdot \tag{3.16}$$

$$p(\mathbf{x}_1, t_1) d\mathbf{x}_1 \cdots d\mathbf{x}_{k-1}.$$

The reduction of the conditional probabilities at time t to depend only on the adjacently previous time step t' is the fundamental property of Markov processes and $p(\mathbf{x}, t | \mathbf{x}', t')$ will be referred to as the Transition Probability Density Function (TPDF). Thus, a Markov process only requires the knowledge of the TPDF and an initial condition to be fully analyzed. As it is discussed in section Sec. 3.3.3, Eq. (3.16) is the core of analyzing stochastic dynamical systems in this thesis.

Before moving on, we need to mention how a process with *periodic* PDF might be defined. If the process is Markovian it obeys equation Eq. (3.16). This, could be shown [171] to be an operator on the probability space. If the system's equations include periodic terms, such as sinusoidal, it is possible for that operator to be also periodic thus producing periodic PDFs ($p(\mathbf{x}, t) = p(\mathbf{x}, t + T)$). From now on, when referring to periodicity in a process we will mean the periodicity of its PDF.

3.1.4 Stochastic Differential Equations

As mentioned before the Wiener process is widely used in stochastic modeling due to its often occurrence in real-world problems. In general a stochastic differential equation, assuming that the stochastic part is governed by a standard Wiener process, is expressed in differential form for a one-dimensional case as follows:

$$dX_t = a(X, t)dt + b(X, t)dW_t \tag{3.17}$$

where X is the unknown stochastic process, a is the deterministic part, b is the noise intensity associated term and W_t a standard Wiener process. Both the coefficients are considered to be dependent on the unknown process and time, thus representing the general case. However, it is very common to ultimately deal with a less complicated system. In the same manner, the higher dimension problem reads in matrix

form:

$$
\begin{bmatrix} X_1 \\ X_2 \\ \vdots \\ X_n \end{bmatrix} = \begin{bmatrix} a_1 \\ a_2 \\ \vdots \\ a_n \end{bmatrix} dt + \begin{bmatrix} b_{11} & b_{12} & \ldots & b_{1r} \\ b_{21} & b_{22} & \ldots & b_{2n} \\ \vdots & \vdots & \ddots & \vdots \\ b_{n1} & b_{n2} & \ldots & b_{nr} \end{bmatrix} \begin{bmatrix} dW_t^1 \\ dW_t^2 \\ \vdots \\ dW_t^r \end{bmatrix} \tag{3.18}
$$

where the vector Wiener process elements $W_t^{1 \ldots r}$ are assumed to be independent and the terms a_i and b_{ij} are functions of both time and the vector process $\mathbf{X}$. Also, it is often the case for some of the elements of the b matrix to be zero, meaning that the noise process is induced to the system only from $m < n$ state variables.

Since the subject of discussion here is random systems the term *solution* becomes quite ambiguous. So, solving a stochastic system could refer to following the random flow function $X(t) = \phi(X(0), t, \omega)$, exploring the stability of the system or finding the response PDF $p(\mathbf{x}, t)$. From here onwards, solution of an SDE will be interpreted as the latter and, in most cases, will be the joint response PDF $p(x_1, \ldots, x_n, t)$ of the state space variables.

Moreover, the systems of interest in this thesis will have a stationary response or at least a periodic one, as were both presented in Sec. 3.1.3. Of course the nature of the response is controlled by the dependence of a and b on time t and the process X. Besides homogeneity, these matrices will determine whether the process follows the Markovian property. This is actually very important within the scope of this thesis, since a large part of the herein approach is based on the Chapman-Kolmogorov equation Eq. (3.15) which characterizes Markov process.

However, there is a counterintuitive issue regarding the treatment of SDEs of the form of Eqs (3.17) and (3.18). A solution of these would require an integration of the RHS part. Even though the deterministic part is quite straightforward to define no matter how complicated it is, the stochastic term is not. As was described in Sec. 3.1.2, a stochastic integral has two interpretations, the Ito sense seen in Eq. (3.10) and the Stratonovich one in Eq. (3.11). As long as the stochastic process in the SDE is known to be pure white noise, the Ito interpretation could be adopted. However, in engineering problems, most often the white noise admission

is an approximation to the real-world problem and, in this case, the Stratonovich interpretation must be adopted as being suitable for "physical" problems. This is when one needs to inquire about the relationship between the two expressions, since the Ito interpretation is more favourable for further analysis of the SDE. An answer to that in the general n-dimensional case with an r-valued stochastic process, due to Wong and Zakai [168], is the following. If the SDE in Eq. (3.18) is understood in the Stratonovich sense, i.e. it reads $b_{ij} \circ dW_t^j$ with $i = 1 \ldots n$ and $j = 1 \ldots r$, then the corresponding Ito expression for which the two solutions converge reads:

$$dX_i = a_i(\mathbf{X}, t)dt + \frac{1}{2} \sum_{k=1}^{n} \sum_{j=1}^{r} b_{kj}(\mathbf{X}, t) \frac{\partial b_{ij}(\mathbf{X}, t)}{\partial x_k} + \sum_{j=1}^{r} b_{ij}(\mathbf{X}, t) dW_t^j \qquad (3.19)$$

The double summation term appearing now in the SDE is known in the literature as *Wong-Zakai correction term*. Notice that, in the case that the matrix b does not depend on the solution vector $\mathbf{X}$, then the two expressions become equivalent without requiring the correction terms.

A special and particularly important class of stochastic processes is the Ito diffusion processes. These are sample-path continuous processes following the Markov property and defined through Eq. (3.18) in the general case, assuming some conditions [168–170] are satisfied which is quite often true in engineering problems. Subsequently, the vector a is called the drift coefficient and the matrix $\frac{1}{2}bb^T$ the diffusion coefficient. A rather important property of diffusion processes is that the TPDF $p(\mathbf{x}, t | \mathbf{x}', t')$ is uniquely determined by the drift and the diffusion terms. This is accomplished through the well-known FPK equation or else the forward Kolmogorov equation:

$$\frac{\partial p}{\partial t} + \sum_{i=1}^{n} \frac{\partial}{\partial x_i} \left[a_i(\mathbf{X}, t)p \right] + \frac{1}{2} \sum_{i=1}^{n} \sum_{j=1}^{n} \frac{\partial^2}{\partial x_i \partial x_j} \left[\sum_{k=1}^{r} b_{ik} b_{jk} p \right] = 0 \qquad (3.20)$$

Unfortunately, obtaining a solution of Eq. (3.20) can be quite cumbersome, even if the process at question is stationary (i.e. $\partial p / \partial t = 0$). Most commonly, approximate

methods are used to acquire a solution for the TPDF, largely divided into two major groups, Finite Elements methods and path integrals.

3.2 Ocean waves modelling

Creating a mathematical model that would accurately describe the waves' kinematic and power properties is rather unfeasible. However, over the years different models have been proposed that approximate the ocean wave properties. The most simplified of them would be the linear model, in which the wave is represented as a pure sinusoidal [15, 27]:

$$f(x,t) = \frac{H}{2} cos \left(\frac{2\pi x}{\lambda} - \frac{2\pi t}{T} \right) \tag{3.21}$$

where f denotes the vertical displacement of the water particle at the x horizontal position on the surface and

$$T = 2\pi \left[\frac{2\pi g}{\lambda} tanh \left(\frac{2\pi h}{\lambda} \right) \right]^{-0.5} \tag{3.22}$$

where h is the sea depth [15, 27] and g the gravitational acceleration. The above model could describe sufficiently well isolated swells for which the wave height over wavelength ratio is smaller than $H/\lambda = 1/50$, practically occurring offshore. When going in shallow water, a non-linear model should be considered such as the *Stoke's Wave* [27]:

$$y = \frac{H}{2} cos \left(\frac{2\pi x}{\lambda} - \frac{2\pi t}{T} \right) + \frac{3H^2}{16k^2 h^3} cos \left[2 \left(\frac{2\pi x}{\lambda} - \frac{2\pi t}{T} \right) \right] \tag{3.23}$$

where k is the wave number, $k = 2\pi/\lambda$. This model describes better the interaction between the waves height and the depth of the seabed when in shallow waters. Another model, simulating the near-breaking swell in shallow waters is the *Solitary Wave*, described as [27]:

$$y = H sech^2 \left[\left(\frac{3H}{4h^3} \right)^{0.5} (x - ct) \right] \tag{3.24}$$

where $c = [gh(1 + H/h)]^{0.5}$ is the phase velocity.

However, the above formula becomes insufficient when real sea conditions are taken into consideration. Useful waves for energy extraction are commonly created by storms and travel as swells. In a stormy climate, waves with different periods, heights and directions are generated, such that their interaction produces *Random Waves*, which could be thought of as a combination of numerous linear waves of different characteristics. Thus, one could state that the energy transfered by the ith component of the random wave per unit area is [15, 27]:

$$E_i = \rho g \frac{H_i^2}{16} \tag{3.25}$$

where ρ is the water density. Since we are dealing with a superposition of linear waves, we should proceed to expressing the above in terms of the random wave. The energy of a wave per unit area is then [15, 27]:

$$E = \rho g H_{RMS}^2 \tag{3.26}$$

where H_{RMS} is the root-mean square wave height. Moreover, we define the spectral moments of order j as [15, 27]:

$$\mu_j = \int\limits_0^\infty f^j S(f) df \tag{3.27}$$

where $S(f)$ is the spectral density of the waves, considering for simplicity one direction. The above is very useful in introducing the *significant wave height H_s*, which is mostly used for ocean waves and is defined as the average height of the 1/3 of the highest waves. It is found that $H_{1/3}$ can be approximated by the zero order moment of $S(\omega)$ by [15, 27]:

$$H_s = 4\sqrt{\mu_0} \tag{3.28}$$

It can also be derived from statistical theory that $H_s = 4H_{RMS}$. Thus, substituting in equation Eq. (3.26) we get [15, 27]:

$$E = \frac{\rho g H_s^2}{16} = \rho g \int\limits_0^\infty S(f) df \tag{3.29}$$

Hence, we see that the energy transfered by sea waves depends only on the integrand $S(f)$.

3.2.1 Wave spectra

So far, there are many semi-empirical relations based on experimental data on different locations and sea states. The most widely used model was proposed by Pierson and Moskowitz [172] and deals with deep waters at the state of *fully developed seas*, i.e. ocean waves after wind has blown for a sufficient amount of time and no more affects the frequency range of the waves. This model in its general form, on which many subsequent studies were based, reads:

$$S(f) = \frac{A_{sp}}{f^5} \exp\left(-\frac{B_{sp}}{f^4}\right) \tag{3.30}$$

Particularly, the authors proposed certain values for A_{sp} and B_{sp} which, in the angular frequency domain, result in:

$$S(\omega) = \frac{A_{sp}g^2}{\omega^5} \exp\left[-B_{sp}\left(\frac{g/U_{19.5}}{\omega}\right)^4\right] \tag{3.31}$$

where A_{sp}, B_{sp} are dimensionless parameters taking values 8.1×10^{-3} and 0.74 respectively, while $U_{19.5}$ is the wind speed at 19.5m above the sea surface. However, it is more common to express the spectra generator with respect to the sea characteristics, the peak frequency ω_{peak} and H_s. First, applying differentiation to Eq. (3.31) and setting it equal to zero we could calculate the peak frequency as:

$$\omega_{peak} = 0.877 \frac{g}{U_{19.5}} \tag{3.32}$$

The obvious substitution in Eq. (3.31) would yield an expression with respect to that peak. Equally often though, the spectra are expressed with respect to H_s. For that, one would need to calculate the zero-order moment from Eq. (3.27) by replacing the formula in Eq. (3.31) for $S(\omega)$. Then, considering Eq. (3.28), H_s would be:

$$H_s = 0.21 \left(\frac{U_{19.5}^2}{g}\right) \tag{3.33}$$
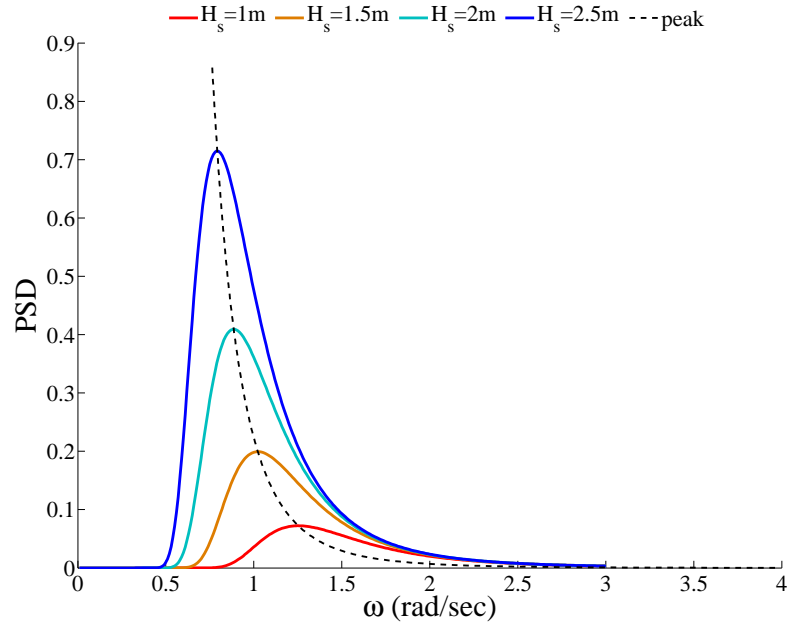
Figure 3.1: Plots of the PM spectra described by Eq. (3.34) for different values of H_s. Increasing H_s results in a more narrow-band spectrum with a lower ω_{peak}.

Substituting then Eq. (3.33) in Eq. (3.31), the spectra read:

$$S(\omega) = \frac{A_{sp}g^2}{\omega^5} \exp\left[-B_{sp,h}\frac{(g/H_s)^2}{\omega^4}\right] \tag{3.34}$$

with $B_{sp,h} = 0.032$. Fig. 3.1 shows plots of the Pierson-Moskowitz (PM) wave spectrum for different values of H_s. Some useful observations could be reported from this figure. First, increasing significant wave height modifies the spectrum into a more narrow-banded one. This would practically mean that more of the available power in waves would be distributed close to the peak frequency even though significant dispersion might still be contained. Besides, the peak frequency itself depends on the significant wave height. Actually, the relationship between these two measures relies on their mutual dependence on the wind speed above the sea surface and as could be seen by Eqs (3.32) and (3.33):

$$H_s = \frac{1.58}{\omega_{peak}^2} \tag{3.35}$$

Eq. (3.35) is plotted in Fig. 3.1 with a dashed line. An overwhelming majority of the power in waves is concentrated in a low frequency range $[0.5 - 2.5]$ rad/sec with

the peak frequencies of the most regularly observed wave heights of 1.5-2.5m having a peak value below 1 rad/sec.

On the groundwork of Pierson and Moskowitz [172], many studies improved the description of sea waves such as Bouws et al (1985), Donelan et al (1985) which can be found in [15]. Among these, the most prominent is the work of Hasselmann et al. [173], who fitted the experimental data taken during the Joint North Sea Wave Project (JONSWAP), proposing what is later referred to as the JONSWAP spectrum [173]:

$$S(f) = E(f) exp\left[-1.25\left(\frac{f_{peak}}{f}\right)^4\right]\gamma^\Gamma \tag{3.36}$$

where $\quad E(f) = \dfrac{\alpha g^2}{(2\pi)^4 f^5}$

$\Gamma = exp\left[-\dfrac{(f - f_p)^2}{2\beta^2 f_p^2}\right]$

α is the Philips constant, found to be $\alpha = 0.076\left(\dfrac{gX}{U^2}\right)^{-0.22}$

f_p is the peak frequency, $\dfrac{Uf_p}{g} = 3.5\left(\dfrac{gX}{U^2}\right)^{-0.33}$

γ is the peak-enhancement factor - usually taken equal to 3.3 and

$\beta = 0.07$ for $f < f_p$ and $\beta = 0.09$ for $f > f_p$

and U is the wind velocity 10m above the surface, X is the fetch over which the wind acts. The above model is more narrow-banded than the PM and is widely used for wind-generated waves with limited fetch. Based on the definition for energy Eq. (3.29), most researchers use the waves' *power level* measured in kW/m given by[15]:

$$J = \rho g^2 \frac{T_J H_s^2}{64\pi} \tag{3.37}$$

where T_J is the energy period, $T_J = m_{-1}/m_0$.

In this thesis, the PM spectrum has been adequate to describe the wave power distribution inasmuch as the sea state is considered to be fully developed, far enough from the shoreline so that the fetch would not considerably influence the shape of
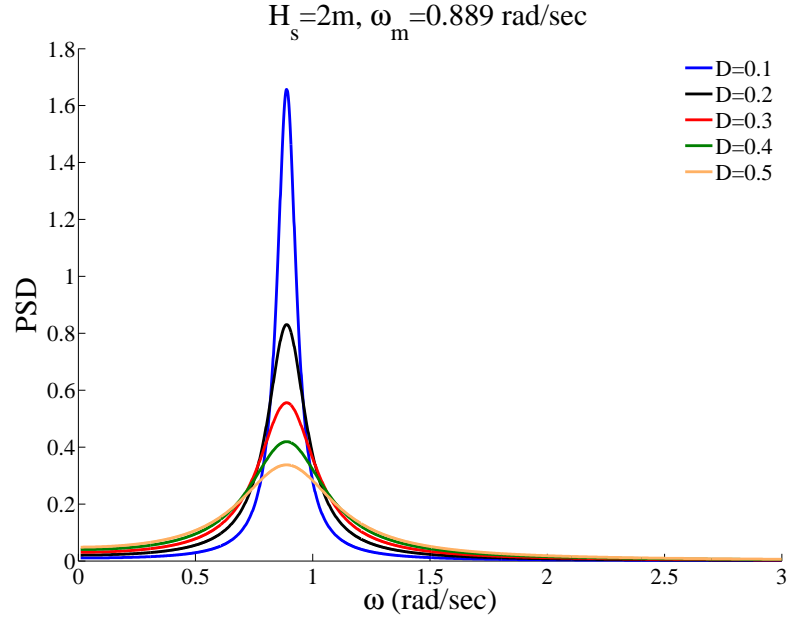
Figure 3.2: Spectrum of the random process $f(t)$ defined in Eq. (3.38), given by Eq. (3.39) for different noise intensity values.

the spectrum.

3.2.2 Random phase modulation

Given that the energy in waves depends on the spectrum , Eq. (3.29), a model aiming to describe the dynamics of any system interacting with ocean waves, would have to carefully consider the representation of the spectrum. So far, in the beginning of this section a number of deterministic models were outlined - Eqs (3.21)–(3.24), which nevertheless fail to describe the influence of randomness inherent in the ocean dynamics and hence, a stochastic approach is required.

Let the motion of a single point on the sea surface be given by $f(t)$. According to the linear wave theory, this function is a pure sinusoid. In order to incorporate the randomness, the phase of this motion is considered random according to:

$$f(t) = A \cos q, \ \dot{q} = \omega_m + \tilde{\sigma}\zeta(t) \tag{3.38}$$

where $\zeta(t)$ is a zero-mean, delta-correlated Gaussian white noise of unit variance, $D = \tilde{\sigma}^2$ is the variance of the stochastic process with modified diffusion, ω_m is the mean frequency, q the phase of the particle's motion and A the amplitude of its
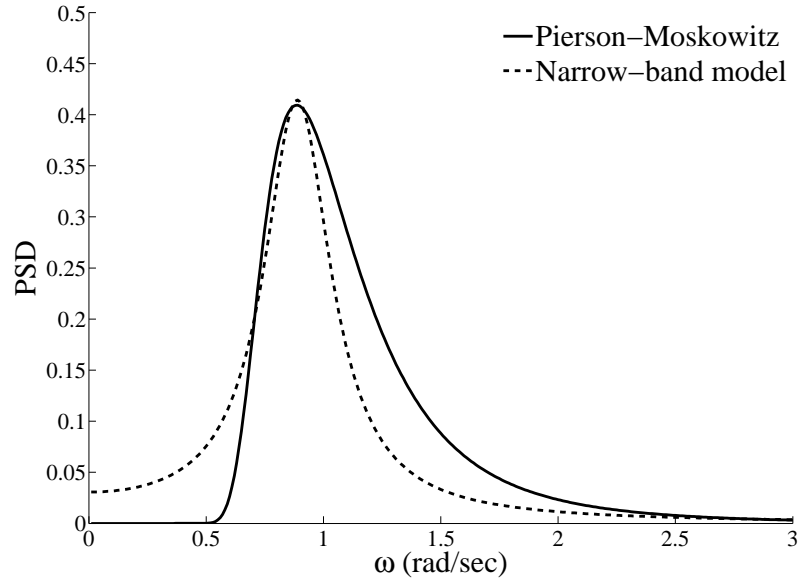
Figure 3.3: Comparison of the PM spectrum for $H_s = 2m$ against $\Phi_{ff}(\omega)$ for $D = 0.3$, $\omega_m = \omega_{peak}$ and $A = 0.475H_s$.

vertical oscillations. This model was introduced as early as 1982 by Kozubovskaya and Khrisanov [174] and is thereafter cited in the literature as an imperfect harmonic process, disordered periodic or Random Phase Modulation (RPM), which will be used in the present thesis. Subsequently, it has found numerous applications in Ocean and Structural Engineering [69, 74, 75, 175]. Thus $f(t)$ is understood as a stochastic process, the PSD of which has been found by Lin and Li [175] to be:

$$\Phi_{ff}(\omega) = \frac{A^2 D}{4\pi} \frac{\omega_m^2 + \omega^2 + D^2/4}{\left(\omega_m^2 - \omega^2 + D^2/4\right)^2 + \omega^2 D^2} \tag{3.39}$$

Fig. 3.2 shows Φ_{ff} for equating the amplitude $A = H_s = 2m$ and the corresponding peak frequency $\omega_m = \omega_{peak}$ for five increasing values of noise intensity D. It is evident from both Fig. 3.2 and Eq. (3.39) that $f(t)$ is not a white noise nor could be approximated by one unless the noise intensity D was extremely large. Especially for the range of noise intensity that will be used in the present thesis, $f(t)$ can be considered as a narrow-band process. Then, a suitable model would be one for which Φ_{ff} approximates the PM spectrum for a particular set of (ω_{peak}, H_s). Yet, one is not restricted in using this exact set as the model's (ω_m, A) as long as the model's spectrum approximates the experimental one. In fact, such a combination would

be rather difficult to produce adequate corroboration just by controlling the noise intensity D, since both the bandwidth and the peak value of the PSD depend on it. Instead, the type of the formula of the model's spectrum will be taken advantage of, by noticing that Eq. (3.39) is linear to A^2. Hence, this could work as a scaling factor in order to achieve good agreement between the spectra and particularly, the peak value will be targeted by scaling A and the bandwidth by controlling D. In such a way, the RPM and the experimentally fitted spectrum could reach a satisfactory agreement, as shown in Fig. 3.3. Here, the scaling factor is $A = 0.475 H_s$ and $D = 0.3$. Even though the agreement is not ideal, it could still represent adequately the dynamics of interest since the peak frequency and the bandwidth match and the distribution of power follows similar pattern. In fact, the model spectrum places more emphasis on lower frequencies, thus including a safety margin in the operational range since lower frequencies are the ones least favoured in terms of energy production.

3.3 Stochastic Methods

Determining a stochastic model to describe the sought dynamics of a random system is the first step in the analysis. However, the tools that can be utilized to extract them are not straightforward, since conventional dynamics methods do not incorporate random processes. Henceforth, the methods of stochastic analysis that are being employed in the present thesis are described in this section, in order to set the ground for the results presented in the following chapters.

3.3.1 Monte-Carlo simulations

A first intuitive approach when across a stochastic problem is to imagine how does the randomness influence the reality. It might be easily understood that a coin toss is random but only in the sense that every trial could have either outcome that cannot be predetermined. Similarly to this simple example, MC methods in the study of engineering problems are used to numerically create realizations of the stochastic response in order to statistically extract some of its properties of interest.

Essentially, MC methods, or, better, simulations of repeated applications of a MC method - MC simulations in short- of a stochastic problem are realizations of possible histories, some might refer to them as experiments too [176], by utilizing a sequence of random numbers conforming to certain desirable conditions.

Since a numerical approach is inherent in these methods, one should start from expressing a time discretization of the dynamical system in Eq. (3.17) as:

$$X_{k+1} = X_k + a(X_k, t_k)dt + b(X_k, t_k)dW_{t_k} \qquad (3.40)$$

where only the 1D case is considered for simplicity. Also X_{k+1} is a random variable at time $t_{k+1} = t_k + \Delta t$ and dW_{t_k} is the increment of the Wiener process at time t_k. Eq. (3.40) reflects the basic discretization scheme of *Euler-Maruyama*. There are a few important conclusions regarding a MC simulation of Eq. (3.40) drawn by this equation. First, $dW_{t_k}, k = 1, 2, \ldots$ correspond to the increments of the Wiener process at different time instances. An important property of these is that they are independent Gaussian random variables with a known distribution (see Sec. 3.1.2). Since they are independent, it follows that $X_k, k = 1, 2, \ldots$ is a Markov chain. Further, since dW_{t_k} is a Gaussian variable, one would need to generate a sequence of numbers extracted by a Gaussian distribution, input them in the equation of the system (3.40) as it is propagated in time and record the statistics. In that way, one might extract crude estimations of, say, the response of a nonlinear oscillator and then apply more elaborate stochastic methods, localized though in a region of increased interest, based on the realizations of the MC simulations. This is ultimately what a MC simulation of a stochastic system comes down to. However, two issues arise regarding the practical implementation: how are the random numbers generated and how many of them are sufficient?

There is a vast literature concerned with the issue of generating random numbers suitable for a MC simulation [176, and references therein]. The requirements are first to obey a distribution which converges to the target limiting distribution, as their number grows infinitely, to fulfill otherwise the Law of Large Numbers [176]. Furthermore, the required length of the array of random numbers is another issue

related to the dynamics of the problem. The rate of convergence of the MC sequence to the stochastic process is given by the central limit theorem [176], which prescribes the volume of the random number to be used. So one might utilize famous algorithms, such as the Metropolis one, due to Metropolis and Ulam [177] or could rely on the central limit theorem to generate Gaussian variables from a sequence of uniformly distributed ones. Another popular approach, due to Shinozuka and Deodatis [128], especially used in structural stochastic dynamics is the harmonic expansion of the stochastic process with a known spectrum with each mode perturbed by uniform independent phase angle variable.

Recent advances in Computer Science, however, progressively simplify the required procedures. Increasing computing capacity makes the otherwise long, expensive MC simulations more attractive than before. And that is simply because the increased capability of repetitions of a stochastic problem allows for higher confidence on the results and expands the range of properties that could be extracted. Furthermore, commercial software packages include sophisticated algorithms for generating random number of a respectable number of different distributions. In this thesis, the utilized model, Eq. (3.38), requires the generation of Gaussian random variables. The International Mathematics and Statistics Library (IMSL) [178] which is integrable into the Fortran 90 programming environment used in this thesis, offers the option of generating a Gaussian normal variable by invoking a built-in subroutine (*rnnoa*) which executes an acceptance/rejection algorithm to produce the desired sequence. Then this sequence can be scaled in mean and variance appropriately so that it fits the requirements of the model. Even though the accuracy of contemporary algorithms is remarkable, one needs to perform statistical tests for the mean, variance, even the PDF, on the generated random sequence so that the accuracy of that sequence is ensured. Another issue arising from the so-called pseudo-random number generation which has just been described, is that the invoked subroutine selects numbers from a prescribed list which amounts to the order of 2×10^9. In order to do so, a seed is read sending the subroutine to the particular number. This seed is automatically selected through the system clock. However, if one is performing simulations in parallel, they have to ensure that the seed of different sequences

are far away from each other to avoid "localization" of the generated distributions. That could be done by manually intervening to the value of the seed and setting it well far away for different sequences.

In order to demonstrate the application of MC simulations, consider the much celebrated Duffing oscillator:

$$\ddot{x} + 2\alpha\dot{x} + \Omega^2 x + \lambda_D x^3 = \sigma\zeta(t) \tag{3.41}$$

with α the viscous damping coefficient, Ω the natural frequency, λ_D the cubic non-linearity coefficient and σ, ζ as defined in Sec. 3.2.2. Thankfully, the solution to the FPK equation for this system has been obtained, yielding for the joint PDF of $x, y = \dot{x}$:

$$p(x,y) = Cexp\left[\frac{4\alpha}{D}\left(\frac{1}{2}y^2 + \frac{\Omega^2}{2}x^2 + \frac{\lambda_D}{4}x^4\right)\right] \tag{3.42}$$

C being a normalization constant.

Knowing Eq. (3.42), one can calculate the first two moments of the displacement x and the velocity y through Eq. (3.3) and Eq. (3.6). Let us now apply the Euler-Maruyama discretization scheme to retrieve the following:

$$\begin{aligned} x_{k+1} &= x_k + y_k dt \\ y_{k+1} &= y_k - (2\alpha y_k + \Omega^2 x_k + \lambda_D x_k^3)dt + \sigma dW_k \end{aligned} \tag{3.43}$$

Since dW_k is a Gaussian random variable it can be generated by the IMSL as described above. However the normal distribution which generates the sequence has to be scaled to the process which is required. Thus, the sequence is multiplied by $\sqrt{dt}$ to convert it to a zero-mean sequence with dt variance. One can then propagate forward the deterministic part of the system of equations (3.43), not being constrained to use the Euler scheme. Actually, any integrator would be suitable including ones of higher accuracy so, in this thesis, the 4th order Runge-Kutta integration is performed for the deterministic part of SDEs. Then, at each time step, a random number is generated and input to the analyzed equation as in (3.43).

N	$<x>$	$<x^2>$	$<y>$	$<y^2>$	$<x>$	$<x^2>$	$<y>$	$<y^2>$
	dt=0.01				dt=0.05			
100	-0.0012	0.3250	0.0000	0.8344	0.0001	0.3256	0.0000	0.8565
200	-0.0007	0.3248	0.0000	0.8338	0.0001	0.3258	0.0000	0.8573
300	-0.0005	0.3247	0.0000	0.8335	-0.0005	0.3262	0.0000	0.8590
400	-0.0002	0.3250	0.0000	0.8347	-0.0003	0.3261	0.0000	0.8591
500	-0.0003	0.3254	0.0000	0.8360	0.0000	0.3263	0.0000	0.8595
600	-0.0003	0.3256	0.0000	0.8366	0.0003	0.3262	0.0000	0.8585
700	-0.0001	0.3256	0.0000	0.8365	0.0005	0.3264	0.0000	0.8591
800	-0.0002	0.3256	0.0000	0.8362	0.0004	0.3264	0.0000	0.8587
900	-0.0002	0.3256	0.0000	0.8359	0.0004	0.3265	0.0000	0.8590
1000	-0.0002	0.3256	0.0000	0.8362	0.0004	0.3266	0.0000	0.8594
2000	0.0000	0.3259	0.0000	0.8371	0.0001	0.3266	0.0000	0.8597
5000	-0.0001	0.3259	0.0000	0.8372	0.0000	0.3263	0.0000	0.8586
10000	0.0000	0.3260	0.0000	0.8376	0.0000	0.3262	0.0000	0.8585

Table 3.1: MC simulations for the first two moments of x, y from Eq. (3.43) for $\alpha = 0.3$, $\Omega = 1.0$, $\lambda_D = 2.0$, $D = 1.0$.

Table 3.1 lists the results of MC simulations for the two first moments of x, y, for a different number of repetitions N and two different time steps. These are the calculated average values of the Gaussian variation they follow, as the central limit theorem demands. First, with increasing the number of repetitions the calculated estimation converges to a certain value. Yet, the accuracy of that is not certain and it depends highly on the time step dt. This is especially important for the variable from which the noise is induced in the system. It could be observed that $<x>, <x^2>$ do not change dramatically when a different time step is chosen. Nor does $<y>$, but $<y^2>$ bears a significant discrepancy among different time steps. That is due to the direct dependence on ζ's variance which is equal to dt. Thus, the time step needs to be selected small enough such that all the nonlinearities are adequately described numerically. Note that for the selected parameters the means would of course be zero and $<x^2> = 0.3262$ and $<y^2> = 0.8333$.

The effectiveness of these methods is highly related to the available computing capability and the required volume of realizations. Thus, this subject is closely discussed along computer science with the challenge for many being the development of effective algorithms that can produce random numbers. However, in the stochastic dynamics community related to engineering problems it is considered a standard

tool of low complexity, following the general procedure described before.

3.3.2 Stochastic averaging

Stochastic averaging is a powerful tool in stochastic analysis of random dynamical systems. It was introduced by Stratonovich [72] for lightly damped 1-DOF systems under broad-band random excitation [73], but, since then, it has been developed to cover more broad classes such as M-DOF systems, quasi-Hamiltonian systems [179], linear and nonlinear parametric systems [71, 89], systems under narrow-band excitation [80, 89], nonlinear damping terms [180], combined harmonic and random excitation [179]. The method results in downsizing the dimension of the problem by approximating the response of the dynamical system by an Ito diffusion process. The class of dynamical systems that applies in the general case is [73]:

$$\dot{\mathbf{X}} = \epsilon^2 \boldsymbol{a}\left(\mathbf{X}, t\right) + \epsilon \boldsymbol{b}\left(\mathbf{X}, t\right) \zeta(t) \tag{3.44}$$

Under particular conditions on $\boldsymbol{a}, \boldsymbol{b}$ which are most commonly met in practical engineering problems [73], the solution process $\mathbf{X}$ can be approximated by a Markov vector satisfying the following Ito equation:

$$d\mathbf{X} = \epsilon^2 \mathbf{m}(\mathbf{X}) dt + \epsilon \boldsymbol{\sigma}(\mathbf{X}) d\mathbf{W}_t \tag{3.45}$$

where $\mathbf{W}_t$ denotes an r-dimensional Wiener process, $\mathbf{m}$ is the n-dimensional drift vector and $\boldsymbol{\sigma}$ the n×m diffusion matrix, with the $\mathbf{X}$ converging to the solution of Eq. (3.44) as $\epsilon \to 0$. The quantities $\mathbf{m}, \boldsymbol{\sigma}$ can be found as [73]:

$$\mathbf{m} = T^{av}\mathrm{E}[\boldsymbol{a}] + \int\limits_{-\infty}^{0} \mathrm{E}\left[\left(\frac{\partial \mathbf{b}}{\partial \mathbf{X}}\right)_t \mathbf{b}_{t+\tau}^T\right] d\tau \tag{3.46}$$

$$\boldsymbol{\sigma\sigma}^T = T^{av} \int\limits_{-\infty}^{\infty} \mathrm{E}\left[\left(\mathbf{b}_t \mathbf{b}_{t+\tau}^T\right)\right] d\tau \tag{3.47}$$

where T^{av} is time-averaging operator, which in the frequently met case of periodic integrands in Eqs (3.46) and (3.47), with period, say, T_0, it reads:

$$T^{av}\{\cdot\} = \frac{1}{T_0} \int\limits_{t_0}^{t_0+T_0} \{\cdot\} dt \tag{3.48}$$

Note that it is quite common when applying stochastic averaging to transform the original Eq. (3.44) to the corresponding amplitude and phase variables. As soon as Eq. (3.45) and the corresponding parameters are extracted, one can apply the theory of Ito diffusions to move forward. So, the FPK equation can be analyzed for the TPDF or one might study the stability of the approximate system (see Sec. 3.3.4) more conveniently, especially if the transformation to the amplitude variable is adopted. Another advantage, related to the RPM model is that the exciting stochastic process is rearranged to be linear and external to the phase of the response, thus allowing for an easier analytical manipulation of the system's dynamics. Yet, the condition of a "lightly damped and excited system" could limit the accuracy of the extracted results.

Let us now again use the Duffing oscillator described in Eq. (3.41) to demonstrate the application of stochastic averaging. Introducing the following transformation:

$$\begin{aligned} x &= A\cos\left(\Omega t + \phi\right) \\ \dot{x} &= -A\Omega\sin\left(\Omega t + \phi\right) \end{aligned} \tag{3.49}$$

with A being the amplitude of the response and ϕ its phase, one arrives to the

transformed equations:

$$\dot{A} = \frac{2\alpha A\Omega \sin\psi + \lambda_D A^3 \cos\psi^3}{\Omega} \sin\psi - \frac{\zeta}{\Omega}\sin\psi$$
$$\dot{\phi} = \frac{2\alpha A\Omega \sin\psi + \lambda_D A^3 \cos\psi^3}{A\Omega} \cos\psi - \frac{\zeta}{A\Omega}\cos\psi \tag{3.50}$$

with $\psi = \Omega t + \phi$. Now, applying Eqs (3.46) and (3.47) ones gets the Ito equation:

$$dA = -\alpha A + \frac{D}{4A\Omega} - \frac{\sigma}{\Omega}dW_1$$
$$d\phi = \frac{3}{8}\frac{\lambda_D A^2}{\Omega} - \frac{\sigma}{A\Omega}dW_2 \tag{3.51}$$

with W_1, W_2 independent Wiener processes. It can be noticed that the equation for the amplitude is decoupled from the phase. As Roberts and Spanos [73] developed, solving the FPK equation for the stationary solution, leads to a uniform PDF for the phase. Correspondingly, the solution for the PDF of the amplitude can be found:

$$p_A(A) = CA \exp\left(-\frac{2\alpha\Omega^2 A^2}{D}\right) \tag{3.52}$$

Applying now Eq. (3.4) to return to the original variables x, y leads to the following expression for the joint PDF:

$$p_{xy}(x, y) = C \exp\left[-\frac{2\alpha\Omega^2}{D}\left(x^2 + y^2/\Omega^2\right)\right] \tag{3.53}$$

Comparing now Eq. (3.53) with the analytical solution to the FPK for the original equation, given by Eq. (3.42), it can be seen that the application of stochastic averaging has eliminated the effect of the nonlinearity. This is a considerable drawback of this method, since it can describe the dynamics of nonlinear systems only when the effect of the nonlinearity is "small". Still, there is a class of dynamical systems, such as the linear parametric ones, for which the method can provide useful information regarding their stability, as will be seen in Chapter 6.

3.3.3   Path Integration

The Path Integration method applies an iterative approach for calculating numerically the response PDF of a system when the stochastic process follows the Markov property. This technique has been developed in the form applied in this thesis by Naess and Moe [181], whereas recently an analytical approach has been proposed utilizing the Wiener path integral and statistical linearization [182]. The numerical PI has been proved very efficient even for strongly nonlinear systems [171, 183–185], while it can also be found applied for some reliability problems [186, 187]. The main advantage of the PI method is related to the so-called tails of the PDF, corresponding to regions of the sample space where rare events are found, considerably away from regions with concentrated probablity. The accuracy of the calculation of these regions of the PDF with the PI, establishes this method as an extremely powerful tool compared to MC methods or stochastic averaging.

Transition Probability Density Function.   The main concept underlying the PI method is the numerical integration of the total probability law as it reads for Markov processes, Eq. (3.16). In view of the numerical approach, the procedure can be adequately described for the discretized system Eq. (3.40) and only one-step transition:

$$p(\mathbf{x}_{k+1}, t_{k+1}) = \int_{-\infty}^{\infty} p(\mathbf{x}_{k+1}, t_{k+1}|\mathbf{x}_k, t_k) p(\mathbf{x}_k, t_k) d\mathbf{x}_k. \tag{3.54}$$

Markov processes are completely described by their TPDF and an initial condition (Sec. 3.1.3). Thus, the challenge is redirected to acquiring a closed form expression for the TPDF $p(\mathbf{x}_{k+1}, t_{k+1}|\mathbf{x}_k, t_k)$. Without loss of generality, it is assumed that the noise is induced in the system only through the last dimension of the matrix equation (3.18), i.e. $b_{ij} = 0$ for $i = 1, \ldots, n-1$ and $j = 1, \ldots, r$, which will be the case for the SDEs discussed in this thesis. The TPDF then reads:

$$p(\mathbf{x}_{k+1}, t_{k+1}|\mathbf{x}_k, t_k) = \prod_{i=1}^{n-1} \delta\left(x_{i,k+1} - x_{i,k} - r_i(\mathbf{x}_k, t_k)dt\right) \cdot \tilde{p}(x_{n,k+1}|\mathbf{x}_k) \tag{3.55}$$

Let us also rewrite Eq. (3.40) considering the 4th order Runge-Kutta-Maruyame scheme, denoting the approximation of the deterministic integral with $r_i(\mathbf{x}, t)$ for $i = 1, \ldots, n$. Then, for the nth dimension:

$$X_{n,k+1} = X_{n,k} + r_n(\mathbf{X}_k, t_k)dt + b_n(\mathbf{X}_k, t_k)dW_{t_k} \tag{3.56}$$

Then from the 1D discretized system in Eq. (3.56), it is seen that the random variable X_{k+1} depends only on the dW_{t_k} increments taking X_n for granted, i.e. the conditional probability $p(x_{k+1}, t_{k+1}|x_k, t_k)$ is a linear function of dW_{t_k}. Due to the Gaussian distribution of the increment of the Wiener process, it is evident that the TPDF is also Gaussian from the linearity expansion property of Gaussian random variables. More formally, one could consider the solution to the FPK equation since the solution process $\mathbf{X}$ is an Ito diffusion, Eq. (3.17). Then, the TPDF has a closed analytical form and is given by [181]:

$$\tilde{p}(\mathbf{x}_{k+1}, t_{k+1}|\mathbf{x}_k, t_k) = \frac{1}{\sqrt{2\pi \sum_{i=1}^{r} b_i(\mathbf{x}_k)^2 \Delta t}} exp\left\{ -\frac{[\mathbf{x}_{k+1} - \mathbf{x}_k - r_3(\mathbf{x}_k, \Delta t)]^2}{2\sum_{i=1}^{r} b_i(\mathbf{x}_k)^2 \Delta t} \right\} \tag{3.57}$$

Thus, given an initial condition for the process $\mathbf{X}$, say $p(\mathbf{x}, t = 0)$, applying equation Eq. (3.54) repeatedly with Eq. (3.57) at hand, yields the desired joint response PDF of the system studied.

Numerical Implementation. Discretization of the system Eq. (3.17) gives rise to two really important requirements. A proper choice of Δt and the initialization of a state space grid $[g_{d_i}]$, $d = 1 \cdots n$ and $i = 1 \cdots k$ where n is the dimension of the system and k is the number of nodes at the d direction. In principle, proper choice means that lowering these values will have no effect to the results. However, there are some critical quantities such as the characteristic time of the system or empirically known proper time steps for describing a known function, e.g. sinusoidal. Moreover, previous studies [184] have shown the time step should not be much different from the grid step or else the error increases. Nonetheless, there is no final answer in

choosing a time step and the requirements change from one system to another.

The PI method has an iterative time-forward approach towards calculating the joint response PDF of the system. Each iteration is split into two basic tasks. First, the calculation of the TPD values and then the calculation of the integral Eq. (3.54). Since the state space has been discretized, calculation of the next step PDF means finding its values at all the nodes of the grid. For a single node at $\mathbf{x}_g$, finding $p(\mathbf{x}_g,t)$ requires $p(\mathbf{x}'_g, t')$ where prime denotes one time step backwards. Almost surely, the backwards position on the grid will not coincide with one of the node values. Thus, an interpolation technique must be adopted for moving the system forward. In this thesis, the method used is cubic B-splines.

B-splines are defined by a recursive formula which produces the j-th order basis functions which reads, for a scalar valued function:

$$
\begin{aligned}
B_{i,j}(x) &= \omega_{i,j}(x)B_{i,j-1}(x) + \left[1 - \omega_{i,j}(x)\right]B_{i+1,j-1}(x) \\
\omega_{i,j}(x) &= \frac{x - \tau_i}{\tau_{j+i-1} - \tau_i} \\
B_{i,1}(x) &= r\begin{cases} 1, & x_i \le x \le x_{i+1} \\ 0, & \text{otherwise} \end{cases}
\end{aligned}
\tag{3.58}
$$

For k nodes the number of basis functions is $i = 1 \cdots k - 2$. Note that 2nd-order is linear interpolation, 3rd-order is parabolic B-splines and 4th-order cubic ones. For a certain domain discretization the basis functions of a single order have the same values. However, they also should satisfy a function-unique condition:

$$
\sum_{i=1}^{k} c_i B_{i,j}(x_g) = f(x_g)
\tag{3.59}
$$

where $(x_g, f(x_g))$ are the interpolated points and $g = 1 \cdots k$. The extra 2 basis functions not defined before come from the boundary conditions. The constants c_k are called spline coefficients and are the next that should be calculated from the above equation. Once the basis functions and the coefficients are known the

interpolated expression $\hat{f}(\mathbf{x})$ for the real function $f(x)$ goes as follows:

$$\hat{f}(x) = \sum_{i=1}^{k} c_i B_{i,j}(x) \tag{3.60}$$

In a deterministic system calculating the backwards value $\mathbf{x}'_g$ is quite trivial. However, in stochastic systems there is no such thing as a previous value rather than *a set of events each with an attached probability.* Hence, the integral in equation Eq. (3.54) goes over this set containing all the possible ways in which the system could reach the state $\mathbf{x}_g$ from the previous time step state. So, if, say, there were only two possible previous events A and B, then the numerical calculation of the integral would be $[p(A, t')p(\mathbf{x}, t|A, t') + p(B, t')p(\mathbf{x}, t|B, t')]\Delta\mathbf{x}'$.

Summing up, let us present a general flow of the code implementing the PI method. For a Δt time-step and a $\Delta\mathbf{x}$ grid with n$\mathbf{x}$ nodes:

(1) The PDF at time t' is inserted as input and interpolated by use of cubic B-splines.

(2) For each grid point the value of the new PDF is calculated as follows:

   (a) Find the points along the q axis where the noise is induced, at which the TPD has significant contribution.

   (b) Map these points backwards with a Δt time step by the Runge-Kutta method. Now we know all the possible paths that could significantly influence the new PDF value at each grid point.

   (c) Through the aforementioned interpolation, calculate the old PDF value at the backwards-mapped points.

   (d) Calculate the new PDF value at the grid point from the integral of equation Eq. (3.54) substituting $p(\mathbf{x}, t|\mathbf{x}', t')$ from equation Eq. (3.57).

(3) Check convergence to steady state of the algorithm through the following

scheme:

$$\int\limits_{\mathbf{x}} |p(\mathbf{x}, t) - p(\mathbf{x}', t')| d\mathbf{x} < \epsilon \qquad (3.61)$$

where ϵ is chosen properly.

Let us now once again use the Duffing oscillator, Eq. (3.41), to demonstrate the PI method. Just a reminder that this system has a known analytical expression for the joint PDF given by Eq. (3.42), facilitating the comparison of the numerical results of the PI technique. If λ_D is taken to be zero then we have a linear problem and the process $\mathbf{X}$ is also Gaussian. In the following, the stationary PDFs of x and y, calculated analytically and by the PI method, are depicted for a linear and a nonlinear case (Fig. 3.4).

(a) $\alpha = 0.25, \Omega = 1.0, \lambda = 0.0, D = 1.0$

(b) $\alpha = 0.30, \Omega = 1.0, \lambda = 2.0, D = 1.0$
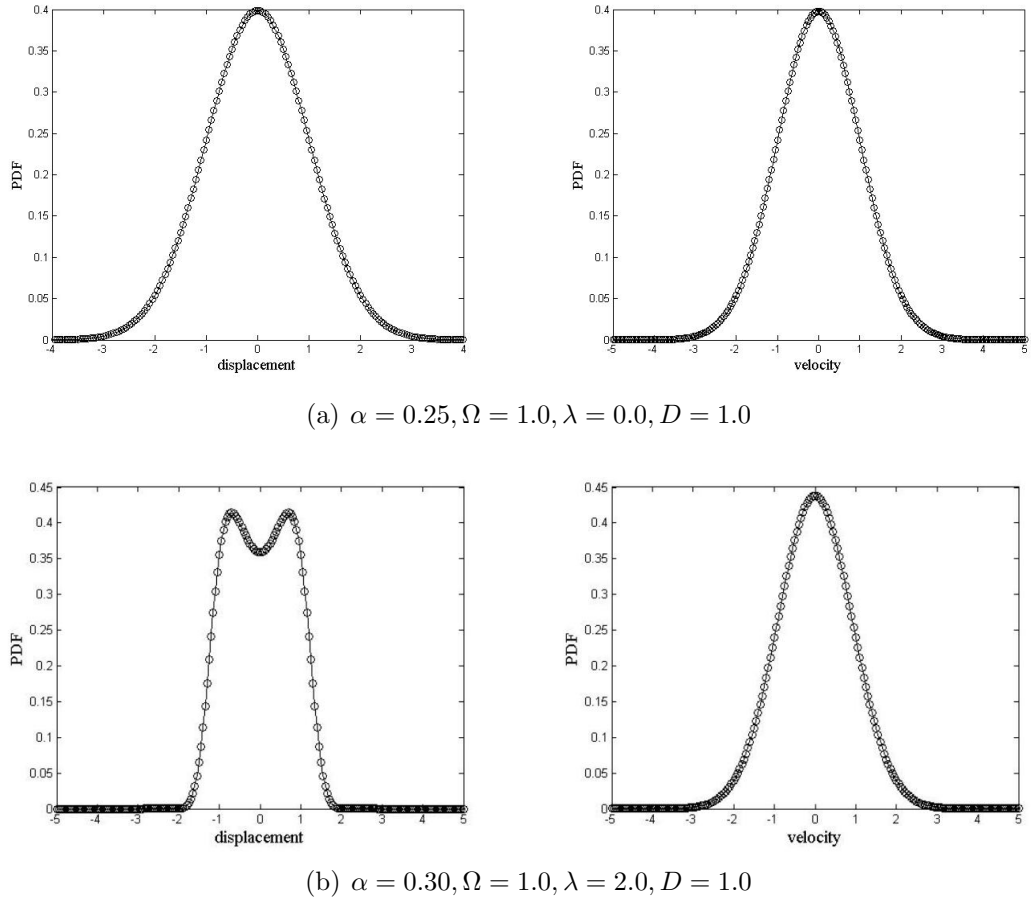
Figure 3.4: PDFs for a linear (upper) and a nonlinear (lower) case for the Duffing oscillator. Solid line represents the analytical solution and circles the PI results.

The corroboration of the numerical results with the analytical known curves of the PDFs is remarkable. The proximity in the tails of the linear system p_x as well as p_y

for the linear and nonlinear cases is nearly ideal. But for the nonlinear case too, the accuracy with which p_x is approximated is impressive even though for the particular set of the parameters the response is bistable and thus the sample space includes a region where the PDF is highly nonlinear, close to the mean value. It is worth comparing the PI results to MC simulations, for which attempting to calculate the PDF is almost in vain, and stochastic averaging where the nonlinearity effects are excluded from the approximate PDF expressions. Such a task, reveals a powerful superiority of the PI technique as opposed to the other two methods, when the expression of the PDF is sought. Yet, nothing comes without a price, and so does the PI which bears a significant computational cost especially when more than 3D systems are considered, the well-known curse of dimensionality. Thus, the selection of a method to analyze a SDE depends on the aim of the conducted study, keeping in mind computational efficiency against powerful information. Therefore, reliability problems of highly nonlinear systems almost have no alternative but to pursue an accurate computation of the PDF, whereas a stability analysis of a linear parametric system can be covered by means of stochastic averaging.

3.3.4   Stochastic stability

Stability of dynamical systems is a vast subject in the deterministic theory (see [53, 65]) which is concerned, not so much with determining the solution x of a system, but rather to estimate qualitatively, and some times quantitatively, some of the properties of the response. The general problems within the scope of stability could be extended to stochastic dynamical systems as well, only that some definitions need to be given regarding the convergence of a stochastic process [70, 167, 168, 188].

Assume that a stochastic process $X(t)$ is generating a sequence of random variables X_n with n representing different time instances and X a random variable. Then, convergence of the sequence X_n is understood in four different ways.

It is said that the sequence X_n converges to X with probability 1 or almost surely when:

$$P\left[\lim_{n\to\infty} X_n = X\right] = 1 \qquad (3.62)$$

A second type of convergence expressed as X_n converging to X in probability, reads:

$$\lim_{n \to \infty} P\left[|X_n - X| \geq \epsilon\right] = 0 \tag{3.63}$$

for every $\epsilon > 0$. When X_n converges to X in distribution it is meant:

$$\lim_{n \to \infty} F_{X_n}(x) = F_X(x) \tag{3.64}$$

This type is also known as weak convergence. Last, convergence can be understood in the moments sense, stating that X_n converges to X in the p-th moment when:

$$\lim_{n \to \infty} \mathrm{E}\left[|X_n - X|^p\right] = 0 \tag{3.65}$$

For the special cases of $p = 1$ and $p = 2$, it is said that X_n converges to X in the mean sense and in the mean-square sense correspondingly. Given the definitions (3.62)-(3.65), we could elaborate on the methods used in this thesis to determine the stochastic stability.

Mean-square stability. From the moment when the stability of a linear SDE is sought then the mean-square stability of its solution vector can be obtained analytically [69, 70]. The same procedure can also be applied for nonlinear systems, which have either been linearized around their origin to study the asymptotic stability of the system or one technique such as the stochastic averaging has been applied leading to a linear SDE. It is possible for this method to be applied to the original nonlinear system depending on the type of the nonlinearity, but it is quite possible for one to confront extreme difficulties during the analytical development. Nevertheless, the option of numerical analysis is always present.

Consider then the 2-D SDE stemming from Eq. (3.18) without loss of generality with $r = 1$ and which can be expressed as:

$$\begin{bmatrix} \dot{X}_1 \\ \dot{X}_2 \end{bmatrix} = \begin{bmatrix} a_1(\mathbf{X}, t) \\ a_2(\mathbf{X}, t) \end{bmatrix} + \begin{bmatrix} b_1(\mathbf{X}, t) \\ b_2(\mathbf{X}, t) \end{bmatrix} \zeta(t) \tag{3.66}$$

Let us now define the following variables $y_{11} = x_1^2, y_{22} = x_2^2, y_{12} = x_1 x_2$ for which we denote their expected values as D_{11}, D_{22}, D_{12}. Note that the latter correspond to the second moments of the original variables. Applying Ito's differentiation rule [169, 170] and taking the expectations yields the following deterministic system:

$$
\begin{bmatrix}
\dot{D}_{11} \\
\dot{D}_{12} \\
\dot{D}_{22}
\end{bmatrix}
= A_{3 \times 1} (D_{11}, D_{12}, D_{22})
\tag{3.67}
$$

where $A_{3 \times 1}$ is 3-rowed vector.

Consequently, the stability in the mean-square sense of the SDE (3.66) has been reduced to the stability study of the deterministic Eq. (3.67) with conventional dynamics tools being available. Thus, should the matrix A be linear to the vector of the second moments, a conventional eigenvalue analysis could be conducted to determine the mean-square stability of the system and potentially quantify the dependence on specific parameters of interest. If that is not possible, numerical integration of Eq. (3.67) could assist the investigation. Usually, the aim is to identify ranges of the system's parameters for which the solution is bounded. The aforementioned procedure could be generalized to the p-th moment and stability in the p-th moment sense.

Largest Lyapunov exponent. Another approach to explore the stability of the stochastic system is the evaluation of the LLE denoted by Λ. The sense in which stability is understood within this approach is with probability 1 - (see Eq. (3.62)). The mathematical background is given by Oseledec's Multiplicative Ergodic Theorem [70, 168, 189] which states that for both deterministic and stochastic dynamical systems, there exist real, deterministic numbers indicating the average exponential growth or decay of the solution. The definition of the LLE is [70, 168]:

$$
\Lambda = \lim_{t \to \infty} \frac{1}{t} \ln ||\mathbf{X}(t)||
\tag{3.68}
$$

The evaluation of Λ is possible in some cases through analytical development [70], widely based on the so-called Khasminskii's formulation [70, 168, 190] for which numerical solution is possible too. However, considering the phase space of a dynamical system, the i-th Lyapunov exponent could be expressed as:

$$\Lambda_i = \lim_{t \to \infty} \frac{1}{t} \ln \frac{a_i(t)}{a_i(0)} \tag{3.69}$$

where $a_i(t)$ represents the time-dependent axis of an ellipse formed around the origin of the system in the i direction. This could also be thought of as the projection of the amplitude in the i-th direction. The propagation of the solution to the equivalent discretized equations would change the value of $a_i(t)$. Then, an algorithm due to Wolf [191] could be applied for the stochastic system to calculate Λ numerically as:

$$\Lambda = \lim_{k \to \infty} \frac{1}{kdt} \sum_{k=1}^{K} \ln ||v_{p,k}|| \tag{3.70}$$

where $||v_{p,k}||$ is the Euclidean distance between the sample solutions of initial conditions $\mathbf{x}_0$ and $\mathbf{x}_0 + \epsilon$ at the k-th time step. Then, this expression can be incorporated in MC simulations in order to evaluate an average value of Λ. This particular algorithm has been proven to be particularly powerful in estimating LLE but one should note that, in order to avoid huge differences that cannot be handled by the numerical algorithm, the evolved initial perturbation is substituted by ϵ every m time steps. Ultimately, Λ could indicate the stability with probability 1 if $\Lambda < 0$ and instability in the same sense if $\Lambda > 0$.

Chapter 4

Directly excited stochastic pendulum

As was outlined in Sec. 1.1, one of the most important challenges in developing the WEC shown in Fig. 1.2 is the random nature of ocean waves. This randomness enforces a stochastic excitation and a random response of the floating pendulum, rendering the results of the determenistic models reviewed in Sec. 2.2.3 less trustworthy depending on the intensity of the randomness. In this Chapter, the equation of motion for a parametric pendulum is revisited, considering a random excitation. It is sought to study the influence of randomness on the potential of rotational motion. This is pursued by constructing PSPs based on MC sampling, charting the parameter regions where rotational response arises and assessing its robustness. The joint PDF of the state space variables is then calculated for selected cases by the PI method, in order to validate the picture drawn in the PSPs.

4.1   Governing equation

Consider a lumped mass M suspended at a point O, called the pivot point, through a non-deformable, massless rod of length L. The pivot is driven in time by the externally applied displacement $f(t)$, which will be considered to be strictly vertical for now. The mass M is free to vibrate in the angular space with its angular displacement θ and velocity $\dot{\theta}$ defining the state space of its response. The equation of motion can then be derived by using the standard Lagrange equations [65]. The
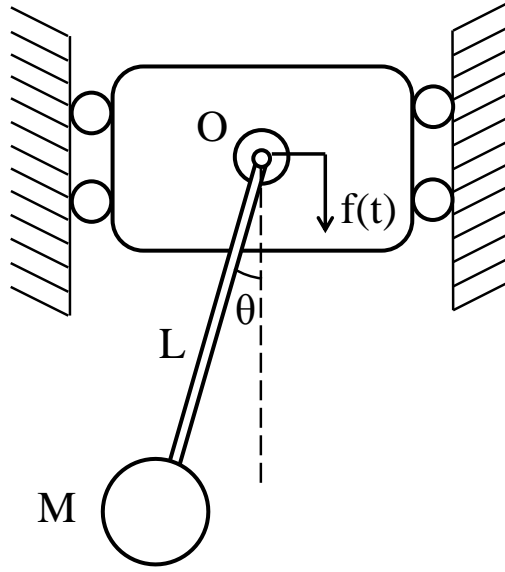
Figure 4.1: Simplified sketch of a parametric pendulum with mass M and length L, with its pivot point O driven by the displacement $f(t)$ in the vertical direction.

Lagrangian $\mathscr{L}$ then for the SDOF system shown in Fig. 4.1 would read:

$$\mathscr{L} = \frac{1}{2}ML^2\dot{\theta}^2 + MgL\left(1 - \cos\theta\right) \tag{4.1}$$

Applying then Lagrange's equation for the conservative system, considering θ as the generalized coordinate and including the forcing acting on the mass M due to the acceleration of the pivot, the equation of motion reads:

$$ML^2\ddot{\theta} + MgL\sin\theta = M\ddot{f}L\sin\theta \tag{4.2}$$

Let us normalize Eq. (4.2) with respect to the inertia of the lumped mass M around the pivot O and assume energy dissipation due to viscous damping, to get the following expression:

$$\ddot{\theta} + c\dot{\theta} + \left(\Omega^2 - \frac{\ddot{f}}{L}\right)\sin\theta = 0 \tag{4.3}$$

where c is the viscous damping coefficient and $\Omega = \sqrt{g/L}$ is the pendulum's natural frequency. It is quite common and rather useful too, to further normalize Eq. (4.3) with respect to the non-dimensional time $\tau = \Omega t$:

$$\theta'' + \gamma\theta' + \left(1 - \frac{f''}{L}\right)\sin\theta = 0 \tag{4.4}$$

with the prime denoting differentiation with respect to τ and $\gamma = c/L$. Eq. (4.5) is the fundamental expression of the parametric pendulum which in the case of a purely harmonic deterministic $f(t)$ becomes:

$$\theta'' + \gamma\theta' + (1 + \lambda\cos\nu\tau)\sin\theta = 0 \tag{4.5}$$

where $\nu = \omega/\Omega$ and $\lambda = A\nu^2/L$. Consideration of this system redirects to the studies presented in Sec. 2.2.3.

The scope of this thesis concentrates on the rotational motion of a lumped mass pendulum when vertically driven, or else, the parametric pendulum. In order to model the stochastic excitation, two approaches will be considered. First, the exciting force will be modeled as a simple Gaussian white noise $\zeta(t)$ – Sec. 3.1.2 – and then the RPM will be used – Sec. 3.2.2 – to manifest the excitation as a narrow-band process.

4.2   White noise excitation

In this simplistic approach, the excitation is modeled as $f''(\tau) = \zeta(\tau)$ resulting in:

$$\theta'' + \gamma\theta' + \left[1 - \frac{\zeta(\tau)}{L}\right]\sin\theta = 0 \tag{4.6}$$

It is much harder to use analytical methods for Eq. (4.6), thus a numerical approach will be used based on MC sampling and the PI method. In the context of the WEC application this modeling approach might describe the case of an extremely
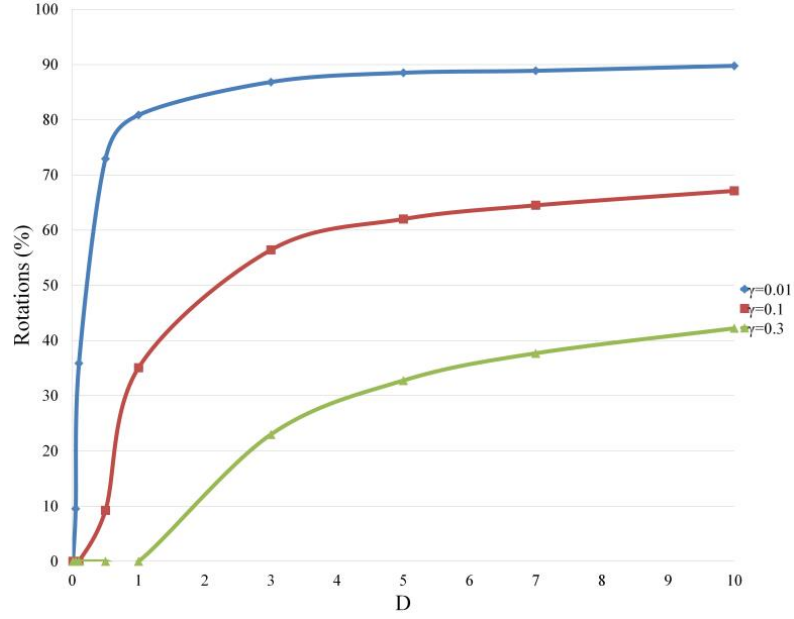
Figure 4.2: Percentage of rotations for system Eq. (4.6) and different values of γ and D.

random sea state such that the PM spectra models fail, e.g. the case of a stormy environment. Nevertheless, a first indication of the effect of noise on the pendulum's response should be drawn, considering the substantial shortage in the subject. In the simulations, the results of which are shown in Fig. 4.2, the noise intensity incorporates the length of the pendulum L, by which the stochastic process $\zeta(t)$ is divided as it could be seen in Eq. (4.6), so that $D = <\zeta(\tau_0)\zeta(\tau_0 + \tau)>/L$.

4.2.1 Rotational response

Considering the system in Eq. (4.6), the only source of input energy is the noise process. This means that the deterministic equivalent ($D = 0$) would be the free-vibrating system which makes no particular fit for comparison. Hence, the stochastic system will be evaluated only regarding its parameters. In that respect, it could be expected at a first glance that the bigger the noise intensity D, the more likely for the system to exhibit rotational motion since more energy enters the system. This is a premise to be evaluated based on the results.

Fig. 4.2 shows the results of MC sampling of a total 100,000 mean periods. In each sample, an online tracking of rotations is conducted given the straightforward implementation of MC methods (see details in Sec. 4.3.1). Then the percentage of the

time spent rotating over the total time of the simulation is extracted and presented in Fig. 4.2 for increasing noise intensity and 3 values of the non-dimensional damping coefficient γ.

Observing the curves in Fig. 4.2, one could first notice that higher damping coefficient requires higher energy levels to perform rotations. This could be seen by comparing the curves for $\gamma = 0.01$ and $\gamma = 0.3$. The former is manifesting rotational response from the very small D values, while the latter is exhibiting rotational motion only after $D > 1$. This is quite reasonable given the fundamental effect of damping on the instability boundaries of the linear system – see Secs (2.2.1) and (2.2.2)– and since larger γ values mean that more energy is dissipated per cycle.

Moreover, it is noticed that within a reasonable range of D as the one used in Fig. 4.2, there is an upper limit of the possible rotational motion percentage to which the system converges, depending on the damping value. For $\gamma = 0.01$ this limit is around 90%, for $\gamma = 0.1$ around 70% and for $\gamma = 0.3$ between 40 and 50%. This contradicts the premise adopted to be tested in the beginning of this subsection in a somewhat counterintuitive manner. White noise is an idealized mathematical description never practically occurring in nature and above all in engineering applications. The constant spectrum, spread along the frequency axis means the process has infinite power which nevertheless is not manifested through rotational motion, expect for up to a level. Thus, the converging behaviour of the rotational percentage, which in fact could acquire a rather low value (50%) depending on the magnitude of the energy dissipated is an attribute worth noticing.

4.2.2 PDF calculation

Even though the approach based on MC sampling draws a clear picture of the influence of stochasticity, the calculation of the PDF of the response is substantial in order to verify these results. Given the type of the conducted analysis and the highly nonlinear attributes of Eq. (4.6), MC sampling does not guarantee that rare events will be taken into account. Thus, a full probabilistic description can only be given by the knowledge of the PDF.
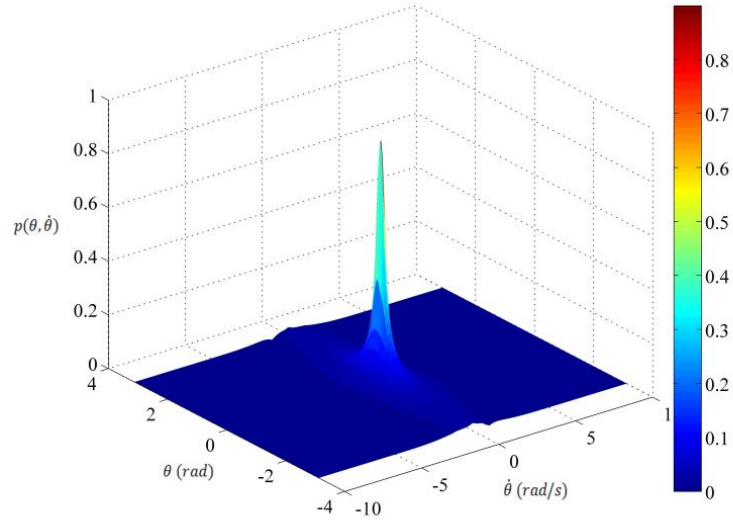
(a)
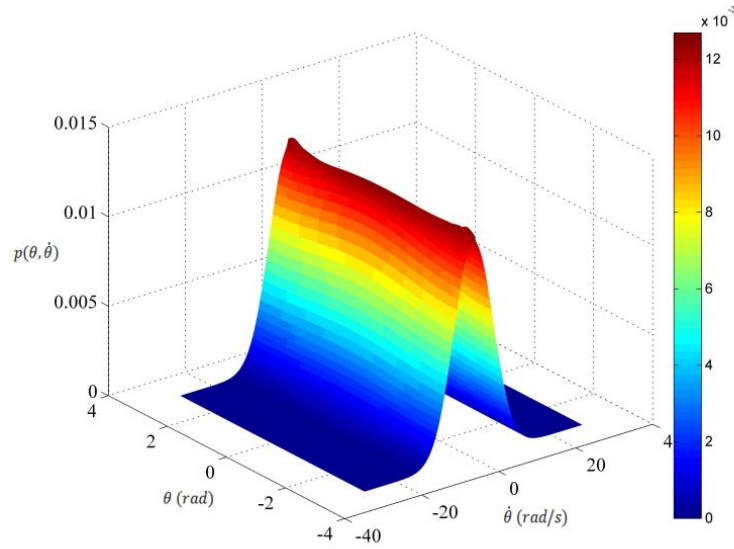
(b)

Figure 4.3: PDFs of Eq. (4.6) response calculated with the PI method for: (a) $\gamma = 0.1$ and $D = 1$; (b) $\gamma = 0.01$ and $D = 5$.

The solution to the FPK equation for the system in Eq. (4.6) is rather hard to acquire by analytical means. Therefore, the PDF is computed by the PI method, implementing the numerical iterative scheme described in Sec. 3.3.3.

Fig. 4.3 shows the joint PDF for the response of Eq. (4.6) for two cases selected from Fig. 4.2. The state space is chosen as $[-\pi, \pi]$ for θ since it is an angle and $[-5\sigma_{\theta'}, 5\sigma_{\theta'}]$ for the velocity with $\sigma_{\theta'}$ being the standard deviation of the velocity process which

is calculated through initial sampling. Formally, the range of the velocity should be infinite which cannot be implemented numerically. A range large enough is chosen, such that the tails of the PDF in that direction smoothly approach zero and thus, the PDF can be assumed to be zero-valued outside this range. Yet, it is always important to verify that the used range is adequate and that can be done by observing the tails of the calculated PDF. Also, a useful indirect but sufficient measure is the integral of the PDF over the state space, which should be approaching 1 if no subsets of the state space with high probability are excluded. The last criterion is also practical because it can be verified online, in each and every time step.

First, Fig. 4.3(a) considers a point from the $\gamma = 0.1$ curve for $D = 1$. The MC sampling indicates 35% of rotational motion. That is equivalent, given the ergodicity of the process, to the integral over the state space points, which correspond to orbits for which the heteroclinic orbit is broken, i.e. the non-dimensional energy is bigger than 1. The PDF in Fig. 4.3(a) presents itself with what appears to be a spike on the origin of the system. Indeed, this is an expected behaviour for the parametric system since the origin is a fixed point which could be stable depending on the excitation parameters. This medium manifestation of rotations allows room for a significant amount of probability being drawn from the origin's potential well, which in terms of the PDF means a growing spike. The limiting case of this spike is the delta function which would mean in turn a deterministic response with all the probability concentrated on one point.

On the other hand, Fig. 4.3(b) depicts a quite different outcome. The PDF of the system for $\gamma = 0.01$ and $D = 5$ is shown, expected from Fig. 4.2 to mostly rotate with 90% of the sampling time in rotations. The calculated PDF verifies this expectation. The spike on the origin is missing with the probability distributed within a much larger range of the velocity, considerably higher than the heteroclinic orbit. Note that, because of the symmetrical initial assumption for the PDF, the resulting response PDF is point-symmetric with respect to the origin. This practically reflects that unbiased initial conditions yield equal probability for the direction of the pendulum's motion.

4.3   Random phase sinusoidal excitation

As soon as the sea state is considered to be fully developed, meaning that the traveling swells are far enough from the generation area and the fetch can be assumed not to influence anymore the shape and the kinematics of waves, the PM spectra model – Sec. 3.2.1 – can be used. In Sec. 3.2.2, the RPM has been used to approximate the PM spectrum and it is utilized herein with a minor modification. In order to avoid differentiating the stochastic process $\zeta(t)$, the excitation is modeled as $\ddot{f}(t) = A\omega_m^2 \cos q$. Note that this expression follows Eq. (3.38), however it is not derived through direct differentiation. Yet, this modification would not incur major implications. Quite often, the bobbing motion of a buoy is modelled as a Gaussian white noise filtered through a linear second order system [69]. It has been found that the spectrum of the output is narrow-band, similar to Eq. (3.39) [83], with the spectrum of the output's second derivative being a mere multiple of that. However, this model would increase the dimensions of the equations of motion. Thus, the herein utilized model is more straightforward with any deviations in the multiplier of the spectrum compensated by the fact that the following analysis is non-dimensional. Then, Eq. (4.3) would now read:

$$\ddot{\theta} + c\dot{\theta} + \left(\Omega^2 + \frac{A\omega_m^2}{L} \cos q \right) \sin \theta = 0 \tag{4.7}$$

Applying the non-dimensionalization in time, $\tau = \Omega t$, the set of equations describing the pendulum's motion reads:

$$\theta'' + \gamma\theta' + (1 + \lambda \cos q) \sin \theta = 0$$
$$q' = \nu + \sigma\zeta(\tau) \tag{4.8}$$

where $\nu = \omega_m/\Omega$ is the ratio of the excitation mean frequency over the pendulum's natural frequency and $\lambda = A\nu^2/L = A\omega_m^2/g$ is the non-dimensional excitation amplitude. The parameter pair (ν, λ) will hold a key role in the following analysis, since it controls the type of the response of the parametrically excited pendulum. The
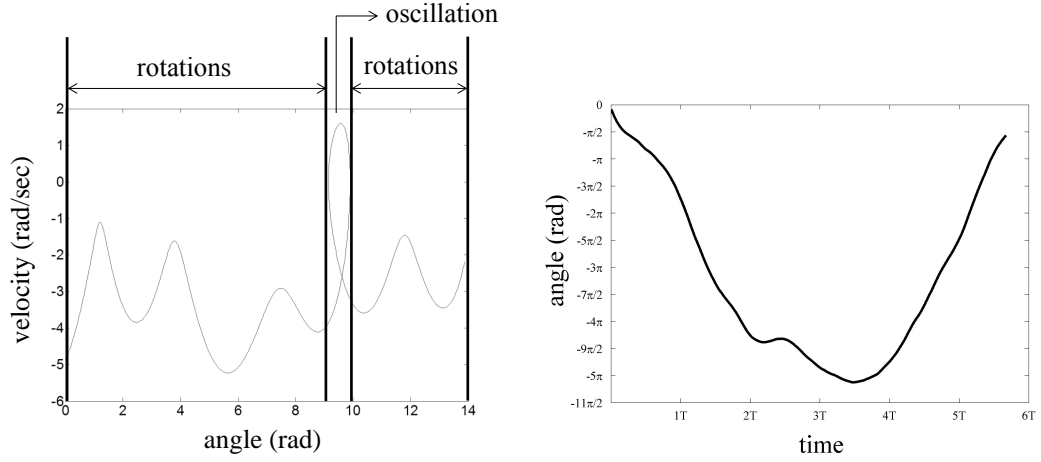
Figure 4.4: Angular velocity against displacement demonstrating the process of counting rotations. Irregular trajectories might occur due to the presence of noise forcing the pendulum to change direction of motion before completing a full rotation. Since this is a random response, this behaviour is not part of a periodic pattern, and thus, a more elaborate perception of a full rotation than the crossing of $\theta = \pi$ is required.

hereinafter investigation focuses on identifying those parameter regions for which the pendulum's random response is rotational and evaluates the robustness of this manifestation. This will be attempted by constructing PSPs based on MC sampling of the response of Eq. (4.8), targeting to spot these regions. Before proceeding to that, it is worth discussing the identification of a rotational trajectory within a random sample.

4.3.1   Identifying rotations

A significant aspect is that of identifying and separating the rotational motion of a pendulum from oscillatory. It is not a trivial task to understand what can be treated as rotational motion. Indeed, some trajectories can easily be identified as rotational, especially for low noise intensity where the trajectories would slightly deviate from the deterministic one. However, there are complex or irregular trajectories (Fig. 4.4(a)), when the system changes the direction of rotation several times. It should be stressed that different definitions of the rotational motion may be adapted. In previous studies, rotations were understood as crossings of the upper equilibrium, $\theta = \pi$, or in other words, according to this definition a rotation is regarded when the mean energy of the system per cycle is larger than the en-

87

ergy needed to overcome the maximum potential energy $2MgL$. Herein, a rotation will be understood as a full 2π angular displacement with a constant velocity sign throughout that interval. This means that the phase plot of a pendulum rotating in one direction would always lie on the one half of the state space defined by the $\theta' = 0$ line. Since this is a numerical approach, an online tracking within the sample is possible. Each point $(\theta, \dot{\theta})$ at a certain time step is evaluated with respect to two criteria. First, the total angular displacement from the starting point and next the velocity of all the points within that range. A starting point with displacement θ_M is defined either by the last point of the last recorded rotation or by the last point failing the criteria. Every point θ_N subsequent to the starting one is required to fulfill the criteria. If one does not, then it becomes the starting point of the tracking. Then, as soon as enough points with the same sign of their velocity accumulate such that $|\theta_N - \theta_M| > 2\pi$ then one rotation is counted and $M = N$ is set to prepare for the tracking of the next rotation. Note that, even though possible, this tracking does not distinguish between clockwise and counterclockwise rotations.

Fig. 4.4(b) shows a part of the time series, where the system's motion starts as rotational with negative velocity. At the beginning of 2T the system's velocity changes to positive and back, so that the system has at this interval an oscillatory motion. Then rotational motion with negative velocity continues until the system crosses $-\pi$(or -5π) with negative velocity. At this point one would count this as rotational motion, according to the definition based on π crossings. However, the system does not continue with negative velocity, but rather changes the velocity back to positive around $3.5T$ and crosses the vertical equilibrium position again. Based on the second definition none of this motion, the points within the $[2T, 3.5T]$ interval would not be counted as rotational, and this is what was called the irregular cycle. Then the system proceeds continuously rotating with some positive velocity, which can be count as rotational motion according to the second definition. Obviously, the first definition overestimates the percentage of the rotational motion, since it is based on the mean energy, and thus the definition of rotational motion considering every point and not only crossings is adopted hereinafter.
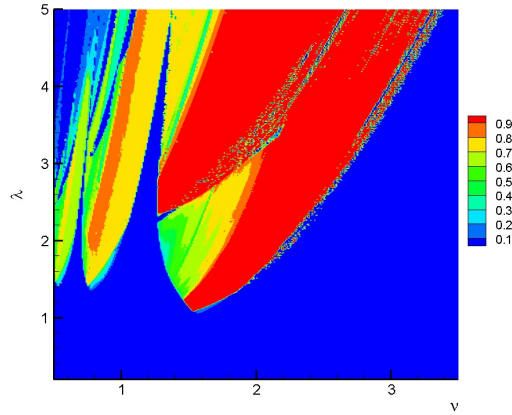
Figure 4.5: PSP of the response of Eq. (4.8) for $D = 0.0$, $\gamma = 0.3$, $\theta(0) = 0.01\pi$ and $\dot{\theta}(0) = 0$;

4.3.2 Parameter space plots

Whereas previous authors have been concentrating on the identification of regions with responses differing in many ways, along with the locus of the corresponding bifurcations, in this thesis the focus is drawn on distinguishing between two fundamentally different types of motion - rotational and oscillatory. Thus, rotational motion with different periods or even direction will be counted here as just rotational, whereas oscillatory motion of different periods or asymptotically stable response will be regarded as non-rotational or, broadly put, oscillatory.

The results demonstrated in Figs 4.5–4.7 show numerical simulations of Eq. (4.8) in the parameter space (ν, λ) for different values of noise intensity D, damping coefficient γ and initial conditions. The results demonstrate the average ratio of the time that the system spent rotating over the total time of the simulation, so that the red area corresponds to this ratio being over 90%, whereas the blue area to values less than 10%, primarily indicating oscillatory or asymptotically stable motion. Fig. 4.5 illustrates the results for the deterministic case ($D = 0$), which in general agree with the plots delivered in [7]. Some difference is related to the definition of rotational motion and combination of rotational and oscillatory motions correspondingly. It should also be emphasized that no distinction between rotational motion in different, clockwise and counterclockwise, directions has been made. This figure shows two distinct domains with dominant rotational motion, which are separated by a strip

of stable upright position points, a phenomenon attributed to parametric excitation (Sec. 2.2.3).

Fig. 4.6 presents the extracted PSPs for the same value of damping coefficient $\gamma = 0.1$, different values of noise intensity and initial conditions. First of all it could be seen that there is minimal influence of the initial conditions on the system's response, attributed rather to the error margin of MC simulations. This observation is different from one, reported for the similar deterministic system, where the initial conditions predefine the system's behavior according to the basins of attraction. Furthermore, it can be seen that the increase of noise intensity significantly reshapes the domains with dominant (over 90%) rotational motion. For small values of noise intensity, shown in Figs 4.6(a) and 4.6(b) and Figs 4.6(d) and 4.6(e), the right boundary distinguishing the oscillatory-stable response from the rotational sub-domains is not far from that of the deterministic system. It is expected to transform to a line with lower slope under the influence of increasing noise. This stems for the observed widening effect on the stability-instability boundaries of the linear counterpart. Indeed, comparing the PSPs of each column in both Figs 4.6 and 4.7, it could be seen that increasing noise incurs a widening effect in the RHS part of the plots ($\nu > 2$) . The same widening effect could be observed on the other side of the plots ($\nu < 2$); however, in a rather more complicated manner due to the interaction with the secondary resonance zone. In particular, the two most noticeable resonance zones, the primary and secondary, tend to merge into a single domain under the diffusing effect of noise. This is especially clear in the bottom PSPs of both figures for $D = 0.1$. The two distinct rotational regions merge into one, surrounded by regions of decreasing presence of rotations ($< 90\%$). Also, the non-rotational parameter region in between the two resonance zones, which occupies a respectable area in the deterministic response in Fig. 4.5 and spikes up to $\lambda = 5$, retracts down to $\lambda = 2$ for the stochastic response. The corresponding area is then gradually flooded by points exhibiting rotational motion as the noise intensity increases, succumbing to the diffusing behaviour of the resonance zones.

Another significant observation extracted from this analysis is related to the damping coefficient. Figure 4.7 shows the results of the numerical simulations for a value of
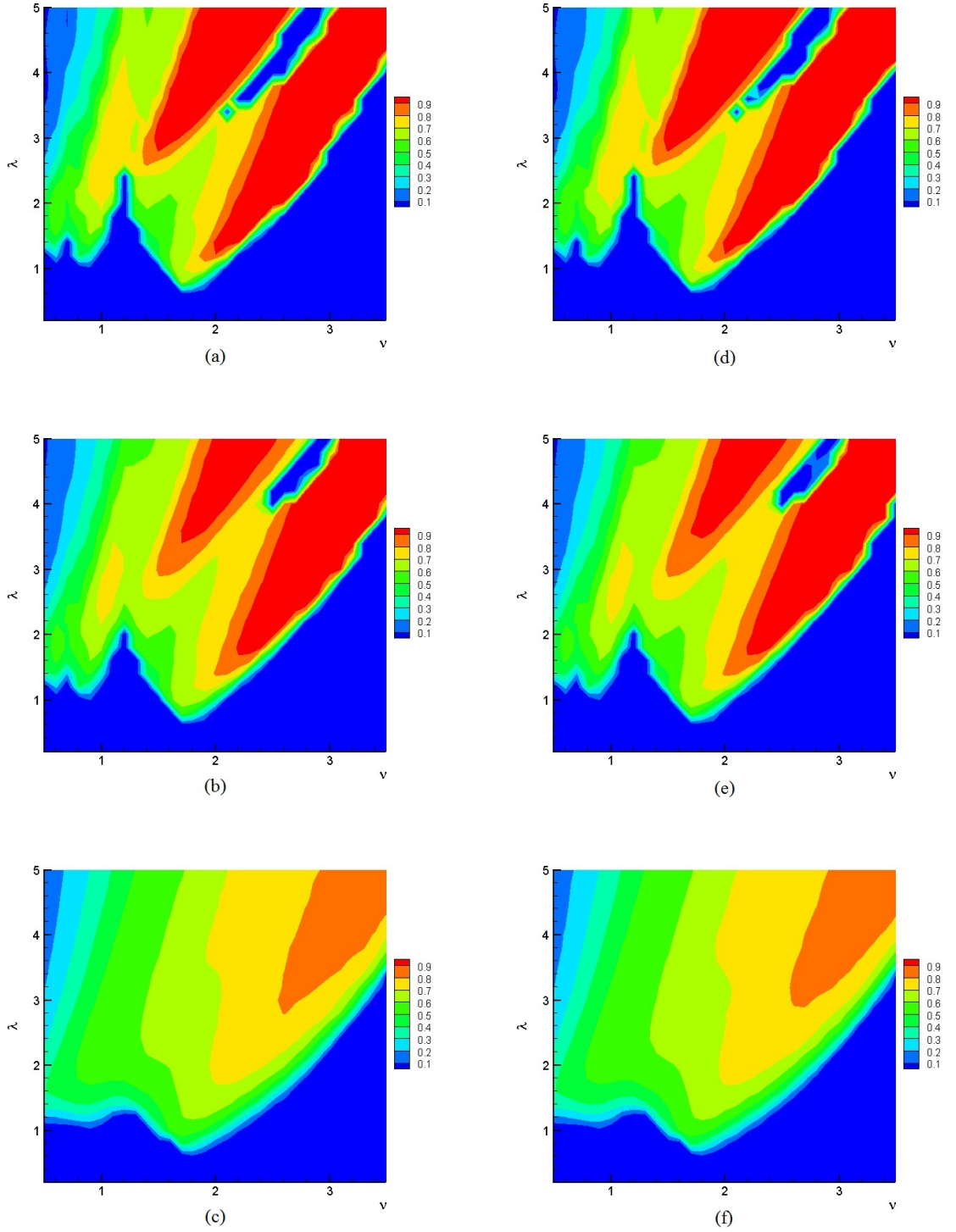
Figure 4.6: PSP with ratio of rotational motion of the response of Eq. (4.8) for $\gamma = 0.1$ and $\dot{\theta}(0) = 0$. (a) $D = 0.005$ and $\theta(0) = 0.01\pi$; (b) $D = 0.01$ and $\theta(0) = 0.01\pi$; (c) $D = 0.1$ and $\theta(0) = 0.01\pi$; (d) $D = 0.005$ and $\theta(0) = \pi/2$; (e) $D = 0.01$ and $\theta(0) = \pi/2$; (f) $D = 0.1$ and $\theta(0) = \pi/2$.

$\gamma = 0.3$. Although it is known that increasing the damping value will slightly
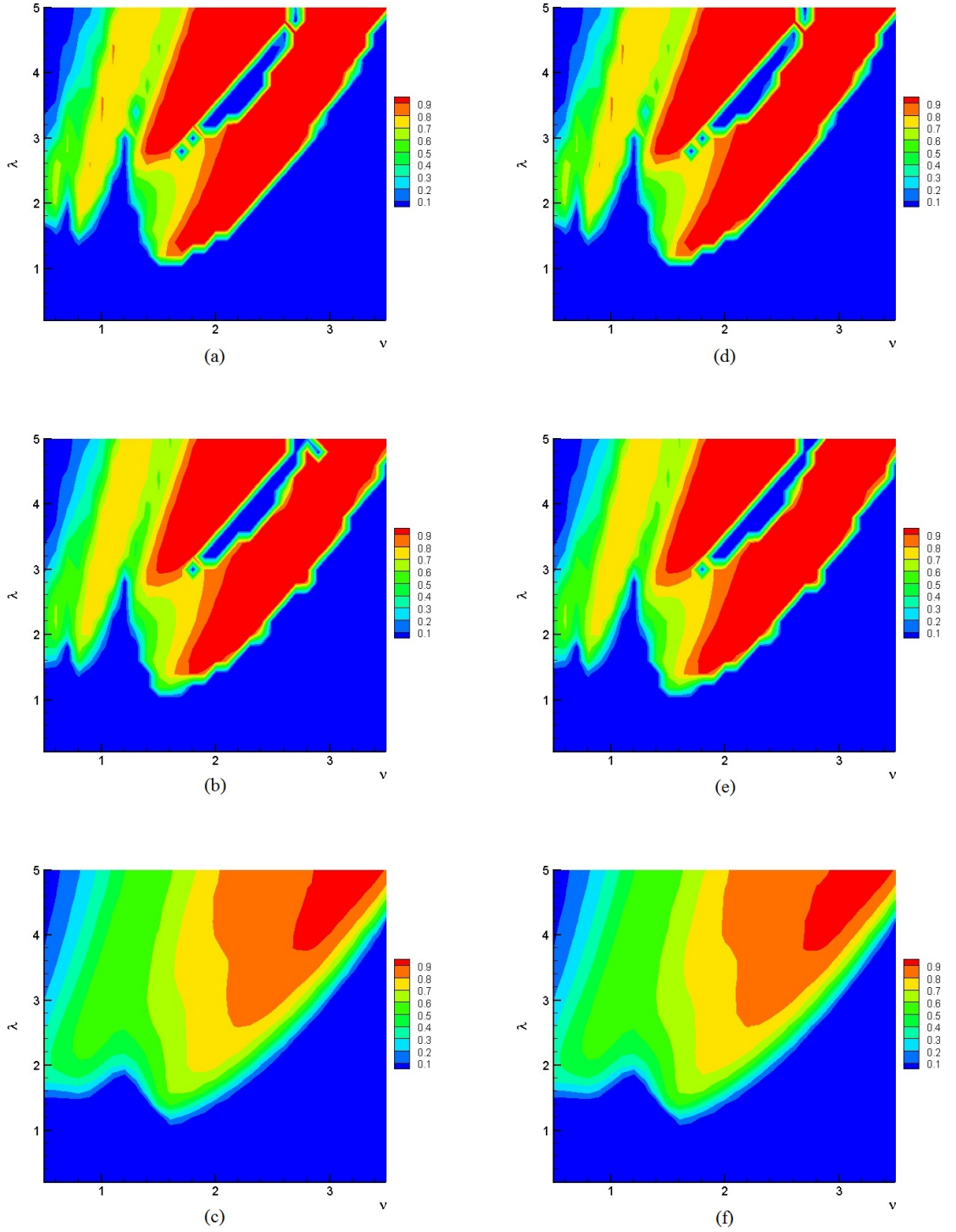
Figure 4.7: PSP with ratio of rotational motion of the response of Eq. (4.8) for $\gamma = 0.3$ and $\dot{\theta}(0) = 0$. (a) $D = 0.005$ and $\theta(0) = 0.01\pi$; (b) $D = 0.01$ and $\theta(0) = 0.01\pi$; (c) $D = 0.1$ and $\theta(0) = 0.01\pi$; (d) $D = 0.005$ and $\theta(0) = \pi/2$; (e) $D = 0.01$ and $\theta(0) = \pi/2$; (f) $D = 0.1$ and $\theta(0) = \pi/2$.

lift the domains upwards, this is not the only noticeable effect. Comparing the
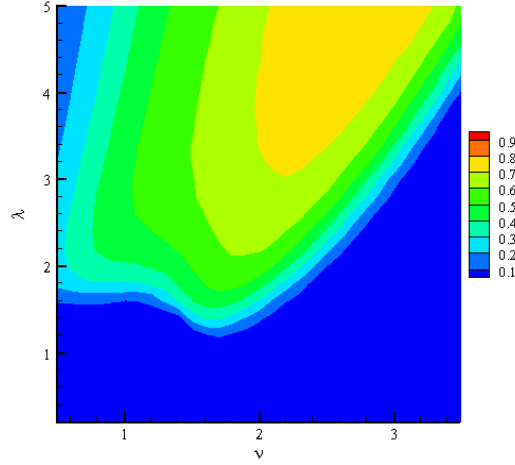
Figure 4.8: PSP of the response Eq. (4.8) for $D = 0.3$, $\gamma = 0.3$, $\theta(0) = 0.01\pi$ and $\dot{\theta}(0) = 0$;

corresponding PSPs where only the damping is different, the domains with dominant rotational motion have slightly increased in size and intensity and became observable for smaller values of λ. It is suggestive that in both Figs 4.7(c) and 4.7(f), the region with the highest rotational percentage overcomes the 90% threshold when the corresponding areas for $\gamma = 0.1$ do not. Thus, reasonably large values of a viscous damping coefficient enhance the probability of rotational motion of the system. This is attributed to the stronger dissipation of small and rapid fluctuations, which would force the system out of tune. Moreover, it should be noted that in the areas of dominant rotational motion, once the rotational motion has started it would not change its direction.

Let us now present the PSP corresponding to $D = 0.3$. It has been shown in Sec. 3.2.1 that the spectrum of the RPM closely approximates the wave spectrum for this noise intensity value. Even though now the transformed equations are considered, this observation still holds because of the dependence of the variance of the stochastic part in the Euler-Maruyama scheme onto the time step. Introducing the time non-dimensionalization that was used in Eq. (4.8), immediately affects the time step and thus the variance of the stochastic sequence. Hence, the PSP shown in Fig. 4.8 could still be connected to the dynamics of the ocean. It is though observed that the influence of this bigger noise intensity has a degenerating effect of the rotational domains, leaving the most frequently observed rotations to just over

70% of the simulated time.

4.3.3   Analysis with PI

Following the construction of the PSPs, the calculation of the PDF for selected cases is reckoned to be essential given the issue of the accuracy and reliability of MC simulations. The PI method, which is used to calculate the PDFs, even though extremely accurate, it suffers from the so-called curse of dimensionality. Increasing number of dimensions of the problem dramatically deteriorates the efficiency of the implementation of the PI method. On the other hand, MC simulations are almost immune to increase of the dimensionality of the investigated system. Thus, the strategy of this analysis is selected in a way that balances between accuracy and efficiency. First, the computation of the PSPs provides a crude, yet efficient estimation of the rotational response of the parametric pendulum. Then, the reliable PDFs resulting from the accurate PI technique enhance the trustworthiness of the PSPs.

The PDFs of three different cases are presented in Fig. 4.9 with 3D views and 2D views shown in the left and right columns correspondingly. Figs 4.9(a) and 4.9(b) correspond to a point with dominant rotations, coming from Fig. 4.7(a) and with $D = 0.005$ and $\gamma = 0.3$, for a frequency ratio $\nu = 2.4$ and amplitude $\lambda = 3.0$. The PDF from Figs 4.9(c) and 4.9(d) was calculated for $D = 0.1$, $\gamma = 0.3$, $\nu = 3.0$ and $\lambda = 4.4$ which corresponds to the red region from Fig. 4.7(c) and the last pair, Figs 4.9(e) and 4.9(f) has the same parameters as the previous one, only for the bigger noise intensity, $D = 0.3$.

The cases, the response of which is mostly rotating, in the first and second pair, find most of the probability concentrated in the regions of the state space with rotational trajectories, i.e. beyond the heteroclinic orbit. However, there are some differences worth mentioning. In the first case with the small noise intensity, the probability attached to the rotating trajectories is unevenly distributed with the points closer to $(\pm\pi, y)$ having bigger values than those closer to $(0, y)$. On the contrary, the probability assigned to rotations in the second pair is evenly distributed along its

(a)

(b)

(c)

(d)

(e)

(f)
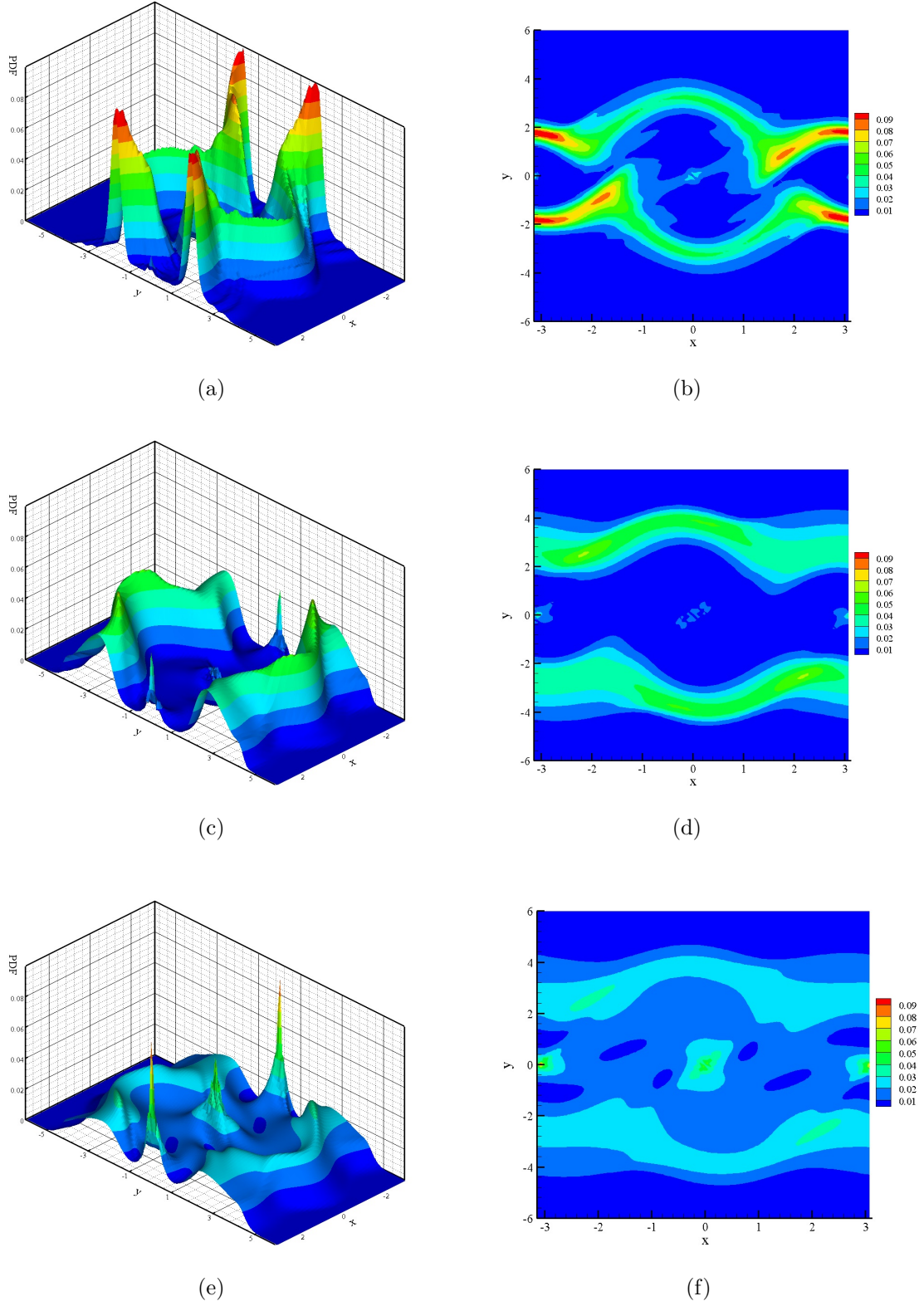
Figure 4.9: PDFs calculated with the PI method for $\gamma = 0.3$; (a) $D = 0.005$, $\nu = 2.4$ and $\lambda = 3.0$; (b) its top view; (c) $D = 0.1$, $\nu = 3.0$ and $\lambda = 4.4$; (d) its top view; (e) $D = 0.3$, $\nu = 3.0$ and $\lambda = 4.4$; (f) its top view;

trajectories. This could be explained by the actual motion of the pendulum in the two cases. When the noise intensity is small, the system's response is close to the deterministic one in which the pendulum crosses the low equilibrium point with high kinetic energy and zero potential energy. Crossing the upper equilibrium point comes with low velocity and high potential energy. Thus, the probability for the pendulum to stay in the low velocity region is higher since it spends more time of its cycle there. However, when the noise intensity is increased, the response bears less resemblance to the deterministic one eliminating the previous observation. Moreover, comparing the second and third PDFs in Figs 4.9(c) and 4.9(d) and Figs 4.9(e) and 4.9(f), one can observe what has been noticed from the PSPs analysis. First, these PDFs where counted as over 90% and 70-80% of rotations respectively, meaning that rotations have degenerated to oscillations in the third pair. Comparing the top views it is seen that even though the main trajectories are unaltered, different probability values is assigned to them. Indeed, as it can be better seen from the 3D views, the probability of rotational motion has significantly dropped in the third pair while the probability of oscillations around the two fixed points has increased along with the noise intensity increase, which is also the only different parameter between the two PDFs concerned.

In order, though, to acquire a quantitative view of the difference between the two methods, the PDF of the energy of the system will be used, derived from transforming $p_{xy}(x, y)$. The total energy of the system is expressed by $E = 0.5ML^2\theta'^2 + V(\theta)$, where V denotes the potential energy. In general, transforming the PDF to new variables follows the standard coordinate transformation, given by Eq. (3.4). For transforming the joint response PDF of a pendulum from the displacement and velocity variables to the energy, the formula would read:

$$p_E(E) = C \int\limits_{V(x) \leq E} p_{xy}(x, y) \left| \frac{1}{\sqrt{2\left[E - V(x)\right]}} \right| dx \qquad (4.9)$$

with C being a normalization constant. Having transformed the PDF to the energy through Eq. (4.9), then the probability for $E > E_0$ can be calculated. Setting
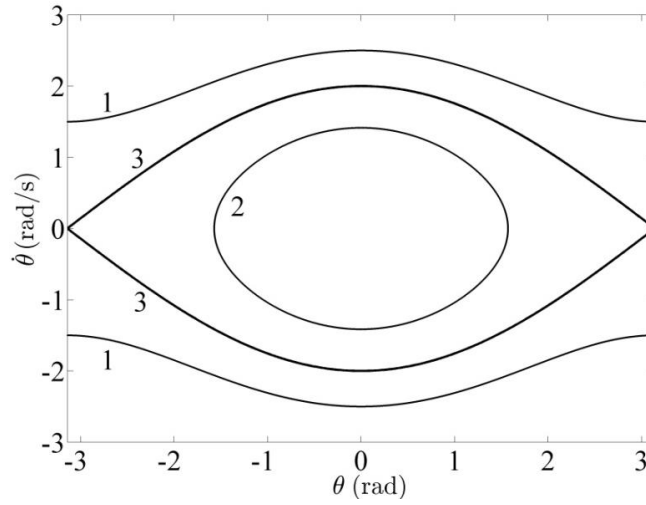
Figure 4.10: State space of the conservative pendulum; rotary (lines 1) and oscillatory orbits (line 2); heteroclinic orbit (lines 3).

$E_0 = 2MgL$, which is the energy value defining the heteroclinic orbit or else the separatrix trajectory, one could calculate the probability for the pendulum to lie in the rotational region of the state space (see Fig. 4.10), considering as a threshold the deterministic value E_0.

In Fig. 4.11, the transformed energy response PDFs are presented against the normalized energy $E^* = E/(MgL)$ with focus on the two largest noise intensity values $D = 0.1$ and $D = 0.3$. Fig. 4.11(a) shows the PDF corresponding to Fig. 4.9(c). A spike at $E^* = 2$ is noticed representing the probability of a stabilized upper fixed point, a case which has been shown to hold when a parametric excitation is applied to the pendulum. Integrating, then, over the part of the PDF to the right of this spike gives the probability of rotational motion. The same spike is also observed in Fig. 4.11(b) and Fig. 4.11(d) where the pendulum motion incorporates rotational trajectories. Fig. 4.11(c) depicts the PDF for a parameter pair resulting in a bottom fixed point response, thus a delta function arises at $E^* = 0$ and the spike at $E^* = 2$ is no longer noticeable.

The calculated probabilities of rotations, denoted as $p(R)$, for the four cases are gathered in Table 4.1. If one refers to the PSPs found in the previous section, the calculated probability values fall into the predicted ranges for $p(R)$. Against these values, the exact estimation of $p(R)$ found through MC simulations of a total 100,000
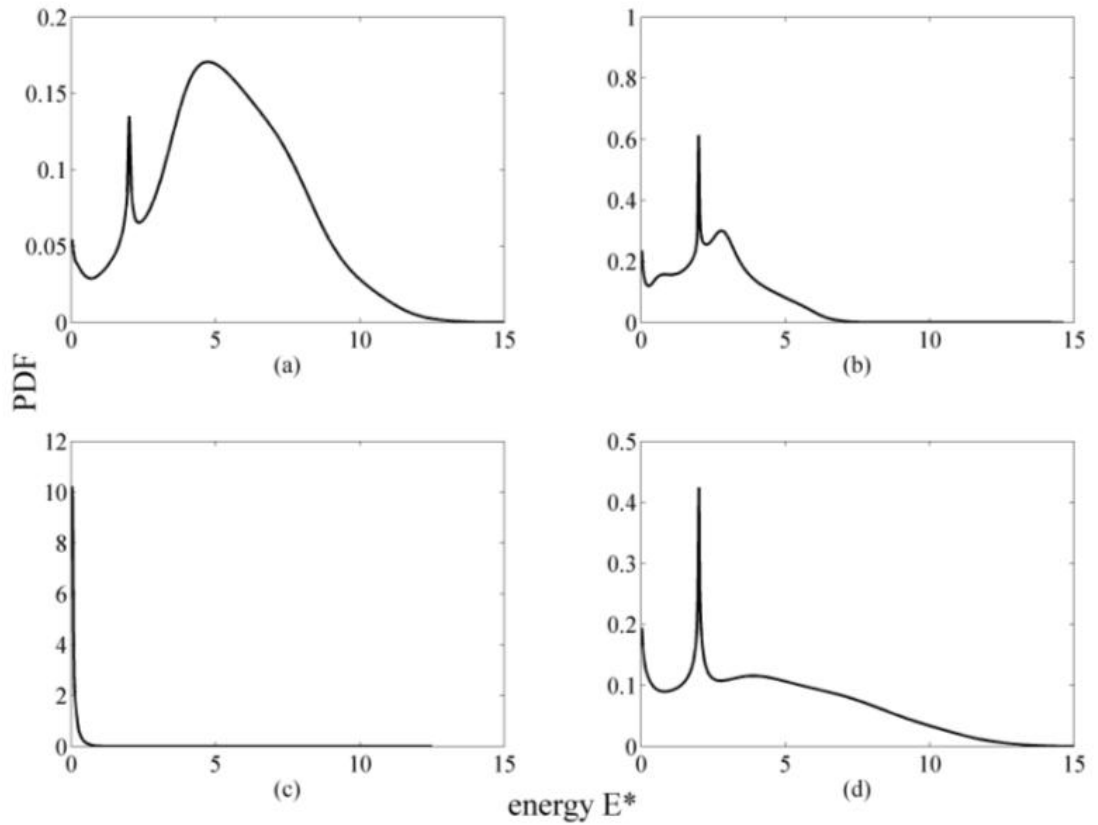
Figure 4.11: Energy PDF of the parametric pendulum for (a) $D = 0.1, \gamma = 0.3, \nu = 3.0, \lambda = 4.4$; (b) $D = 0.1, \gamma = 0.3, \nu = 1.8, \lambda = 3.0$; (c) $D = 0.1, \gamma = 0.3, \nu = 2.6, \lambda = 1.0$; (d) $D = 0.3, \gamma = 0.3, \nu = 3.0, \lambda = 4.4$.

periods is listed. It can be seen that, the $p(R)$ values coming from the two methods are rather close, even though it is expected for the MC modeling to ignore a considerable amount of information and thus yielding erroneous estimations. Moreover, the mean values of the energy $<E^*>$, along with the standard deviation σ_{E^*} are computed for the two different methods. Direct comparison of the values presented in Table 4.1, shows that there is sufficient agreement between the statistical properties of the samples and the PDF-based numerical values. It is worth noting that the mean energy is higher when $p(R)$ is high too (see, for example, case (a) against cases (b) and (d)). This validates the nevertheless reasonable expectation that rotational response is beneficial regarding energy extraction. The same observation can be made for the standard deviation too, when the same noise intensity is considered, e.g. $D = 0.1$ in cases (a) and (b). For larger noise intensity case (d), the standard deviation is greater than in case (b) even though the rotational probability gets similar values.

Overall, it could be argued that the disagreement between the two methods indicating the error of the MC simulations is sufficiently small when $p(R)$ is sought. However, it could also be concluded that imposing higher resolution in the colourmap of the PSPs than the currect 10% would be meaningless since these estimations would not be reliable.

4.3.4 Nonlinear damping

So far, the assumption has been made that the damping function of the pendulum is linear based on the viscous damping model. However, in most practical applications the mechanism regarding the energy dissipated from the system is generally non-linear. In order to better estimate the actual behaviour of the system, a nonlinear damping function is introduced taking the following form:

$$d\left(\dot{\theta}\right) = \gamma\dot{\theta} + Rsign\left(\dot{\theta}\right) \tag{4.10}$$

where d is the damping function, γ - the viscous damping coefficient and R - a constant representing the Coulomb friction. In this section, the effect of a nonlinear damping function on the rotational regions of the parameter space will be discussed, focusing mainly on the Coulomb friction since the viscous damping effect has been addressed in the previous sections.

A rather unrealistic case, yet interesting from a dynamics point of view and particularly indicative will be considered. The damping is taken as having only the nonlinear part, i.e. the viscous damping is omitted from Eq. (4.10). In Fig. 4.12, only dry friction is resisting the motion at a value of $R = 0.005$ and four different

Table 4.1: Probability of rotational motion, $p(R)$, corresponding to the cases of Fig. 4.11. Mean energy $<E^*>$ and its standard deviation σ_{E^*}. Comparison of the MC samples with the PI method.

	$p(R)$-MC	$p(R)$-PI	$<E^*>$-MC	$<E^*>$-PI	σ_{E^*}-MC	σ_{E^*}-PI
(a)	0.930	0.917	5.522	5.401	2.267	2.401
(b)	0.725	0.656	2.643	2.661	1.465	1.467
(c)	0.000	0.015	5.194E-9	0.121	1.237E-6	0.155
(d)	0.704	0.778	4.534	4.613	3.001	2.979
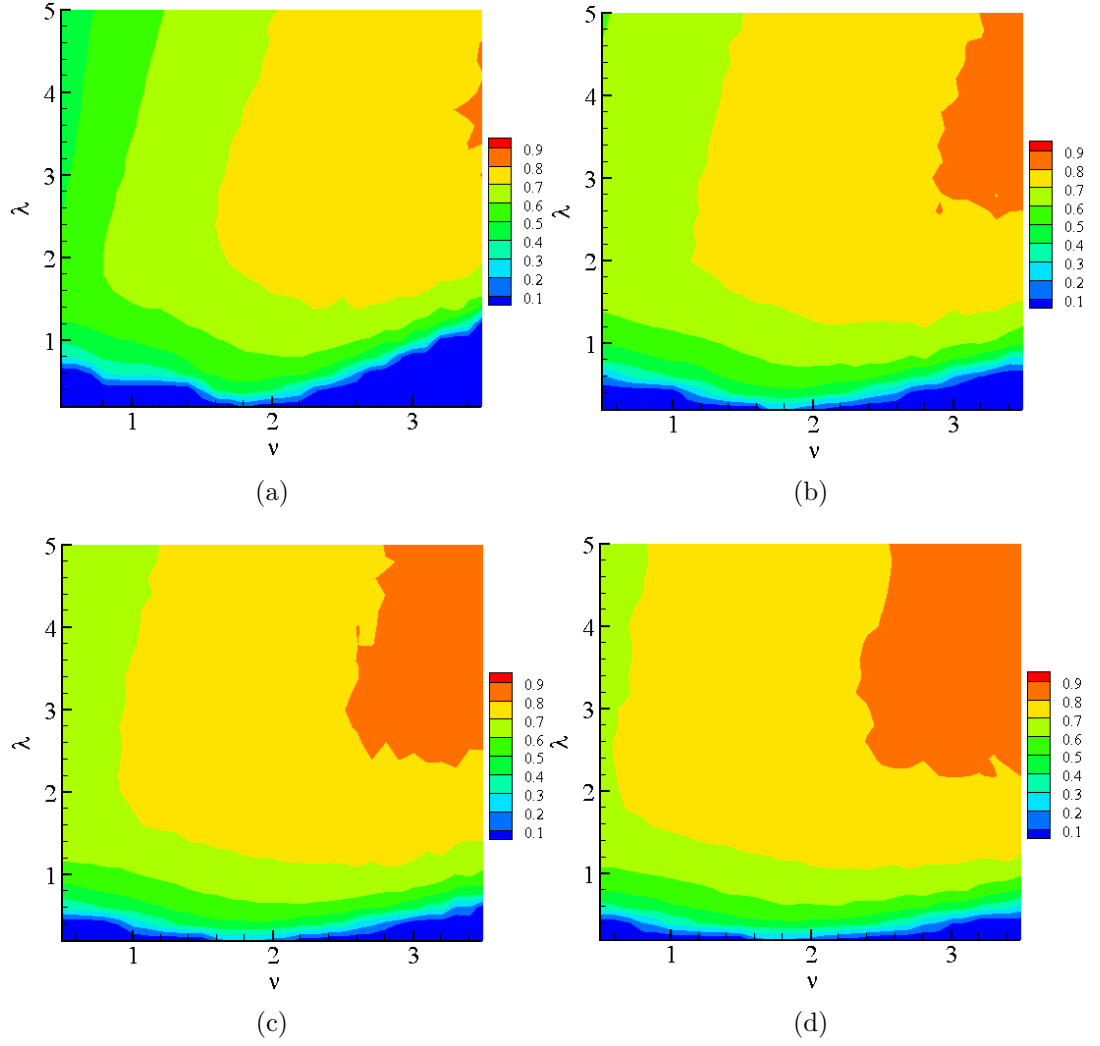
Figure 4.12: PSPs for Eq. (4.8) and but with nonlinear damping – Eq. (4.10) – for $\gamma = 0.0$, $R = 0.005$ and (a) $D = 0.1$; (b) $D = 0.3$; (c) $D = 0.5$; (d) $D = 0.7$.

values of noise intensity are considered. Comparing the plots for increasing noise intensity – Figs 4.12(a)–4.12(d), the opposite effect to viscous damping is observed. Increased noise intensity ($D = 0.7$) drives the pendulum to more robust rotational motion than the lower ones, while the instability boundaries appear to move to lower λ values. It is observed that, unlike viscous damping, the rotational response of the system with dry friction rises to higher levels with increased noise intensity. This could be attributed to the constant dissipation of energy for a given R, while increasing noise intensity indicates higher input power of the excitation (see Eq. (3.39)). However, further investigation of this case is out of the scope of this thesis since a viscous damping model shall always be present hereinafter.

4.4 Tilted rectilinear pivot motion

So far the response of the parametric pendulum has been considered under the assumption that the excitation is purely vertical, i.e. rectilinear and aligned with the gravitational field. However, this simplification is scarcely true with environmental loads unless such a DOF is strictly structurally imposed. For example, water particles do not heave vertically, but their trajectory is rather circular or elliptical, depending mainly on the wavelength and the seabed depth [15, 27]. Moreover, it is possible to impose a misalignment of the excitation's linear space with the gravity vector through the design of the structure or allow the excitation to be planar.

In view of that, it is interesting to investigate the response of the parametrically excited pendulum when the excitation has a horizontal component as well. The deterministic response of a pendulum in such a case has received some attention – see Sec. 2.2.3. A general mathematical expression including a horizontal component for the excitation is:

$$f = [A_h \sin{(\omega t + \phi)}, A_v \cos{(\omega t)}] \tag{4.11}$$

where A_v, A_h are the vertical and horizontal components of the amplitude for which we define $\rho = A_h/A_v$. When the phase difference between the components is $\phi = 0$, the motion is elliptical while for $\phi = \pi/2$ it is linear but tilted from the vertical direction by an angle $\psi = \tan^{-1}\rho$. In this section, the motion of the pivot is considered to be tilted by the vertical excitation and the influence of such a modification on the regions of rotational response is evaluated.

Based then on the two components of the excitation's amplitude for $\phi = \pi/2$, the corresponding dimensionless amplitudes λ_v, λ_h are defined in a similar manner as in Eq. (4.8), upon which, the governing equation of motion would now be:

$$\theta'' + \gamma\theta' + (1 + \lambda_v \cos q)\sin\theta + \lambda_h \cos q \cos\theta = 0$$
$$q' = \nu + \sigma\zeta(\tau) \tag{4.12}$$

where the RPM is included.

4.4.1 Parameter space plots

Previous deterministic studies [106, 111] have reported that the saddle-node bifurcation leading to rotations happens for lower values of λ with increasing tilt angle. However, these studies considered adding a horizontal component to the otherwise identical vertical excitation. This would lead to $\lambda_v = \lambda$ and $\lambda_h = \rho\lambda$ meaning that the input energy to the system would increase with the tilt angle, since the excitation amplitude would have been increased.

Another option is to attach the definition of λ to the stroke of the pivots displacement. In that way, the input energy in Eq. (4.12) preserves its magnitude having only a portion distributed to the horizontal direction. Such an approach would lead to the following definition:

$$\lambda_v = \frac{\lambda}{\sqrt{1+\rho^2}}, \ \lambda_h = \frac{\rho\lambda}{\sqrt{1+\rho^2}} \tag{4.13}$$

Herein, both definitions are considered and numerically constructed PSPs with the added influence of randomness are presented. The numerical construction of the PSPs follows the practice used so far in this Chapter. In the following, Figs 4.13 and 4.14 use the definition of Eq. (4.13) and Fig. 4.15 is based on the vertical amplitude of the excitation.

The first case considered is the deterministic one in Fig. 4.13 which shows the results for two tilt angles. Comparing these two plots with one another, not much difference is spotted. Rotational regions still exist as before even though increase of the tilt angle results in them being compressed mostly from the low frequency ratio side. In general, the primary resonance zone occurring for $\nu = 2$ and expanding for growing values of λ almost remains intact when seen against the vertical deterministic excitation (see Fig. 4.5). The heteroclinic orbit boundaries for frequencies bigger than the primary resonance are almost identical regardless of the tilt angle. This practically means that the required energy to cross the bifurcation from oscillatory motion to
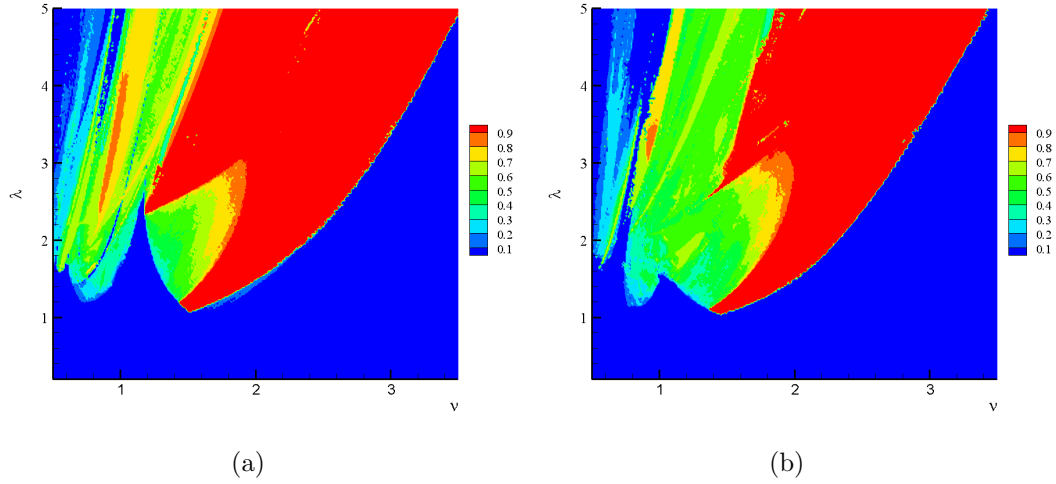
Figure 4.13: PSPs for Eq. (4.12) for $\gamma = 0.3$ and $D = 0.0$; (a) $\psi = 20^o$; (b) $\psi = 40^o$.

rotatory remains the same and it is reasonable since λ is defined through the pivot's stroke. However, when the secondary resonance zone is considered there is a mismatch between the vertical and the tilted excitation, growing with the tilt angle. This affects the PSPs mainly in two ways. First, the boundaries alter with oscillatory points escaping the blue area and jumping to rotational regions, even though not to be the dominant ones. However, the left boundary of the dominant rotations region occurring through the primary resonance zone degenerates to a lower ratio of rotations, an influence that grows by increasing the tilt angle. Note that in the tilted case there is no asymptotically stable attractor, now having been replaced by oscillatory ones. After examining the effect of tilting on the deterministic case the phase of the excitation is modelled to be random.

Fig. 4.14 shows the PSPs for a noise intensity value of $D = 0.1$ and different tilt angles. The difference incurred by increasing the tilt angle is minimal when Figs 4.14(a) and 4.14(b) are compared. The rotational regions are very much alike with when the pendulum is excited purely vertically. However, for Figs 4.14(c) and 4.14(d), rotations gradually degenerate to lower levels. The right, almost linear, heteroclinic boundary of the primary resonance zone is preserved when compared to Fig. 4.7(c) for all the tilt angles presented in Fig. 4.14. The major alterations of the secondary resonance zone $\nu = 1$ observed in Fig. 4.13, hold in the stochastic system as well. Moreover, when randomness is included and the tilt angle is less than 45° (see
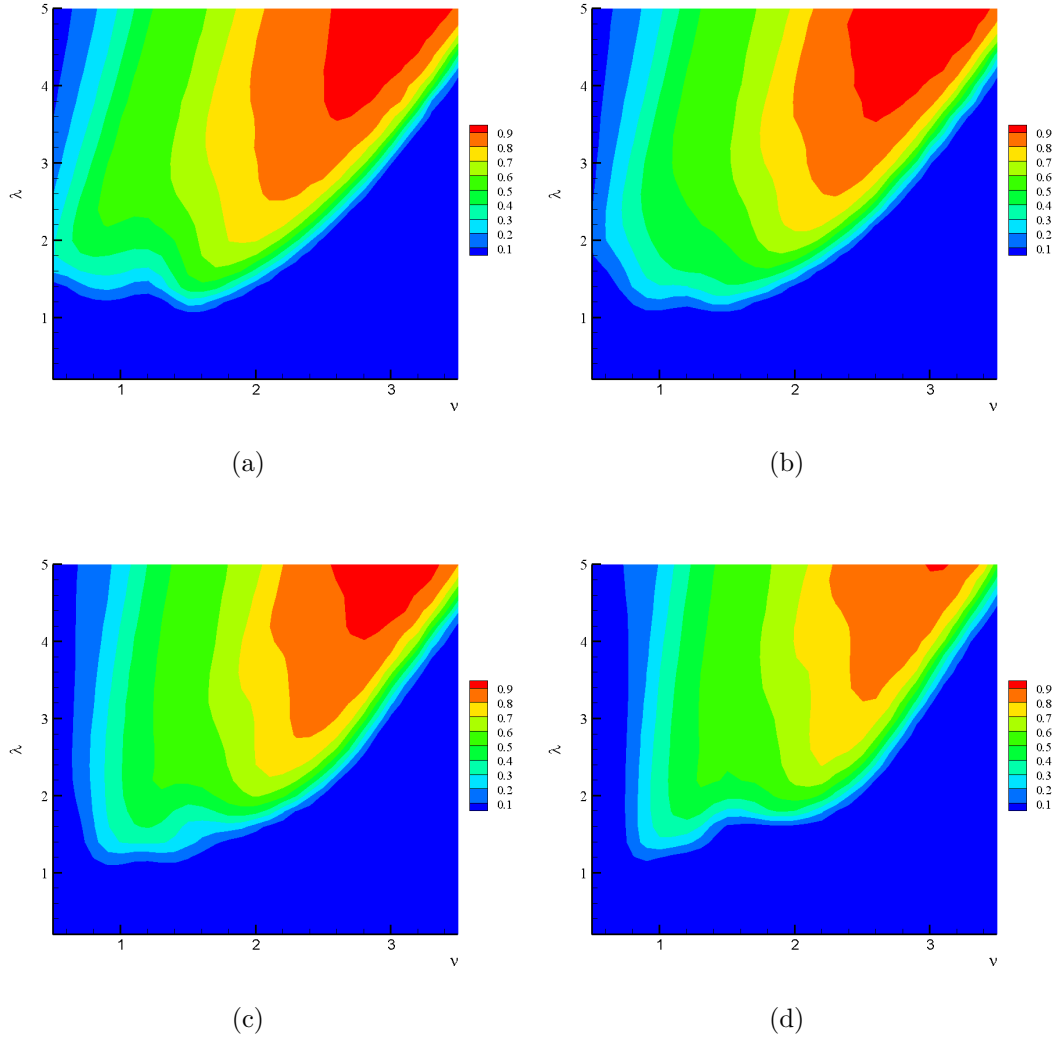
Figure 4.14: PSPs for Eq. (4.12) for $\gamma = 0.3$, $D = 0.1$ and λ defined by the half stroke; (a) $\psi = 20^o$; (b) $\psi = 40^o$; (a) $\psi = 60^o$; (b) $\psi = 80^o$.

Figs 4.14(a) and 4.14(b)), the dominant rotations region expands, which indicates that setting the pivot to oscillate along a tilted line slightly enhances the potential of rotational motion.

Fig. 4.15 shows the PSPs for the same noise intensity, damping coefficient and tilt angles as previously. However, a different approach is adopted for defining λ. The vertically excited pendulum presented in Fig. 4.13(b) is forced by an additional horizontal component keeping the vertical component unchanged for all tilt angles. Straightforward observations reveal that the rotational regions expand for Figs 4.15(a) and 4.15(b) with the boundaries pulled down to lower λ values. The required input energy to cross them keeps decreasing for Figs 4.14(c) and 4.14(d)
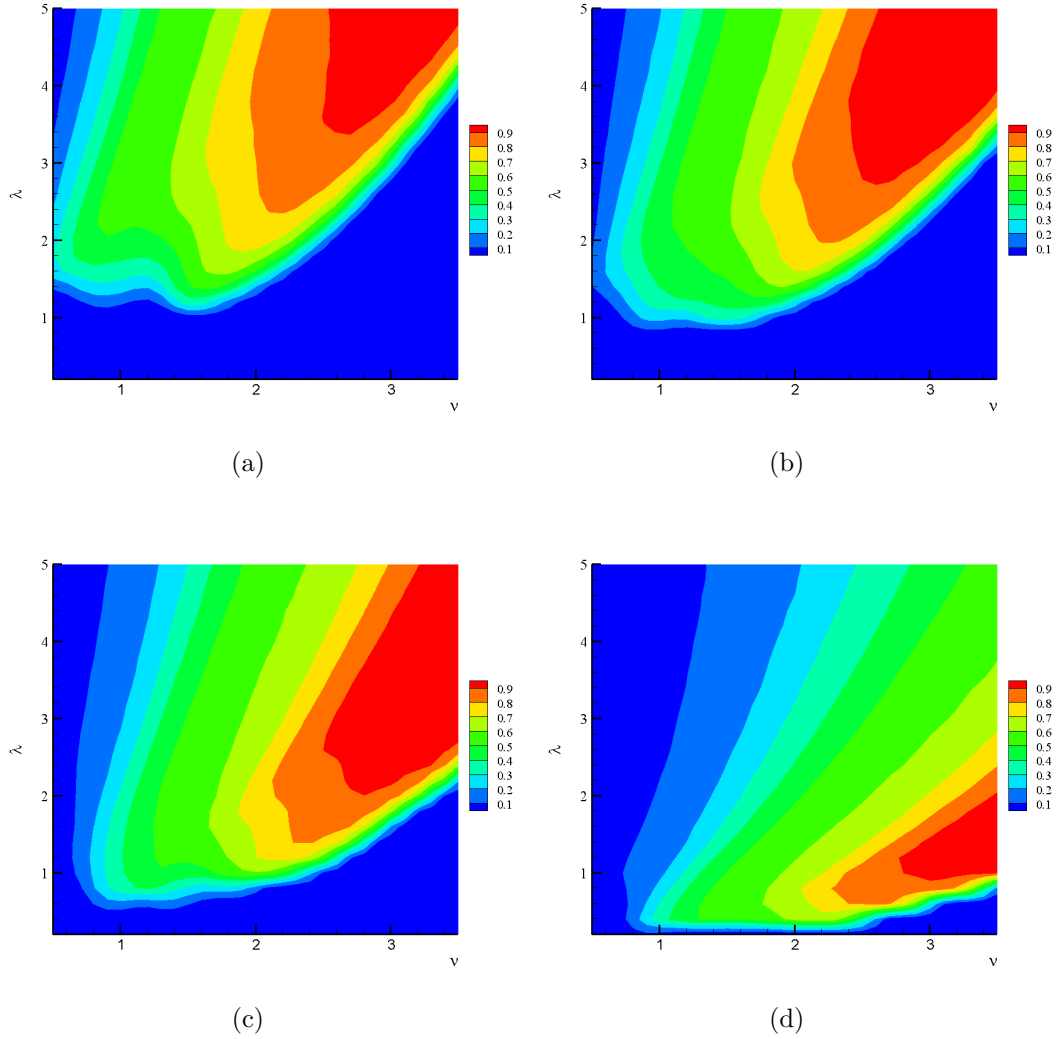
Figure 4.15: PSPs for Eq. (4.12) for $\gamma = 0.3$, $D = 0.1$ and λ defined by the vertical component of the half stroke; (a) $\psi = 20^o$; (b) $\psi = 40^o$; (a) $\psi = 60^o$; (b) $\psi = 80^o$.

as well; however this is not interpreted to larger rotational regions due to the fact that extremely large stroke values are needed to maintain the vertical amplitude constant when ψ approaches 90°.

4.5   Summary

The very first approach of investigating the effect of randomness onto the potential of rotational motion of the fundamental SDOF pendulum system definitely provides valuable conclusions. Previous deterministic analyses have shown that there is a quite broad region of dominant rotational steady-state response. Fig. 4.5 shows

that the lowest amplitude leading to such a response is just $\lambda > 1$ around a frequency ratio $\nu = 1.6$. Modulating the frequency of the excitation with a Gaussian white noise has shown that it is still possible for rotational motion to be established, although with an accompanying degenerative effect on the corresponding parameter regions. Increasing intensity of the randomness results in the lowest point of the, now merged, rotational region to be displaced in the PSP, towards higher values of both λ and ν. This is attributed to the diffusing effect of noise, as it unfolds in the stability of the linearized system too, which forces the response of the pendulum to be simultaneously influenced by the co-existing rotational and oscillatory attractors, regardless of the particular initial conditions. Inevitably, this development leads dominant rotations to be downgraded to 70-80% within the examined range of parameters, for the target noise intensity of $D = 0.3$. In terms of designing a device then, it is apparent that deterministic modelling would fall short of describing the real-world dynamics.

On a subsequent level, the influence of damping bears a rather significant conclusion, considering that the damping coefficient is crucial in energy harvesting applications. The analyses of both the deterministic parametric pendulum and the stochastic linearized system show that the saddle-node bifurcation and the stability boundaries correspondingly move upwards with increased damping, as a result of the higher energy dissipation. This is also observed in the herein constructed PSPs under stochastic excitation; however, increased damping was found to counteract the degenerative effect of noise leading to more robust rotational regions, due to the dissipation of small random fluctuations that would otherwise influence the system's response. Contrary to the narrow-band excitation, a pure white noise has an upper bound of the rotary response which is controlled by the non-dimensional damping coefficient. Last, modelling of the pendulum's response to a tilted excitation, has shown that as the tilt angle approaches the purely horizontal direction, rotational regions are further displaced to higher λ values.

Chapter 5

The pendulum on an elastic base

The previous Chapter 4 unveiled the behaviour of the pendulum's response when the stochastic excitation given by the RPM is directly applied at its pivot. However, in the majority of engineering applications, a more realistic approach would require to take under consideration the intermediate elements between the pivot and the excitation source. In the case of the WEC application, these would unavoidably include a buoy as well as structural connectors. Thus, the next step is to investigate the potential of rotational response of the parametric pendulum when the stochastic excitation is applied to its mounting platform, modelled by a linear SDOF system. This class of multi-DOF system is widely referred to as autoparametric. In the same manner as in Chapter 4, a broad investigation is conducted aiming to study the influence of the intermediate system stiffness and damping in a more generalized context attempting to fill the gap in the literature. Furthermore, the possibility of multiple pendulums being mounted on the same platform is considered, along with the interaction between them.

5.1 Equations of motion

To begin with the equations modelling the system at hand have to be presented. The more general case of two pendulums on a base is considered, since any simplification could be thereafter easily extracted. Then, the dynamics of two pendulums coupled
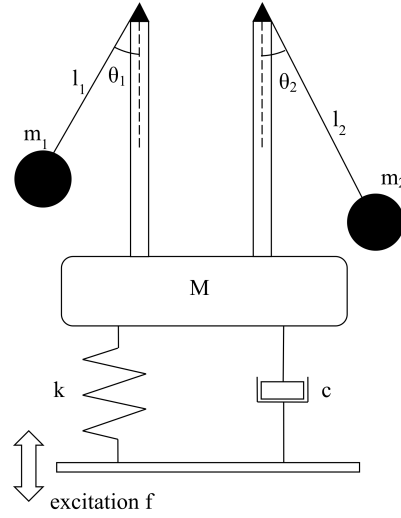
Figure 5.1: Sketch of two autoparametric pendulums coupled by their common linear elastic base M with f acting as base excitation.

through being mounted on the same linear SDOF base are considered. The system, also found as autoparametric in the literature, is experiencing a narrow-band excitation, modelling the heaving motion of ocean waves and acting on the base where thereby the pendulums are parametrically excited (see Fig. 5.1). It is considered that the pendulums are out of each other's plane or at large enough distance apart so that impacts between them are impossible. Such a system can be described by the set of the following nonlinear equations:

$$
\begin{aligned}
&\ddot{\theta}_1 + c_1\dot{\theta}_1 + \left(\Omega_1^2 + \frac{\ddot{x}}{l_1}\right)\sin\theta_1 = 0 \\
&\ddot{\theta}_2 + c_2\dot{\theta}_2 + \left(\Omega_2^2 + \frac{\ddot{x}}{l_2}\right)\sin\theta_2 = 0 \\
&\ddot{x} + 2\alpha\dot{x} + \eta^2 x = \eta^2 f + 2\alpha\dot{f} + m_1^r l_1\ddot{\theta}_1\sin\theta_1 + \\
&\qquad + m_1^r l_1\dot{\theta}_1^2\cos\theta_1 + m_2^r l_2\ddot{\theta}_2\sin\theta_2 + m_2^r l_2\dot{\theta}_2^2\cos\theta_2 \\
&f = A\cos q, \ \dot{q} = \omega_m + \tilde{\sigma}\zeta(t)
\end{aligned}
$$

(5.1)

with the indices $i = 1, 2$ referring to each one of the two pendulums and the dot denoting differentiation with respect to time t. Also, θ_i are the inclination angles, c_i the pendulums' damping coefficients, $l_{1,2}$ are the corresponding pendulums' lengths, $\Omega_{1,2}$ the pendulums' natural frequencies with $\Omega_i^2 = g/l_i$, x - the base's vertical displacement, $\alpha = c/2(M + m_1 + m_2)$ the base's damping coefficient with M the mass

of the base and m_i the pendulums' masses, η is the base's natural frequency with $\eta^2 = k/2(M + m_1 + m_2)$, f - the excitation with amplitude A and mean frequency ω, $m_i^r = m_i/(M + m_1 + m_2)$ are the mass ratios which, if $\psi_i = m_i/M$, become $m_i^r = \psi_i/(1 + \psi_1 + \psi_2)$. Last, $\zeta(t)$ is a Gaussian white noise with zero mean and $\tilde{\sigma}^2$ variance, or else, noise intensity.

Introducing the dimensionless time $\tau = \Omega_1 t$ to the set of Eq. (5.1) one would get:

$$\theta_1'' + \frac{c_1}{\Omega_1}\theta_1' + \left(1 + \frac{x''}{l_1}\right)\sin\theta_1 = 0$$

$$\theta_2'' + \frac{c_2}{\Omega_1}\theta_2' + \left[\left(\frac{\Omega_2}{\Omega_1}\right)^2 + \frac{x''}{l_2}\right]\sin\theta_2 = 0$$

$$x'' + 2\frac{\alpha}{\Omega_1}x' + \frac{\eta^2}{\Omega_1^2}x = \frac{\eta^2}{\Omega_1^2}f + 2\frac{\alpha}{\Omega_1}f' + \tag{5.2}$$

$$+ m_1^r l_1\theta_1'' \sin\theta_1 + m_1^r l_1\theta_1'^{\,2}\cos\theta_1 +$$

$$+ m_2^r l_2\theta_2'' \sin\theta_2 + m_2^r l_2\theta_2'^{\,2}\cos\theta_2$$

$$f = A\cos q, \quad q' = \frac{\omega}{\Omega_1} + \frac{\tilde{\sigma}}{\Omega_1}\zeta(\tau)$$

with the prime denoting differentiation with respect to τ. Defining $\nu = \omega/\Omega_1$, $\sigma = \tilde{\sigma}/\Omega_1$, $\beta = \alpha/\Omega_1$, $e = \eta/\Omega_1$, $\gamma_i = c_i/\Omega_1$ and introducing $\kappa = \Omega_2/\Omega_1$ as the ratio of the pendulums' natural frequencies which would also result in $\kappa^2 = l_1/l_2$, Eq. (5.2) becomes:

$$\theta_1'' + \gamma_1\theta_1' + \left(1 + \frac{x''}{l_1}\right)\sin\theta_1 = 0$$

$$\theta_2'' + \gamma_2\theta_2' + \kappa^2\left(1 + \frac{x''}{l_1}\right)\sin\theta_2 = 0$$

$$x'' + 2\beta x' + e^2 x = e^2 A\cos q - 2\beta A\nu \sin q + \tag{5.3}$$

$$+ m_1^r l_1\theta_1'' \sin\theta_1 + m_1^r l_1\theta_1'^{\,2}\cos\theta_1 +$$

$$+ \frac{m_2^r}{\kappa^2}l_1\theta_2'' \sin\theta_2 + \frac{m_2^r}{\kappa^2}l_1\theta_2'^{\,2}\cos\theta_2$$

$$q' = \nu + \sigma\zeta(\tau)$$

where $\beta\sigma \ll 1$, hence the corresponding term arising in f' has been omitted.

Note that the detuning between the two pendulums is now expressed through the parameter κ so, whence ν is the frequency ratio for the first pendulum, for the second one it is ν/κ. Non-dimensionalization of x through $y = x/l_1$ and defining $\lambda = A\nu^2/l_1$ results in the final expression of the equations of motion:

$$
\begin{aligned}
&\theta_1'' + \gamma_1\theta_1' + (1 + y'')\sin\theta_1 = 0 \\
&\theta_2'' + \gamma_2\theta_2' + \kappa^2(1 + y'')\sin\theta_2 = 0 \\
&y'' + 2\beta y' + e^2 y = \frac{e^2\lambda}{\nu^2}\cos q - \frac{2\beta\lambda}{\nu}\sin q + \\
&\qquad\qquad + m_1^r\theta_1''\sin\theta_1 + m_1^r\theta_1'^2\cos\theta_1 + \\
&\qquad\qquad + \frac{m_2^r}{\kappa^2}\theta_2''\sin\theta_2 + \frac{m_2^r}{\kappa^2}\theta_2'^2\cos\theta_2 \\
&q' = \nu + \sigma\zeta(\tau)
\end{aligned}
\tag{5.4}
$$

Eq. (5.4) is the final set of equations which will be hereafter analyzed via numerical means.

5.2 Single pendulum

The herein investigation starts from considering a single pendulum on a floating platform. Then, the system would be governed by Eq. (5.4) with the constraint $\theta_2 = \theta_2' = 0$. Then, only the pendulum with the index 1 would be present, denoted without any indices throughout Sec. 5.2.

5.2.1 The $m^r = 0$ case

In general, the interaction between the pendulum and the base might exhibit a quite complicated behaviour. As a first step then, aiming to consider only the influence of the filtering of the stochastic excitation, the interaction is neglected. That is achieved by setting $m^r = 0$ will corresponds to $m \ll M$. This would simplify the third equation in Eq. (5.4) leaving only the first two terms in the RHS. To compare the results of numerical simulation with previous results $\lambda - \nu$ notation is kept as previously. Fig. 5.2(a) demonstrates the results of numerical simulation for primary
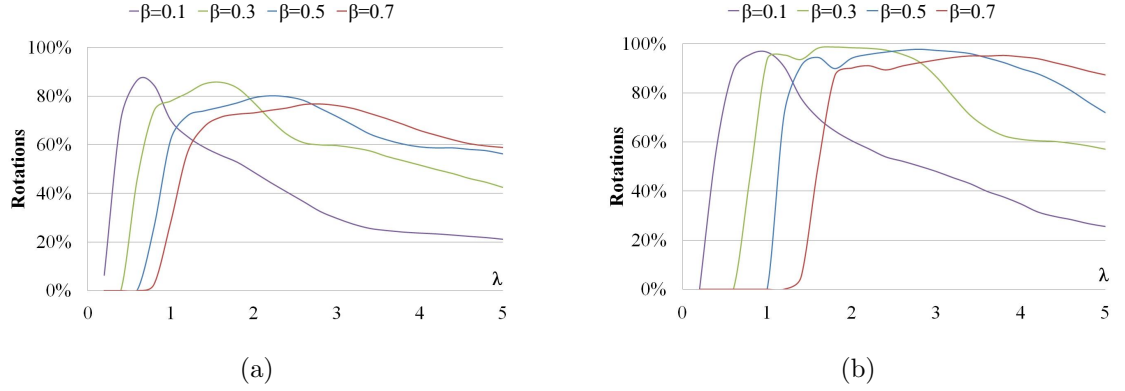
Figure 5.2: Rotational ratio for a single pendulum from Eq. (5.4) for: (a) $\nu = 2$, $e = 2$, $D = 0.3$, $\gamma = 0.3$; (b) $\nu = 3$, $e = 3$, $D = 0.3$, $\gamma = 0.3$.

resonance $\nu = 2$, $e = 2$, $D = 0.3$, $\gamma = 0.3$ and different values of viscous damping coefficient β. It can be seen from Fig. 5.2(a) that although the rotational motion starts at smaller values of λ none of the curves reaches 90% threshold. Moreover, smaller values of β provide a relative short domain for high percentage rotational motion. On the contrary, relatively large values of viscous damping provide wide region of rotational motion. Obviously, the larger the rotational region the easier to keep the system in this region.

Fig. 5.2(b) demonstrates numerical results for the system when $\nu = 3$, $e = 3$, $D = 0.3$, $\gamma = 0.3$ with different values of the damping coefficient. It can be observed that all the curves cross the 90% line, however smaller values of the damping coefficient provide a narrower region of rotational motion. On the other hand, the low boundary of the dominant rotational domain (90%) starts from smaller values of λ when the damping coefficient is small, so that for $\beta = 0.1$ the dominant domain is reached at $\lambda = 0.5$, whereas for $\beta = 0.5$ it is reached when $\lambda = 1.2$. This result is well expected since smaller values of damping provide large response amplification.

Having seen the influence of the SDOF system introduction between the pendulum and the wave excitation for certain frequencies, a more wide investigation on the parameter space (ν, λ) is reasonable to follow. Fig. 5.3 depicts results of the numerical simulations of Eq. (5.4) over the parameter space for $m^r = 0$. It should be noted that the examined frequency range could not exceed certain values since large detuning would eliminate the narrow-band characteristics of the SDOF response
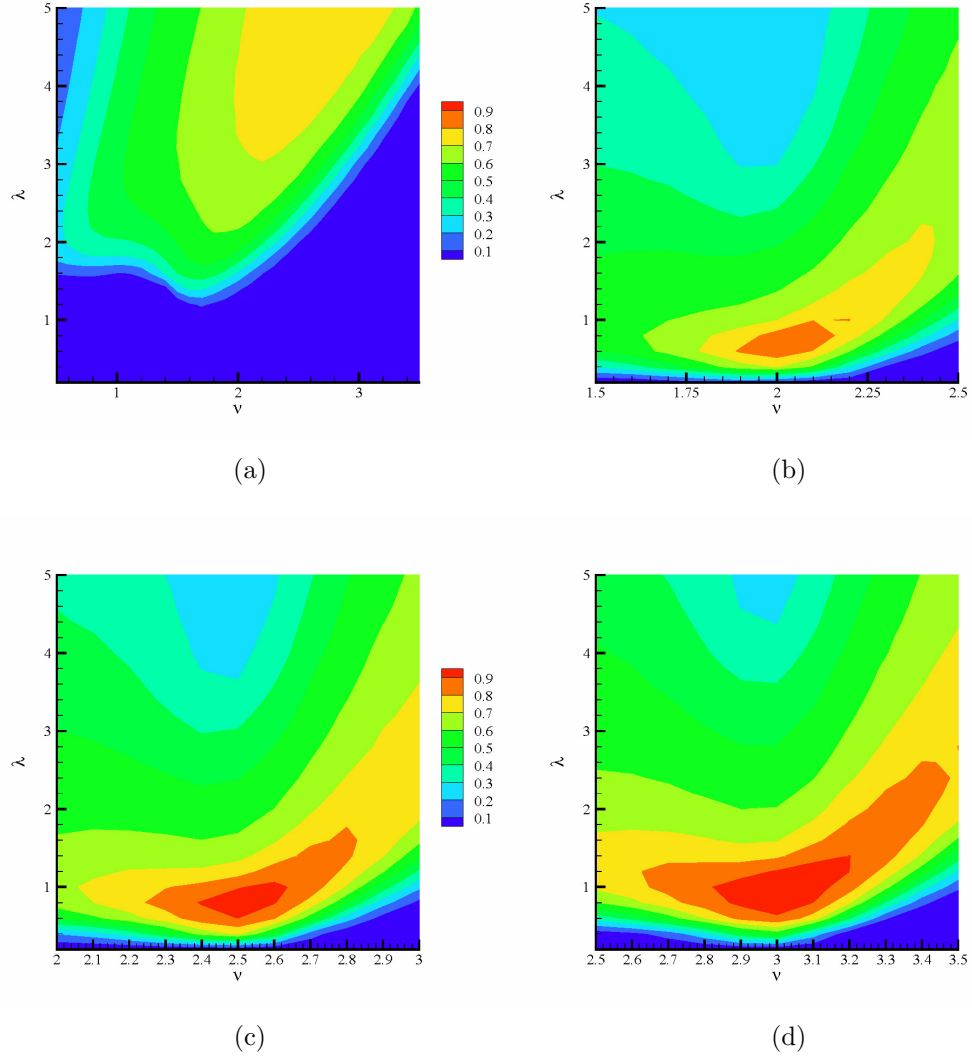
Figure 5.3: PSPs of a single autoparametric pendulum from Eq. (5.4) for $D = 0.3$, $\gamma = 0.3$ *and* $\beta = 0.1$: (a) without SDOF; (b) $e = 2$; (c) $e = 2.5$; (d) $e = 3$.

limiting to a white noise. Thus, the previously examined frequency range $(0.5 - 3.5)$ was divided to 3 regions $(0.5 - 1.5)$, $(1.5 - 2.5)$ and $(2.5 - 3.5)$ with each one's central value also chosen as the natural frequency, e. Several simulations showed that the last frequency range is the most favourable, providing higher rotational motion ratio. This is why only simulations for this range and the adjacently lower one are being shown in Fig. 5.3 for 3 different e values.

First, the comparison of results in the PSP with and without the SDOF system for the same noise intensity $D = 0.3$, is made for different values of the platform's natural frequency e and $\beta = 0.1$. It can be seen from Fig. 5.3, which has already been
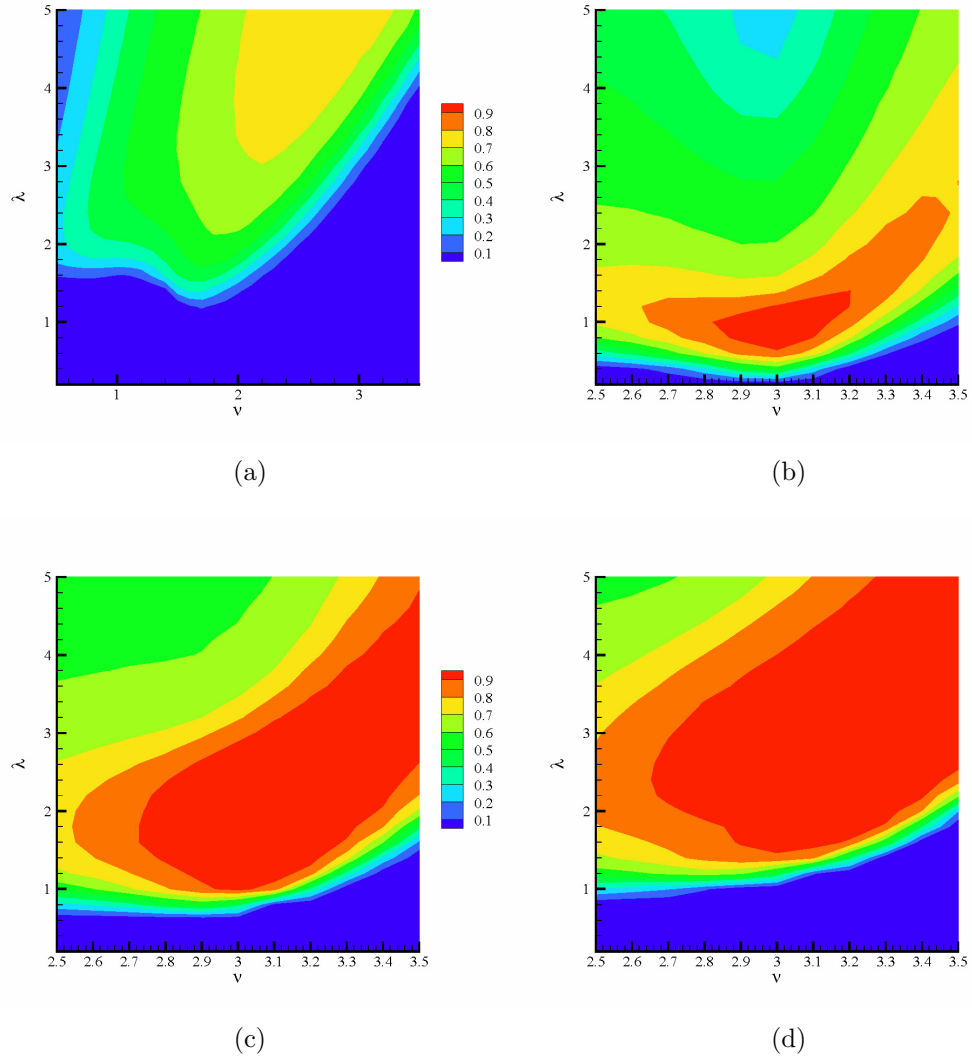
Figure 5.4: PSPs for a single autoparametric pendulum from Eq. (5.4) for $D = 0.3$, $\gamma = 0.3$ and $e = 3$: (a) without SDOF system; (b) $\beta = 0.1$; (c) $\beta = 0.3$; (d) $\beta = 0.5$.

reported from Fig. 5.2, that the larger values of the natural frequency provide larger instability area with dominant rotational motion. This result is expected taking into account the deterministic map, which shows large range of λ for larger values of ν. However, to reach these values, higher natural frequency of the SDOF system is needed. It is also important, that the values of λ for these regions are relatively small, which indicates that the rotational motion can be observed for small values of wave amplitude.

Fig. 5.4 demonstrates the numerical results for the same value of natural frequency $e = 3$ and three different values of the viscous damping coefficient β. It can be seen

that, while the highest rotational ratio was between 70-80% for a rather narrow region, here a rather wide area of dominant rotational region ($> 90\%$) has appeared (Fig. 5.4(c) or Fig. 5.4(d)). Moreover, this region instead of initiating at high amplitude values ($\lambda > 6$), it starts from as low as $\lambda = 0.6$ even for the narrow region case of low β values. Larger values of damping shift the boundary of the rotational region upwards, while simultaneously widening the area. This is not only the result of the amplitude amplification but also of the filtering out the fast fluctuations of the noise due to the property of the SDOF system. In general, the PSPs in Fig. 5.4 confirm the observations made for Fig. 5.2. Low β values initiate rotational region at lower λ values, since the former provides higher values of mean response amplitude of the SDOF system. On the other hand, low values of β provide large values of mean square amplitude, leading to large amplitude fluctuations, which results in narrowing down the instability domain. Thus, the range of $\lambda's$ for which rotations persist is narrower for lower β values.

5.2.2 Interacting pendulum-base system

The rotational motion of the pendulum is investigated when the influence of its mass m onto the response of the linear SDOF filter cannot be neglected. The problem now is formulated by the Eq. (5.4) with the full expression of the RHS in the third equation and thus, the parameter m^r becomes a subject of study. Fig. 5.5 shows the PSPs characterizing the amount of rotational motion in the same way as previously. The Left-Hand-Side (LHS) column of the plots depicts the numerical results for the value of damping coefficient, $\beta = 0.1$, while the RHS for $\beta = 0.5$. A first observation can be made with regard to the influence of the damping coefficient, β. Considering that the natural frequency of the linear SDOF filter is $e = 2$, the filter is a system at or around its resonance. When β is small, the amplification of the response drives it to very high amplitude values forcing the pendulum to move closer to the region above the rotational one, thus reducing the rotational amount in comparison with higher values of β. The latter values drive the pendulum inside the rotational parameter region providing a better response for the pendulum to rotate. Obviously, there is a critical damping, larger values than which, force the filter's response to be smaller in amplitude, up until the point it dies out.
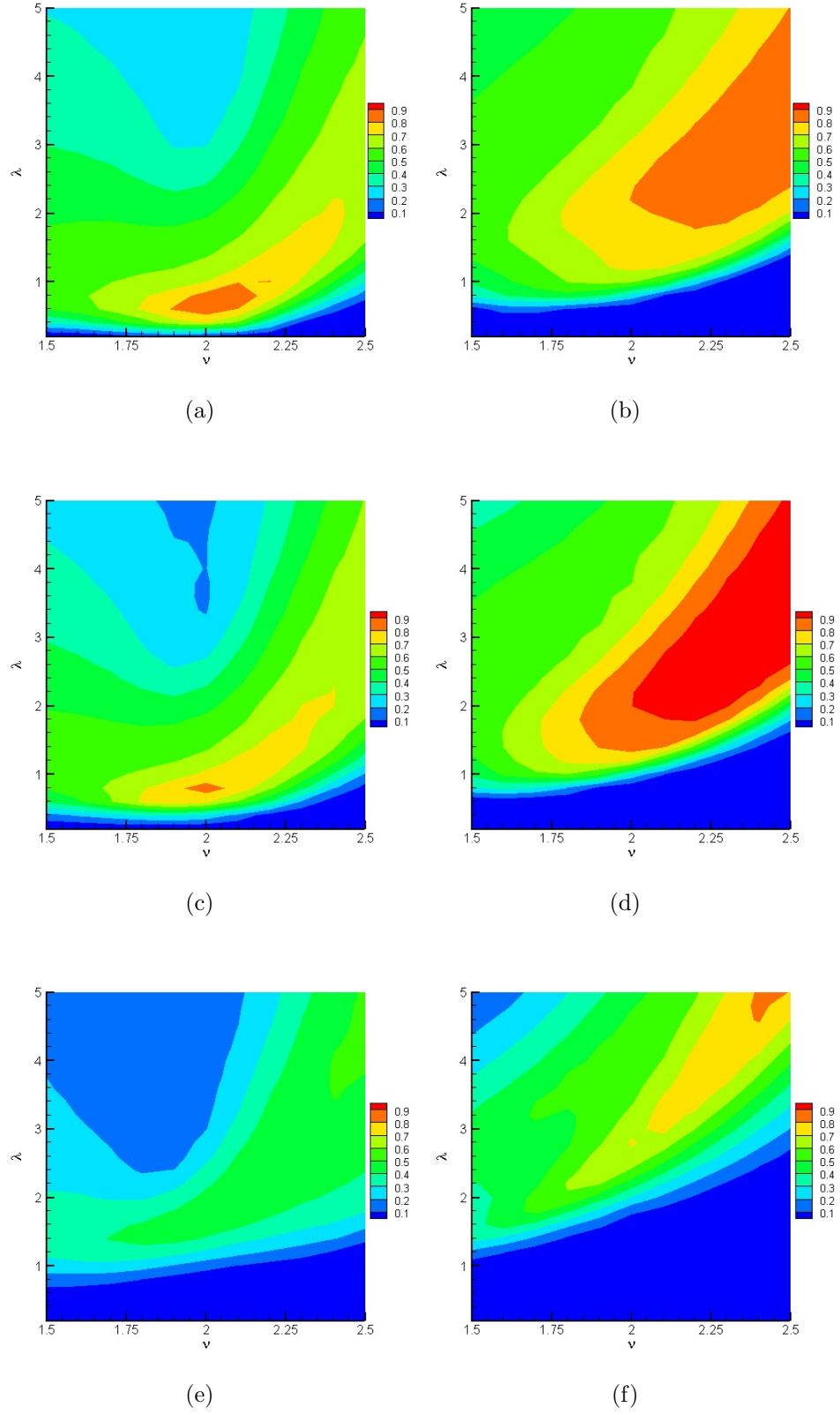
Figure 5.5: PSPs with ratio of rotational motion for $D = 0.3$, $\gamma = 0.3$, $e = 2$. (a) $m^r = 0.0$, $\beta = 0.1$; (b) $m^r = 0.0$, $\beta = 0.5$; (c) $m^r = 0.1$, $\beta = 0.1$; (d) $m^r = 0.1$, $\beta = 0.5$; (e) $m^r = 0.5$, $\beta = 0.1$; (f) $m^r = 0.5$, $\beta = 0.5$;

Furthermore, the plots in the same line present results for the same mass ratio, m_r. Figs 5.5(a) and 5.5(b) correspond to cases with $m^r = 0$ and have been added for comparison purposes. When the mass ratio gets slightly bigger, and particularly equal to $m^r = 0.1$ shown in Figs 5.5(c) and 5.5(d), the whole plots resemble the ones without the pendulum's influence (Figs 5.5(a) and 5.5(b)), with the only difference being a slight increase in the experienced rotational motion. However, when the value of the mass ratio gets even higher, as in Figs 5.5(e) and 5.5(f)) for which the pendulum's mass equals the filter's, the response of the pendulum contains less rotations than before. Nevertheless, a respectable amount of around 75% is maintained with the appropriate damping conditions . Also, it is observed that some lower amplitude points of the plot get stabilized, turning into blue asymptotically or marginally stable points.

As soon as the pendulum's mass m cannot be considered negligible compared to the base's mass M, the inertial and centrifugal forces acting on the SDOF system due to the pendulum's angular motion have to be considered. In this case, the response of the coupled system is governed by the full expression in Eq. (5.4) for a single pendulum.

First, the system is examined when the base is excited at its resonance frequency in the mean sense. Fig. 5.6(a) demonstrates the results for the primary resonance $\nu = 2$, $e = 2$, $m_r = 0.3$, $D = 0.3$, $\gamma = 0.3$ and different values of the viscous damping coefficient β. It can be seen that although the rotational motion initiates at smaller values of λ none of the curves reaches the 90% threshold characterized as the dominant rotational region. Moreover, smaller values of β provide a relatively short range for high percentage of rotational motion even though the escape boundary is normally found at lower λ values. On the contrary, relatively large values of viscous damping provide wider region of rotational motion and shift the boundary to higher λ values. The larger the rotational region the easier to keep the system in this region.

In Fig. 5.6(b) the system's parameters are $\nu = 3$, $e = 3$, $m_r = 0.3$, $D = 0.3$, $\gamma = 0.3$. Since the highest frequency is considered, it is expected for the rotational response
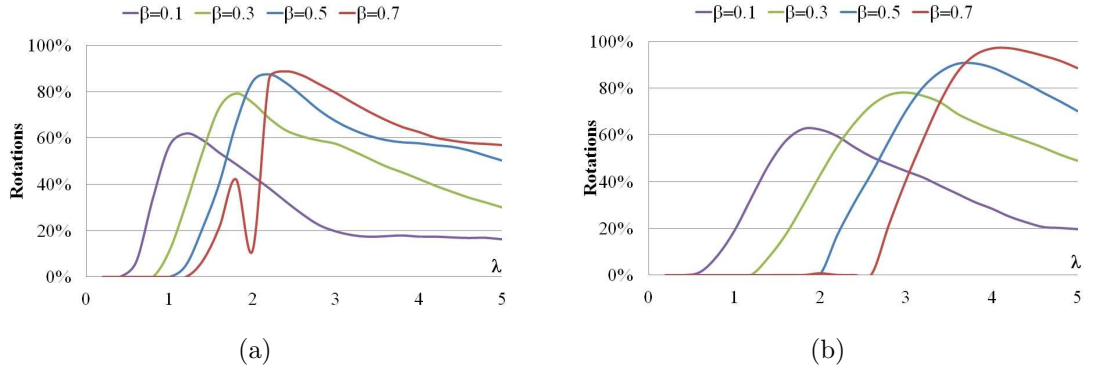
Figure 5.6: Rotational response from Eq. (5.4) for $m_r = 0.3$, $D = 0.3$, $\gamma = 0.3$: (a) $\nu = 2$, $e = 2$; (b) $\nu = 3$, $e = 3$.

to be more intense. However, the level of rotations does not demonstrate significant differences with Fig. 5.6(a), apart from the fact that their intensity fades away at a slower rate with increasing λ. This is a major alteration in the response of the pendulum induced by the influence of the pendulum's mass onto the base. Thus, the assumption of negligible mass m cannot accurately describe the pendulum's behaviour and further investigation to include it, should provide a more realistic picture.

PSPs are presented in Figs 5.7 and 5.8 in the same pattern as previously, incorporating the interaction between the pendulum and the base. In both figures, all the influential parameters are kept constant with only the mass ratio, m^r, taking different increasing values. The noise intensity is taken as $D = 0.3$, the pendulum's damping, $\gamma = 0.3$ and the SDOF system's damping, $\beta = 0.3$

In Fig. 5.7, the frequency ratio range $\nu = [1.5 - 2.5]$ is considered. Hence, the base's natural frequency is kept constant, $e = 2$, throughout the whole figure. Fig. 5.7(a) shows the case of $m^r = 0.0$ and is included for comparison purposes. Increasing the mass ratio is generally against the rotational regions. First, the joint stable oscillatory - fixed point regions are increasing in proportion to the mass ratio covering more λ values. Hence, the rotational regions are getting narrower. A general observation would be that the latter's robustness is also tampered. Increasing the influence of the pendulum on the base prevents the pendulum from maintaining a high rotational amount. However, it is noticed that for a relatively small value of
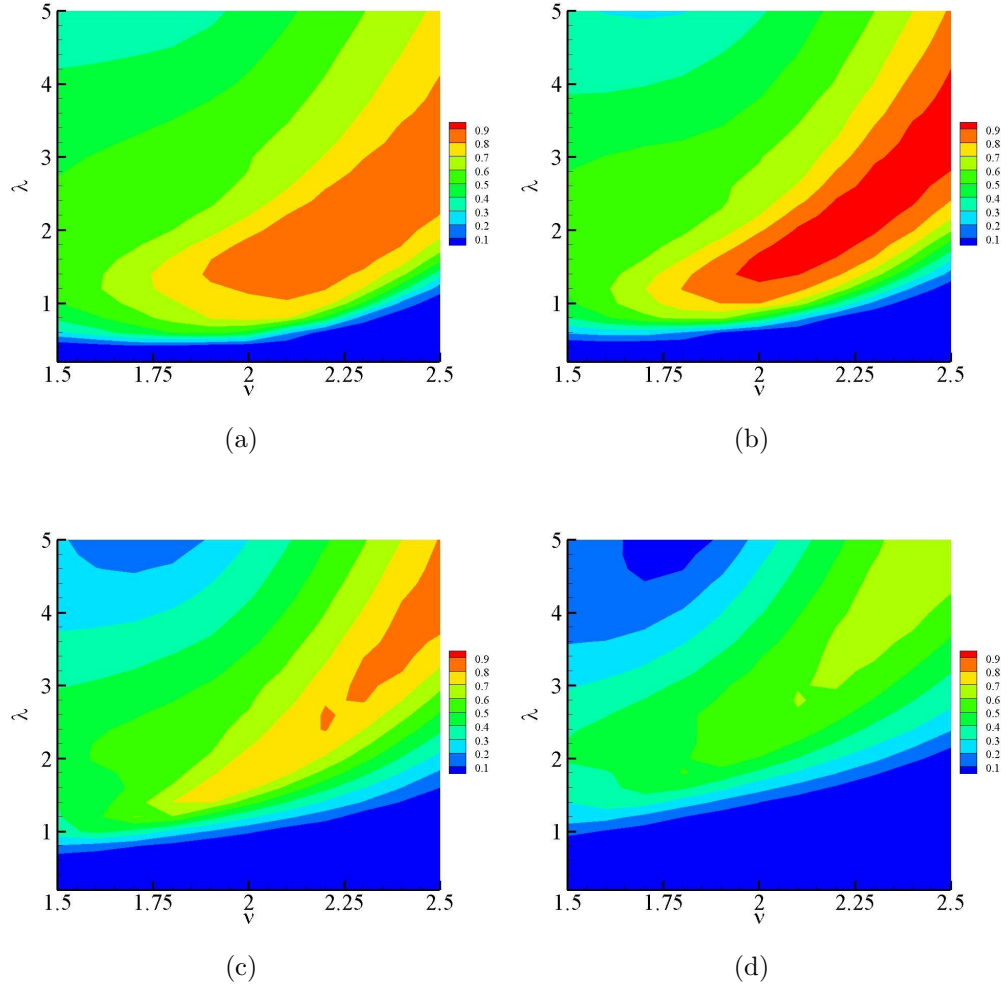
Figure 5.7: PSPs of Eq. (5.4) for $D = 0.3$, $\gamma = 0.3$, $\beta = 0.3$ and $e = 2$: (a) $m_r = 0.0$; (b) $m_r = 0.1$; (c) $m_r = 0.3$; (d) $m_r = 0.5$.

the pendulum's mass (Fig. 5.7(b)) the rotational region is more intense even though narrower. In general, the inertial and centrifugal forces depend on the angle, θ and its derivatives, $\dot{\theta}$ and $\ddot{\theta}$. These are stochastic processes and so, the randomness of the base's response increases. Since the pendulum is excited through the base's response, the increased randomness acts against its rotational response. However, keeping the mass ratio relatively small could be in favour or at least not against rotations for this frequency ratio range.

Fig. 5.8 depicts the numerical results of Eq. (5.4) in the same way as in Fig. 5.7 but it examines the next frequency ratio range, $\nu = [2.5 - 3.5]$ and so the base's natural frequency is fixed at $e = 3$. The behaviour of the pendulum is close to
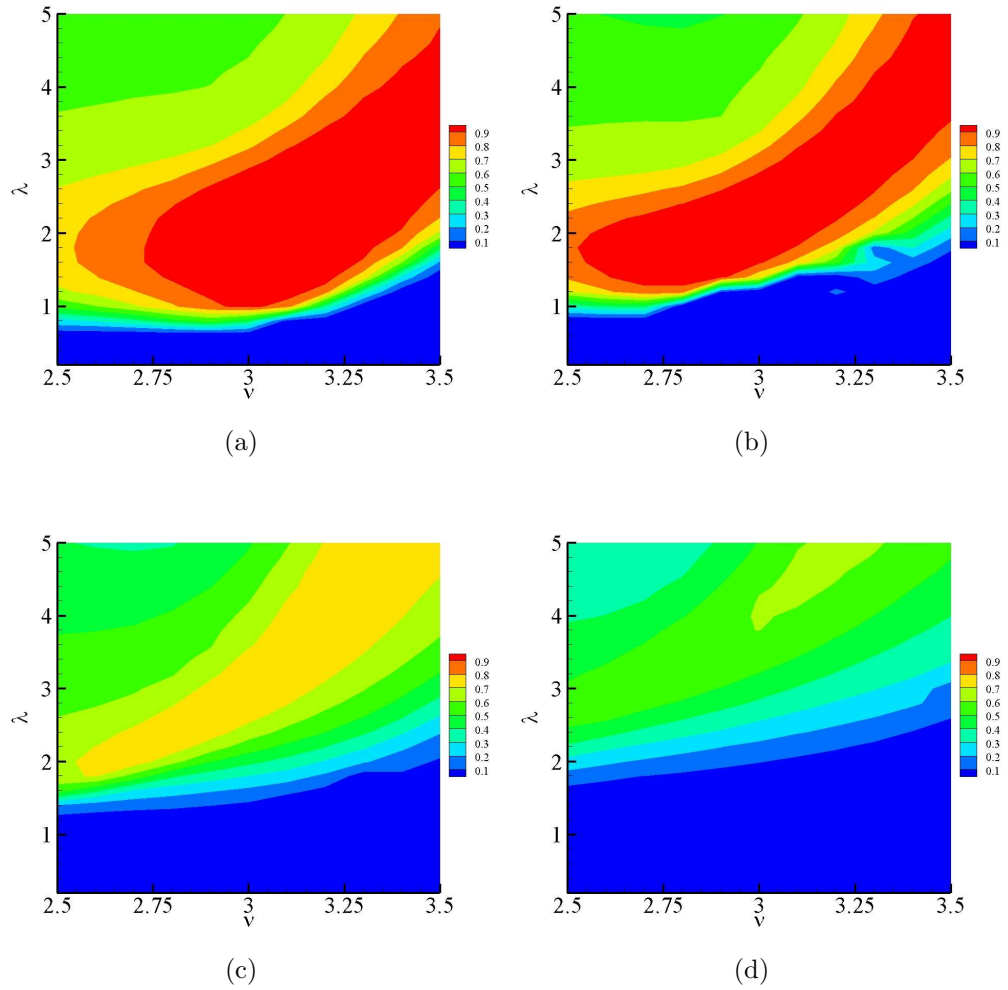
Figure 5.8: PSPs of Eq. (5.4) for $D = 0.3$, $\gamma = 0.3$, $\beta = 0.3$ and $e = 3$: (a) $m_r = 0.0$; (b) $m_r = 0.1$; (c) $m_r = 0.3$; (d) $m_r = 0.5$.

before, with increasing mass ratio causing rotations to degenerate. Their regions in the parameter space get narrower, with the stable response earning more space on the plots. Again, relatively low values of the mass ratio are, at least, not against rotations.

5.3 Synchronization

Let us now discuss the dynamics of the system described by the full expressions in Eq. (5.4), corresponding to two pendulums on a common base. The concept of synchronization has attracted significant attention in the study of deterministic and stochastic systems. Within the field of stochastic dynamics, it is most commonly

understood as the phase or the mean-frequency locking of a self-sustained oscillator to an external periodic excitation in the presence of noise [192]. Herein, the dynamic system at hand is indeed a self-sustained oscillator under a narrow-band excitation, yet the investigation revolves around the interaction between the two pendulums and, particularly, whether rotational motion can be established and preserved when their parameters are not necessarily identical. So, the phenomenon of synchronization here is not understood in its classical sense, but rather in the sense of identical motion.

The investigation is focused on the exhibited rotational response of the, generally not identical, pendulums. The results demonstrate the ratio of rotational motion over the total response which ranges from 0 to 1. In terms of implementation, numerical MC simulations totaling up to 100,000 mean excitation periods are performed for Eq. (5.4) on an 8-core, 16 threads Xeon processor with the MPI protocol used for multi-processing. The understanding of rotational motion and the estimation of the probability to rotate follows the procedure described in Sec. 4.3.1. The overall question could be summarized in whether rotations would become more likely compared to the case of a single pendulum on a base.

5.3.1 Direct comparison of the pendulums' responses

As an exploratory approach we evaluate the motion of the pendulums for specific parameter pairs presented in Fig. 5.9. Here, taking into account previous results for the single pendulum, we configure one of them to always operate for the same constant parameters located at the centre of the rotational parameter region. This pendulum will be referred to as the tuned one, while the other is spanning along different frequencies and will be labeled as the detuned one. For each pair examined, three different values for the rotational motion are plotted - the rotations experienced by the tuned pendulum, those of the detuned when coupled with the tuned one and the case of the detuned single pendulum with no assumed coupling with the tuned pendulum. The latter will be referred to as the decoupled pendulum and looking at Fig. 5.1, one could think of it as if only the second pendulum was free to move (i.e. $\theta_1 = 0$ was imposed). It represents the response of a single pendulum
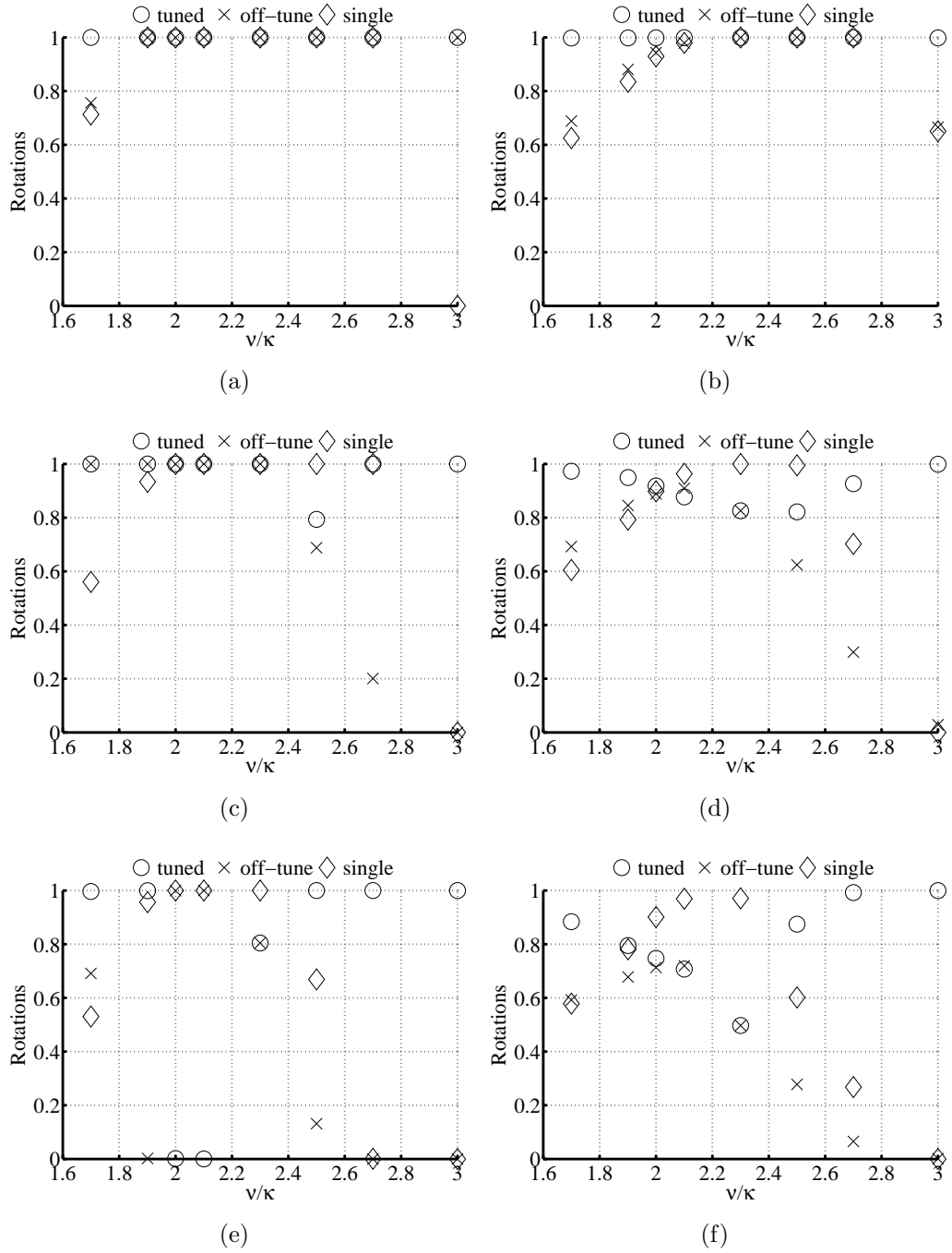
Figure 5.9: Rotational motion described by Eq. (5.4) for $\nu = 2.3$, $\lambda = 3.0$ and (a) $\sigma^2 = 0.0$, $\psi = 0.1$, (b) $\sigma^2 = 0.1$, $\psi = 0.1$, (c) $\sigma^2 = 0.0$, $\psi = 0.3$, (d) $\sigma^2 = 0.1$, $\psi = 0.3$, (e) $\sigma^2 = 0.0$, $\psi = 0.5$. (f) $\sigma^2 = 0.1$, $\psi = 0.5$.

mounted on the platform M on its own and will be used to compare the response of the detuned pendulum when under the influence of the tuned one with when it is mounted on its own. Hence, direct comparison between the coupled and the decoupled configuration for both pendulums is possible. The decoupled response of the tuned pendulum is not plotted since it remains unaltered throughout the

121

different parameters pairs examined and thus, its expected decoupled response is always rotational. Moreover, the effect of the detuning between the pendulums is considered and, in particular, when does the interaction between them become more intense and with what consequence.

In Fig. 5.9 the pendulums' damping coefficient is kept constant, $\gamma_1 = \gamma_2 = 0.3$. The deterministic case is shown in the LHS column of Fig. 5.9 while the stochastic one with a noise intensity $\sigma^2 = 0.1$ in the RHS one. Both pendulum masses are considered equal, $m_1 = m_2$ and three mass ratios ψ are considered. Since the tuned pendulum remains unaltered, one constant parameter pair (ν, λ) has to be chosen. Considering previous results [193, 194], the centre of the noisy rotational region is preferred, $(\nu, \lambda) = (2.3, 3.0)$, in order to ensure that the tuned pendulum has a rotational response. For the detuned one, the spanning along the frequency axis is realized through the κ parameter. The mean excitation frequency ω in the time t domain is constant and mutual for the two pendulums and so the dimensionless ratio controlling the response of the tuned pendulum is equal to ν and for the detuned one is ν/κ.

The LHS of Fig. 5.9 shows the resulting rotational motion versus $\nu/\kappa = \omega/\Omega_2$, which represents the frequency ratio for the detuned pendulum, for the ψ values – 0.1, 0.3 and 0.5 – when no noise is taken into consideration. In Fig. 5.9(a), the low mass ratio $\psi = 0.1$ incurs hardly any significant interaction between the pendulums. The tuned pendulum remains uninfluenced exhibiting robust rotational motion for all the detuning values of the detuned pendulum. The latter also does not demonstrate any particular difference apart from the case where $\nu/\kappa = 3.0$. Here, the upper fixed point of the single decoupled pendulum ($\Diamond$) becomes unstable due to the coupling and converts to purely rotational ($\times$). Keeping the mass ratio low, provokes little influence of the centrifugal and inertial forces of the pendulums' masses on the base, thus scarcely modifying their response.

However, when the mass ratio is increased, a rather different picture is drawn. In Fig. 5.9(c), the tuned pendulum jumps to a chaotic attractor for $\nu/\kappa = 2.5$, as the detuned one does too. The detuned pendulum ends up rotating from chaos and

rotations-oscillations for $\nu/\kappa = 1.7$ and 1.9 respectively. However for $\kappa = 2.5$ and $\kappa = 2.7$, while the decoupled pendulum ($\Diamond$) would purely rotate, the coupling drives the detuned pendulum ($\times$) to less rotational motion. For $\psi = 0.5$, the total mass of the pendulums equals the mass of the base. The effect of the coupling is seen to grow near the resonance curves and forces even the tuned pendulum away from the rotational attractor, with the response of the detuned configuration presenting no differences ($\nu/\kappa > 2.5$).

The RHS in Fig. 5.9 shows the results for a stochastic case with $\sigma^2 = 0.1$ in a similar way as in the LHS ones. As it was reported in [193, 194], induction of noise to the single pendulum system results in narrower and less intense rotational regions. Even so, a dominant rotational region can still be found. In Fig. 5.9(b), the response resembles the deterministic one especially for the tuned pendulum, since the low mass ratio value deteriorates the influence of one pendulum on the other. Here, there is also a significant range of ν/κ values for which both pendulums lie in the dominant rotational area. Increasing the detuning between them drives the detuned one outside the purely rotational domain maintaining though a higher rotational ratio than the decoupled, meaning that the coupling acts in favour of rotations or at least not against them in the stochastic case as well.

Higher mass ratio - Fig. 5.9(d), brings up the effect of the interaction between the pendulums. The tuned pendulum is less robust, maintaining a purely rotational motion only for relatively high detuning values. Inducing noise has extended what was found only for one parameter pair in the deterministic case, being consistent with the previously observed destructive effect of noise onto rotations. When the detuning is low, though both pendulums lie inside the rotational region, none of them preserves purely rotational motion. As soon as the detuned one exits the rotational region for $\nu/\kappa > 2.5$ and enters the oscillatory region, the interaction between them fades away as well and so the tuned pendulum returns to pure rotations while the detuned one approaches the decoupled response. Closer to the second resonance curves, for $\nu/\kappa < 2.0$, where the detuned lies in the general instability area, the response of both pendulums improves. In Fig. 5.9(f) with $\psi = 0.5$, the same pattern is observed only intenser.
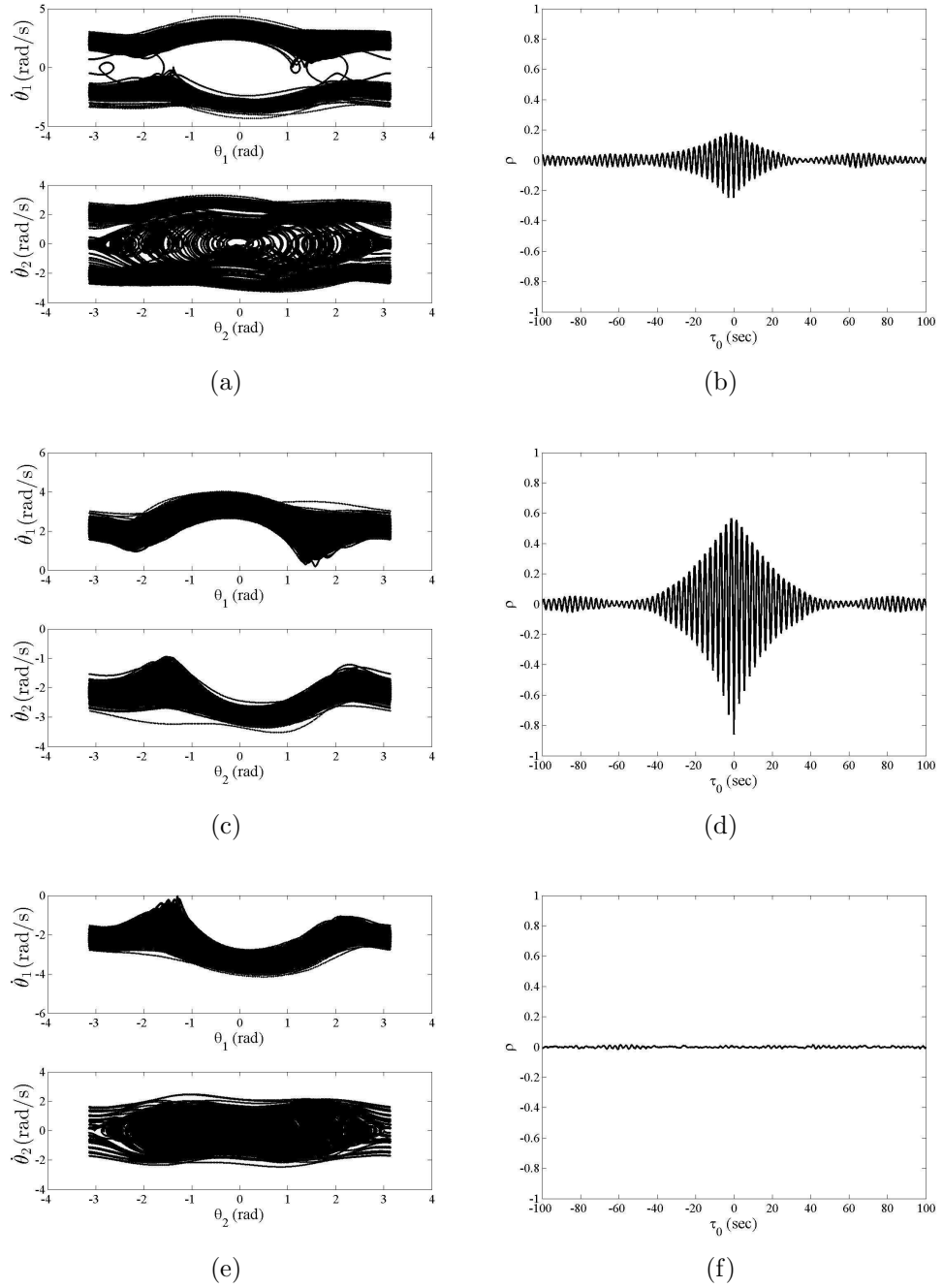
Figure 5.10: LHS: phase plots for points chosen from the RHS of Fig. 5.9 with (a) $\nu/\kappa = 3.0$, $\psi = 0.1$, (c) $\nu/\kappa = 2.7$, $\psi = 0.1$, (e) $\nu/\kappa = 3.0$, $\psi = 0.3$; RHS: corresponding cross-correlation coefficient of (θ_1, θ_2).

5.3.2 Correlation coefficient

So far, examining the demonstrated rotational motion reflects a rather macroscopic view on the trajectories of the pendulums. In order to acquire a better insight, possible synchronization is sought. One of the simplest, yet descriptive, measures

of this phenomenon is the cross-correlation coefficient of the angular displacements defined as:

$$\rho(\tau_o) = \frac{< \theta_1(t)\theta_2(t + \tau_0) >}{\sigma_{\theta_1}\sigma_{\theta_2}} \tag{5.5}$$

which always lies in $[-1, 1]$ and σ_{θ_i} is the i-th's pendulum standard deviation.

If ρ attains its extrema values that would mean complete synchronization between the pendulums with a constant phase difference revealed by the time lag τ_0. In the case of rotating response, unidirectional rotations would lead to the maximum ρ value, whilst opposite directions to the minimum. Fig. 5.10 presents the numerically calculated correlation coefficient for some characteristic cases, seeking whether this measure could indicate the rotational response of the detuned pendulum when the tuned one's is taken for granted. It is important to stress that, in general, the correlation coefficient reveals the similarity between two responses. That means that if both pendulums were oscillating in phase, then ρ would approach 1. However, since the tuned pendulum is configured to rotate, one could interpret a high correlation to both pendulums rotating. The figures at the top show the trajectories taken into account in sets, with the calculated coefficient being depicted in the corresponding positions at the bottom. Three cases drawn from the RHS of Fig. 5.9 are shown, in the presence of noise. Figs 5.10(a) and 5.10(b) refer to Fig. 5.9(b) and $\nu/\kappa = 3.0$, where the detuned pendulum exhibits mixed oscillatory-rotary response. The cross-correlation coefficient is bounded between $[-0.2, 0.2]$ indicating weak correlation between them, hence the partly rotational response. In Figs 5.10(c) and 5.10(d) which refer again to Fig. 5.9(b) but for $\nu/\kappa = 2.7$, the common rotational response reflects a strong correlation even though not a complete one due to the presence of noise. In the last case referring to Fig. 5.9(d) and $\nu/\kappa = 3.0$ where the detuned pendulum mostly oscillates, there is hardly anywhere a non-zero cross-correlation value translated to no correlation at all. In total, this measure has been seen to align with the observation made from identifying rotations. Particularly, it seems as if it could provide a good indication for separating rotational response from oscillatory, yet an adjustment to the exact percentage of rotations is not possible.

5.3.3   Parameter space plots

The previous sections revealed the potential of rotational motion in the coupled pendulums system as well. However, a better understanding can be acquired if a wider range of the amplitude was considered. To that end, parameter space plots are constructed with respect to rotational motion, following the ones created previously [183, 193, 194]. These plots (see Fig. 5.11) demonstrate the percentage of rotational motion performed by the detuned pendulum over the total length of the numerically calculated response, for a range of forcing parameters. The depicted values are leveled by a color-scale such that red indicates $> 90\%$ of rotational motion and blue $< 10\%$. The identification and quantification of rotations is based on MC simulations and the procedure explained in the beginning of this section. Compared to previous studies, the only difference is that the response is evaluated against (κ, λ) since the tuned pendulum has to remain unaltered and the frequency spanning of the detuned is controlled through κ.

The top three plots in Fig. 5.11 show the PSPs constructed for the same mass ratio value, $\psi = 0.1$, with the noise intensity taking the values $\sigma^2 = 0.0, 0.1, 0.3$ from left to right. At the bottom, the plots are organized in the same manner as far as the noise intensity is concerned, with $\psi = 0.3$. Naturally, as κ appears in the denominator of the frequency ratio exciting the detuned pendulum, the rotational region is directed towards the lower κ values. Since, the tuned pendulum is configured to rotate and so it does in most of the cases, only the response of the detuned one is considered. When the mass ratio is low - $\psi = 0.1$ - the rotational response presents a remarkable robustness even in the highest noise intensity examined, Fig. 5.11(e). However, increasing the pendulums' masses – Figs 5.11(b)–5.11(f) – acts against dominant rotations deteriorating their region. This observation is consistent with what has been found previously for the single pendulum system [193, 194]. Moreover, the noise maintains the destructive effect on the rotational regions noticed in all previous studies, even though it is more obvious when combined with relatively high mass ratio.
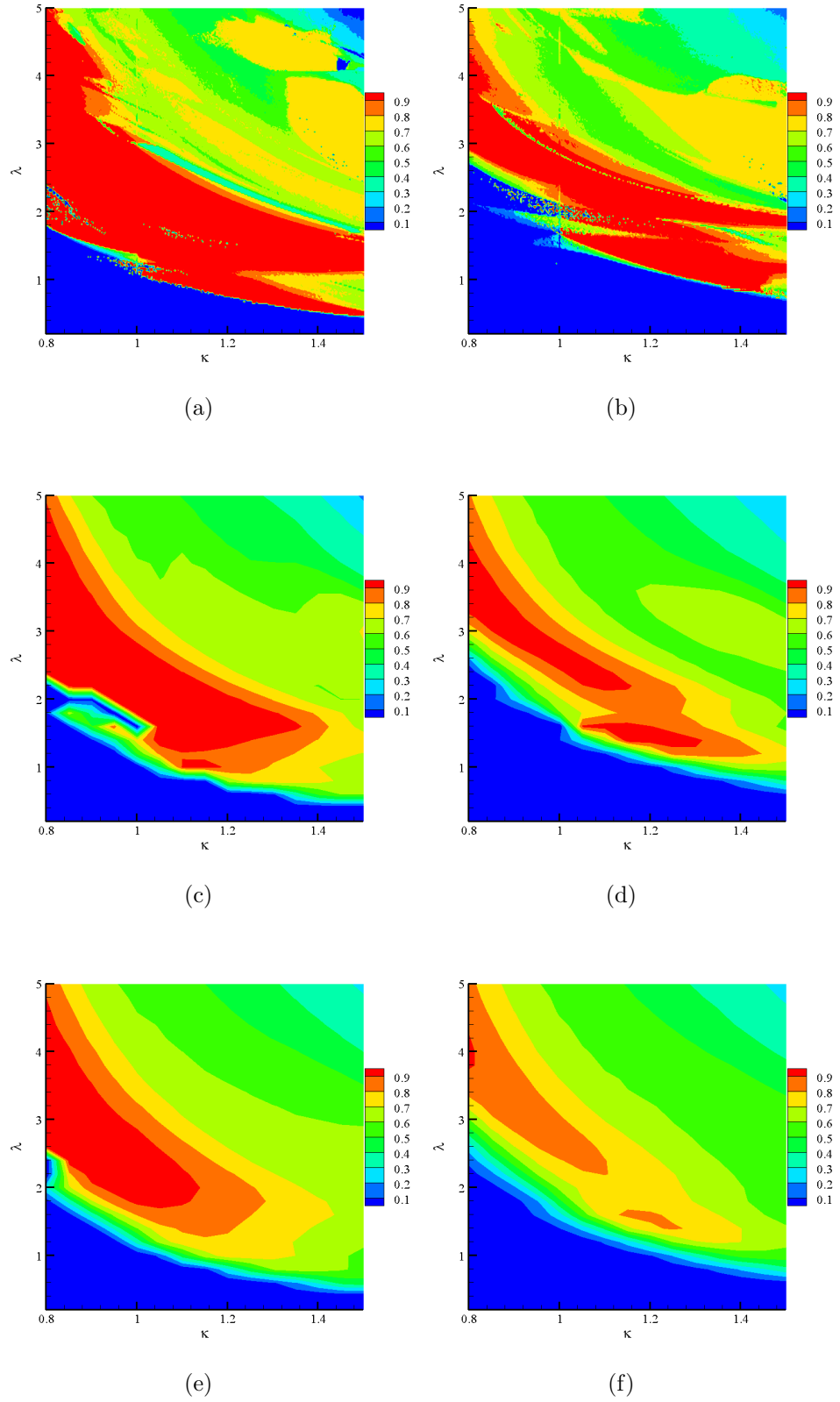
Figure 5.11: Rotational motion of the detuned pendulum (index 2 in Eq. (5.4)) against (κ, λ) for $\nu = 2.3$, $\gamma = 0.3$, $\beta = 0.5$, $e = 2.3$ and (a) $\sigma^2 = 0.0$, $\psi = 0.1$, (c) $\sigma^2 = 0.1$, $\psi = 0.1$, (e) $\sigma^2 = 0.3$, $\psi = 0.1$, (b) $\sigma^2 = 0.0$, $\psi = 0.3$, (d) $\sigma^2 = 0.1$, $\psi = 0.3$, (f) $\sigma^2 = 0.3$, $\psi = 0.3$.

5.4 Summary

The introduction of a mounting platform of the pendulum, modelled as a SDOF linear system, reshapes the studied dynamics to the base-excited autoparametric case. The centre of attention is again the construction of PSPs in order to evaluate the potential of rotational motion in a more realistic context. The preceding analysis revealed that the diffusing effect of randomness, observed in Chapter 4, could be compensated by the introduced platform. This is first demonstrated by the PSPs in Figs 5.3 and 5.4, where regions of dominant rotational motion can be found as low as $\lambda = 0.6$ for the target noise intensity of $D = 0.3$. This is a reasonable outcome for when the primary system is resonant, i.e. $\nu = e$, due to its dynamic amplification factor, that practically magnifies the displacement of the pendulum's pivot. However, even when the noise intensity is relatively large, this effect is located in a range of frequencies around the resonance, with the width depending on the primary system's parameters. In other words, the diffusing effect of noise is proven beneficiary, since it increases the bandwidth of the primary system's response spectrum, providing a non-localized amplification of the pendulum's pivot driving. The extent of these regions increases with higher natural frequency of the primary system which is attributed to the existence of wider rotational regions in the high frequency range, even in the deterministic PSP. Damping is also seen to facilitate expansion of the rotational regions with the same mechanism as in Chapter 4.

However, within the context of harvesting the energy stored as rotational motion of the pendulum, its mass has to be as large as possible. Thus, the interaction between the vibrating pendulum and the primary mass would play an important role. It was found that increasing mass ratio (secondary mass over total mass) acts against the regions of dominant rotations. There is only a small range, $m^r \leq 0.1$, for which the interaction could be beneficiary, or at least non-destructive, with respect to establishing rotational motion. Nevertheless, wide regions of 70-80% ratio are possible, especially when the beneficiary effect of the primary system's parameters is taken advantage of.

Furthermore, the potential of multiple non-identical pendulums mounted on a mu-

tual platform was considered. In this layout, the pendulums are coupled through the primary system itself, posing the additional issue of the interaction between the pendulums. In particular, since, given the excitation characteristics, the natural frequency of each pendulum controls its response, the influence of a tuned pendulum onto a detuned one was investigated. The tuned pendulum was configured such that it would exhibit rotational response. A detuning parameter was introduced, κ, as the ratio of the pendulums' natural frequencies and the response of the detuned pendulum was evaluated against it. It was found that the tuned rotating pendulum would force the detuned pendulum, which otherwise would not rotate, to enter a rotational regime. This could be achieved for a relatively wide range around $\kappa = 1$. Further detuning has been seen to render the coupling between the pendulums insignificant, the motion of which is then directed closer to the corresponding response they would have, if they were independent. Moreover, the rotational regions would maintain their robustness even for a high mass ratio, $\psi = 0.3$, which is an improved performance compared to the PSPs of a single pendulum. The practical importance is that this layout could act as an indirect passive control. Since two different frequencies are defined by $\kappa \neq 1$, each of the pendulums could act as the tuned pendulum, depending on the driving frequency, which follows a narrow-band spectrum in the case of ocean waves. Then, the tuned pendulum would force the detuned one into a rotational regime, with both pendulums being capable of adopting the role of the tuned system, depending on the, subject to random changes, forcing conditions. Thus, such a layout would provide a wider operating range of relatively good performance, as the PSPs characterizing the response of the detuned pendulum have shown.

Chapter 6

Impacting base

The dynamics of a mass-pendulum autoparametric vibro-impact system subjected to a narrow-band excitation are investigated in this chapter. The primary mass is modeled by a linear SDOF system with a unilateral barrier, in general shifted from its equilibrium position (Fig. 6.1). Such dynamics may be encountered in Ocean Engineering where floating structures are anchored to the sea bed by mooring chains [195]. Within this context lies the point absorber type of WEC, a special case of which is considered in this thesis. Due to the unpredicted nature of waves, unexpected wave heights could arise, termed as rare events in a probabilistic framework. The limited sag of the mooring chains could be stretched by high waves forcing abrupt stopping of the heaving motion. Moreover, given the operational range for any floating structure, it is important to protect it from high waves by imposing limiters, restricting the vertical motion of the floater. Thus high waves will cause the vibro-impact like motion of the system. Some basic information on dynamics, modeling and analysis of stochastic vibro-impact systems may be found in [196–198]. Impacting motion of an autoparametric pendulum has been recently investigated by R. Leine [199], where a pendulum mass was subjected to a vibro-impact motion against a unilateral constrain. The impact was modeled as an instant event with energy losses due to a given restitution coefficient. Hill's equation of motion was used to described the dynamics of the system and stability boundaries were derived using the averaging technique. In [200], the authors consider vibro-impact dynamics of a SDOF system subjected to a narrow-band stochastic excitation.
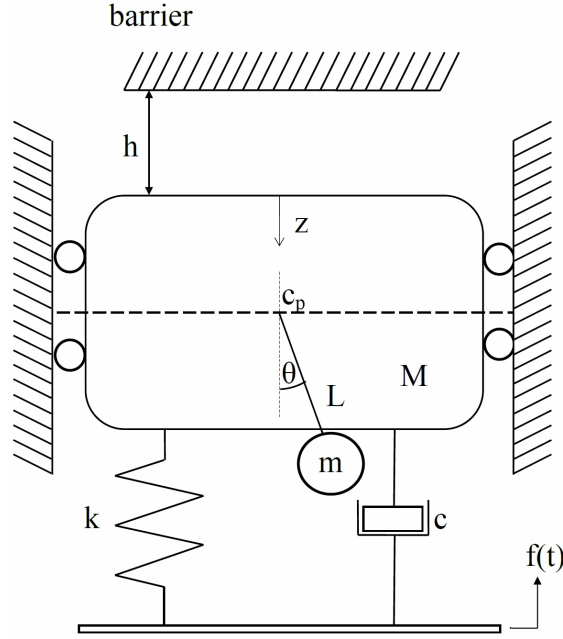
Figure 6.1: Sketch of the impacting autoparametric system

6.1 Problem statement

The dynamics of a pendulum positioned on a vertically excited mass may be written as:

$$\ddot{x} + 2\alpha\dot{x} + \Omega_M^2 x = \lambda L \Omega_M^2 \cos q(t) + \frac{m}{M+m} L\ddot{\theta} \sin\theta + \frac{m}{M+m} L\dot{\theta}^2 \cos\theta$$
$$\ddot{\theta} + 2\beta\dot{\theta} + \left(\Omega_p^2 - \ddot{x}/L\right)\sin\theta = 0 \qquad (6.1)$$
$$\dot{q}(t) = \omega_m + \sigma\zeta(t), \lambda = \frac{A\omega^2}{L\Omega_M^2}$$

Here, M, m are the masses, Ω_M and Ω_P - the natural frequency of the primary mass and the pendulum correspondingly, ω - the excitation frequency, L - the pendulum's length, α, β the damping coefficients of the primary system and the pendulum respectively, A - the excitation amplitude, ζ - zero mean Gaussian white noise [193]. When the inclination angle θ is small, Eq. (6.1) can be simplified:

$$\ddot{x} + 2\alpha\dot{x} + \Omega_M^2 x = \lambda L \Omega_M^2 \cos q(t) + \gamma L(\ddot{\theta}\theta + \dot{\theta}^2)$$
$$\ddot{\theta} + 2\beta\dot{\theta} + \left(\Omega_p^2 - \ddot{x}/L\right)\theta = 0 \qquad (6.2)$$
$$\gamma = \frac{m}{M+m}$$

There is a considerable gap in the literature concerning the dynamics of the au-

toparametric pendulum hinged on an impacting base. Thus, it is important to study the linearized system in Eq. (6.2), pursuing to understand the stability behaviour manifested under these circumstances. Besides, in the event of rare unexpectedly high waves, such that the impacting motion due to the limiters or the mooring chains is initiated, one would be interested in designing the WEC so that the pendulum would first escape the asymptotically stable well. This is a task that could be analyzed solely by the linearized Eq. (6.2). That is dictated by the purpose of energy production which is favoured by rotational motion, yet the rare nature of the system considered in this Chapter allows room for the lower efficiency of oscillatory motion in these extreme conditions. On the other hand, it might be preferable to "shut down" the device keeping the pendulum at its equilibrium position, ergo aiming at a stable response of Eq. (6.2). Thus, investigating the dynamics of Eq. (6.2) fulfills a multi-fold requirement of the development of the present WEC.

Returning to Eq. (6.2), since the motion of M is restricted by a barrier (Fig. 6.1) located at a distance $h^*\lambda$ from its equilibrium, its motion is limited. The reason behind such a notation is clear if one thinks about the response of the SDOF system, which will be different for different values of λ. Thus, if an unscaled distance is used, the actual distance to the barrier will be different every time the excitation amplitude is changed, but it is not convenient for the comparison of results and parametric study. The mass M will have impacts against the barrier when its displacement is larger than or equal to the distance to the barrier, therefore the first equation is valid only when M is between the impacts. To incorporate this feature into equations of motion lets rewrite Eq. (6.2) as follows:

$$
\begin{aligned}
&\ddot{z} + 2\alpha\dot{z} + \Omega_M^2 z = \lambda\Omega_M^2 \cos q(t) + \gamma(\ddot{\theta}\theta + \dot{\theta}^2), z < -h \\
&\ddot{\theta} + 2\beta\dot{\theta} + \left(\Omega_p^2 - \ddot{z}\right)\theta = 0 \\
&\dot{z}_+ = -r\dot{z}_-, z = -h = -h^*\lambda/L,
\end{aligned}
\tag{6.3}
$$

where $z = x/L$, $\dot{z}_+$ and $\dot{z}_-$ are the velocities of mass M right before and after the impact, r - the restitution coefficient, $0 < r \leq 1$, and the last equation describes the impact condition.

To incorporate the impact into the equation of motion lets introduce the following Zhuravlev transformation [69]:

$$z = |y| - h, \dot{z} = \dot{y}\,\text{sign}(y), \ddot{z} = \ddot{y}\,\text{sign}(y), \tag{6.4}$$

so that

$$\ddot{y} + \Omega_M^2 y = -2\alpha\dot{y} + \left[\Omega_M^2 h + \lambda\cos q(t) + \gamma(\ddot{\theta}\theta + \dot{\theta}^2)\right]\text{sign}(y)$$
$$\dot{y}_+ = r\dot{y}_-, \tag{6.5}$$
$$\ddot{\theta} + \Omega_p^2\theta = -2\beta\dot{\theta} + \ddot{y}\,\text{sign}(y)\theta$$

The benefit of this transformation is that if $r = 1$, the response y is everywhere differentiable as could be seen in Fig. 6.2 avoiding the inconvenient condition in Eq. (6.3) for the velocity at the instance of impacts. The above set of equations will be analyzed analytically and numerically next.

6.2 Analytical Development

6.2.1 Stochastic averaging

To derive a set of shortened equations the method of stochastic averaging described in Sec. 3.3.2 is employed. Lets introduce a slowly varying amplitude and phase of
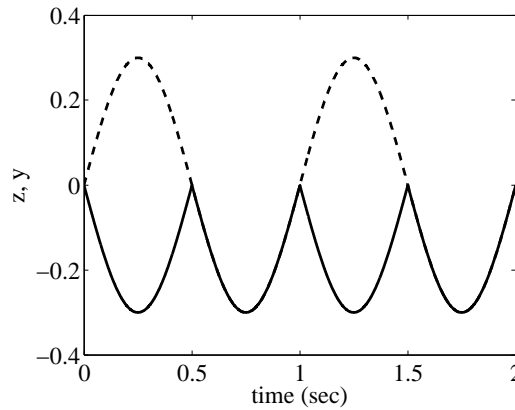
Figure 6.2: The effect of the Zhuravlev transformation, Eq. (6.4), for $h = 0$. The original not-everywhere differentiable response z (solid line) is transformed to a smooth response y (dashed line).

the primary mass and the pendulum, assuming $r = 1$ throughout the rest of this Chapter, unless stated otherwise:

$$y = A_1 \sin \phi_1, \dot{y} = A_1 \Omega_M \cos \phi_1$$
$$\theta = A_2 \sin \phi_2, \dot{\theta} = A_2 \Omega_p \cos \phi_2, \tag{6.6}$$

which will result in:

$$\dot{A}_i = \frac{\cos \phi_i}{\Omega_i} R_i, \dot{\phi}_i = \Omega_i - \frac{\sin \phi_i}{A_i \Omega_i} R_i, i = 1, 2, \tag{6.7}$$

where R_1, R_2 are the RHS of the first and third equation in Eq. (6.5) correspondingly and $\Omega_1 = \Omega_M$, $\Omega_2 = \Omega_p$. Since the frequency of the vibroimpact motion is doubled, consider a subharmonic response with the excitation frequency close to the double of the natural frequency of the primary mass, so that $\Delta = \omega - 2\Omega_1$, $\delta = \Omega_2 - \Omega_1$ are small parameters. Assuming the RHS of all the equations is proportional to a small parameter, introducing two new variables, $\chi = q - 2\phi_1$ and $\psi = \phi_2 - \phi_1$, and averaging over the period, taking into account that $\text{sign}[A_1 \sin \phi_1] = \text{sign}[\sin \phi_1]$, one gets the following set of stochastic differential equations:

$$\dot{A}_1 = -\alpha A_1 - a_1 \sin \chi - 2a_2 A_2^2 \sin(2\psi),$$

$$\dot{\chi} = \Delta + \sigma \zeta(t) + \frac{2a_4}{A_1} - a_1 \frac{\cos \chi}{A_1} + 3a_2 \frac{A_2^2}{A_1} \left[1 - \frac{1}{3} \cos (2\psi)\right],$$

$$\dot{A}_2 = -\beta A_2 + a_3 A_1 A_2 \sin(2\psi), \tag{6.8}$$

$$\dot{\psi} = \delta + 3a_3 A_1 \left[1 + \frac{1}{3} \cos (2\psi)\right] + \frac{a_4}{A_1} - a_1 \frac{\cos \chi}{2A_1} + 3a_2 \frac{A_2^2}{2A_1} \left[1 - \frac{1}{3} \cos (2\psi)\right]$$

$$a_1 = \frac{4\lambda}{3\pi\Omega_1}, a_2 = \frac{2\gamma\Omega_2^2}{3\pi\Omega_1}, a_3 = \frac{\Omega_1^2}{3\pi\Omega_2}, a_4 = \frac{2\Omega_1 h}{\pi}.$$

Note that a_i, $i = 1, 4$ are all positive parameters. This is a system of nonlinear stochastic differential equations and therefore it is difficult to analyze it analytically. However, the case of little or no interaction between the pendulum and the primary

mass $(\gamma = 0, a_2 = 0)$ can simplify the system making the primary mass independent:

$$
\begin{aligned}
\dot{A}_1 &= -\alpha A_1 - a_1 \sin \chi, \\
\dot{\chi} &= \Delta + \sigma \zeta(t) + \frac{2a_4}{A_1} - a_1 \frac{\cos \chi}{A_1}, \\
\dot{A}_2 &= -\beta A_2 + a_3 A_1 A_2 \sin(2\psi), \\
\dot{\psi} &= \delta + 3a_3 A_1 \left[1 + \frac{1}{3} \cos \left(2\psi \right) \right] + \frac{a_4}{A_1} - a_1 \frac{\cos \chi}{2A_1}
\end{aligned}
\tag{6.9}
$$

6.2.2 The deterministic system

Considering the steady-state deterministic $(\sigma = 0)$ response of the primary system, i.e. $\dot{A}_1, \dot{\chi} = 0$. It can be seen that the first two equations can be solved independently, meaning that the dynamics of the primary mass is not influenced by the pendulum. Thus, the steady state response amplitude is:

$$
A_1 = \frac{-2a_4 \Delta \pm \sqrt{a_1^2(\Delta^2 + \alpha^2) - 4\alpha^2 a_4^2}}{\Delta^2 + \alpha^2}
\tag{6.10}
$$

However, when the barrier is located at the system's equilibrium position $(h = 0)$ Eq. (6.10) can be simplified:

$$
A_1 = \frac{a_1}{\sqrt{\Delta^2 + \alpha^2}}
\tag{6.11}
$$

The equations for the pendulum amplitude and phase can be written from Eq. (6.9) as:

$$
\begin{aligned}
\dot{A}_2 &= -\beta A_2 + a_3 A_1 A_2 \sin(2\psi), \\
\dot{\psi} &= \delta + 3a_3 A_1 \left[1 + \frac{1}{3} \cos \left(2\psi \right) \right] - \frac{\Delta}{2}
\end{aligned}
\tag{6.12}
$$

Introducing another set of new variables $u = A_2 \sin(\psi)$ and $v = A_2 \cos \psi$ and substituting them into Eq. (6.12) results in a set of two equations:

$$
\begin{aligned}
\dot{u} &= -\beta u - \mu v + 4a_3 A_1 v, \\
\dot{v} &= -\beta v + \mu u - 2a_3 A_1 u,
\end{aligned}
\tag{6.13}
$$

where $\mu = \Delta/2 - \delta = \omega/2 - \Omega_2$ and which could finally describe the dynamics of the approximate pendulum system with respect to the response amplitude of the primary system.

Taking into account Eq. (6.13), stability of this system will depend on the sign of the real part of the roots p of the characteristic equation:

$$(\beta + p)^2 - (\mu - 2a_3A_1)(4a_3A_1 - \mu) = 0 \tag{6.14}$$

leading to the following condition for the pendulum instability:

$$3a_3A_1 + \sqrt{a_3^2A_1^2 - \beta^2} \geq \mu \geq 3a_3A_1 - \sqrt{a_3^2A_1^2 - \beta^2}, \tag{6.15}$$

In the case of negligibly small pendulum damping ($\beta = 0$) the condition for instability will then be:

$$4a_3A_1 \geq \mu \geq 2a_3A_1, \tag{6.16}$$

If $\Omega_1 = \Omega_2$ ($\delta = 0$) and α, β are considered sufficiently small, then the above formula can be simplified down to:

$$2\Omega_2 + \frac{4\sqrt{2\lambda}}{3\pi} \geq \omega \geq 2\Omega_2 + \frac{4\sqrt{\lambda}}{3\pi}, \tag{6.17}$$

It is possible to extract the instability boundaries for non-zero α and β considering an expression for λ with respect to Δ. Then, Eq. (6.15) would lead to the following condition for instability:

$$\lambda_L(\Delta, \alpha, \beta) \geq \lambda \geq \lambda_R(\Delta, \alpha, \beta) \tag{6.18}$$

where:
$$\lambda_{L,R} = \frac{3}{16}\pi^2\sqrt{\Delta^2 + \alpha^2}\left(\frac{9}{4}\Delta \pm \frac{3}{4}\sqrt{\Delta^2 - 32\beta^2}\right) \tag{6.19}$$

with the index L referring to $+$ and R to $-$. It is worth noting that Eq. (6.19) gives

rise to the following restriction, since the amplitude λ has to be real:

$$|\Delta| \geq 4\beta\sqrt{2} \tag{6.20}$$

This is a rather interesting fact since it reveals an additional influence of the pendulum's damping coefficient β on the structure of the instability domain when the primary mass is subjected to impacts. It is well-known that in the parametrically excited system described by the Mathieu equation, the instability domain is shifted upwards with increasing values of β. However, formula Eq. (6.20) suggests that it also moves the instability region away from the resonance frequency ($\Delta = 0$). Furthermore, Eq. (6.15) bounds μ between two quantities which are both positive. Thus, for the case of $\delta = \Omega_1 - \Omega_2 = 0$ the unstable domain can be found only in the half-plane of the positive Δ axis. In general, δ could be used to move the instability region to higher detuning ($\delta > 0$) or lower ones ($\delta < 0$) including negative values due to the definition of μ. However, throughout this Chapter it will be taken $\delta = 0$. Coming back to that, the placement of the instability region at positive detuning is another interesting distinction from the Mathieu equation where the instability region is well known to be symmetrical about the $\Delta = 0$ axis (see Fig. 2.14). Thus to avoid or target the instability in this case it is enough to have a negative or proper positive detuning, at least for small values of λ, which is either way a requirement of the averaging technique.

In addition, the initiation point must satisfy the condition $\lambda_L = \lambda_R$, which can be found to have only one positive solution for Δ_{init} being given by the equality in Eq. (6.20):

$$\lambda_{init} = \frac{27}{16}\beta\,\pi^2\sqrt{64\,\beta^2 + 2\alpha^2} \tag{6.21}$$

In other words, Δ_{init} is the point where two curves, describing the instability domain, collide and the instability domain can only exist to the right of this point. However, the initiation point is not the lowest λ resulting in instability, as could be seen in
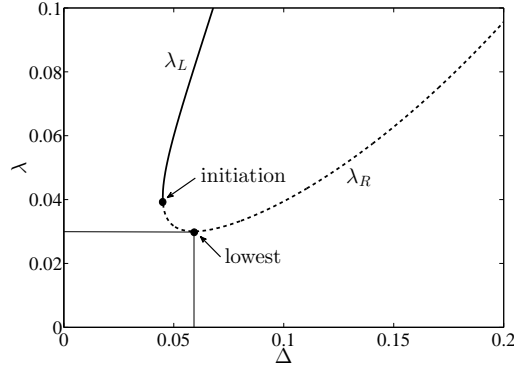
Figure 6.3: Instability boundaries for the system in Eq. (6.35) for $\alpha = 0.1$, $\beta = 0.005$, $h = 0.0$, $\sigma^2 = 14\beta$ separating the left boundary λ_L (——) from the right one λ_R ($---$). Indication of initiation point being different from the lowest unstable one.

Fig. 6.3. The lowest unstable point can be found by minimizing the λ_R function and which is, for $\alpha = 0.0$:

$$\lambda_{low} = \frac{9\pi^2\beta^2}{4}\left(3 + 2\sqrt{2}\right) \tag{6.22}$$

This is the formula which provides the lowest boundary of the instability domain.

6.2.3   Offset barrier

Eqs (6.17)-(6.22) were derived under the assumption of $h = 0$, using the expression in Eq. (6.11). As long as a barrier is located slightly offset from the equilibrium at $h = h^*\lambda$, one has to ensure that the expression in Eq. (6.10) is real and positive. Taking into account that $\delta = 0$, which leads to positive Δ, one arrives at the following condition:

$$a_1 \geq 2a_4 \Rightarrow 1 \geq 3\Omega_1^2 h^* \tag{6.23}$$

This condition may be thought of as the condition of a vibro-impacting motion, or the motion with impacts within each period. Including impacts at a distance offset from the equilibrium along with the influence of damping coefficients α, β is rather hard to treat analytically. The derived expressions are quite long (see Appendix
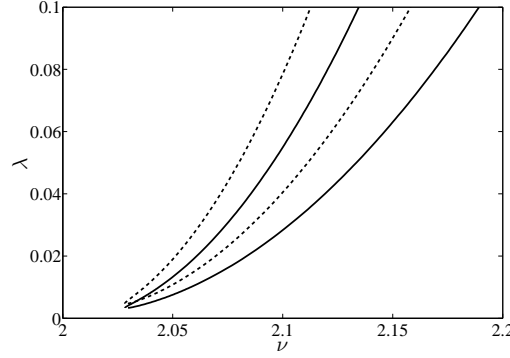
Figure 6.4: Stability boundaries for deterministic excitation and $\gamma = 0.0$, $\beta = 0.005$, $\alpha = 0.0$ calculated approximately analytically from Eq. (6.24) and $h^* = 0$ (solid line) and $h^* = 0.1$ (dashed line).

A.1) and thus it is difficult to evaluate the influence of the parameters. Hence, a simplification is adopted where each of the damping parameters are individually set to zero. First the joint influence of β and h^* is considered leading to the following expressions for the stability boundaries:

$$\lambda_{L,R} = \frac{9\Delta}{64} \frac{\pi^2 \left(3\Delta \pm \sqrt{\Delta^2 - 32\beta^2} \right)}{1 - 3\Omega_2^2 h^*} \qquad (6.24)$$

with the $\pm$ notation as before. The closest unstable solution to the resonance axis is again found by Eq. (6.20) with the lowest λ value leading to unstable response being:

$$\lambda_{low} = \frac{9\pi^2\beta^2}{4\left(1 - 3\Omega_2^2 h^*\right)} \left(3 + 2\sqrt{2} \right) \qquad (6.25)$$

Fig. 6.4 shows the analytical instability boundaries for $h^* = 0$ and $h^* = 0.1$ with $\alpha = 0$ and $\beta = 0.005$. It is noticed that a non-zero h rotates the instability region anticlockwise with respect to the initiation point, as well as moving the lowest point upwards, compared to $h = 0$ in Eq. (6.22). Moreover, the latter is predicted to alter slightly its coordinates in the parameter space. These curves are presented to extract a qualitative view on the influence of the offset parameter h^*.

Applying the same procedure for the joint influence of α and h^*, the following
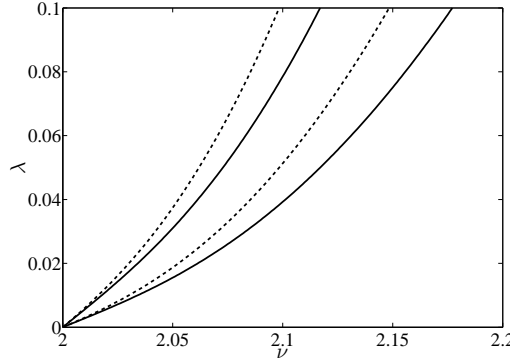
Figure 6.5: Stability boundaries for deterministic excitation and $\gamma = 0.0$, $\beta = 0.0$, $\alpha = 0.1$ calculated approximately analytically from Eq. (6.26) for $h^* = 0$ (solid line) and $h^* = 0.1$ (dashed line).

formulas are derived.

$$\lambda_L = \frac{9\pi^2\Delta}{16} \frac{\left(3\,\Omega_2{}^2 h^* + \sqrt{-9\,\Omega_2{}^4 h^{*2}\alpha^2 + \Delta^2 + \alpha^2}\right)}{1 - 9\,\Omega_2{}^4 h^{*2}} \qquad (6.26)$$

$$\lambda_R = \frac{\lambda_L}{2}$$

Since β is assumed to be zero then the initiation point lies at $(\Delta, \lambda) = (0,0)$. Fig. 6.5 shows that a displaced barrier incurs a similar effect on the stability boundaries by rotating them anticlockwise.

As soon as α and β are considered to be non-zero, it is more convenient to conduct a numerical study which will be discussed in Sec. 6.3.1.

A few words should be mentioned regarding the case of negative δ, which according to Eq. (6.14) allows negative values of Δ as long as $\mu > 0$. Then, it is possible to have either one or two real values of the primary mass response amplitude in the deterministic case. The condition for the existence of a single solution leads again to condition Eq. (6.24). In order to have two real and positive solutions for $\Delta < 0$ it is essential to ensure that

$$a_1^2 > \frac{4\alpha^2}{\Delta^2 + \alpha^2} a_4^2,$$

$$4a_4^2\Delta^2 > a_1^2(\Delta^2 + \alpha^2) - 4\alpha^2 a_4^2 \qquad (6.27)$$

The above conditions may be rewritten as:

$$2a_4 > a_1, \quad 1 > \frac{\alpha^2}{\Delta^2 + \alpha^2} \tag{6.28}$$

Whereas the second condition is always satisfied for $\Delta \neq 0$, the first condition is opposite to Eq. (6.24) for positive values of Δ, i.e. $1 < 3\Omega_1^2 h^*$. The latter corresponds to the case of large gap and therefore two possible amplitudes will correspond to impacting and impact free motions. The behaviour of the pendulum in this case is out of the scope of this thesis and thus not considered herein.

6.2.4 Stochastic mean stability

An effort to derive an approximate expression of the stability boundaries of the linearized stochastic autoparametric pendulum through Eq. (6.9) requires a few further approximations. First of all, since the stationary response is sought and ϕ_1, ϕ_2 are slowly varying, one could enforce $\dot{\chi} = 0$. Therefore, the set of differential equations dictating the response of the pendulum becomes:

$$
\begin{aligned}
\dot{A}_2 &= -\beta A_2 + a_3 A_1 A_2 \sin(2\psi), \\
\dot{\psi} &= \delta + 3a_3 A_1 \left[1 + \frac{1}{3}\cos(2\psi)\right] - \frac{\Delta}{2} - \frac{\sigma}{2}\zeta(t)
\end{aligned}
\tag{6.29}
$$

Further on, introducing a set of new variables $u = A_2 \sin\psi$ and $v = A_2 \cos\psi$ and substituting them into Eq. (6.29), results in the following set:

$$
\begin{aligned}
\dot{u} &= -\beta u - \mu v + 4a_3 A_1 v + \frac{\sigma v}{2}\zeta(t), \\
\dot{v} &= -\beta v + \mu u - 2a_3 A_1 u - \frac{\sigma u}{2}\zeta(t),
\end{aligned}
\tag{6.30}
$$

where $\mu = \Delta/2 - \delta = \omega/2 - \Omega_2$ and which could finally describe the dynamics of the approximate pendulum system with respect to the response amplitude of the primary system.

In this section, the stability of the pendulum's response is approached in terms

of the mean stability. Applying the expectation operator $< \cdot >$ to both sides of the equations in Eq. (6.30) and accounting for the Wong-Zakai correction terms, a deterministic matrix differential equation for the mean values is derived. One should notice though that in this approach, A_1 should be considered uncorrelated with u, v. Moreover, the mean value of A_1 is essential for the extraction of the stability boundaries and so, A_1^* will be denoting this value in the following set of equations:

$$\begin{bmatrix} \dot{m}_u \\ \dot{m}_v \end{bmatrix} = \begin{bmatrix} -\beta - \dfrac{\sigma^2}{8} & 4a_3 A_1^* - \mu \\ \mu - 2a_3 A_1^* & -\beta - \dfrac{\sigma^2}{8} \end{bmatrix} \begin{bmatrix} m_u \\ m_v \end{bmatrix} \tag{6.31}$$

where m_u, m_v denote the mean values of the corresponding variables.

Thus, the stability of the system of ordinary differential equations in Eq. (6.31) would unveil the mean stability of the system Eq. (6.30). It is well-known in the stability theory of linear systems, that the stability of their response is determined by the sign of the real part of the eigenvalues κ of the 2×2 matrix in Eq. (6.31), with positive sign leading to instability. Requiring at least one eigenvalue to have a positive real part and setting $\Omega_1 = \Omega_2 = 1$ leads to the following condition for A_1^*:

$$b_- < A_1^* < b_+ \tag{6.32}$$

where
$$b_\pm = \frac{3\pi \left(3\Delta \pm \sqrt{\Delta^2 - 32\beta^2 - 8\beta\sigma^2 - \sigma^4/2} \right)}{16}$$

Of course, the root argument in the above equation has to be positive in order for the amplitude boundaries to be real. Thus, the following condition should hold:

$$|\Delta| \geq \frac{\sqrt{2}}{2} \left(8\beta + \sigma^2 \right) \tag{6.33}$$

Eq. (6.33) reveals a distinct characteristic of the stability boundaries of the au-
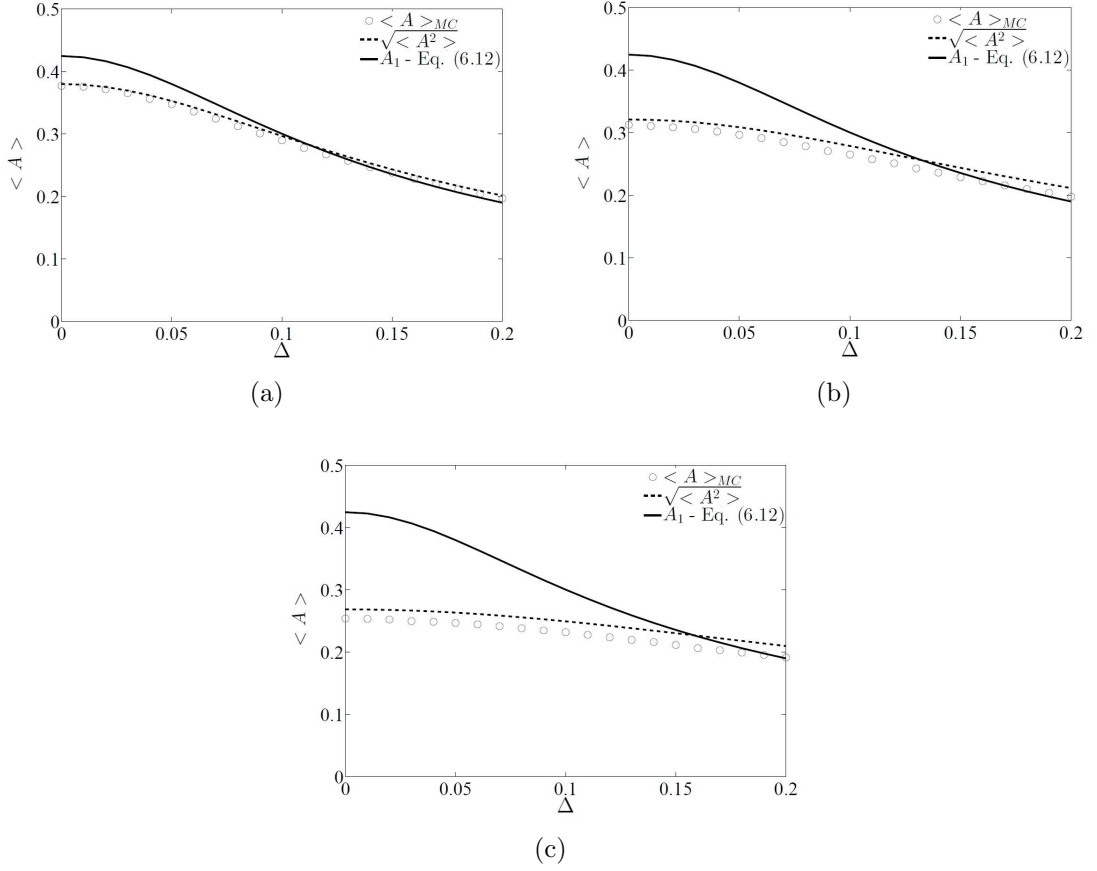
Figure 6.6: Comparison of MC simulations of $<A>$ ($\circ$) with the square root of the mean-square amplitude $(---)$ and the deterministic amplitude (———) for $\alpha = 0.1$, $\Omega_1 = 1.0$; (a) $\sigma^2 = 0.05$; (b) $\sigma^2 = 0.15$; (c) $\sigma^2 = 0.3$.

toparametric system when the primary mass experiences impacts against a barrier, as has been the case with the deterministic system as well (Sec. 6.2.2. The typical Mathieu equation becomes unstable for a symmetric region around $\Delta = 0$ extending to both the positive and negative Δ semi-axis. However, when impacts are imposed due to a barrier, Eq. (6.33) determines that the instability region lies only on the positive detuning Δ semi-plane, introducing a qualitatively different behaviour of the response of the pendulum. Yet, under the influence of noise, it is interesting to investigate the robustness of this observation.

Approximations. The expression of the instability boundaries in Eq. (6.32) reflect their dependence onto the mean value A_1^*. However, in order to express them in the (Δ, λ) space with analytical means, one would need an expression for the primary's mass' average amplitude A_1^*. Unfortunately, only the mean-square response

143
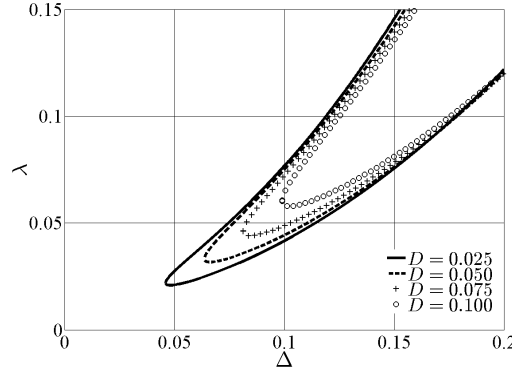
Figure 6.7: Analytical mean-stability boundaries for the system Eq. (6.13) for $r = 1.0$, $\alpha = 0.1$, $\beta = 0.005$, $h = 0.0$; and different $\sigma = \sqrt{D}$ values.

amplitude can be derived analytically and that only for $h = 0$ and $\gamma = 0$, with the latter decoupling the response of the primary system by the pendulum's motion. Thus, an approximation has to be adopted exploiting the, necessary for the stochastic averaging technique to hold, small noise intensity and that is, $A_1^* = \sqrt{<A_1^2>}$, where [201]:

$$<A_1^2> = \frac{(a_1^2/\alpha^2)\,(1 + \sigma^2/2\alpha)}{(1 + \sigma^2/2\alpha)^2 + (\Delta/\alpha)^2} \qquad (6.34)$$

In fact, even though it is known to be erroneous, A_1^* has been seen to closely approximate numerical estimations of $<A>$ calculated by MC simulations (see Fig. 6.6) even for relatively large noise intensity. Nonetheless, this approximation assumes an overestimated response amplitude which draws the instability downwards, thus keeping the analysis on the safe side regarding instability.

Combining Eqs (6.32) and (6.34) one could reach an expression for the mean stability boundaries in the (Δ, λ) space. Due to the length of this expression, only a graphical representation is provided for $r = 1$ and different noise intensities in Fig. 6.7. The acutal formulas are shown though in Appendix A.2. A direct comparison with numerical calculation of these boundaries is also performed through estimation of the LLE, a procedure described in Sec. 6.3.1.

6.2.5 Stochastic mean-square stability

Coming back to the stochastic system in Eq. (6.9), it should be mentioned that the first two equations have been extensively studied in [201] by the stochastic averaging approach. It has been shown that an exact analytical result for a mean square amplitude is possible to obtain only in the case when the barrier is placed at the system's equilibrium position $(h = 0)$, which will be considered as such throughout this section. Rewriting the equations governing the pendulum motion to incorporate noise leads again to Eq. (6.30).

In order to examine the mean-square stability of the system Eq. (6.30), the differential equations for the second-order moments are derived. Applying stochastic averaging and denoting $D_{uu} = <u^2>$, $D_{vv} = <v^2>$ and $D_{uv} = <uv>$, the system of linear differential equations in Eq. (6.35) is derived dictating the time-evolution of the second-order moments of the variables in Eq. (6.30), where the Wong-Zakai correction terms [168] have been included.

$$
\begin{bmatrix} \dot{D_{uu}} \\ \dot{D_{vv}} \\ \dot{D_{uv}} \end{bmatrix} = \begin{bmatrix} -2\beta - \dfrac{\sigma^2}{4} & \dfrac{\sigma^2}{4} & 8a_3A_1^* - 2\mu \\ \dfrac{\sigma^2}{4} & -2\beta - \dfrac{\sigma^2}{4} & 2\mu - 4a_3A_1^* \\ \mu - 2a_3A_1^* & 4a_3A_1^* - \mu & -2\beta - \dfrac{\sigma^2}{2} \end{bmatrix} \begin{bmatrix} D_{uu} \\ D_{vv} \\ D_{uv} \end{bmatrix} \qquad (6.35)
$$

Thus, the stability of the system Eq. (6.35) of ordinary differential equations would infer the mean-square stability of Eq. (6.30). Note that the approximations regarding the expression for the mean value of A_1 that have been introduced in Sec. 6.2.4 are being adopted herein too and so, $A_1^* = \sqrt{<A_1^2>}$ along with Eq. (6.34). It is well-known in linear systems' theory, that the stability of such systems is determined by the sign of the real part of the eigenvalues κ of the 3×3 matrix in Eq. (6.35), with positive leading to instability. The eigenvalues in turn would be the solutions to the

characteristic polynomial of Eq. (6.35):

$$P(\kappa) = c_3 \kappa^3 + c_2 \kappa^2 + c_1 \kappa + c_0 = 0$$

where

$$
\begin{aligned}
c_3 &= 1 \\
c_2 &= 6\beta + \sigma^2 \\
c_1 &= \frac{32\,A_1{}^2 - 36\,\Delta\,\pi\,A_1}{9\pi^2} + \Delta^2 + 12\,\beta^2 + 4\,\beta\,\sigma^2 + \frac{\sigma^4}{4} \\
c_0 &= \frac{64A_1{}^2\beta - 72\Delta\pi\beta A_1 - 2A_1{}^2\sigma^2}{9\pi^2} + \\
&\quad + 2\beta\left(\Delta^2 + 4\beta^2 + 2\beta\sigma^2 + \frac{\sigma^4}{4}\right)
\end{aligned}
\tag{6.36}
$$

The full expressions for the eigenvalues even though possible to derive are quite long. Thus, the standard Routh-Hurwitz stability criterion that could be found in many dynamics textbooks (eg [65]) will be utilized, yielding the condition $\lambda_L^{\sigma\tau} \geq \lambda \geq \lambda_R^{\sigma\tau}$ with:

$$
\begin{aligned}
\lambda_{L,R}^{\sigma\tau} = &\frac{9\pi^2}{8\,(32\,\beta - \sigma^2)}\sqrt{\frac{2\alpha\,(\Delta^2 + \alpha^2 + \alpha\sigma^2 + \sigma^4/4)}{2\alpha + \sigma^2}}\left[12\,\beta\,\Delta\,\pm\right. \\
&\left. \pm\sqrt{\beta\,(4\,\beta + \sigma^2)\,(\sigma^4 - 128\,\beta^2 - 28\,\beta\,\sigma^2 + 4\,\Delta^2)}\right]
\end{aligned}
\tag{6.37}
$$

with the superscript $\sigma\tau$ denoting the stochastic case. To begin with, the limiting case of $\sigma \to 0$ returns one back to the formulas and the analysis presented in Sec. 6.2.2. The formula in Eq. (6.37) elucidates the significance of a critical noise intensity value $\sigma_{crit}^2 = 32\beta$.

Let us then first investigate the construction of the instability boundaries for noise $\sigma < \sigma_{crit}$. The instability region is again composed of two curves, $\lambda_{L,R}^{\sigma\tau}$ which enclose the unstable domain. The initiation point of these curves could be found by equating them and keeping in mind that only positive Δ is accounted for, yielding:
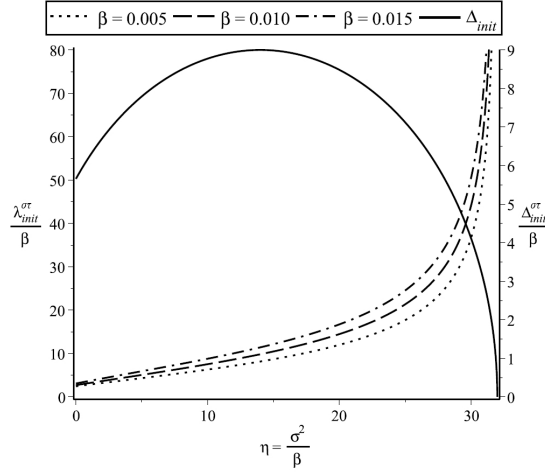
Figure 6.8: Evolution of Δ_{init} (——) and λ_{init}, non-dimensionalised over β from Eq. (6.38) and for $\beta = 0.005$ ($\cdots$), $\beta = 0.010$ ($---$), $\beta = 0.015$ ($-\cdot-$) with respect to noise over system bandwidth ratio, $\eta = \sigma^2/\beta$ and $h^*, \gamma = 0.0$.

$$\Delta_{init}^{\sigma\tau} = \sqrt{32\,\beta^2 + 7\,\beta\,\sigma^2 - \frac{\sigma^4}{4}} \tag{6.38a}$$

$$\lambda_{init}^{\sigma\tau} = \frac{27\beta\pi^2\Delta_{init}^{\sigma\tau}\sqrt{\alpha\left(32\beta^2 + 7\beta\sigma^2 + \alpha^2 + \sigma^2\alpha\right)}}{\left(32\,\beta - \sigma^2\right)\sqrt{2\left(2\alpha + \sigma^2\right)}} \tag{6.38b}$$

Since only the case $\sigma < \sigma_{crit}$ is considered at the moment, it could be seen that $\Delta_{init}^{\sigma\tau}$ is real for all values of β, σ satisfying this condition. Moreover, the initiation point is the closest unstable point to the $\Delta = 0$ axis, bounding the instability region from the left side for a given set of parameters β, σ reassuring the stability of the system for $\Delta < \Delta_{init}^{\sigma\tau}$. Looking at the formula in Eq. (6.38a), there is a supremum of that distance with respect to σ acquired for $\sigma^2 = 14\beta$ at which the initiation point takes the value $\Delta = 9\beta$. One could observe in Fig. 6.8 the bounded shape of $\Delta_{init}^{\sigma\tau}$ with increasing $\eta = \sigma^2/\beta$. In fact, starting from the deterministic value for $\sigma = 0$ which redirects back to Eq. (6.20), $\Delta_{init}^{\sigma\tau}$ reaches its maximum value and then reduces, retracting closer to the resonance axis than the deterministic response for values $\sigma^2 > 28\beta$ and with a trend of $\Delta_{init}^{\sigma\tau} \to 0$ as $\sigma^2 \to 32\beta$.

Larger values of the noise intensity drive the unstable response to expand to the negative semi-plane too, crossing the $\Delta = 0$ axis. This effect is consistent with the one observed for the Mathieu equation where increasing noise leads to wider
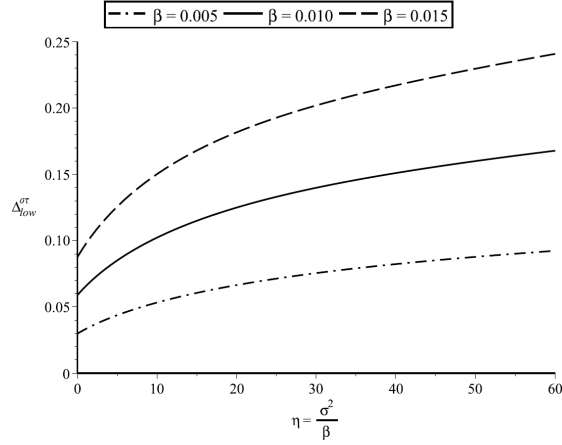
Figure 6.9: Distance, Δ_{low}, of the lowest point leading to unstable response of Eq. (6.30) from the resonance axis ($\Delta = 0$) calculated analytically for $\gamma = 0.0$, $\alpha = 0.1$ and $h^* = 0.0$ with respect to $\eta = \sigma^2/\beta$ and $\beta = 0.005(-\cdot-)$, $\beta = 0.010$ (———), $\beta = 0.015$ $(---)$.

instability region in the parameter space. As soon as $\sigma^2 > 32\beta$, with respect to λ, there is only one real and positive solution to the instability condition coming from the Routh-Hurwitz criterion and that is $\lambda > \lambda_R^{\sigma\tau}$, as it is defined in Eq. (6.37). In that case an initiation point cannot be defined in the parameter space (other than infinity which has no particular interest), and only the position of the lowest unstable point bears a significance compared to the impact-free response.

However, the behaviour of the origin (wherever this is defined) does not dictate the lowest unstable point too, as this does not coincide with the origin of the two curves, which was also the case in the deterministic analysis (Fig. 6.3). It can be seen from Eq. (6.38b), as well as in Fig. 6.8, that $\lambda_{init}^{\sigma\tau} \to \infty$ with $\sigma^2 \to 32\beta$. In that Figure, one could also notice the different slope with which $\lambda_{init}^{\sigma\tau}$ develops depending on β, as well as the monotonic increase with increasing noise intensity. Yet, the lowest unstable point in the parameter space could be found by calculating the minimum of $\lambda_R^{\sigma\tau}$ curve. Unfortunately, the derived expressions for the coordinates of the lowest unstable point are impossible to be depicted on paper. Thus, only a graphical representation of these formulas is included showing their dependence on the noise intensity.

Fig. 6.9 shows the evolution of the Δ coordinate of the lowest unstable point. It is seen that increasing noise shifts that point further to higher detuning, maintaining a dependence on β, also observed in the deterministic analysis. However, the λ
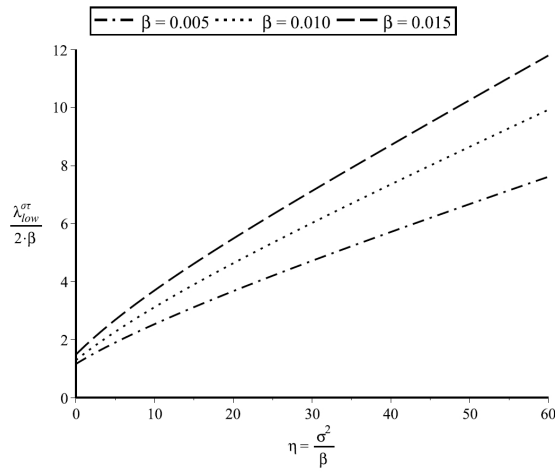
Figure 6.10: Lowest amplitude, $\lambda_{low}/2\beta$, leading to unstable response of Eq. (6.30) calculated analytically for $\gamma = 0.0$, $\alpha = 0.1$ and $h = 0.0$ with respect to $\eta = \sigma^2/\beta$ and $\beta = 0.005$ $(-\cdot-)$, $\beta = 0.010$ $(\cdots)$, $\beta = 0.015$ $(---)$.

coordinate is more important as it defines the threshold for instability. Fig. 6.10 depicts a similar pattern for $\lambda_{low}^{\sigma\tau}$ with an ever increasing threshold, again dependent on β with higher values of the latter demanding higher λ values to escape to instability, a situation known from the Mathieu equation as well. Yet, a direct comparison of the impacting response against the impacts-free vibrations would be biased since in the former case, the primary system is very close to resonance while in the latter is around the double of its resonance frequency. This would result in the impacting system to reach instability with lower λ than the vibrations without impacts. Overall, Figs 6.9 and 6.10 reveal the advance of the lowest unstable point in the parameter space with the influence of impacts onto the instability regions (contained in the positive Δ axis) being assistant to the stabilizing effect of noise. An interesting attribute is that, apart from the amplitude, the detuning needed to reach the lowest unstable point increases too, which practically expands the "safe zone", should one be interested in avoiding instability.

Furthermore, Fig. 6.11 shows the dependence of λ_{low} on the damping coefficient β. In the SDOF Mathieu equation, for a given excitation to system bandwidth ratio, there is a linear relationship between the lowest unstable point and β. However, in the examined impacting system a higher order relationship is revealed. That means in turn, that an enhanced stabilization occurs with increasing damping.
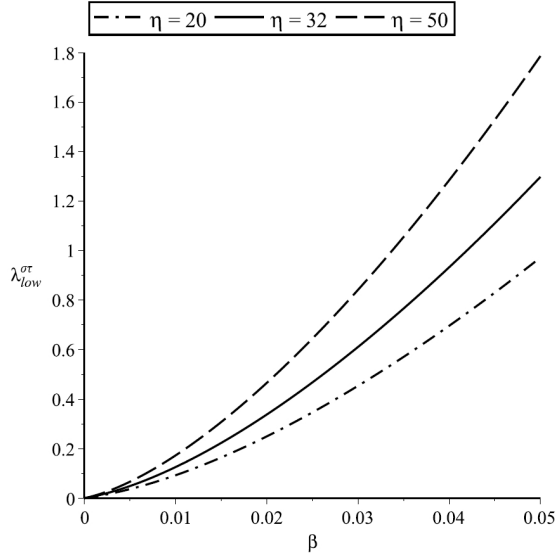
Figure 6.11: Lowest amplitude, λ_{low}, for unstable response of Eq. (6.30) calculated analytically with respect to β for $\gamma = 0.0$, $\alpha = 0.1$, impacts at $h = 0.0$ and $\eta = 20$ ($- \cdot -$), $\eta = 32$ (——), $\eta = 50$ ($- - -$).

It has become apparent so far that the $\sigma^2 = 32\beta$ value shoulders a control role in the system's stability. Let us now discuss the response when this critical value is adopted. If this noise intensity value is substituted into the characteristic polynomial in Eq. (6.36) and a similar procedure through the Routh-Hurwitz criterion is followed, then it can be seen $\lim_{\sigma^2 \to 32\beta} \Delta_{init}^{\sigma\tau} = 0$ and $\lim_{\sigma^2 \to 32\beta} \lambda_{init}^{\sigma\tau} = \infty$. That defines the upper threshold of the instability region being contained by two curves instead of only one as was noted for $\sigma^2 = 32\beta$. In the critical case then, the instability condition would be:

$$\lambda > \frac{3\pi^2 \left(324\beta^2 + \Delta^2\right)}{16\Delta} \sqrt{\frac{\alpha \left[\Delta^2 + (\alpha + 16\beta)^2\right]}{\alpha + 16\beta}} \tag{6.39}$$

which can be thought of as the special case of $\lambda_R^{\sigma\tau}$. The critical role lies in the fact that the far left unstable point is now asymptotically approaching the $\Delta = 0$ axis, yet with the instability domain still constrained in the positive detuning semi-plane. The exact case of the critical noise and the development of the lowest amplitude with β is depicted in Fig. 6.11. Besides that, one has to consider that the impacts-free boundary extends to the negative Δ semi-plane symmetrically with respect to the resonance axis. Therefore, a much more intensive stabilization is attributed to

the influence of impacts onto the parametric instability boundaries with σ_{crit} being the threshold of the instability region existing only in the positive detuning area. Nevertheless, impacts against a rigid barrier do not entirely eliminate the instability domain.

6.3 Numerical modelling

The analysis presented in Sec. 6.2 revealed a prosperous ground for a distinct behaviour of the instability domain of the vibro-impacting system. However, the analytical development is restricted by the difficulty of treating the interaction between the two modes of the autoparametric system and having to consider purely elastic impacts. In order to investigate the dynamics of the system in these two cases, as well as compare against the analytical expressions derived in Sec. 6.2, a numerical approach is employed in this section.

The procedure aims at calculating the stability boundaries through numerical MC simulations which are performed in an 8-core, 16 threads Xeon processor utilizing the MPI protocol for multi-processing. A random number generator is used to apply the Runge-Kutta-Maruyama scheme of the 4th order in a custom-made algorithm written in Fortran 90 programming language. The LLE is calculated, which is defined by Eq. (3.68), from the sign of which the stability of each point of the parameter space is determined.

6.3.1 Comparison to analytical results

It is quite a common practice for approximate analytical expressions to be benchmarked against numerical results, in order to check their accuracy. Under this rationale the LLE are calculated and used to construct the stability boundaries numerically. In this section, a deterministic and a stochastic case are computed and plotted jointly with the analytical results. Also, the offset barrier is considered and a qualitative comparison to the analytical results is performed.

Returning to the deterministic boundaries for $\gamma, h^* = 0$ given in Eq. (6.18), the case
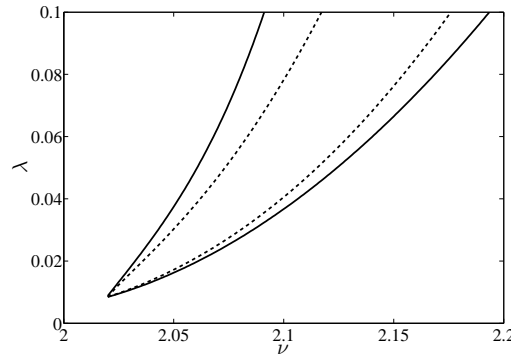
Figure 6.12: Stability boundaries for deterministic excitation and $\gamma = 0.0$, $\beta = 0.005$ $\alpha = 0.1$, $h^* = 0.0$ calculated numerically (solid line) and approximately analytically (dash line) through Eqs (6.18) and (6.19).

of $\alpha = 0.1$ and $\beta = 0.005$ is computed numerically. In Fig. 6.12, one can see the comparison of the approximate analytical formula Eq. (6.18) and the results of the numerical simulation of the original system Eq. (6.5). A good agreement is found between the numerical and analytical boundaries regarding the originating point of instability. However, increasing values of λ and ν lead to higher error as expected due to the restrictions of the approximate averaging technique. It is observed that the numerical boundaries occupy a wider region from the analytical ones.

Considering the stochastic system, Fig. 6.13 shows the instability regions of the approximating linearized pendulum system for two noise intensity values, as they were computed according to Eq. (6.37) and compared against numerical results based on MC simulations. Furthermore, the well known effect of widening instability boundaries in parametrically excited stochastic systems with increasing noise is clearly observed, as well as the stabilization of regions of lower values of λ. There is a good agreement between the analytical and numerical predictions given the approximate character of stochastic averaging and the approximation adopted for the mean value of A_1. Additionally, it could be shown that the solutions in Eq. (6.37) acquire a positive value only for $\Delta > 0$ (see Fig. 6.13(a)), meaning that the instability region is still constrained in the positive Δ semi-plane, for as long as the noise intensity is lower than the critical (Fig. 6.13(b)), crossing the resonance axis for higher noise (Fig. 6.13(c)).

Further on, in Sec. 6.2.3 the stability conditions were derived only for considering

(a)

(b)

(c)
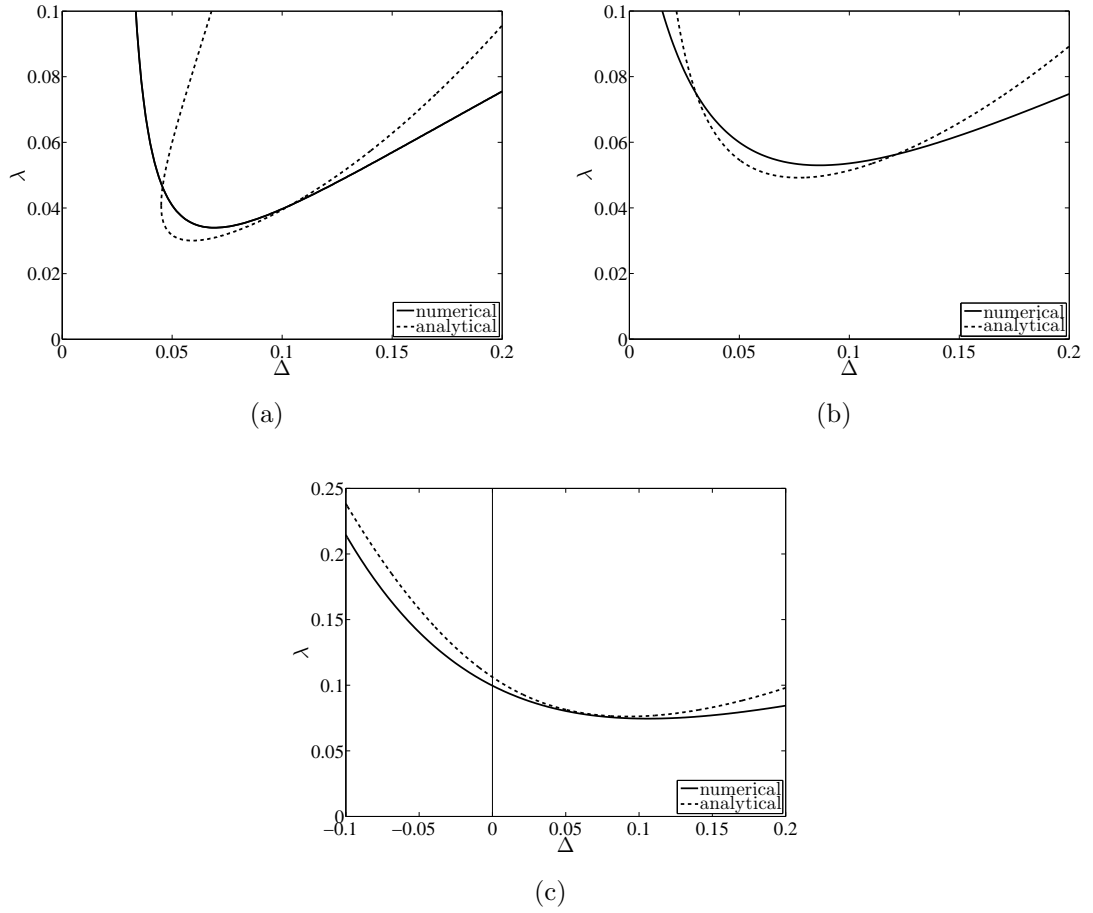
Figure 6.13: Stability boundaries for $\gamma = 0.0$, $\beta = 0.005$, $\alpha = 0.1$, $h^* = 0.0$ and increasing noise intensity of the excitation, conditioned by the Routh-Hurwitz criterion upon Eq. (6.36) $(- - -)$ and compared against numerical results (———); (a) $\sigma^2 = 14\beta$; (b) $\sigma^2 = 32\beta$; (c) $\sigma^2 = 60\beta$.

zero-valued α and β in turn. In order to acquire a full understanding of the offset vibro-impact system, numerical calculation of the instability regions is performed to estimate the validity of the previous approximate analytical results. Fig. 6.14 depicts a comparison of the system impacting at the equilibrium ($h = 0$) with the case of an offset equal to $h = 0.1$ with damping added to the primary system for numerical purposes. It could be seen that the observations from the analytical curves that described the influence of a displaced barrier are confirmed by numerical simulations. Note that the numerical results were based on MC simulations and a thereafter fitting of the boundaries. It is observed that shifting the barrier into a non-zero position unveils a similar effect on the boundaries as when one of the damping coefficients was set to zero. The anticlockwise rotation of the boundaries is therefore linked to vibro-impacting motion of the base onto an offset barrier.
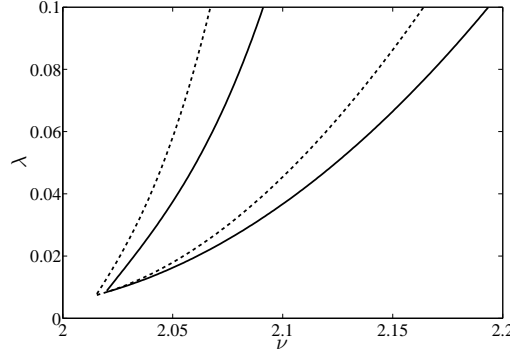
Figure 6.14: Stability boundaries for deterministic excitation and $\gamma = 0.0$, $\beta = 0.005$, $\alpha = 0.1$ calculated numerically for $h^* = 0$ (solid line) and $h^* = 0.1$ (dashed line).

6.3.2 The $\gamma \neq 0$ case

As soon as the influence of the motion of the linearized pendulum onto the response of the primary mass is taken into account, one could rely on a numerical approach for the stability of the autoparametric vibro-impact system. In that case, γ, and therefore a_4, are considered to be non-zero and the dynamics of the system are now described by Eq. (6.5), where the applied transformation ensures a continuous response as long as a purely elastic impact ($r = 1$) is considered.

According to the Lyapunov exponent analysis, a positive value for Λ infers unstable response. The numerical implementation is based on extending the work by Wolf [191] to MC samples totaling up to 100,000 mean excitation periods for each point in the parameter space. In [191], the calculation of the LLE is based on applying a small perturbation $\epsilon \ll 1$ to the system and observing the thereafter response. The value of the LLE is extracted by calculating the rate of convergence or divergence of the perturbed system to the unperturbed one, after a preset amount of time steps. Later on, the perturbation is periodically reapplied and the steady-state rate is calculated. The analyses were performed for a discretization of the parameter space by $d\nu$, $d\lambda = 0.05$ and a range $\nu = [1.5, 3.5]$ and $\lambda = [0, 3]$. However, only the range of interest where the instability boundaries can be found is presented.

Fig. 6.15 shows the numerical results for the deterministic case and two values of γ. First the effect of increasing h^* of shifting the instability region towards the $\Delta = 0$ axis is re-observed in Fig. 6.15(a) for the large scale λ as well. The offset barrier

(a) (b)
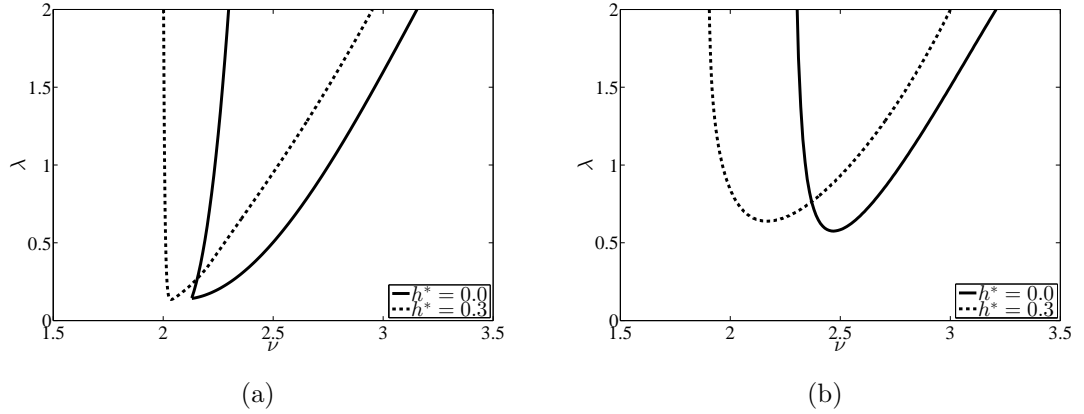
Figure 6.15: Numerically calculated instability boundaries of the deterministic autoparametric system impacting with $h^* = 0$ (———) and $h^* = 0.3$ ($---$), for $\beta = 0.005$, $\alpha = 0.1$ and (a) $\gamma = 0.0$; (b) $\gamma = 0.3$;

can be also seen to have a significant influence on the interacting system too in Fig. 6.15(b) with $\gamma = 0.3$. Moreover, a stabilization of the lower λ points appears with increasing γ, with the instability also covering a wider space than before. In some sense, inducing interaction of the primary system with the parametric one results in an effect similar to the one caused by noise.

Fig. 6.16 shows the instability boundaries extracted with the aforementioned procedure after an appropriate fitting of the results was applied. A total of three different values of γ, h^* and two noise intensities are shown. Figs 6.16(a) and 6.16(b) depict the case of $\gamma = 0.0$ to be used for direct comparison with Figs 6.16(c) and 6.16(d) and Figs 6.16(e) and 6.16(f) with $\gamma = 0.15$ and $\gamma = 0.3$ respectively. The boundaries shown in the left column were extracted for noise intensity $\sigma^2 = 0.1$ and the ones in the right column for $\sigma^2 = 0.3$. Moreover, the damping coefficients were $\alpha = 0.1$, $\beta = 0.005$ and thus the LHS figures would fall into $\sigma < \sigma_{crit}$ subcategory, while the RHS into $\sigma > \sigma_{crit}$. Note that the primary resonance could not be separated by the latter ones since the range of this investigation started at $\nu = 1.5$. The widening effect of noise also drives different parametric resonance zones to merge at lower λ's.

First, it could be seen that the coupling of the two subsystems through γ incurs a stabilization effect of the region of relatively low λ and close to resonance ($\nu = 2$), with minimally influencing the higher λ regions. Yet, increasing γ has no further
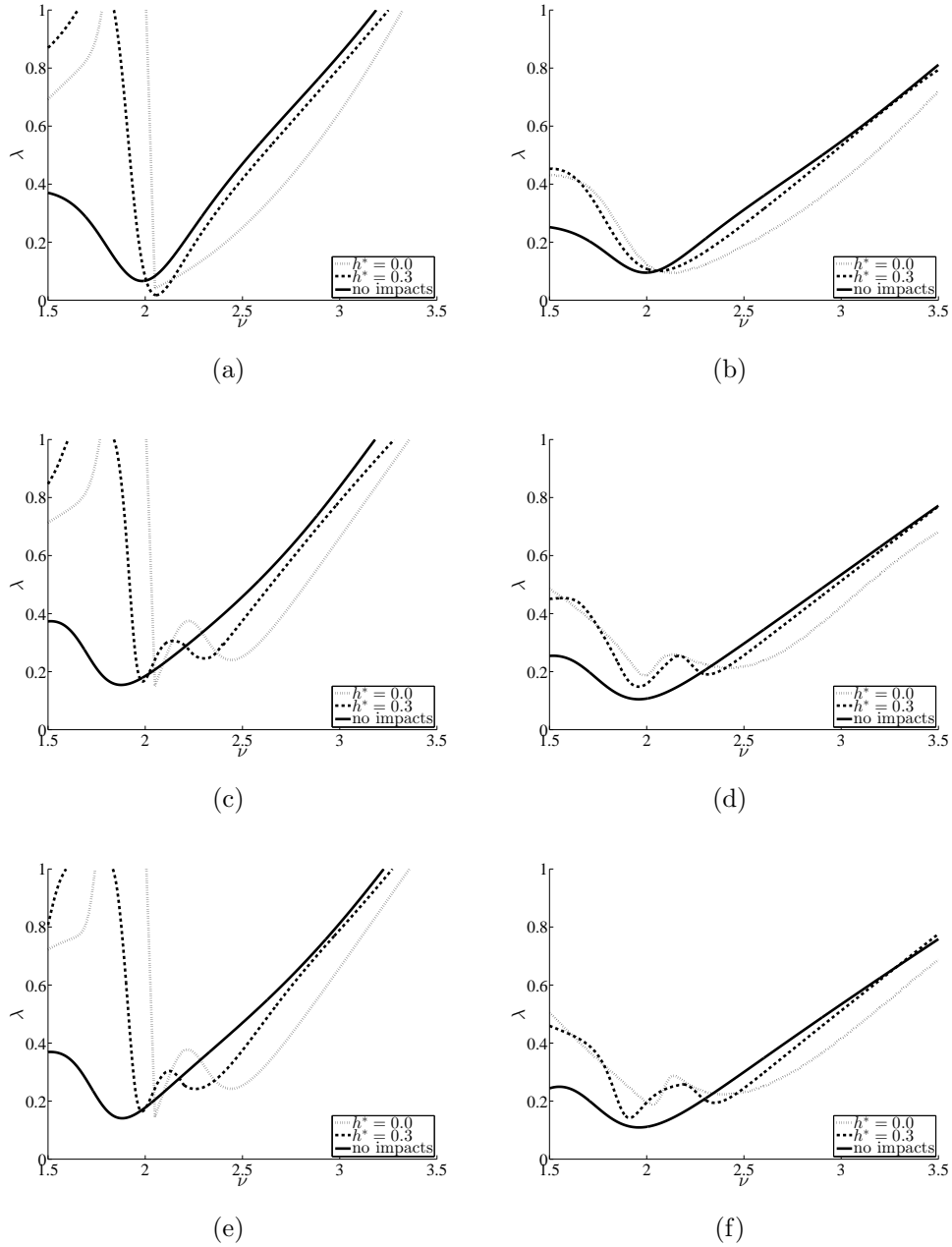
Figure 6.16: Instability boundaries of the impacting system in Eq. (6.5) with different h^*, calculated through MC-based LLEs for $\alpha = 0.1$, $\beta = 0.005$ and (a) $\sigma^2 = 0.1$, $\gamma = 0.0$; (b) $\sigma^2 = 0.3$, $\gamma = 0.0$; (c) $\sigma^2 = 0.1$, $\gamma = 0.15$; (d) $\sigma^2 = 0.3$, $\gamma = 0.15$; (e) $\sigma^2 = 0.1$, $\gamma = 0.30$; (f) $\sigma^2 = 0.3$, $\gamma = 0.30$,

effect as could be seen by comparing Fig. 6.16(c) with Fig. 6.16(e) or Fig. 6.16(d) with Fig. 6.16(f). Additionally, one could notice the anticlockwise rotation of the boundaries with increasing h^*, which appears to be less significant as soon as higher noise intensity is considered (LHS figures against RHS).

6.3.3 Inelastic impacts ($r < 1$)

From the moment that the energy losses caused by the impacts cannot be ignored, the restitution coefficient gets the values $r < 1$. That though makes the velocity discontinuous and thus the analytical development shown previously is rather troublesome. Instead, a numerical approach is adopted to derive the stability boundaries again based on the LLE analysis as in Sec. 6.3.2. However, it is not the Wolf algorithm [191] that is utilized herein. Instead, a procedure due to Wedig [74] is followed, to exploit its simplicity. Moreover, in order to avoid the complexity of the response $\gamma = 0$ is assumed. Note also that Eq. (6.9) is derived based on a purely elastic impact ($r = 1$). In order to incorporate the energy losses due to impacts, the restitution coefficient r will be expressed through the damping coefficient. Since the motion between impacts is considered to have small losses as a requirement to apply the stochastic averaging, the dissipation of energy at the moment of impacts could be distributed into the whole period of the motion [202]. Thus, an equivalent viscous damping coefficient will be used, incorporating r as:

$$\alpha_{eq} = \alpha + \frac{\Omega_1}{\pi} \frac{1 - r^2}{1 + r^2} \tag{6.40}$$

Moving on, the expression used to evaluate the LLE follows Eq. (3.68), after defining $s = \log(A_2)$ and considering from Eq. (6.29) that:

$$\dot{s} = \dot{A}_2/A_2 = -\beta + a_3 A_1 \sin(2\psi) \tag{6.41}$$

Taking the expectation operator on both sides of Eq. (6.41) and exploiting the
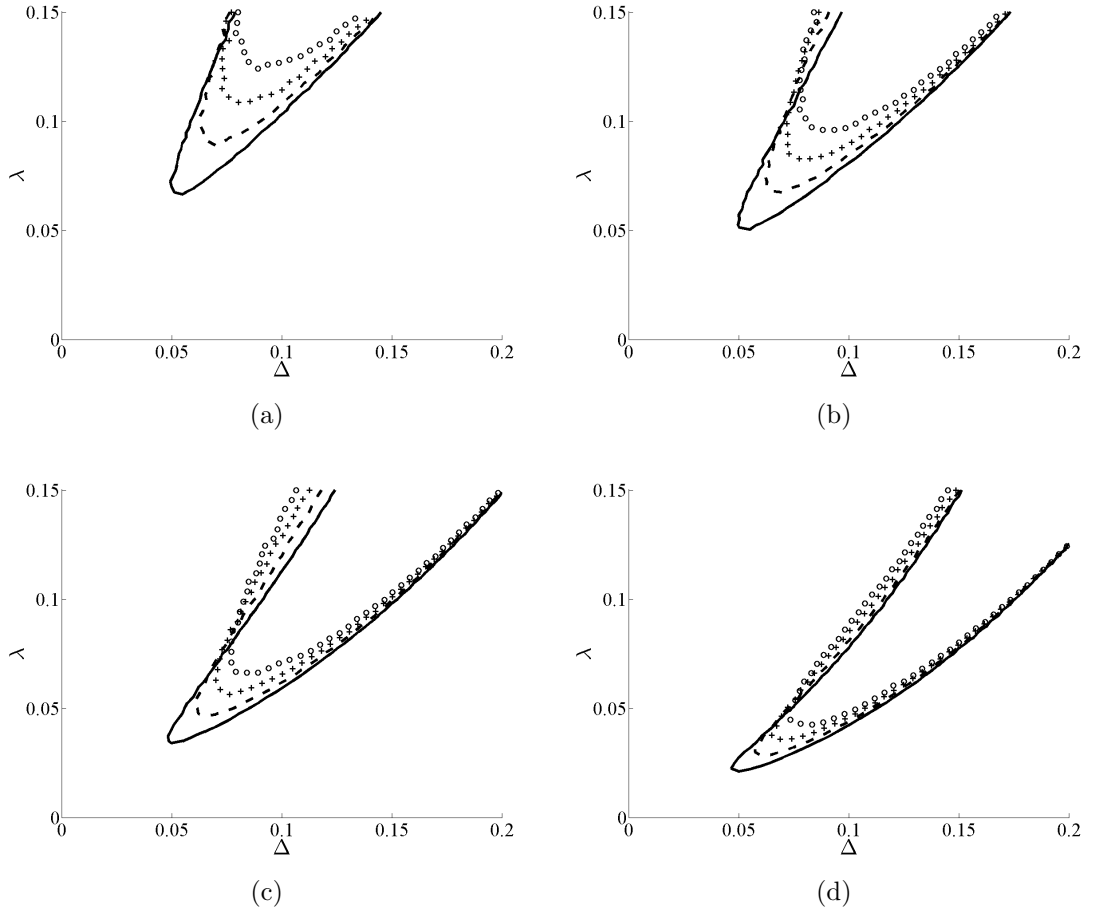
Figure 6.17: LLE based on Eq. (6.43) through MC simulations (50 repetitions) for $\alpha = 0.1$, $\beta = 0.005$; $D = 0.025$ (——); $D = 0.050$ ($---$); $D = 0.075$ (+); $D = 0.100$ ($\circ$) and (a) $r = 0.4$; (b) $r = 0.6$; (c) $r = 0.8$; (d) $r = 1.0$, with r expressed through Eq. (6.40).

interchange property of the expectation with the differentiation, one arrives at:

$$\frac{d}{dt} < \log A> = <-\beta + a_3 A_1 \sin(2\psi)> \qquad (6.42)$$

Thus, the LLE is found as:

$$\Lambda = -\beta + a_3 <A_1 \sin(2\psi)>, \ t \rightarrow \infty \qquad (6.43)$$

The last Eq. (6.43) is used in the MC simulations of Eq. (6.9) to calculate the LLE and numerically construct the stability boundaries. Fig. 6.17 shows the numerically calculated stability-instability boundaries for the linearized autoparametric
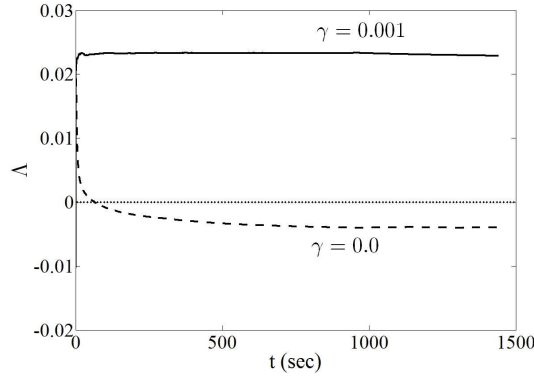
Figure 6.18: Evolution of LLE for $\Delta = 0.18$, $\lambda = 0.18$, $r = 1.0$, $\alpha = 0.1$, $\beta = 0.005$, $D = 0.05$ and $\gamma = 0.0$ (———); $\gamma = 0.001$ ($- - -$).

pendulum for different noise intensities and restitution coefficients incorporated as in Eq. (6.40).

It could be seen that increasing noise lifts the lowest unstable point upwards. With respect to the analytical approximate boundaries shown in Fig. 6.7, the corresponding numerical results are shown in Fig. 6.17(d). It could be noticed that the general shape of the unstable region as well as its evolution with increasing noise match in both figures. Yet, increasing noise induces a significant error in the analytical and numerical estimations, eg for $D = 0.1$, with lower noise values (see the $D = 0.025$ curves) presenting themselves with a very good agreement in both approaches. This effect could be attributed to the necessary approximations that were applied in order for the analytical results to be expressed in the (Δ, λ) space.

Moreover, decreasing the restitution coefficient has a more or less expected effect of pushing the boundaries upwards to higher λ values. As soon as lower r means higher energy losses due to impacts the last observation is reasonable. Besides that though, the instability regions slightly rotates anti-clockwise, an effect which is not as clear as in higher order stability analysis. One could also verify through the numerical analysis the existence of the instability region only on the positive Δ semi-axis, as implied by Eq. (6.33).

The analysis of the stability of the response becomes more complicated as soon as the interaction between the pendulum and the primary mass is taken into consideration. Previous studies have shown a stabilization of the response of the full nonlinear

pendulum equations [193]. Here, since the stochastic averaging technique assumes the excitation parameters to be small, this effect is more rapid. Indicatively, the time evolution of the LLE is presented in Fig. 6.18 for a single point of the parameter space when only a weak interaction ($\gamma = 0.001$) is considered. Even though the point lies in the middle of the instability region, as shown in Fig. 6.17(d) for $\gamma = 0.0$, it is found that even this weak interaction results in negative LLE, stabilizing the response.

6.4 Summary

The fundamental question of the stability of the hanging-down equilibrium of a simple lumped mass pendulum has been addressed in this chapter. The contemporary challenge in this analysis was the introduction of a unilateral rigid barrier, against which, the primary system of an autoparametric 2DOF system would impact. The stability analysis, both in the mean and in the mean-square sense, have brought about a radical relocation of the stability boundaries in the forcing parameters space. In particular, it is known that the unstable region of the linearized pendulum under harmonic excitation, described by the Mathieu equation, is symmetrical around the resonance ($\Delta = 0$). As soon as the impacting condition is introduced at the primary system's equilibrium ($h^* = 0$), approximate analytical development revealed that the unstable regions are confined in the positive Δ half space, with the distance from the axes zeros controlled by the values of the damping coefficient and the noise intensity. The critical value of the latter, for which the boundaries asymptotically approach the resonance axis, has been calculated, reflecting the diffusing effect of randomness that leads to wider unstable regions.

Besides this major overall conclusion, the particular influence of important parameters was examined, though both analytical and numerical results. First, the position of the barrier affects the shape of the stability boundaries. The further away from the equilibrium, the more that the boundaries approach the shape of the impacts-free unstable region, with the limiting value being $h^* = 1$ where the boundaries would be symmetrical again. In addition, the restitution coefficient of the impacts

acts in a similar manner with damping. For $r < 1$, the system bounces back with lower velocity than when impacts are perfectly elastic, indicating an instantaneous dissipation of the primary system's energy. Thus, there is a reasonable upwards shift of the boundaries for inelastic impacts. Last, the interaction between the pendulum and the primary system has been seen to incur stabilization of the lower λ region.

This development contributes to the practical design of an autoparametric pendulum system with a deeper insight on the influence of impacts on the manifestation of parametric resonance. Within the context of offshore structures and mechanical devices (e.g. WECs), the random changes of the sea state necessitate the precaution of positioning limiters about a floater, in order to avoid excessive vibrations that could jeopardize the integrity and the functionality of the floating system. Moreover, there is another class of offshore floating devices that need to be anchored to the seabed. In both cases, extremely high waves would force the floating systems to vibro-impacting motion, either by directly hitting against the limiters or due to stretching of the anchor chain. Regardless of whether the instability of the equilibrium is desired or to be avoided, the analysis presented in this chapter allows for a more accurate design of floating systems, through the examination of influential parameters and especially, connecting the unstable regions with positive detuning.

Chapter 7

Experiments on a novel design

In the previous Chapters 4-6, the centre of attention was the primary objective of the present thesis, i.e. investigating the potential of rotational response of a floating pendulum under stochastic generic and specialized conditions. Forasmuch as the behaviour of the stochastically excited pendulum has been understood, the next step is to consider the technological limitations imposed on the development of the WEC discussed herein by the nature of the physical resource, consisting the secondary objective of this thesis. Towards that, a specialized design is proposed to substitute the simple lumped mass pendulum. The advantages of this design are discussed in the first part of this Chapter (Secs 7.1–7.3), with experimental investigation following thereafter.

7.1 A challenge to overcome

The mathematical pendulum - a lumped mass oscillating on an unstretchable massless string, is an important system in studying the theory of vibrations. This fruitful example introduces us to a sinus type nonlinearity and things related to nonlinear systems, such as dependence of the pendulum's period on its amplitude, stability. Since it is difficult to deal with the nonlinear equation of motion, most often this equation is linearized around its lower equilibrium point. Then, the squared natural frequency of the system is proportional to the acceleration of gravity and inversely

proportional to the pendulum's length. As has been discussed earlier, it has been proposed to exploit the heaving motion of waves as the source of parametric excitation of a floating structure bearing a pendulum. The potential of rotational motion even in the stochastic framework placed in the oceans, which has been investigated in this thesis, sets a rather prosperous field for the development of a WEC.

Unfortunately, this idea could not be implemented so far due to a significant drawback, related to the size of the system. The rotational response of the pendulum originates from a saddle-node bifurcation and a period-doubling cascade, which could be found to occur for relatively low amplitudes around the primary parametric resonance. It is also within this region where robust rotational response could be found to dwell in a rather broad range of the excitation parameters (see Figs 2.16 and 2.17). Recall that the ocean waves have a frequency of about $f_e = 0.1$Hz or $\pi/5$ rad/sec [15] - see also Sec. 3.2.1. For the primary parametric resonance, the excitation frequency should be around twice as much as the natural frequency of the system $f_e = 2f_0$. This leads to the following expression for the pendulum's length:

$$l = \frac{g}{\Omega^2} = \frac{g}{4\pi^2 f_0^2} = \frac{g}{\pi^2 f_e^2} \approx 100m \tag{7.1}$$

where g - acceleration due to gravity and Ω - the natural frequency of the simple pendulum.

Thus, the length of the pendulum should be around $10m$ to get a frequency of about 1 rad/sec, and it must be around $100m$ long to lower the frequency to 0.316 rad/sec. Obviously, such a bulky device is difficult to build and operate. The only well known example of such a long pendulum (67 meters) is related to Foucault, who built it in 1851 to demonstrate the rotation of the Earth. Yet, the numerical simulations conducted by Xu et al. [7] for the deterministic system in Eq. (4.4), as well as the analysis of the stochastic system presented in Chapters 4 and 5 of the present thesis, revealed that the rotational motion of the pendulum in its mathematical description is possible for values of $\lambda > 1$. Ergo, a technological novelty is required, to materialize the mathematical potential.

Instead of a simple pendulum, a physical or else compound pendulum, which natural frequency depends on the distance to its center of gravity and the moment of inertia, may be used to achieve any frequency, since its natural frequency does not depend only on the distance to the centre of gravity. In fact, the natural frequency is defined by the relation between the first and the second order static moments of the pendulum. Unfortunately, in practice it is not that easy to achieve low frequency due to physical tolerance and other constrains, dictated by a specific application. For instance, if one uses a disk of radius R, so that its moment of inertia with respect to its center is $mR^2/2$, which is pinned at a slightly shifted distance h from its center of gravity, then the natural frequency of this system may be expressed as:

$$\omega_n = \sqrt{\frac{gh}{R^2/2 + h^2}} \qquad (7.2)$$

The same natural frequency of 0.316 rad/sec can be reached with a relatively small pendulum of $R = 1m$ and $h = 5.1 \times 10^{-3}m = 5mm$, or $R = 0.5$ m and $h = 1.27 \times 10^{-3}m = 1.27mm$. It is easy to see that it is extremely difficult to achieve such an accuracy, since the pin's diameter d_p may have to be significantly bigger than h in order to hold the structure. Assuming that one could achieve this accuracy and tolerance in practice, it is impossible to adjust the natural frequency and torque, if needed, since they are connected with each other and the only value, which can be adjusted is h. Thus, a physical pendulum with given R leaves no options to develop a system with prescribed frequency and torque, which is required in some applications. It may be confirmed that other cross sections, such as rectangular or square, make the design even worse in terms of the achievable low frequency.

The discussed shortcoming can be overcome using the design of the tri-pendulum, a sketch of which is shown in Fig. 7.1. The main idea is that, from the point of view of the dynamics of a SDOF nonlinear system, the kinematic response of the parametric simple pendulum in the state space would be identical with the tri-pendulum's provided that the natural frequency of the simple pendulum would be equal to the tri-pendulum's, i.e. $\Omega = \Omega_{eq}$, as it can be seen from Eq. (7.4). The major difference is that for a simple pendulum an unfeasible size would be required,

while a trivially-sized design of the tri-pendulum could match the requirements as it will be demonstrated in Sec. 7.2. Moreover, the more general N-pendulum is proven to be much more suitable for the particular application, since it allows not only rendering the natural frequency of the pendulum independent of its length, but also adjusting the frequency and torque of the system independently. The latter is especially important in developing a wave power take-off device.

Although only strictly rectilinear motion of the buoy is considered herein, in general the motion may be more complex, incorporating planar deviations from the vertical position (pitch angle) due to incoming and outgoing waves [106, 107, 110].
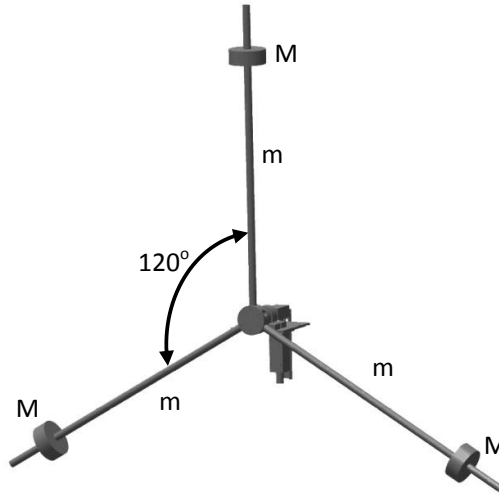
Figure 7.1: Sketch of the proposed horizontal axis PTO

Furthermore, it should be stressed that the current design opens a wide range of possibilities, including capturing large waves and adjusting to a wave frequency by moving the carried masses along the arms, using a threaded rod for instance. From here on, the rods that are connected to the central pivot point and carry the masses M, will be refered to as the arms of the design.

7.2   The N-pendulum

Lets introduce an N-pendulum - a system of N pendulums rigidly connected to a common ring, positioned at equally spaced intervals of $2\pi/N$, so that the bi-pendulum and tri-pendulum will have two and three arms of equal masses m cor-

respondingly. Although it is possible to create a pendulum with not-equally-spaced arms, such a design is not considered herein. All arms except one carry a lumped mass M, positioned at distance L_2 whereas the last arm carries the same mass at distance L_1, so that $L_1 > L_2$. The cases of even and odd number of arms could be considered separately.

The simplest example of an odd number of arms is the tri-pendulum, which is illustrated in Fig. 7.1. For the tri-pendulum the arms will be positioned at equally spaced intervals of 120° so that the equation of free motion may be written as:

$$\left[3ml^2 + M(L_1^2 + 2L_2^2)\right]\ddot{\theta} =$$
$$= -MgL_1\sin\theta - MgL_2\sin\left(\frac{2\pi}{3} + \theta\right) + \qquad (7.3)$$
$$+ MgL_2\sin\left(\frac{2\pi}{3} - \theta\right)$$

It should be noted that there is no restoring force from the equidistant arms themselves, since they have equal masses and shapes, therefore they are in equilibrium. Then Eq. (7.3) after some simplifications will reduce to:

$$\ddot{\theta} + \Omega_{eq}^2\sin\theta = 0$$
$$\Omega_{eq}^2 = Mg\frac{(L_1 - L_2)}{[3ml^2 + M(L_1^2 + 2L_2^2)]} = \frac{g}{L_2}\frac{\gamma - 1}{3\psi + \gamma^2 + 2} \qquad (7.4)$$
$$\psi = \frac{ml^2}{ML_2^2}, \gamma = \frac{L_1}{L_2} > 1$$

If $M >> m$ the first term in the denominator ψ can be neglected. Eq. (7.4) indicates that the natural frequency of the system depends on the difference between L_1 and L_2 only. Figs 7.2(a) and 7.2(b) show the equivalent natural frequencies (in Hz) of the system for $L_2 = 1$m, $L_2 = 3$m and $L_2 = 5$m for the case of $M >> m$, so that $\psi = 0$. It can be seen from Fig. 7.2(a) that some desired natural frequencies may be achieved by two different configurations for a given value of L_2, one of which corresponds to a relatively large value of the arm's length L_1 (large values of γ). Moreover, the same frequency may be achieved for different values of L_1 and L_2; however, there is an upper boundary on the frequency which can be achieved by
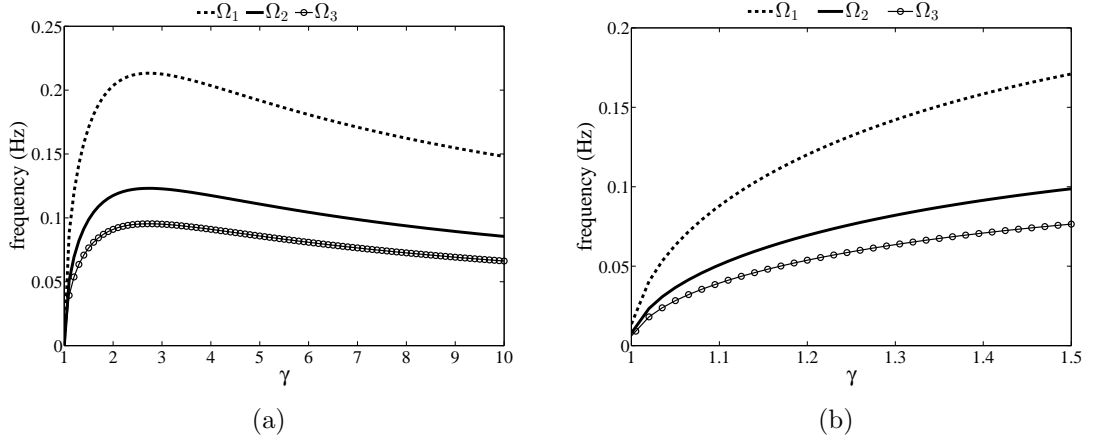
Figure 7.2: (a) Equivalent frequency of the tri-pendulum given by Eq. (7.4) in Hz: $\Omega_1 - L_2 = 1$m, $\Omega_2 - L_2 = 3$m, $\Omega_3 - L_2 = 5$m; (b) Zoom in of Fig. 7.2(a).

each pendulum size. Namely, the larger the distance L_2, the lower the maximum frequency it can reach. Thus, the desired frequency equal to 0.316 rad/sec can be achieved by different layouts.

At this point one can generalize the model to any odd number of equally spaced arms. The equation of motion of such a system may be written as:

$$\left[Nml^2 + M(L_1^2 + (N-1)L_2^2) \right] \ddot{\theta} =$$
$$= -MgL_1 \sin\theta + MgL_2 \sum_{i=1,2,3,}^{(N-1)/2} \left\{ \sin\left(\frac{2i\pi}{N} - \theta \right) - \right.$$
$$\left. - \sin\left(\frac{2i\pi}{N} + \theta \right) \right\}, \tag{7.5}$$
$$N = 1, 3, 5, 7, \ldots$$

After simplification once again, one arrives to the well-known pendulum equation - Eq. (7.3), with the following expression for the natural frequency:

$$\Omega_{eqF}^2 = Mg \frac{L_1 - L_2}{\left[Nml^2 + M(L_1^2 + (N-1)L_2^2) \right]} =$$
$$= \frac{g}{L_2} \frac{\gamma - 1}{N\psi + \gamma^2 + N - 1} \tag{7.6}$$

The even number of arms is much easier to analyse since the contribution to the restoring force will come only from two arms located opposite to each other (at
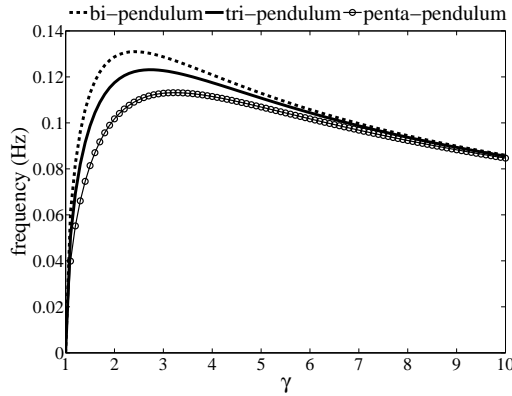
Figure 7.3: Equivalent natural frequency, Ω_{eq} of the N-pendulum with 2, 3 and 5 arms correspondingly for $L_2 = 3m$.

180°), one of length L_1 and the other L_2. Thus Eq. (7.6) for the equivalent natural frequency is valid for odd as well as even number of equally spaced arms. Fig. 7.3 shows the variation of Ω_{eq} for a different number of arms (two, three and five), the same value of $L_2 = 3$m and for the case of $M >> m$. As expected, the more arms the system has, the less the maximum frequency it may achieve.

It should be stressed that such a design is very easy to calibrate and it is not sensitive to small descrepancies of the arms during the manufacturing process, since moving the carried masses to a proper distance $\bar{L}_1$ would eliminate them.

7.3 Natural frequency & inertia

7.3.1 Unconstrained lengths

One might consider even more flexible configurations of the design regarding the arms' length and the carried masses. To that end, let us first consider the case of a tri-pendulum of equal lumped masses M as introduced before, only that the arms' lengths are not constrained by $L_2 = L_3$, leading to the more generic $L_1 \neq L_2 \neq L_3$. In the following, the length of the arms will be non-dimensionalised with respect to the length of the shortest arm. Since this is a parametric study, in each case presented one arm will be assumed as being the shortest and the others will be normalized with respect to it. This is a useful manipulation, because as it can be seen in Figs 7.2(a) and 7.2(b) the resulting natural frequency is not the same for

different sizes of the tri-pendulum, an indicator of which is the shortest arm's length. Then, correspondingly to the previous definitions, let $\gamma_2 = L_2/L_1$ and $\gamma_3 = L_3/L_1$. Following similar manipulations as for Eq. (7.4) and considering again the arms' masses negligible, one would end up with:

$$\Omega_{eq}^2 = \frac{g\sqrt{\left(1 - \dfrac{\gamma_2 + \gamma_3}{2}\right)^2 + 0.75(\gamma_2 - \gamma_3)^2}}{L_1(1 + \gamma_2^2 + \gamma_3^2)} \tag{7.7}$$

$$I = ML_1^2\left(1 + \gamma_2^2 + \gamma_3^2\right)$$

where I is the inertia of the rotating parts.

Fig. 7.4(a) shows a contour plot of the equivalent natural frequency of the tri-pendulum with respect to what is considered to be the shortest arm's length, i.e. $\Omega\sqrt{L_1}$. It can be seen that the desired frequency range, around $0.314rad/s$, could become easily achievable by regulating L_1 at values such as 2 or 3m, which are reasonably low from a structural point of view. However, another aspect for consideration would be the inertia of the rotating device and that is due to the fact that the bigger the inertia of the rotating parts, the bigger the generator it could drive. Thus, whereas the manufacturing and maintenance processes favor an as small as possible size, energy production would benefit from larger sizes. In Figs 7.4(b)-7.4(d), the normalised inertia of the rotating system over the mass M of the lumped masses is presented for different values of $L_1 = 1, 3, 5m$. Along that, the target-frequency is plotted ($\Omega = 0.3rad/sec$) so as to attach the inertia values that could be achieved with such a design to the desired frequency.

Obviously, the inertia of the rotor is proportional to the squared length of the arms so its value is increasing to the upper right of each figure. Let us now discuss the impact of the inertia on the potentially produced energy. A main advantage of the proposed concept is the straightforward PTO system where a conventional generator is to be attached directly to the shaft of the rotor. This is important in a sense that no intermediate system is required for transforming the wave power into electrical other than a coupling and a gearbox in contrast with existing WEC technologies
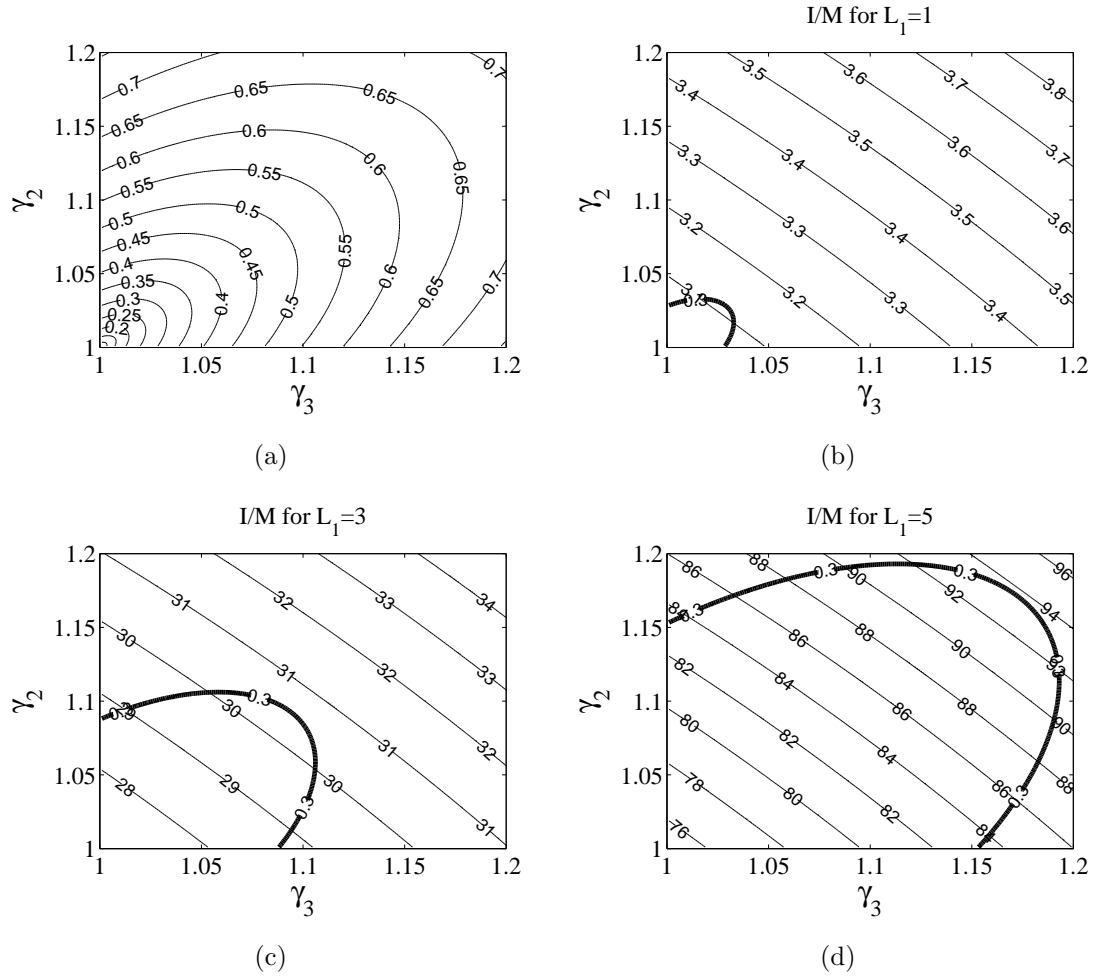
Figure 7.4: (a) Natural frequency of the tripendulum with $L_1 \neq L_2 \neq L_3$ and $M_i = M$ with respect to the shortest length, $\Omega\sqrt{L_1}$, against $\gamma_2 = L_2/L_1$ and $\gamma_3 = L_3/L_1$; Normalised inertia I/M for: (b) $L_1 = 1m$, (c) $L_1 = 3m$, (d) $L_1 = 5m$.

where it is rather common for hydraulic systems, linear generators or turbines to be used for ultimately producing electricity. Having the generator driven directly by the rotor's shaft would definitely decrease the complexity of the WEC. In that case, the generator would add in Eq. (7.3) a resisting torque which would be normalized by the rotor's inertia. So, the bigger the inertia that is excited by the waves, the bigger the generator that could be run.

7.3.2 Uneven masses

Moving forward, let us now consider again a tri-pendulum where for the arms' lengths it holds $L_1 > L_2 = L_3$ as before, but now the corresponding relation holds for the lumped masses as well, i.e. $M_1 > M_2 = M_3$. Again, we define $\gamma = L_1/L_2$

and we introduce $n = M_1/M_2$. The natural frequency and the system's inertia in this case could be expressed by the following:

$$\Omega_{eq}^2 = \frac{g\,(n\gamma - 1)}{L_2\,(n\gamma^2 + 2)}$$

$$I = M_2 L_2^2\,(n\gamma^2 + 2) \tag{7.8}$$

Fig. 7.5 presents the values for the normalised frequency and inertia against γ and n in the same manner as in Fig. 7.4. The natural frequency with respect to the shortest length which is now assumed to be L_2, $\Omega\sqrt{L_2}$, is plotted in Fig. 7.5(a). The desired application-oriented frequency range is again achievable for reasonable values of L_2, fulfilling the structural requirements discussed previously. The rest of the plots, Figs 7.5(b)-7.5(d), depict the variation of the normalised system inertia, I/M_2, along a short range of the parameters for different length values, $L_2 = 1, 3, 5m$. The range of the inertia is seen to be similar with the previous case however the frequency follows rather linear isolines which slightly changes the possible matches of the targeted frequency with the system's inertia.

Closing this section, two remarks could be made upon the behaviour of the frequency with respect to the given parameters. First, from both Figs 7.4(a) and 7.5(a) it is noticed that for bigger values of the shortest arm's length, the required ratios to achieve the same frequency increase as well. This means that the length increase is not proportional in between the arms and rather extreme values would be required if the shortest arm is heavily lengthened. Secondly, these extreme values could well enough introduce impulse-like excitations of the pivot which would result in undesirable response of the rotor, let alone the thereafter structural concerns. In the same manner, it is fortunate that the sought frequency range is achievable for $n, \gamma, \gamma_2, \gamma_3$ ratio values close to 1 and thus extreme phenomena are avoided.

Performing a rough estimation of the mechanical power harvested from ocean waves by use of the tri-pendulum, consider the design as described last with $n = M_1/M_2$ and $\gamma = L_1/L_2$ and suppose $M_2 = 500kg$ and $L_2 = 5m$. That would direct us to Fig. 7.5(d). In order to approach the necessary natural frequency one would
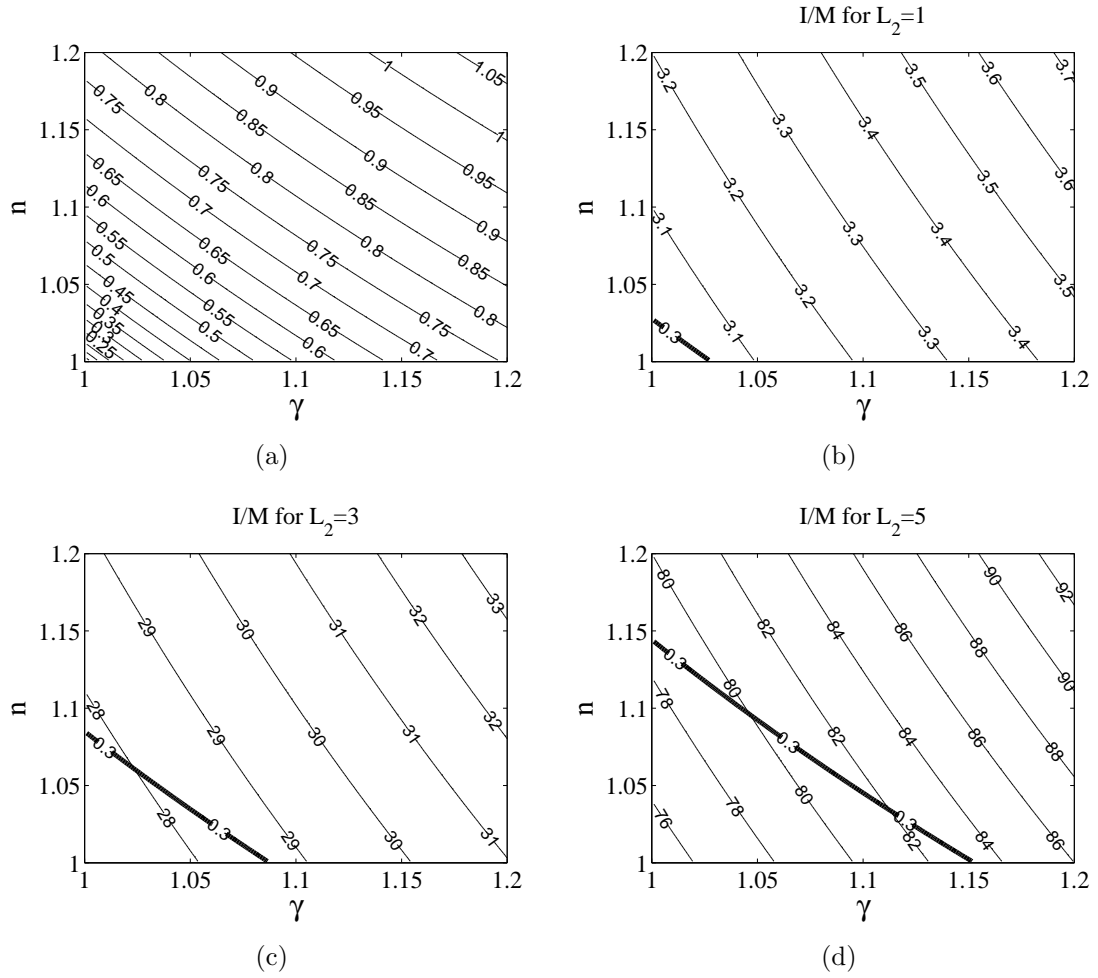
Figure 7.5: (a) Natural frequency of the tripendulum with $L_1 > L_2 = L_3$ and $M_1 > M_2 = M_3$ with respect to the shortest length, $\Omega\sqrt{L_2}$, against $\gamma = L_1/L_2$ and $n = M_1/M_2$; Normalised inertia, I/M_2 for: (b) $L_2 = 1m$, (c) $L_2 = 3m$, (d) $L_2 = 5m$.

have to choose $n, \gamma \approx 1.1$ leading to $I/M_2 \approx 83m^{-2}$. Taking into account that the mechanical power of the rotor could be expressed as $P = I\ddot{\theta}\dot{\theta}$ and considering a period-1 rotational point of the parameters (ν, λ), then the average power extracted by the heaving motion of waves and transformed to mechanical power of the rotor would be around 4kW.

Scaling up the device for practical applications shows that it is possible to achieve much higher inertia values (see Fig. 7.6) therefore leading to greater power generation, however in this case one mass should be several times larger than the others and should be positioned far away from them, an extreme case of $n = 10, \gamma = 10$ shown in Fig. 7.6 being an example. In this configuration the desired natural frequency would be achieved only by applying unrealistic sizes due to the constrain
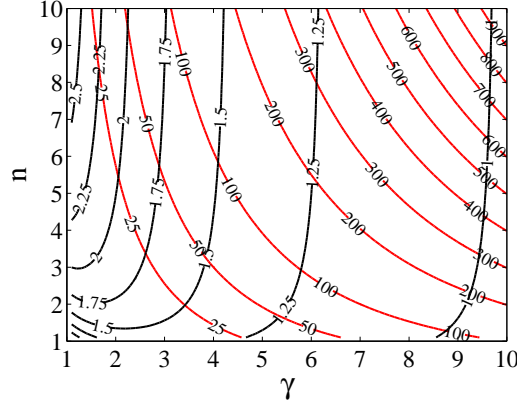
Figure 7.6: Parametrised natural frequency, $\Omega\sqrt{L_2}$, (black solid line) and inertia, $I/(M_2 L_2^2)$, (red solid line) against large range of $\gamma = L_1/L_2$ and $n = M_1/M_2$.

imposed by the frequency of the waves. This fact clearly states that in the scaling process the tri-pendulum tends to a structure of a regular pendulum.

7.4 Experimental setup

Parametric excitation of a pendulum has attracted significant interest of the scientific community regarding the stability boundaries, chaotic attractors and the bifurcations that have been observed. It is only reasonable that experimental investigation has been part of the ongoing research with the scope varying from identification of the chaotic attractors [8, 93] to the bifurcations occurring in an inverted pendulum [161] or even a double pendulum [162]. In the context of developing a pendulum-based WEC, rotational response of a parametric pendulum driven by a shaker was sought [163] and a benchmark - proof of concept - experimental study was conducted in a wave tank [164, 166].

However, most of the previous experiments concentrated on considerably higher frequencies than those observed in ocean waves. In this section, the development of an experimental apparatus is discussed, aiming to demonstrate the functionality of a tri-pendulum regarding wave energy extraction, as it was introduced in the previous sections. The main distinction is that the exciting force is designed to simulate ocean waves by applying frequencies and amplitudes much closer to those occurring in nature. Note that in the following, a tri-pendulum with three lumped masses and

massless arms and shaft will be refered to as the idealized system to distinguish it from the physical one.

7.4.1 The model

The underlying idea consists of a system capable of achieving the natural frequency that is required to fall into the primary parametric resonance given the limitations of the natural resource in the ocean. It has been proposed in the previous sections of this Chapter, to adopt a design consisting of three arms equally spaced at 120°. The basic design refers to three equal masses distributed at the three arms. The frequency variations are realized by placing these masses at different distances and specifically, two of them at L_2 and the third one at $L_1 > L_2$. Of course, a much greater flexibility underlies by varying the masses that each arm carries as well as introducing three unequal distances. However, the experimental work is only concerned with the basic design, both in the presentation of the model and the experimental investigation. In the case of the basic design then, with the pivot vertically displaced by $f(t)$, the equation of motion reads:

$$(I_c + I_v)\ddot{\theta} + c\dot{\theta} + M(L_1 - L_2)\left[g + \ddot{f}(t)\right]\sin\theta = 0 \qquad (7.9)$$

with I_c being the constant inertia of the parts free to move in the angular space and I_v the configurable inertia. Also, c is the viscous damping coefficient modelling the energy losses, M the mass held by each arm and θ the angular displacement.

It is evident, that the natural frequency of Eq. (7.9) is mostly affected from the varying lengths L_1 and L_2 and indeed, by their difference. Thus, the achievable values of the natural frequency are decoupled by the length, contrary to the case of a simple pendulum [203]. One should note however, that the range of admitted values is not infinite but it is constrained by both I_c and I_v. Thus, given an excitation frequency ω, one could properly configure the tri-pendulum through L_1 and L_2 so that the parametric system would fall into the range of the primary resonance, and specifically in the corresponding rotational region. For the sake of an example, if the given $\omega = 1$ rad/sec, then a simple pendulum would need to extend to 39.24 m

Figure 7.7: Drawing of the full experimental rig.

in order to establish the primary resonance response at $\omega/\Omega = 2$, while one possible configuration of the idealized tri-pendulum is $L_1 = 0.52$ m and $L_2 = 0.5$ m.

Having raised then the potential usage of a tri-pendulum, the development of an experimental rig could be discussed. The main requirements could be condensed to the following: (a) vertical periodic motion of the tri-pendulum (Fig. 7.1) (b) amplitude and frequency of that considerably close to the realistic observations (c) capability of varying the frequency at will (d) recording of the angular response. The realization of this design would also need to comply with constrains on the total size imposed by the indoor infrastructure. A computer-based drawing of the experimental rig is shown in Fig. 7.7. First of all, the source of the vertical motion has to be chosen. A crank attached to a motor placed on the bottom of the rig will function as a reciprocal piston-like mechanism as to provide the vertical excitation to the tri-pendulum. A frame is required to support the tri-pendulum which is allowed though to move up and down through a roller-rail system with the latter rigidly attached to the frame. The design of the experiments targets an excitation amplitude of 0.5m at most. Furthermore, the radius of the tri-pendulum at test is designed at 1m. The circular motion of the crank of the motor is transduced to rectilinear through a connecting rod, connecting the edge of the crank to the pivot of the tri-pendulum. It is well known that the working point of that mechanism,

which could be also thought as the translation of the pendulum's pivot, will follow a sinusoidal profile augmented by superharmonic excitations depending on the ratio of the length of the connecting rod over the crank's. The acceleration of the pivot in this case can be fairly approximated by the following expression:

$$\ddot{x} = \omega^2 r \left(\cos \omega t + \frac{\cos 2\omega t}{j} \right) \tag{7.10}$$

where ω - the motor's speed in rad/sec, r - the crank's radius, $j = l/r$ - the size ratio and l - the length of the connecting rod. Obviously, in the limiting case of $j \to \infty$ the excitation reduces to a perfect sinusoidal as in Eq. (4.4). It is also seen that the speed of the motor defines the excitation frequency and the crank radius defines the amplitude. The response of a tri-pendulum carrying equal masses M and excited by Eq. (7.10) is analyzed by means of numerical analysis and PSPs are constructed describing the amount of the exhibited rotational motion. Then, the governing equation would be:

$$\theta'' + 2\beta\theta' + \left[1 + \lambda \left(\cos \nu\tau + \frac{\cos 2\nu\tau}{j} \right) \right] \sin \theta = 0 \tag{7.11}$$

where β denotes the normalized coefficient of viscous damping. Fig. 7.8 shows the PSP calculated for different values of the size ratio. In these figures, red colors the parameter regions where over 90% of rotations were observed while blue those with less than 10%. Here, the period-doubling bifurcations are not considered and thus period-1, period-2 and so on responses are not separately displayed nor do different attractors such as the chaotic ones. The target of this investigation is to identify the parameters that would lead to rotational motion of the tri-pendulum simulating the vertical translation imposed by the described rig's reciprocal mechanism. The damping coefficient is kept constant for all the plots taking a small value, $\beta = 0.005$, approaching the one of the experimental setup's.

Fig. 7.8(d) assumes a size ratio $j \to \infty$ practically devolving to the perfect harmonic excitation described in Eq. (4.4). This plot resembles as expected the ones
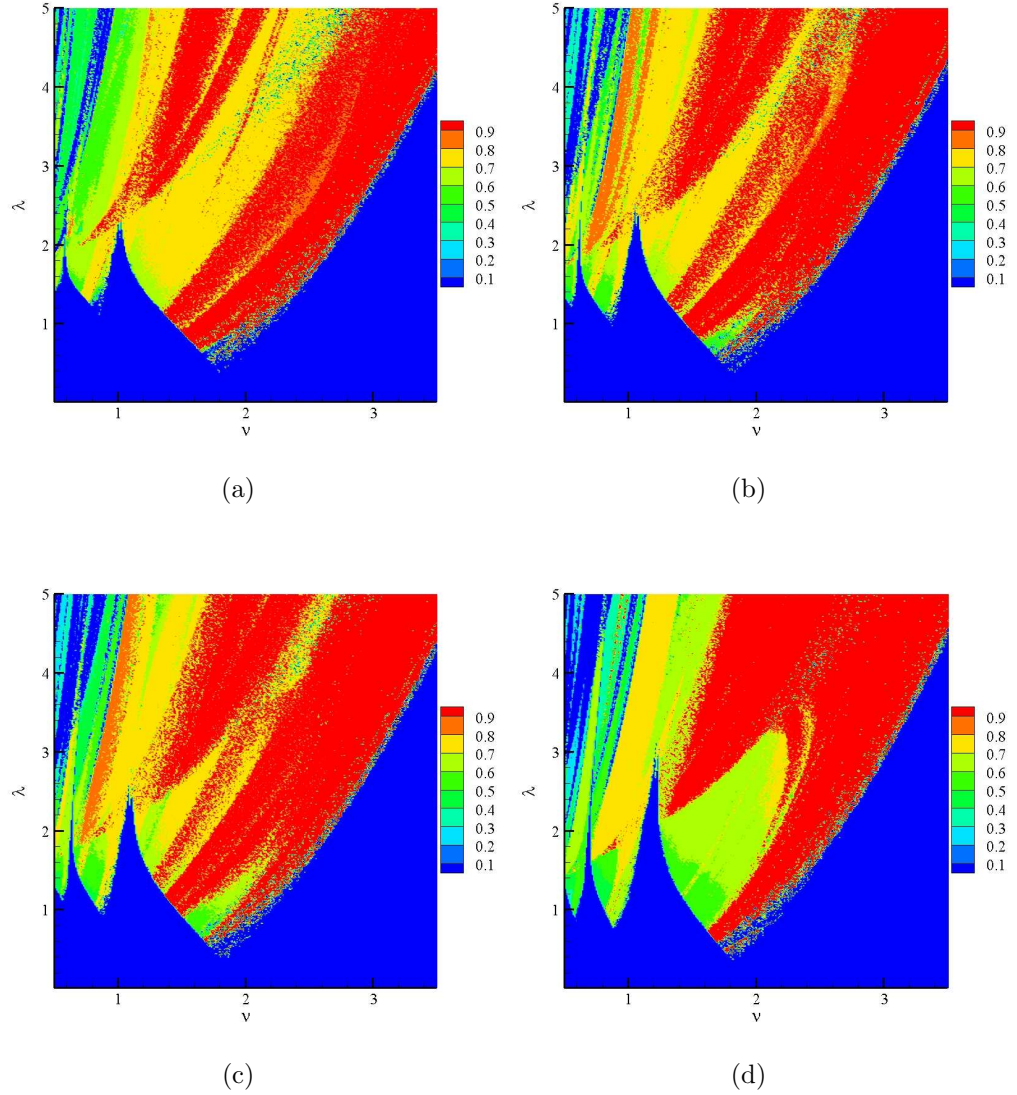
Figure 7.8: PSPs for a physical pendulum parametrically excited by Eq. (7.10) for: (a) $j = 2$ (b) $j = 3$ (c) $j = 4$ (d) $j = \infty$.

previously created for the perfect harmonic signal [183] and is shown to facilitate comparison. Further on, three values for the size ratio $j = 2, 3, 4$ are considered and the corresponding plots are shown in Figs 7.8(a)-7.8(c). A first observation would be that the boundaries separating oscillatory and asymptotically stable motion from the rotary and chaotic ones remain almost independent of the parameter j something that especially holds for the primary resonance zone around $\nu = 2$. However, the picture is rather different when it comes to rotational and chaotic regions. While in the purely harmonically excited case the two rotational regions merge for $\lambda > 3.2$, they remain completely distinct for $j = 2$ shown in Fig. 7.8(a), separated by a long
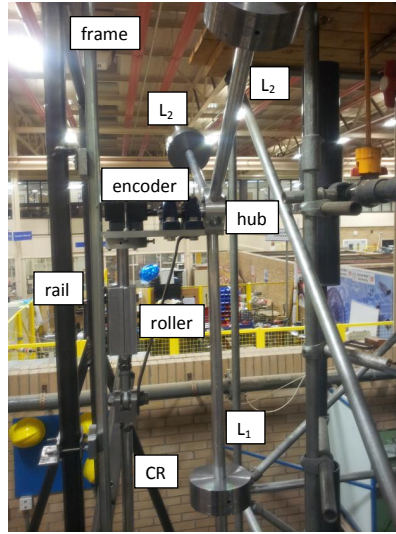
Figure 7.9: The apparatus sub-system of the tri-pendulum. CR stands for connecting rod.

chaotic attractor. Increasing the size ratio reshapes the plots towards the limiting case of $j \to \infty$ retaining though distinguishable differences in the internal structure of the map. Thus, an experimental investigation as the one described that would be based on Eq. (4.4) and not take into account the superharmonic excitation, would reflect significantly erroneous results depending on the selected size ratio j.

In order to render the superharmonics of the resulting motion negligible, the length of this crank has to be considerably bigger than the amplitude. Considering all these constrains, the design of the frame is led to a total 4m in height, 2m in width and 1m in depth.

7.4.2 Description

The experimental apparatus could be divided into three major sub-systems; the tri-pendulum, the mechanism that provides the motion and ensures its structural integrity and the data acquisition sub-system extending from the angular sensor to the post-processing of the data. A detailed technical information is provided in Appendix B, along with the preliminary tests of the damping identification in the tri-pendulum system.

Fig. 7.9 shows the tri-pendulum part. This is allowed to slide along a linear bearing – a rail-roller system, following the displacement imposed by the connecting rod.
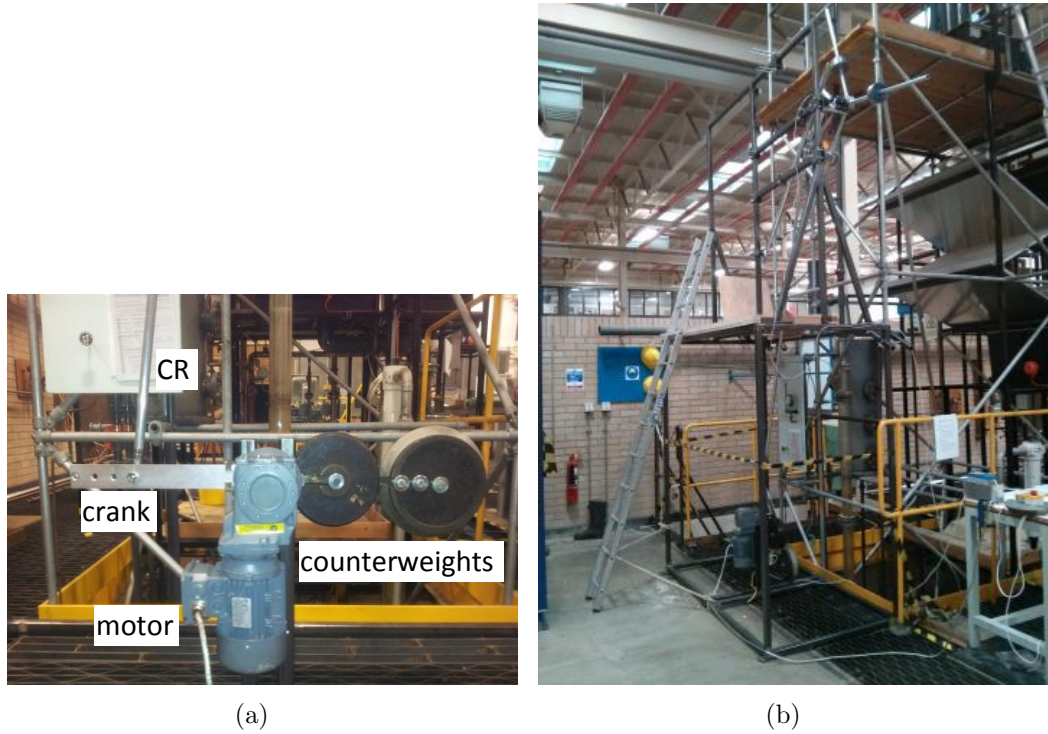
Figure 7.10: Parts of the apparatus; (a) The motorizing sub-system of the tri-pendulum.; (b) View of the full experimental rig. The rail is tilted from the vertical direction resulting in excitation at a constant angle.

Thus the displacement is applied on the tri-pendulum's pivot resulting in its parametric excitation. The excitation is provided by the motor-crank system shown in Fig. 7.10(a), where the other end of the connecting rod is mounted. The crank has been designed with three mounting positions for the connecting rod to allow some flexibility on the excitation's amplitude. The requirement for an amplitude close to the ones observed in the ocean along with structural concerns, have therefore led to a frame of 4 metres high and 2 metres wide, as it is shown in Fig. 7.10(b).

7.5 Results and analysis

In this section, the results of the experimental efforts concerned with the described tri-pendulum and rig are presented. The main goal driving the actualization of these experiments is twofold. On a first level, it is sought to demonstrate the equivalence of a realistic tri-pendulum design to a simple pendulum of unrealistic size. This equivalence is dictated by the need to fall into the primary parametric resonance leading to robust rotations in the context of developing a pendulum-based WEC. On

a second level, the multiplicity of the possible configurations standing as kinematically identical solutions is raised. This is rather important considering the direct relation of not only the magnitude of mass m to the total inertia of the system, but of the distances L_1 and L_2 as well, and the consequential implications onto the potential generated power.

7.5.1 Preliminaries

Before getting into the main body of the experiments, one would have to clarify specific issues concerning the calculation of the natural frequency in the realized system, the damping accompanying the angular response of the pendulum, the modelling of the experimentally observed responses as well as the post-processing of the data involved in the presentation of the results.

Natural frequency Ω. A short note on the calculation of the natural frequency of the experimental tri-pendulum is required since the idealized system can no longer describe it. This value is thought of as the natural frequency of an equivalent simple lumped mass pendulum and so, considering Eq. (7.9) it is defined as:

$$\Omega_{eq} = \sqrt{Mg\left(L_1 - L_2\right)/\left(I_c + I_v\right)} \tag{7.12}$$

I_c refers to the inertia of the necessary parts for the structural realization of the tri-pendulum and include the moment of inertia with respect to the pivot O, of the shaft, the disk (or hub), the arms and the masses. Since these are solid bodies, their moment of inertia, following Stainer's theorem, needs to consider the inertia around an axis perpendicular to the plane of angular motion. The configurable part, I_v, refers to the moment of inertia of the centre of mass of the masses carried by the arms with respect to the pivot O, directly related to and affected by the lengths L_1 and L_2 and thus characterized as configurable.

Damping identification. The selection of the excitation parameters and the possible combinations of the lengths L_1 and L_2 depend on the energy damped per cycle. This is expressed through the well-known effect of increasing viscous damping coefficient onto the parameter space response. Higher damping requires higher input energy meaning that the map of the different types of responses (oscillatory, rotary etc) is pushed to higher excitation amplitudes. Thus, in order to design a series of experiments that could be predicted by numerical simulations, the latter should be conducted for a viscous damping coefficient that closely models the damped energy. Before proceeding to the main part of the experiments, a series of free vibrations tests were undertaken to evaluate the energy losses. The logarithmic decrement method was applied – see Appendix B.4 – and an average value of $c = 0.10 \ kgm/s$ has been found which will be used for the numerical simulations. Of course, the viscous damping coefficient β will depend on the varying inertia as well since $2\beta = c/(I_c + I_v)$, but due to the very small value of the damping these changes will not drastically influence the numerical construction of the map of the responses (Figs 7.11(a) and 7.11(b)).

The construction of a map with respect to the excitation parameters separating the different types of responses will be used as a guide for the targeted experimental tests which in turn will be used to verify the capability of rotations for different configurations of the tri-pendulum, i.e. of L_1 and L_2.

PSPs. Modelling the response of the tri-pendulum follows a rationale that places rotational motion under the microscope. The target is to characterize the rotational capability for a range of the influencing parameters which are expressed through $\nu = \omega/\Omega$ and $\lambda = A\omega^2/g$ where A is the excitation amplitude. This selection is not random but emerges by a common useful transformation of the time variable in Eq. (7.9) [183, 193].

This experimental study utilizes a reciprocal mechanism to replicate the motion of waves. As it was analyzed in Sec. 7.4.1, the motion of the working point includes superharmonics. In the experimental setup, $\max(j) = 4.8$ is used and thus, modelling
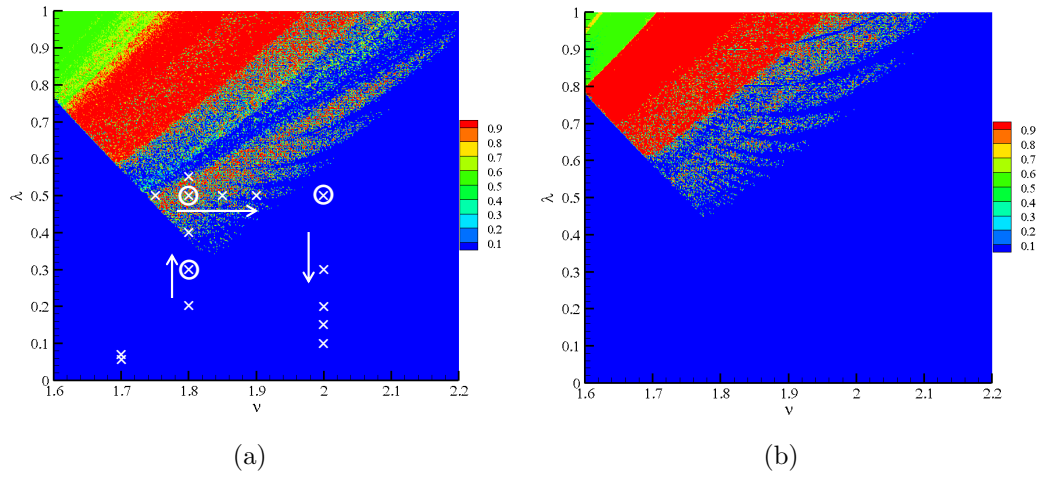
Figure 7.11: Numerically constructed PSP of the response of the tri-pendulum to vertical periodic excitation. Colormap characterizes the percentage of rotational motion in the steady-state response with blue < 10% and red > 90%. The points marked with $\times$ denote the different parameter pairs that were recorded irregardless of the multiplicity of the tri-pendulum configuration. The points marked with $\circ$ denote those points that were used to record identical response with different L_1, L_2 configuration. (a) non-dimensional damping coefficient $\gamma = 0.01$; (b) $\gamma = 0.05$.

the response to a monochromatic excitation is sufficient.

Fig. 7.11(a) shows the PSP for a low non-dimensional damping coefficient, $2\beta = c/(I\Omega) = 0.01$. Red again indicates the desired region of $> 90\%$ rotations with blue denoting the $< 10\%$. This map is constructed by counting the rotational motion for each case in the steady-state response with the specifics of their numerical construction being the same as in the previous chapters. Of course, once I and Ω change, γ changes with the possibility of an oscillatory point to become rotary with increased $I\Omega$ because the PSP itself would have been drawn downwards. Yet, this change would have to be considerably larger than those considered herein since c is of very small value and this issue does not ultimately affect the experiments.

One aspect of the goal of the herein presented experiments is to demonstrate agreement between the numerical prediction of the response through PSPs with the experimentally recorded response of the tri-pendulum. To that end, the marked points in the PSP in Fig. 7.11(a) are targeted and investigated by use of the experimental rig. These points are selected in such a way so that experimental verification of the prediction of their response would attribute consistency to the PSP.

On a second level, the flexibility and configurable capability of the design is sought
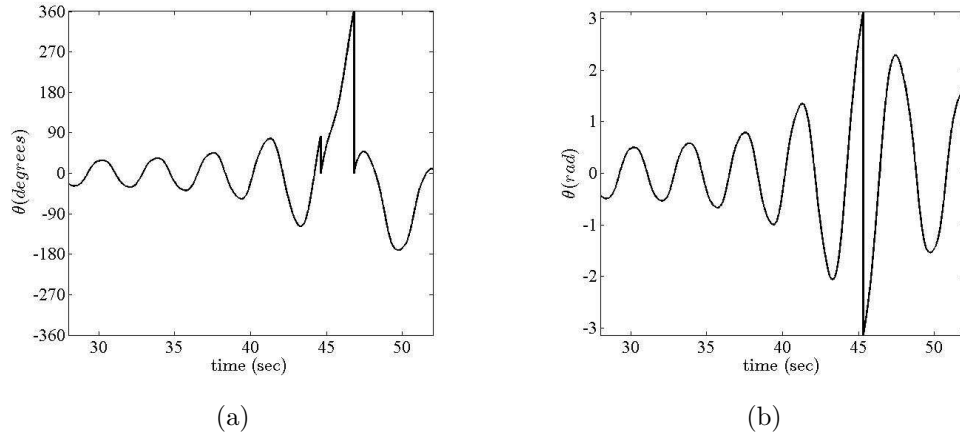
Figure 7.12: Angular output of the encoder; (a) Data as were recorded through the DAQ subsystem. Measurement is done in degrees, covering a range of 720° and reporting inexistent jumps; (b) Data resulting from post-processing of the raw data in Fig. 7.12(a) within the MATLAB environment. The issues raised have been corrected.

to be demonstrated by attempting to achieve identical response attached to one point in the PSP, with different values of L_1 and L_2.

Post-processing. The angular sensor is an optical encoder that is attached to the tri-pendulum's shaft and has three digital outputs. Two of these are used to count how many of the 3000 marks dividing the circle have been observed. In that way the sensor gives exact information on the total angle run from the initiation of the measurements. The third one, known also as the index signal I, is used to signify the crossing of a unique mark which is utilized to denote a full revolution.

However, when the sensor powers up, it assumes an angular value equal to zero and this is because it cannot perform explicit angle measurements but only changes in angular position. Then, at the first activation of the index signal I, the output is normalised to zero again which results in a falsified output as could be seen in Fig. 7.12(a). It could also be seen that the range of the measurements extends up to two revolutions. In order to correct these two issues, a MATLAB script has been applied normalising the output within $[-\pi, \pi]$ and correcting the false jump. Note that the post-processed data assume for zero degrees the correct equilibrium point as this was the starting point of each measurement. This normalization leads to jump from $-\pi$ to π when the motion is rotational, which nevertheless causes no

Table 7.1: Specifications of the experimentally recorded responses of the tri-pendulum to vertical excitation.

ω (rad/s)	r (m)	L_1 (m)	L_2 (m)	Ω (rad/s)	I_{tot} (kgm^2)	l_{eq} (m)	ν	λ	Re
1.255	0.400	0.400	0.370	0.741	2.533	17.876	1.690	0.060	F
1.255	0.450	0.400	0.370	0.741	2.533	17.876	1.690	0.070	F
2.215	0.400	0.298	0.249	1.235	1.488	6.435	1.800	0.200	F
2.710	0.400	0.390	0.300	1.506	1.839	4.323	1.800	0.300	F
3.150	0.400	0.281	0.200	1.743	1.233	3.228	1.800	0.400	O
3.745	0.350	0.430	0.249	2.078	1.944	2.273	1.800	0.500	R
3.678	0.400	0.321	0.200	2.039	1.347	2.360	1.800	0.550	R
3.500	0.400	0.410	0.249	2.001	1.863	2.451	1.750	0.500	R
3.500	0.400	0.481	0.300	1.947	2.214	2.587	1.800	0.500	R
3.500	0.400	0.386	0.249	1.892	1.772	2.741	1.850	0.500	R
3.745	0.350	0.403	0.249	1.971	1.838	2.525	1.900	0.500	R
3.502	0.400	0.533	0.350	1.750	2.770	3.202	2.000	0.500	O
3.500	0.400	0.433	0.300	1.753	2.006	3.191	2.000	0.500	O
2.760	0.400	0.300	0.240	1.383	1.452	5.128	1.990	0.310	O
2.215	0.400	0.288	0.249	1.112	1.460	7.934	2.000	0.200	F
1.920	0.400	0.277	0.249	0.952	1.431	10.829	2.020	0.150	F
1.565	0.400	0.268	0.249	0.790	1.480	15.701	1.980	0.100	F

difficulties except for the calculation of the velocity where they are accounted for in the post-processing script.

As a final note before the presentation of the experimental results, the initial conditions of the tests have to be addressed. Recording of the angle would have to start as early as to capture the tri-pendulum at equilibrium, thus ensuring consistency of the measurements. However, due to the trivial stability of the equilibrium, the system had to be displaced even slightly by an external source in order for the excited response to unfold. The mathematical side of this could also be understood by observing Eq. (7.9) and noticing that $(\theta, \dot{\theta}) = (0, 0)$ is a fixed point.

7.5.2   Vertical excitation

The first set of experiments is related to using the PSP in Fig. 7.11(a) as a guide for predicting the response of the tri-pendulum. Let us note again that this map can only be used as guide and not as an exact predictor since the damping coefficient is approximated as a constant value among the different trials. The specifications of the configuration of the lengths and the rest of the parameters for these experiments are concentrated in Table 7.1. For each case, the parameter set ν, λ is reported with

Table 7.2: Three points from the PSP corresponding to different responses (R, O, F) with three different configurations of L_1, L_2 each.

ω (rad/s)	r (m)	L_1 (m)	L_2 (m)	Ω (rad/s)	I_{tot} (kgm^2)	l_{eq} (m)	ν	λ	Re
3.500	0.400	0.284	0.200	1.946	1.029	2.591	1.800	0.500	R
3.500	0.400	0.481	0.300	1.947	2.214	2.587	1.798	0.500	R
3.500	0.400	0.610	0.350	1.945	3.186	2.593	1.800	0.500	R*
2.710	0.400	0.246	0.200	1.512	0.933	4.293	1.794	0.300	F
2.710	0.400	0.390	0.300	1.506	1.839	4.323	1.801	0.300	F
2.710	0.400	0.471	0.350	1.505	2.476	4.329	1.802	0.300	F
3.500	0.400	0.265	0.200	1.754	0.979	3.187	1.996	0.500	O
3.500	0.400	0.433	0.300	1.753	2.006	3.191	1.997	0.500	O
3.500	0.400	0.533	0.350	1.750	2.770	3.202	2.001	0.500	O

*extreme vibrations caused by the large inetria did not allow rotational motion to settle

the experimental response characterized as {R,O,F} for rotating, oscillating and fixed point steady-state response respectively. The target is for points leading to rotations to demonstrate agreement with the predictions.

First, two points were investigated with very low λ (0.06 and 0.07), expected to end up in a fixed point response, something that was verified. Further on, moving to a frequency ratio $\nu = 1.8$, the gradual increase of the amplitude was expected to drive the tri-pendulum to bifurcate from fixed point to rotations through oscillations. In fact, starting from $\lambda = 0.2$, for which the response could not escape the equilibrium well, the first rotating point was found for $\lambda = 0.5$ as expected. A second point for $\lambda = 0.55$ was recorded rotating so that the entrance into the rotational region would be further supported.

Next, it was attempted to cross the right boundary of the rotational region. The non-dimensional excitation amplitude was fixed at $\lambda = 0.5$ and the advance of the investigation was performed through changing ν, expecting to cross the right boundary and bifurcate from rotations to oscillations. Indeed, the far left point was for $\nu = 1.75$, predicted to have a rotational response, as in fact was experimentally recorded. The rotational motion should be sustained for frequency as high as $\nu = 1.9$, totaling up to 4 recorded points leading to rotations. As soon as ν was increased to 2 the rotational motion bifurcated to oscillatory.

Then, decreasing the amplitude λ, the PSP informed us of returning to a fixed point

response as the input energy would decrease, a development that was recorded for $\lambda < 0.310$, and is reported in Table 7.1. One could note that different configurations of L_1 and L_2 were used with no particular constraint as with the simple pendulum.

However, the capability of achieving the same natural frequency with different layouts, and thus decoupling the non-dimensional parameter pair (ν, λ) from the size of the device is demonstrated in the second set of the experiments, shown in Table 7.2. This table is divided into three sets. Each of them corresponds to one point in the PSP marked with ○ in Fig. 7.11(a). The target here is to use different layouts within each set, keeping however the controlling parameters constant and thus recording the same response. The results reported in Table 7.2 validate the configurable attribute of the tri-pendulum with the exception of one point were the inertia value was too big to be properly supported by the experimental rig. For the sake of an example, two different layouts of $L_1 = 0.284m$-$L_2 = 0.2m$ and $L_1 = 0.481m$-$L_2 = 0.3m$ lead to the same point in the PSP and fall into the rotational attractor. This flexibility in selecting the lengths is very important from the energy harvesting standpoint, since the bigger the moment of inertia the bigger the generator that could be attached to the rotor's shaft. Moreover, the overall size of the device compared to a simple pendulum has been reduced several times for all the examined cases. This is evident by simply comparing the length of a simple pendulum, l_{eq}, that would be required to achieve the same parameter pair with the longest of the arms, L_1, for each of the cases reported in the tables.

In Fig. 7.13, the recorded post-processed signals coming from two different sets, one rotational and one oscillatory are shown for consistency. The angular signal includes the transient period as well, while the velocity and the phase space incorporate only the steady-state response.

7.5.3 Tilted excitation

Previous studies [106, 110] have reported that planar excitation of the pendulum's pivot draws the threshold for rotations towards lower λ values. Here, this numerically supported argument is investigated experimentally.
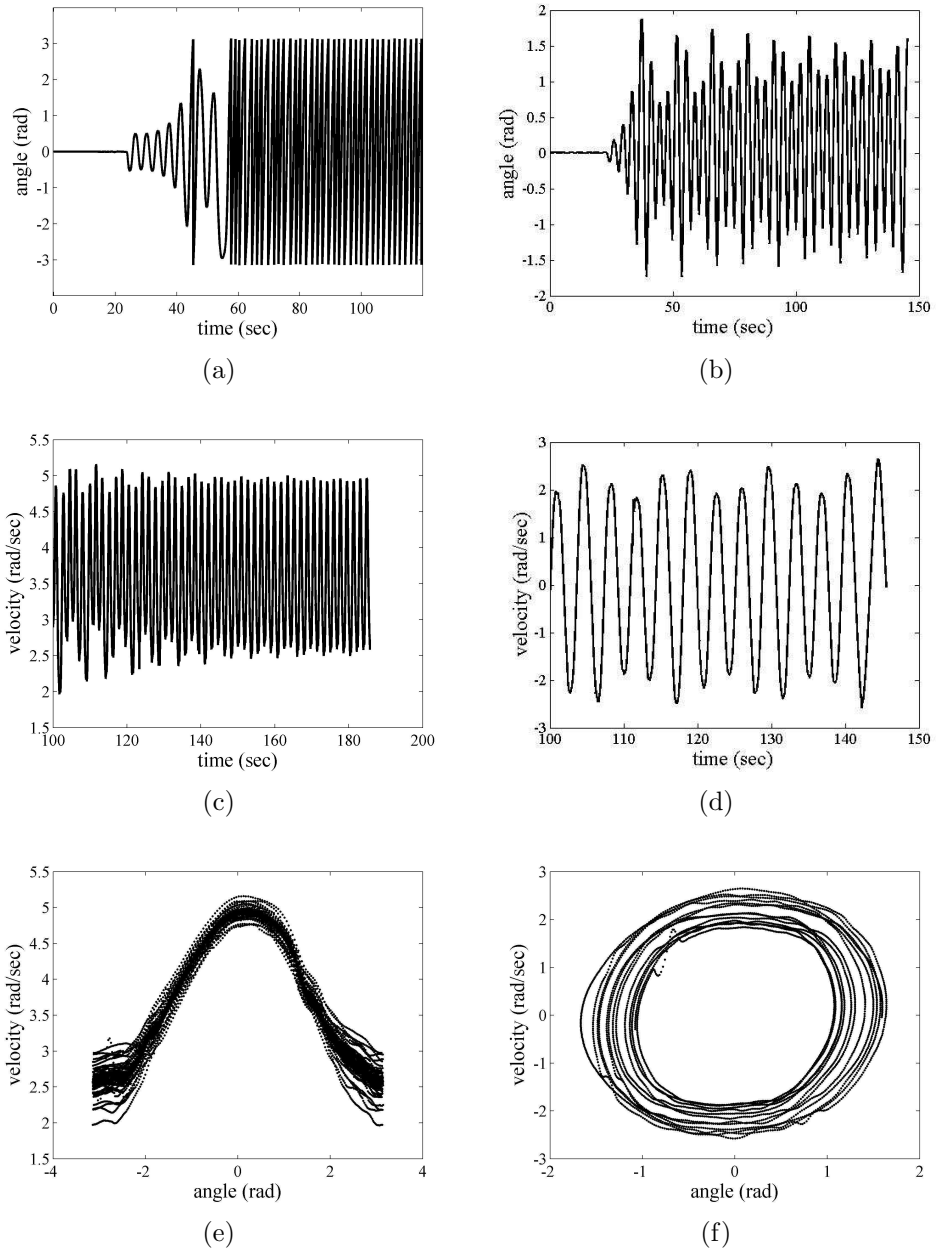
Figure 7.13: Experimental post-processed recorded response to vertical excitation; rotating response for $\nu = 1.800$, $\lambda = 0.500$ ((a)-(c)-(e)); oscillating response for $\nu = 2.000$, $\lambda = 0.500$ ((b)-(d)-(f)).

Planar excitation is thought to be the forcing of the pivot outside the vertical line. The elliptical trajectory of the pivot and the rectilinear one but at a tilt angle from the vertical direction have been studied by means of analytical [106] and numerical [110] methods. Due to the limitations of the rig, the only possible alteration in the imposition of the excitation was to divert its direction. Therefore, instead of a vertical driving of the tri-pendulum, the rail that guides its motion is tilted at

187

Table 7.3: Specifications of the experiments and responses with the excitation along a line tilted by 10°.

ω (rad/s)	r (m)	L_1 (m)	L_2 (m)	Ω (rad/s)	I_{tot} (kgm^2)	l_{eq} (m)	ν	λ	Re
2.900	0.350	0.325	0.249	1.613	1.355	3.771	1.800	0.300	R
3.350	0.350	0.358	0.249	1.859	0.671	2.839	1.800	0.400	R
3.745	0.350	0.399	0.249	2.080	1.608	2.268	1.800	0.500	R
3.745	0.350	0.182	0.130	2.024	0.585	2.395	1.850	0.500	R
3.350	0.350	0.176	0.140	1.674	0.602	3.500	2.000	0.400	O
2.900	0.350	0.298	0.250	1.319	1.280	5.641	2.200	0.300	O
2.370	0.350	0.276	0.250	0.986	1.219	10.083	2.400	0.200	O

10° with respect to the vertical axis, as could be seen in Fig. 7.10(b). Hence, the tri-pendulum is excited by a planar force and expected to demonstrate rotations for lower λ values.

In order to test this premise, direct comparison with the experimental results obtained from the vertical driving is sought. In particular, the points in the PSP in Fig. 7.11(a) consisting an upwards path, denoted by the up-pointing arrow, are
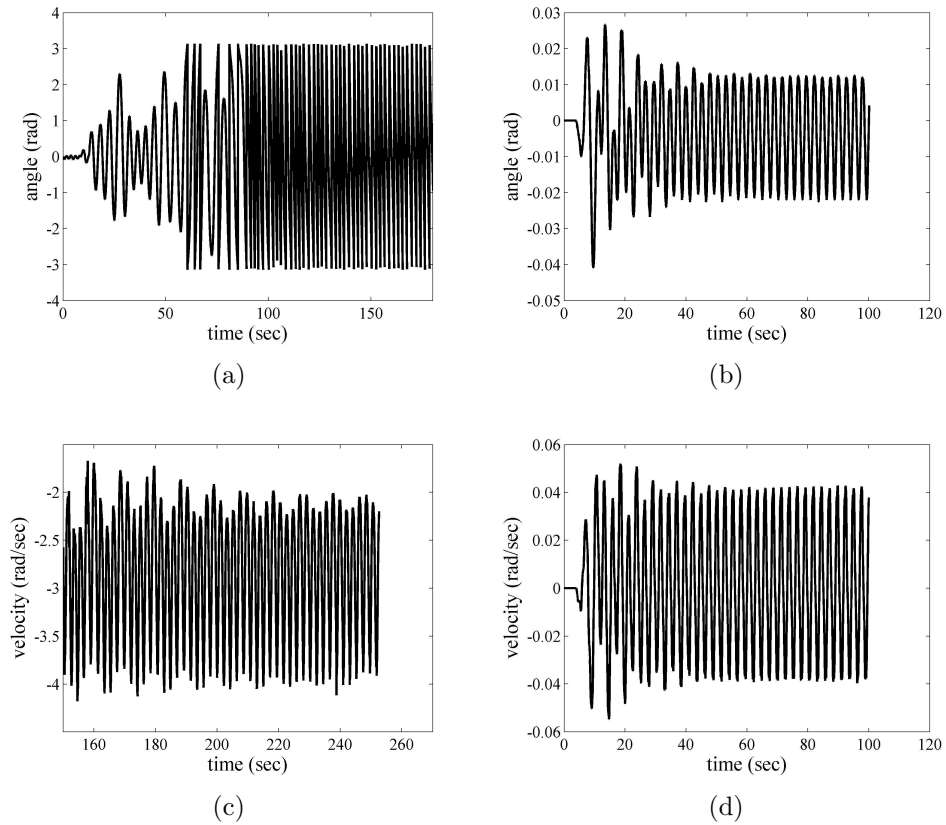
Figure 7.14: Experimental post-processed recorded response to tilted excitation; rotating response for $\nu = 1.800$, $\lambda = 0.300$ ((a)-(c)); oscillating response for $\nu = 2.400$, $\lambda = 0.200$ ((b)-(d)).

revisited. Starting from a point which already demonstrated rotational response $\nu = 1.800$, $\lambda = 0.500$, the amplitude is decreased down to the other points that were tested ($\lambda = 0.4$ and 0.3). This corresponds to the first three cases presented in Table 7.3. Comparing the response to the vertical excitation with the one to the tilted one, it could be extracted that the rotational region expands to lower λ values. Instead of the oscillatory response observed for $\lambda = 0.4$ and the fixed point one ($\lambda = 0.3$), purely rotational response was recorded (see Fig. 7.14(a)).

Moreover, another characteristic of the system under tilted excitation is that the fixed point response observed for vertical excitation tranforms to oscillatory [110]. Decreasing λ does not lead to equilibrium but rather in an steady-state oscillatory response with its amplitude reducing with lower λ. Indicatively, one could see the last three cases presented in Table 7.3 and the recorded signal in Fig. 7.14(b).

7.6   Summary

Ocean waves are characterized by a rather low mean frequency. This physical property imposes a technological limitation on the development of the pendulum-based WEC, since an unfeasibly long pendulum would be required for rotational motion to be established. In this chapter, a novel design of a compound pendulum is proposed to overcome this issue, consisting of three pendulums integrated into one.

The investigation of the natural frequency of the tri-pendulum has shown that the required size of this device is several times smaller than a simple pendulum's. Moreover, the analysis demonstrated that it is possible to achieve a particular value of the natural frequency with different configurations of the masses carried by the arms of the tri-pendulum. This means that a device, manageable in size, could be set to rotate from ocean waves. Furthermore, different layouts are possible, such that a maximized performance is achieved, given that the size of the generator that could be driven by this device depends on the position of the masses.

An experimental rig was developed in order to verify the theoretical predictions that the response of the tri-pendulum is equivalent to that of a simple pendulum. Several

points in the numerically constructed PSP were tested, confirming the advantages of this design. In addition, three points in the PSP were selected and the response of the tri-pendulum was recorded for different layouts of the masses, aiming to demonstrate the flexibility in the configuration of the device.

However, the experimental endeavour revealed an issue too. Even though the frequency ratio ν could be manipulated to take the desired value, it was much more difficult to control the second influential parameter λ. This is because ν explicitly depends on the system's natural frequency, while λ depends only on the excitation characteristics since $\lambda = A\nu^2/l_{eq} = A\omega^2/g$. This is the reason why it was not possible to test points in the PSP for $\lambda > 0.6$.

Chapter 8

Conclusions and Future Work

The study included in this thesis initiates from the development of a WEC, based on the dynamics of the parametric pendulum. It is well-known in the deterministic theory that there is a rich diversity of different types for the response of the pendulum to parametric excitation applied to its pivot. The therein potential of establishing rotational motion could be exploited for transforming the kinetic energy of the bobbing ocean waves to rotary kinetic energy. Thus, the possibility of conversion to electricity acquires an enthusiastic groundwork. Yet, two main issues had remained unanswered in the literature. First, the motion of ocean waves is random, a property which may as well draw a significantly different picture for the resulting dynamics. This stochastic dynamical system though is a rather fundamental one, surpassing the boundaries of a single application. And so, an added interest arises when the rotary response of the pendulum under stochastic environmental excitation is sought, motivating a broader investigation. Second, there had been an important technological limitation that needed to be overcome, relating to the low mean frequency observed in the ocean. In the present thesis, it has been attempted to address these two issues. The recognized necessary steps were delineated in Sec. 1.2 and the major conclusions stemming from the present work are discussed in the following section, with recommendations for further development closing this Chapter.

8.1 Major conclusions

Overall, rotational motion of a pendulum under stochastic parametric excitation is possible and could be sustained even for relatively large noise intensity values. This could be achieved especially for the designs that allow better performance and have been discussed herein. However, a significant impact of the noise intensity has been revealed on the parameter regions for which this could be observed, incorporating elements of the behaviour of the linear system but introducing new effects as well. The topography of the maps documented for the deterministic response has been found to follow particular patterns with increasing noise intensity, regarding both the intensity and robustness of rotations but the displacement of the rotational parameter regions too. The stochastic properties of the excitation then, hold a key role in the design process of pendulum-based systems when the parametric interaction with the environment is random. Moreover, a particularly interesting finding is related to the stability of a pendulum's node equilibrium when the mounting platform is undergoing impacting motion. The instability boundaries have been found to succumb to significant alterations with respect to the case of impacts-free motion; yet, new relationships have been found that dictate the evolution of these boundaries in the parameter space against the controlling parameters: noise intensity, distance to the barrier, energy dissipation, mass distribution.

8.1.1 *Vertically excited parametric pendulum*

Random parametric excitation of a lumped mass pendulum in the purely vertical direction was first considered . The excitation was modelled as both a simple white noise and a narrow-band excitation given by the RPM. The latter has been seen to closely approximate the power distribution spectrum of ocean waves. Besides, this model quite adequately represents a number of environmental loads. The focus of the analysis was on the potential of rotational motion as a response to the stochastic parametric excitation. PSPs with respect to the non-dimensional forcing parameters (ν, λ) were constructed based on MC simulations so as to explore this potential and moreover, to match the presence of rotary response with the parameter regions that lead to it for different noise intensity values.

It has been found that increasing magnitude of the variance of the random phase, D, degenerates the purely rotational regions to less robust rotations. Indicatively, the highest rotational ratio observed for $D = 0.3$ varies between 70-80% for a much narrower parameter region than the robust, $> 90\%$ one recorded for lower D values. This is also reflected in the PDFs that were calculated through a numerical PI method. Furthermore, increasing noise introduces the tendency of the two separate rotational regions of the deterministic response to merge into a single one. Additionally, small changes in the noise intensity function in a similar way to the damping coefficient, displacing upwards in the λ axis the parameter regions leading to different rotational ratios. Furthermore, the damping coefficient not only controls the placement of the different types of response on the parameter map, but higher values have been found to enhance the robustness of rotary motion due to the increased capacity of dissipating small fluctuations. The opposite effect was observed for the white noise excitation, where a given damping coefficient has an upper bound of the rotational ratio to which the response converges for increasing noise intensity. When only dry friction is considered, the PSPs have shown an intensification of the rotational motion with increasing noise. Another effect of noise is that the boundaries separating the oscillatory or asymptotically stable regions from the rotational have been found to be wider for higher D values. Last, the stochastic properties of the excitation render the initial conditions of this dynamical system less important.

8.1.2 Tilted excitation

A step forward in the modelling of the stochastic parametric pendulum was taken, considering a still rectilinear but non-vertical excitation. In this case an extra term arises in the equation of motion representing the forcing of the system in the horizontal direction. This component is considered to be in phase with the vertical one resulting in a rectilinear displacement of the pendulum's pivot. Then, the tilt angle of the line of the excitation with respect to the vertical axis becomes another influential parameter worth investigating. PSPs were extracted from MC simulations characterizing the rotational ratio of the response for two different approaches. First, the vertical and horizontal amplitudes were selected such that the half stroke of the pivot would be directly comparable to the previous analysis for the vertical

excitation. It has been found that in this case, increasing tilt anlge ψ changes the PSP at the expense of rotational regions. On the other hand, if the vertical amplitude is kept the same as in the purely vertical excitation, then the major effect of increasing tilt angle is that the boundaries between rotational and oscillatory regions are brought downwards in the λ axis.

8.1.3   Autoparametric system

The fundamental autoparametric system consisting of a lumped mass pendulum mounted on a linear SDOF base has been considered, always regarding the potential of rotational motion of the pendulum. The coupled system is examined when a narrow-band stochastic process is induced as base excitation. MC-based PSPs have been constructed with a slightly different procedure in order to ensure the narrow-band properties of the base's response. It has been shown that introducing the linear base intermediate to the stochastic excitation and the pendulum results in significant enforcement of the rotational response when the pendulum's mass is considerably smaller than the base's, rendering it negligible. This is a result of the combined influence of the base's dynamic amplification factor depending on the base's damping coefficient and the filtering of the fast fluctuations of the excitation through the base's stiffness. Wider regions of dominant rotations ($> 90\%$) for even smaller λ values have been observed. It has been seen that higher values of damping result in more robust and intense rotational regions and the rotations are reinforced against the randomness of the exciting frequency. Moreover, it has been found that when the coupling is considered, relatively high mass ratio values effectively cancel the advantage of filtering the excitation leading to a response that approaches the one without the SDOF system. On the other hand, small values of this ratio slightly enhance the rotational motion, while when these masses are equal, the desired response decreases. However, the rotational motion is still maintained even at a lower level, around 75%, when the damping coefficient is chosen properly. The latter also gives rise to the option of using the filter for controlling purposes as well.

8.1.4   Multiple pendulums

The response of two coupled pendulums has been considered when being mounted on the same linear SDOF base. A narrow-band stochastic process based on the RPM provides a base excitation to the system. The aim of this investigation was to explore the potential of both pendulums - a tuned and a detuned - to establish rotational motion with emphasis put onto the influence of one onto the other. Direct comparison of the pendulums' response with the performance of a single decoupled pendulum has been done by examining selected parameters and reporting the exhibited rotational motion in contrast with oscillatory. Moreover, synchronizing phenomena were sought through computation of the cross-correlation coefficient ρ. It has been shown that ρ could be used to indicate the existence of rotational trajectories of the detuned pendulum when the tuned one is always rotating.

Furthermore, PSPs have been constructed describing the rotational motion of the detuned pendulum for a wide range of the system's exciting parameters. These are used to demonstrate the influence of the coupling between the pendulums and the noise intensity on the parameter regions were rotational response is found. Numerical MC simulations have shown that rotational motion is achievable in the case of the two coupled pendulums, in both the deterministic and stochastic cases. Increasing noise intensity has the effect of reducing the rotational capability of the system, previously observed for the single parametric pendulum. Moreover, the joint influence of the coupling and the uncertainty drives the tuned pendulum to experience less robust rotations, even though as a single pendulum it is configured to acquire a rotational response. It has also been observed that increasing the value defining the mass ratio ψ leads to more intense interaction between the pendulums as expected and less rotations, although a range where both pendulums purely rotate could be found. The interaction has also been found to incur jumps between different types of attractors, while the detuning between the pendulums affects their response since higher detuning drives each pendulum closer to their corresponding uncoupled response.

8.1.5   Impacting motion

Approximate analytical and numerical stability analysis of an impacting autoparametric pendulum was considered. The impacts were first considered to be elastic ($r = 1$) and the perfect detuning case between the primary mass and the pendulum ($\delta = \Omega_2 - \Omega_1 = 0$) was analyzed. The averaging procedure, applied to the original set of equations, has shown, for the uncoupled motion of the primary mass and pendulum ($\gamma = 0$), that the impact condition significantly changes the shape of the instability domain both in the mean and mean-square sense, making it asymmetric and shifted to the right from the original resonance axis ($\Delta = \omega - 2\Omega_1 = 0$). Thus, it has been shown that the instability domain has been reduced in size, making the system stable where it would not be for impact free oscillations. Moreover, it has been shown that there is a critical value of noise intensity $\sigma_{crit}^2 = 32\beta$, crossing of which moves the instability domains to the region of negative Δ values. Therefore, to make the system stable for noise intensities values below the critical, one has to keep a negative detuning Δ. It has also been demonstrated that increasing the distance to the barrier not only reduces the instability domain, but also turn it counterclockwise.

Numerical MC simulations were used to calculate the system response for the general case of $\gamma \neq 0$. It has been shown that the coupling between the two subsystems is accompanied by a greater stabilization effect for low values of λ. On the other hand, starting from a certain value of γ this effect diminishes, leading to a limiting shape of the instability domain. Moreover, numerical MC simulations were utilized to calculate the LLE and evaluate the influence of non-elastic impacts ($r < 1$). The instability domain is still found on the same Δ semi-plane with lower r increasing the lowest unstable point, due to the higher energy dissipation at the moment of impacts that these restitution coefficients represent.

Finally, it should be stressed that although the impacting motion can reduce the instability domain and even shift it to the right, it does not remove it completely. Varying the parameter δ would make it possible to move the instability domain even further to the right or left.

8.1.6   Experiments

An experimental investigation of the response of a parametrically excited physical pendulum has been also conducted. The system at hand, a tri-pendulum, consists of three simple pendulums integrated into one. The interest is focused onto the capability of establishing rotational response in view of the WEC application. The purpose of introducing this design is to overcome the limitations imposed by the physical resource of ocean waves onto the capability of a simple pendulum to fall into the primary parametric resonance.

The motivation for the herein presented experiments is twofold. First, a correspondence to the response exhibited by a simple pendulum was sought. In that sense, the target of the first set of the experiments was to demonstrate the equivalence between the response of the tri-pendulum to the one of a simple pendulum under the same exciting conditions. The benefit attached to the tri-pendulum however, is that of its size. Whereas a simple pendulum would require an extremely long structure, sometimes even unfeasible for technological applications, the tri-pendulum would provide an equivalent behaviour (i.e. rotational) with not only realistic size but a multiplicity of configurations. Hence, this first sets of the experiments demonstrated that one could use the numerically constructed PSP characterizing the type of the response for the tri-pendulum with a direct equivalence.

Moreover, a second set of experiments was conducted, concerned with just three exciting cases, unique in the non-dimensional parameter space that controls the nature of the response. For each of these points, different configurations of the distances of the masses from the pivot were tested, resulting though in the same parameter space point, only by changing the distances and keeping the rest of the parameters constant. This is impossible to be accomplished by a simple pendulum which natural frequency is one-on-one related to its length. Thus, the experiments demonstrated the capability of the tri-pendulum to change its size but not the controlling parameters that regulate its response. This is a rather important characteristic when energy harnessing is concerned, holding a relatively strong decoupling of the size of the device with its functionality. One needs only to consider the potential of an

enlarged generator attached to the device's rotor without the functionality being affected since the lengths L_1 and L_2 could be configured to maintain the exact same functionality.

Last but not least, a modification of the classical vertical excitation was examined in the available experimental rig. The direction of the driving force was tilted by 10° and the conclusions of previous numerical studies were partly tested. Particularly, it had been found that a tilted direction of the excitation would draw the λ threshold for rotations downwards. Indeed, it has been experimentally found that points in the PSM that would fall into the oscillatory or fixed point attractor, would inherit rotational response only by shifting the direction of the excitation.

8.2 Future work

The herein investigation demonstrated several interesting findings related to the rotational response of a pendulum under stochastic parametric excitation. At the same time though, it gave rise to new challenges, listed in the following:

1. The representation of the stochastic excitation for real-world systems could be better achieved with more complicated models, such as the CARMA process. Then, the influence of stochasticity on the rotational parameter regions could be studied in a more realistic context.

2. A further improvement of the stochastic excitation should be considered with an elliptic mean trajectory of the pendulum's pivot. Rotational motion under this type of excitation should then be investigated.

3. Based on the herein investigation of the occurrence of rotational motion in a given random environment, the next step would be to evaluate the reliability of this motion. The first-time passage over a suitable threshold connected to the rotary trajectory would reveal the elapsed time between the initiation of the motion and the first rotation.

4. A computational challenge that emerged is the application of the numerical PI method for M-DOF systems. Contemporary advances in numerical analysis should be exploited to deteriorate the "curse of dimensionality".

5. A control method based on the stochastic optimal control techniques would be rather beneficiary with the target being to sustain rotational motion. Preferably, a passive control law should be sought to minimize the energy requirements for its application.

6. Building upon the investigation of the stability of the pendulum's bottom equilibrium, the impacting autoparametric system with the original pendulum dynamics should be looked upon. Numerical investigation of the rotational motion should then be conducted to reveal the influence of the impacting motion of the platform.

7. The novel design proposed herein might have offered a solution to the problem of the low frequency of ocean waves, however only very low values of the non-dimensional amplitude λ would be possible, detaining the pendulum response outside the rotational regions. Therefore, another technological breakthrough is required.

8. Since rotational motion has been recorded with a configurable design, the extracted power should then be measured.

Appendix A

Formulas for impacting motion

A.1 Joint influence of h^*, α and β in the deterministic case

Substituting Eq. (6.10) into Eq. (6.15) and solving with respect to λ, the boundaries of the instability domains could be extracted. Then, the RHS boundary reads:

$$
\lambda_R = \frac{9\pi^2}{64} \frac{9\,\Delta^2 h^* \Omega_2{}^2 - 3\,\Delta\,h^* \Omega_2{}^2 \sqrt{\Delta^2 - 32\,\beta^2}}{\left(1 - 9\,h^{*2}\Omega_2{}^4\right)} +
$$

$$
+ \frac{9\pi^2}{64} \frac{\sqrt{2}\sqrt{\left(\Delta^2 + \alpha^2 - 9\,\alpha^2 \Omega_2{}^4 h^{*2}\right)\left(5\,\Delta^2 - 3\,\sqrt{\Delta^2 - 32\,\beta^2}\Delta - 16\,\beta^2\right)}}{\left(1 - 9\,h^{*2}\Omega_2{}^4\right)}
$$

$$(A.1)$$

while for the LHS, the formula would be:

$$
\lambda_L = \frac{9\pi^2}{64} \frac{9\,\Delta^2 h^* \Omega_2{}^2 + 3\,\Delta\,h^* \Omega_2{}^2 \sqrt{\Delta^2 - 32\,\beta^2}}{\left(1 - 9\,h^{*2}\Omega_2{}^4\right)} +
$$

$$
+ \frac{9\pi^2}{64} \frac{\sqrt{2}\sqrt{\left(\Delta^2 + \alpha^2 - 9\,\alpha^2 \Omega_2{}^4 h^{*2}\right)\left(5\,\Delta^2 + 3\,\sqrt{\Delta^2 - 32\,\beta^2}\Delta - 16\,\beta^2\right)}}{\left(1 - 9\,h^{*2}\Omega_2{}^4\right)}
$$

$$(A.2)$$

A.2   Mean stability for $h^* = 0$

In order to extract the mean stability boundaries in this case, Eq. (6.34) is substituted in Eq. (6.32) and the resulting equation is solved with respect to λ. That gives for the RHS boundary:

$$\lambda_R^{\sigma\tau} = \frac{9\pi^2}{128} \frac{\sqrt{(2\,\alpha + \sigma^2)\,\alpha\,(4\,\alpha^2 + 4\,\alpha\,\sigma^2 + \sigma^4 + 4\,\Delta^2)}}{2\,\alpha + \sigma^2}.$$
$$\frac{20\,\Delta^2 - 6\,\Delta\,\sqrt{4\,\Delta^2 - 128\,\beta^2 - 32\,\beta\,\sigma^2 - 2\,\sigma^4} - 64\,\beta^2 - 16\,\beta\,\sigma^2 - \sigma^4}{2\,\alpha + \sigma^2} \tag{A.3}$$

and for the LHS one:

$$\lambda_L^{\sigma\tau} = \frac{9\pi^2}{128} \frac{\sqrt{(2\,\alpha + \sigma^2)\,\alpha\,(4\,\alpha^2 + 4\,\alpha\,\sigma^2 + \sigma^4 + 4\,\Delta^2)}}{2\,\alpha + \sigma^2}.$$
$$\frac{20\,\Delta^2 + 6\,\Delta\,\sqrt{4\,\Delta^2 - 128\,\beta^2 - 32\,\beta\,\sigma^2 - 2\,\sigma^4} - 64\,\beta^2 - 16\,\beta\,\sigma^2 - \sigma^4}{2\,\alpha + \sigma^2} \tag{A.4}$$

Fig. 6.7 presents the boundaries based on these two equations.

Appendix B

Supplementary material of experiments

B.1 Tri-pendulum part.

The core of this experimental study lies within the tri-pendulum part (Fig. 7.9). In this figure, one could see at the bottom, the connecting rod that transfers the circular motion provided by the motor to the tri-pendulum sub-system. The plate holding the bearings that carry the shaft of the tri-pendulum shown in Fig. B.1, is attached to the frame through a roller that is allowed to perform translational motion within a rail. The latter is rigidly bolted onto the frame.

The frequency configuration is achieved through the position of the masses that the tri-pendulum carries. These masses were parted from a 5" (127mm) stainless steel bar to a thickness of 50mm before being drilled with a 1" (25.4mm) hole through the centre for the arm and two grubscrews opposite one another to secure it in place on the arm. The masses were then weighed and the heaviest two had material removed until they were identical to the lightest mass, producing 3 identical masses of 4.725kg each, shown in Fig. B.2.

Aluminium tubes of 1" (25.4mm) outer diameter with a wall thickness of 1/16" (1.5875mm) and 1.25m in length were used as arms. These were chosen to keep the weight of the arms to a minimum while still providing enough strength and stiffness in the arm not to cause vibrations. Each arm fits into one of the six available mounting points on the disk (the hub) – Fig. B.3– and has a 1" (25.4mm) solid

aluminium push transition fit plug inserted into the bottom to locate securely in the disk and further increase the stiffness and strength at the point of highest stress. Each plug had two threaded holes through it and using four bolts each arm was secured in place with two bolts fastened from each side. This gave a very secure fixing between the arm and the disk ensuring minimal movement and vibrations in the arm.

Fig. B.3 presents computer based drawings of the hub. The disk is made from 4" (101.6mm) diameter, 40mm thick aluminium bar with six 1" push transition fit holes as mounting points 60° apart for the arms, drilled onto the curved face of the cylinder. Each mounting point has two "through all" M5 sliding clearance fit holes for the M5 bolts to be used to secure the arms in place. A maximum of three mounting points were used at any one time however six mounting points were necessary to allow flexibility in the setup. It is possible for a bi-pendulum to be configured by removing one arm and placing the other two arms opposite each other. The other advantage of six mounting points is that one (up to a possible three depending on their location on the disk) of the mounting points can sustain damage without needing to scrap the disk as it would still be possible to use it. The disk was designed to be as symmetrical as possible to avoid any imbalance as it spins and to be as small as possible to reduce weight and overall size of the device.

The disk is mounted on a horizontal shaft, Fig. B.1, made from aluminium bar 1" (25.4mm) diameter to allow the tri-pendulum to rotate about a horizontal axis. This shaft is supported by two 1" (25.4mm) plumber bearings that have the dust caps and grease removed to minimise the damping in the system. This is acceptable as the tri-pendulum is rotating at a fraction of the design speed of the bearings. At the end of the shaft is an adapter and coupling to connect an angular encoder (Fig. B.4) to record the angular response of the tri-pendulum. The coupling was added between the shaft adapter and the encoder to allow for small misalignments and vibrations.

The two plumber bearings and encoder are mounted on an aluminium plate. Under this plate there is an adapter to connect the vertical rod, or the "piston" of the

reciprocal mechanism, to the tri-pendulum. The bottom edge of this rod is threaded for a spherical joint to be mounted, intended to connect the connecting rod to the tri-pendulum sub-system. This is necessary since the reciprocal mechanism forces the connecting rod to move in the vertical plane, while the roller has to pushed upwards and drawn downwards on a straight line.

B.2 Motorizing

The experiemtnal apparatus is housed in a frame made from $40 \times 40 \times 4mm$ black steel square section and was constructed in two pieces for manufacture and assembly (Figs B.5 and B.6). The top section is a $2D$ $2 \times 2m$ frame supported by four legs at 18.3^o. In the middle of the $2D$ frame is a vertical bar to allow the mounting of the $1.5m$ T-rail along its length. The bottom section of the frame is a box measuring 2x2x1m with two additional bars traversing the bottom of the frame to locate the verticals bars on which the motor and gearbox drive is mounted (Fig. 7.10(a)).

The connecitng rod is made from the same tubes that were used for the arms. The top edge of the connecitng rod is connected through a spherical joint to the vertical rod where the roller is clamped on. The length of the connecitng rod had to be considerably larger than the amplitude of the excitation. This is imposed so that the superharmonics that arise in the motion of the working point of the reciprocal mechanism (the top egde of the crank) would be rendered negligible thus approximating a sinusoidal motion. Since the designed maximum amplitude is 0.5m, a length of 2.4m for the crank is chosen to overcome the discussed issue. Note that this leads to a required height for the frame >3.5m with the total design of 4m-high frame covering that.

The bottom edge of the 2.4m long 1" (25.4mm) diameter aluminium connecitng rod is then connected through another spherical joint to the crank, drawings of which are shown in Fig. B.7. The connecitng rod is attached to the crank through a studded rod end and can be placed at any of the 4 drilled threaded holes on the crank. These holes basically provide 4 positions for the connection at 0.35, 0.4, 0.45, 0.5

m, forming 4 different radii of the reciprocal mechanism. In that way, each of these positions regulates the amplitude of the excitation. However, the crank extends in both ways with respect to the shaft of the motor (Fig. 7.10(a)). One side is used for the connection with the connecitng rod and the transfer of the motion to the tri-pendulum. The other one carries counterweights in order to reduce the load applied to the motor gearbox and soften impulse loads arising at 0 and π angle of the crank position.

The reciprocal mechanism to simulate waves is driven by an electric motor: NORD SK 80 S/4 with a gearbox: SK92172VF-80 S/4 ratio 22.78:1. The speed of the motor is set in RPM using an inverter: SK500e. The speed of the motor however is not the speed of the output as there is a 22.78:1 ratio gearbox on the motor, the speed of the motor on the inverter therefore had to be set at 22.78x the desired output speed.

B.3   Measurement

For measuring the angular displacement of the excited tri-pendulum, an Agilent AEDA-3300 AM encoder – Fig. B.4 – with resolution of 3000 counts per revolution, outputting a digital signal was attached to the tri-pendulum shaft (see Fig. 7.9). The signal from the encoder was sent to the DAQ card: NI USB 6211, which was then connected by USB to a computer running Labview software. Any post-acquisition data processing required on the raw data was done in MATLAB before plotting for analysis.
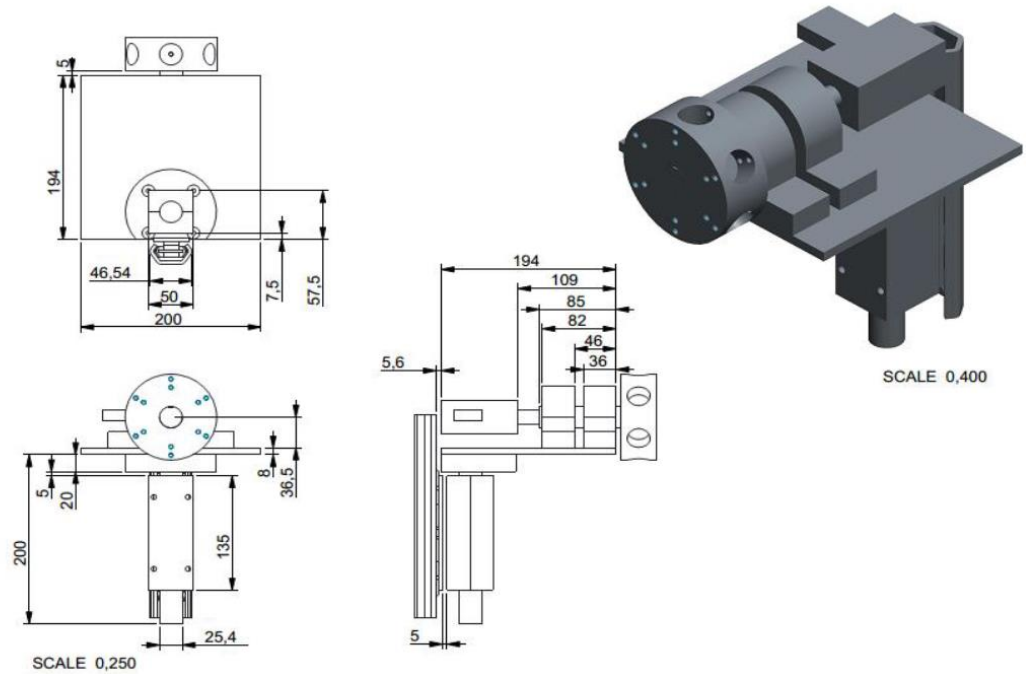
Figure B.1: CAD drawings of the designed tri-pendulum without the arms. The mounting plate, ball bearings, encoder and the hub are assembled.

Figure B.2: The weights grab-screwed on the the arms to configure the tri-pendulum's natural frequency.
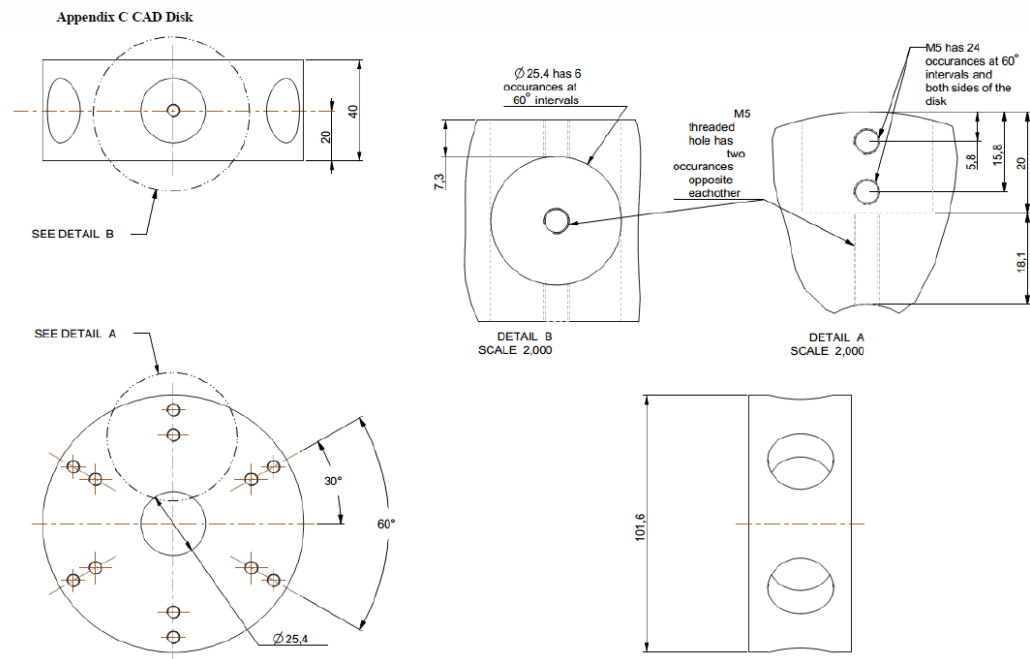
Figure B.3: CAD drawings of the hub.
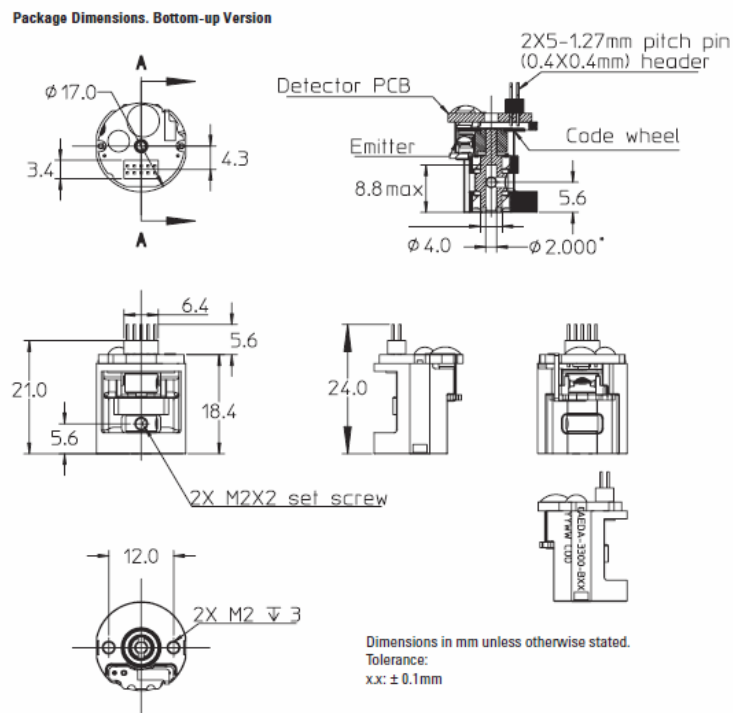
Figure B.4: CAD drawings of the angular encoder.
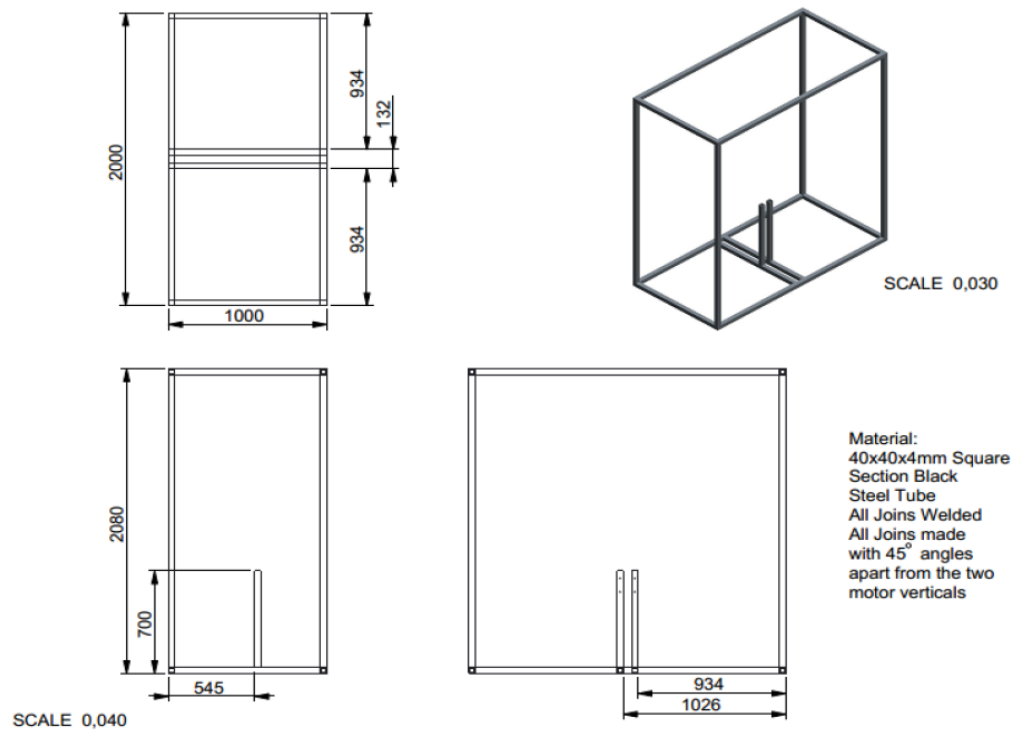
Figure B.5: CAD drawings of the frame: 3D, front and right views of the bottom part.
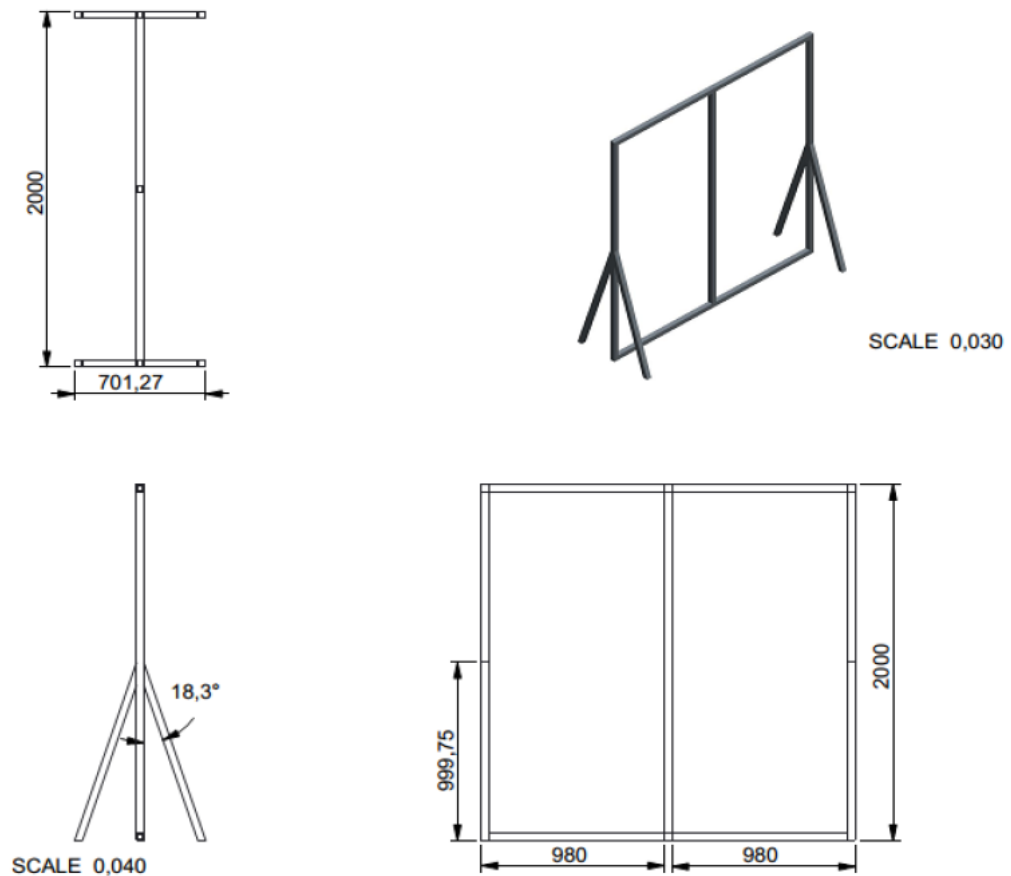
Figure B.6: CAD drawings of the frame: 3D, front and right views of the top part.
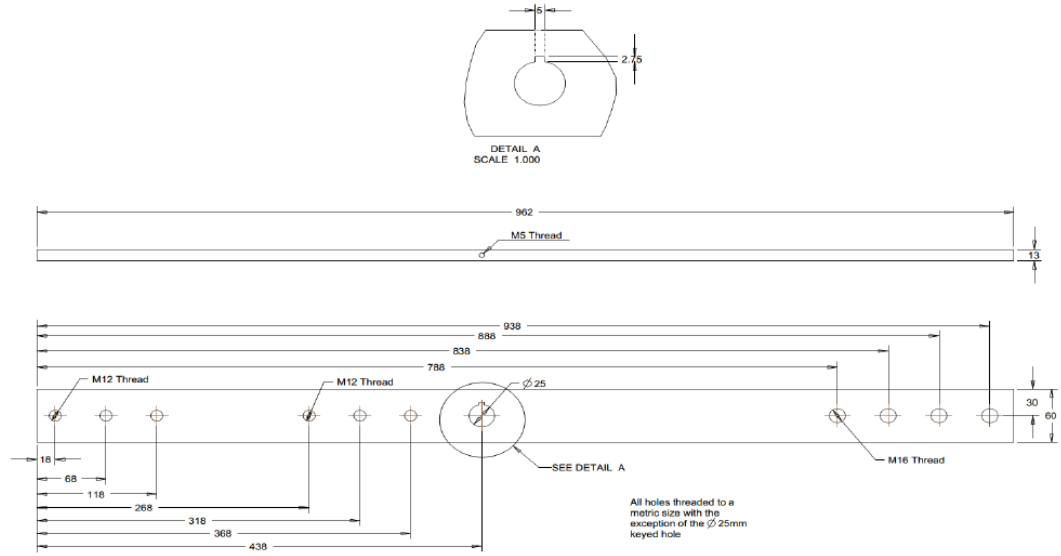
Figure B.7: CAD drawings of the crank.

B.4 Damping identification

In order to quantify the damping coefficient c of Eq. (7.11) the logarithmic decrement method is used. This procedure includes free vibrations of the tri-pendulum that are recorded, Fig. B.8. Then, the damping coefficient is estimated based on the
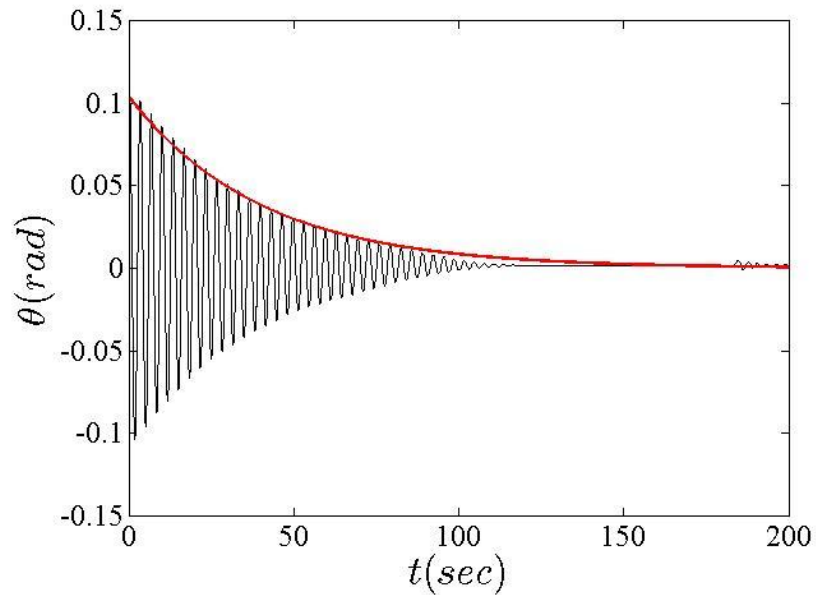
Figure B.8: Application of the logarithmic decrement method. Free decaying vibrations (black line); Time-dependent amplitude with the estimated damping coefficient (red line).

response amplitude values:

$$c = \frac{1}{\pi} \ln \frac{A_i}{A_{i+1}} \tag{B.1}$$

where A_i is the amplitude at the i-th cycle and A_{i+j} – the amplitude j cycles after.

References

[1] *EU energy in figures - statistical pocketbook*, Technical Report ISSN 1977-4559, European Union (2013)

[2] *International Energy Outlook 2013*, Technical Report DOE/EIA-0484(2013), U.S. Energy Information Administration (July 2013)

[3] US Energy Information Administration, *www.eia.gov* (accessed 20 June 2014)

[4] *Industry vision paper 2013*, Technical report, European Ocean Energy Association (2013)

[5] K. Gunn and C. Stock-Williams, *Quantifying the global wave power resource*, Renewable Energy, **44**, 296–304 (2012)

[6] *The state of renewable energies in Europe*, Technical report, Observer (2013)

[7] X. Xu, M. Wiercigroch and M. P. Cartmell, *Rotating orbits of a parametrically-excited pendulum*, Chaos Soliton Fractal, **23**, 1537–1548 (2005)

[8] R. W. Leven, B. Pompe, C. Wilke and B. P. Koch, *Experiments on periodic and chaotic motions of a parametrically forced pendulum*, Phys D: Nonlinear Phenom, **16**(3), 371–384 (1985)

[9] B. P. Koch and R. W. Leven, *Subharmonic and homoclinic bifurcations in a parametrically forced pendulum*, Phys D: Nonlinear Phenom, **16**(1), 1–13 (1985)

[10] A. Clément, P. McCullen, A. F. d. O. Falcão, A. Fiorentino, F. Gardner, K. Hammarlund, G. Lemonis, T. Lewis, K. Nielsen, S. Petroncini et al., *Wave*

energy in Europe: current status and perspectives, Renewable and Sustainable Energy Reviews, **6**(5), 405–431 (2002)

[11] S. Salter, *Wave power*, Nature, **249**, 720–724 (1974)

[12] A. E. Mynett, D. D. Serman and C. C. Mei, *Characteristics of Salter's cam for extracting energy from ocean waves*, Applied Ocean Research, **1**(1), 13–20 (1979)

[13] D. D. Serman and C. C. Mei, *Note on Salter's energy absorber in random waves*, Ocean Engineering, **7**(4), 477–490 (1980)

[14] S. H. Salter, D. C. Jeffery and J. R. M. Taylor, *The architecture of nodding duck wave power generators*, The Naval Architect, **1**, 21–24 (1976)

[15] J. Cruz, Ocean Wave Energy. Current status and future perspectives, Springer, Berlin (2008)

[16] Y. Masuda, *Experimental full-scale results of wave power machine Kamei in 1978*, in Proceedings of First Symposium on Wave Energy Utilization, Gothenburg, Sweden (30 October-1 November 1979)

[17] European Comission: Resarch & Innovation, Energy, *ec.europa.eu/research/energy* (accessed 20 June 2014)

[18] World Energy Council, Renewable Energy Resources: Opportunities and Constraints, World Energy Council, London, UK (1993)

[19] T. Thorpe, *A brief review of wave energy*, Technical Report R120, The UK Department of Trade and Industry (1999)

[20] Atlas of UK Marine Renewable Energy Resources, *www.renewables-atlas.info* (accessed 19 June 2014)

[21] T. Thorpe, *A review of wave energy*, Technical Report R72, The UK Department of Trade and Industry (1992)

[22] The Queen's University of Belfast, *The UK's shoreline and nearshore wave energy resource*, Technical Report WV1683, The UK Department of Trade and Industry (1992)

[23] B. Golding, *Computer calculations of waves from wind fields*, Power from Sea Waves, pp. 115–134 (1980)

[24] B. Drew, A. R. Plummer and M. N. Sahinkaya, *A review of wave energy converter technology*, Proceedings of the Institution of Mechanical Engineers, Part A: Journal of Power and Energy, **223**(8), 887–902 (2009)

[25] S. Matthews, J. Adams, B. Valpy and D. Krohn, *Marine energy in the UK. State of the industry report 2012*, Technical report, Renewable UK (2012)

[26] H. N. Southgate, *Wave prediction in deep water and at the coastline*, Technical Report SR114, Hydraulics Research Limited (1987)

[27] M. E. McCormick, Ocean Wave Energy Conversion, John Wiley & Sons, New York, NY (1981)

[28] J. Falnes, *A review of wave-energy extraction*, Marine Structures, **20**(4), 185–201 (2007)

[29] A. F. d. O. Falcão, *Wave energy utilization: A review of the technologies*, Renewable and Sustainable Energy Reviews, **14**(3), 899–918 (2010)

[30] European Marine Energy Centre, *www.emec.co.uk* (accessed 20 June 2014)

[31] M. G. de Sousa Prado, F. Gardner, M. Damen and H. Polinder, *Modelling and test results of the Archimedes wave swing*, P I Mech Eeng A-J Pow, **220**(8), 855–868 (2006)

[32] J. P. Kofoed, P. Frigaard, E. Friis-Madsen and H. C. Sørensen, *Prototype testing of the wave energy converter Wave Dragon*, Renewable energy, **31**(2), 181–189 (2006)

[33] T. Whittaker, D. Langston, N. Fletcher, M. Shaw and A. F. d. O. Falcão, *Islay Limpet wave power plant - Publishable report 1 November 1998 to 30 April 2002*, Technical Report JOR3-CT98-0312, The Queen's University of Belfast (2002)

[34] Y. Torre-Enciso, I. Ortubia, L. López de Aguileta and J. Marqués, *Mutriku*

wave power plant: from the thinking out to the reality, in Proc 8ᵗʰ European Wave and Tidal Energy Conference, pp. 319–329, Uppsala, Sweden (2009)

[35] Pelamis Wave Power, *www.pelamiswave.com/image-library* (accessed 19 June 2014)

[36] R. Yemm, D. Pizer, C. Retzler and R. Henderson, *Pelamis: experience from concept to connection*, Phil. Trans. R. Soc. A, **370**(1959), 365–380 (2012)

[37] R. Yemm, D. Pizer and C. Retzler, *The WPT-375 – a near-shore WEC submitted to SRO3*, in Proceedings of the EWEC3, Patras, Greece (September, 30– October, 2 1998)

[38] M. C. Carcas, *The OPD Pelamis WEC: Current status and onward programme (2002)*, International Journal of Ambient Energy, **24**(1), 21–28 (2003)

[39] Pelamis Wave Power, *www.pelamiswave.com* (accessed 20 June 2014), p2 Demonstration at EMEC, Orkney

[40] T. Whittaker, D. Collier, M. Folley, M. Osterried, A. Henry and M. Crowley, *The development of Oyster – a shallow water surging wave energy converter*, in Proceedings of the 7ᵗʰ European Wave and Tidal Energy Conference, Porto, Portugal (September, 11–13 2007)

[41] D. Collier, T. Whittaker and M. Crowley, *The construction of Oyster – A nearshore surging wave energy converter*, in Proceedings of the 2ⁿᵈ International Conference on Ocean Energy, Brest, France (October, 15–17 2008)

[42] A. Henry, K. Doherty, L. Cameron, T. Whittaker and R. Doherty, *Advances in the design of the Oyster wave energy converter*, in Marine and Offshore Renewable Energy Conf., London, UK (April, 21–23 2010)

[43] L. Cameron, R. Doherty, A. Henry, K. Doherty, J. Vant Hoff, D. Kaye, D. Naylor, S. Bourdier and T. Whittaker, *Design of the next generation of the Oyster wave energy converter*, in 3ʳᵈ International Conference on Ocean Energy, pp. 1–12, Bilbao, Spain (October, 6–8 2010)

[44] E. Renzi, K. Doherty, A. Henry and F. Dias, *How does Oyster work? The*

simple interpretation of Oyster mathematics, European Journal of Mechanics - B/Fluids, **47**(0), 124 – 131 (2014)

[45] *http://www.climateandfuel.com/individualpages/wavedragon.htm* ()

[46] S. Parmeggiani, J. F. Chozas, A. Pecher, E. Friis-Madsen, H. Sørensen and J. P. Kofoed, *Performance assessment of the Wave Dragon wave energy converter based on the EquiMar methodology*, in The 9th European Wave and Tidal Energy Conference: EWTEC, Southampton, UK (September, 5–9 2011)

[47] Subsea World News, *http://subseaworldnews.com* (accessed 19 June 2014)

[48] Sustainable Energy Research Group, *www.energy.soton.ac.uk/anaconda-wave-energy-converter-concept/* (accessed 19 June 2014), university of Southampton

[49] J. Salvatore, *World energy perspective: Cost of energy technologies*, Technical report, World Energy Council (2013)

[50] I. Webb, C. Seaman and G. Jackson, *Oscillating water column wave energy converter evaluation report*, Technical report, Carbon Trust (February 2005)

[51] *Accelerating marine energy - the potential for cost reduction*, Technical report, Carbon Trust (July 2011)

[52] SETIS, *Ocean wave energy*, Technical report, European Commission (2011)

[53] A. H. Nayfeh and D. T. Mook, Nonlinear Oscillations, Wiley, New York (1979)

[54] M. Cartmell, Introduction to linear, parametric and nonlinear vibrations, Chapman and Hall, London (1990)

[55] A. Tondl, T. Ruijgrok, F. Verhulst and R. Nabergoj, Autoparametric resonance in mechanical systems, Cambridge University Press, Cambridge, UK (2000)

[56] T. I. Fossen and H. Nijmeijer, Parametric resonance in dynamical systems, Springer, New York (2012)

[57] R. A. Ibrahim, Parametric random vibration, Dover Publications, New York (2008)

[58] Z. Feng, X. Lan and X. Zhu, *Principal parametric resonances of a slender cantilever beam subject to axial narrow-band random excitation of its base*, International Journal of Non-Linear Mechanics, **42**(10), 1170–1185 (2007)

[59] J. Miles and D. Henderson, *Parametrically forced surface waves*, Annual Review of Fluid Mechanics, **22**(1), 143–165 (1990)

[60] G. Song, V. Sethi and H.-N. Li, *Vibration control of civil structures using piezoceramic smart materials: A review*, Engineering Structures, **28**(11), 1513–1524 (2006)

[61] J.-L. Lilien and A. P. Da Costa, *Vibration amplitudes caused by parametric excitation of cable stayed structures*, Journal of Sound and Vibration, **174**(1), 69–90 (1994)

[62] O. Cuvalci and A. Ertas, *Pendulum as vibration absorber for flexible structures: experiments and theory*, Journal of Vibration and Acoustics, **118**(4), 558–566 (1996)

[63] K. L. Turner, S. A. Miller, P. G. Hartwell, N. C. MacDonald, S. H. Strogatz and S. G. Adams, *Five parametric resonances in a microelectromechanical system*, Nature, **396**(6707), 149–152 (1998)

[64] W. Magnus and S. Winkler, Hill's equation, Courier Dover Publications, New York (2013)

[65] L. Meirovitch, Fundamentals of Vibrations, McGraw-Hill, New York (2001)

[66] É. Mathieu, *Mémoire sur le mouvement vibratoire d'une membrane de forme elliptique*, Journal de mathématiques pures et appliquées, **13**, 137–203 (1868)

[67] B. van der Pol and M. Strutt, *II. On the stability of the solutions of Mathieu's equation*, Phil Mag 7, **5**(27), 18–38 (1928)

[68] S. S. Rao, Mechanical Vibrations, Pearson Prentice Hall, New Jersey (2004)

[69] M. Dimentberg, Statistical Dynamics of Nonlinear and Time-Varying Systems, Research Studies Press, Taunton, UK (1988)

[70] W.-C. Xie, Dynamic stability of structures, Cambridge University Press, Cambridge, UK (2006)

[71] S. Ariaratnam and D. Tam, *Parametric random excitation of a damped Mathieu oscillator*, ZAMM, **56**(11), 449–452 (1976)

[72] R. L. Stratonovich, Topics in the Theory of Random Noise, volume 2, Gordon and Breach, New York (1963)

[73] J. B. Roberts and P. D. Spanos, *Stochastic averaging: An approximate method of solving random vibration problems*, International Journal of Nonlinear Mechanics, **21**, 111–134 (1986)

[74] W. V. Wedig, *Invariant measures and Lyapunov exponents for generalised parameter fluctuations*, Structural Saf., **8**, 13–25 (1990)

[75] M. F. Dimentberg, Z. Hou, M. Noori and W. Zhang, *Non-Gaussian response of a single-degree-of-freedom system to a periodic excitation with random phase modulation*, Recent Advances in Mechanics of Structured Continua, **160**, 27–23 (1993)

[76] H. W. Rong, G. Meng, X. D. Wang, W. Xu and T. Fang, *Largest Lyapunov exponent for second-order linear systems under combined harmonic and random parametric excitations*, Journal of Sound and Vibration, **283**, 1250–6 (2005)

[77] M. Dimentberg, Z. Hou, M. Noori and W. Zhang, *Response of an SDOF system to periodic external and parametric excitations with random phase modulations*, J Sound Vib, **192**(3), 621–627 (1996)

[78] H. W. Rong, G. Meng, X. D. Wang, W. Xu and T. Fang, *Invariant measures and Lyapunov exponents for stochastic Mathieu system*, J Sound Vib, **283**, 1250–6 (2005)

[79] R. Bobryk and A. Chrzeszczyk, *Stability regions for Mathieu equation with imperfect periodicity*, Physics Letters A, **373**, 3532–3535 (2009)

[80] Z. L. Huang, W. Q. Zhu, Y. Q. Ni and J. M. Ko, *Stochastic averaging of strongly nonlinear oscillators under bounded noise excitation*, Journal of Sound and Vibration, **254**, 245–267 (2005)

[81] J. Li, W. Xu, Z. Ren and Y. Lei, *Maximal Lyapunov exponent and almost-sure stability for stochastic Mathieu-Duffing systems*, J Sound Vib, **286**, 395–402 (2005)

[82] W.-C. Xie and R. So, *Parametric resonance of a two-dimensional system under bounded noise excitation*, Nonlinear Dynam, **36**(2-4), 437–453 (2004)

[83] M. F. Dimentberg, E. Mo and A. Naess, *Probability density and excursions of structural response to imperfectly periodic excitation*, Journal of Engineering Mechanics, **133**(9), 1037–1041 (2007)

[84] A. H. Nayfeh, Perturbation methods, John Wiley & Sons, New York (1973)

[85] A. H. Nayfeh, Introduction to perturbation techniques, John Wiley & Sons, New York (1981)

[86] M. Dimentberg, *Stability and subcritical dynamics of structures with spatially disordered travelling parametric excitation*, Probabilistic Engineering Mechanics, **7**(3), 131 – 134 (1992)

[87] M. Dimentberg, Z. Hou and M. Noori, *Stability of a SDOF system under periodic parametric excitation with a white-noise phase modulation*, Stochastic and Nonlinear Dynamics: Applications to Mechanical Systems, pp. 341–359 (1995)

[88] W.-C. Xie, *Moment Lyapunov exponents of a two-dimensional system under bounded noise parametric excitation*, J Sound Vib, **263**(3), 593–616 (2003)

[89] N. Sri Namachchivaya, *Almost sure stability of dynamical systems under combined harmonic and stochastic excitations*, Journal of Sound and Vibration, **151**(1), 77–90 (1991)

[90] H. Rong, W. Xu and T. Fang, *Principal response of Duffing oscillator to combined deterministic and narrow-band random parametric excitation*, Journal of Sound and Vibration, **210**(4), 483–515 (1998)

[91] A. Stephenson, *On a new type of dynamical stability*, Mem. Proc. Manch. Lit. Phil. Soc., **52**, 1–10 (1908)

References

[92] M. J. Clifford and S. R. Bishop, *Inverted oscillations of a driven pendulum*, Proc. R. Soc. Lond. Series A, **454**, 2811–2817 (1998)

[93] R. W. Leven and B. P. Koch, *Chaotic behaviour of a parametrically exited damped pendulum*, Phys Lett A, **86**(2), 71–74 (1981)

[94] S. Bishop and M. Clifford, *The use of manifold tangencies to predict orbits, bifurcations and estimate escape in driven systems*, Chaos, Solitons & Fractals, **7**(10), 1537–1553 (1996)

[95] M. J. Clifford and S. R. Bishop, *Locating oscillatory orbits of the parametrically-excited pendulum*, J. Aust. Math. Soc. Ser. B. Appl. Math., **37**, 309–319 (1996)

[96] M. J. Clifford and S. R. Bishop, *Approximating the escape zone for the parametrically excited pendulum*, J. Sound Vib., **172**(4), 572–576 (1994)

[97] S. R. Bishop, A. Sofroniou and P. Shi, *Symmetry-breaking in the response of the parametrically excited pendulum*, Chaos Soliton Fractal, **25**, 257–264 (2005)

[98] A. Sofroniou and S. R. Bishop, *Breaking the symmetry of the parametrically excited pendulum*, Chaos, Solitons & Fractals, **28**(3), 673–681 (2006)

[99] W. Szemplińska-Stupnicka, E. Tyrkiel and A. Zubrzycki, *The global bifurcations that lead to transient tumbling chaos in a parametrically driven pendulum*, International Journal of Bifurcation and Chaos, **10**(09), 2161–2175 (2000)

[100] W. Szemplińska-Stupnicka and E. Tyrkiel, *The oscillation-rotation attractors in the forced pendulum and their peculiar properties*, Int J Bifurcat Chaos, **12**(01), 159–168 (2002)

[101] S. Bishop and M. Clifford, *Zones of chaotic behaviour in the parametrically excited pendulum*, J Sound Vib, **189**(1), 142 – 147 (1996)

[102] A. S. De Paula, M. A. Savi, E. Pavlovskaia and M. Wiercigroch, *Bifurcation control of a parametric pendulum*, Int. J. Bifurc. Chaos, **22**(5), 1250111 (2012)

[103] S. Lenci and G. Rega, *Competing dynamic solutions in a parametrically excited pendulum: attractor robustness and basin integrity*, Journal of Computational and Nonlinear Dynamics, **3**(4), 041010 (2008)

[104] S. Lenci, E. Pavlovskaia, G. Rega and M. Wiercigroch, *Rotating solutions and stability of parametric pendulum by perturbation method*, J. Sound Vib., **310**, 243–259 (2008)

[105] X. Xu and M. Wiercigroch, *Approximate analytical solutions for oscillatory and rotational motion of a parametric pendulum*, Nonlinear Dyn, **47**, 311–320 (2007)

[106] E. Pavlovskaia, B. Horton, M. Wiercigroch, S. Lenci and G. Rega, *Approximate rotational solutions of pendulum under combined vertical and horizontal excitation*, Int J Bifurc. Chaos, **22**(5), 1250100 (2011)

[107] A. O. Belyakov, *On rotational solutions for elliptically excited pendulum*, Phys lett A, **375**, 2524–2530 (2011)

[108] M. J. Clifford and S. R. Bishop, *Rotating periodic orbits of the parametrically excited pendulum*, Phys. Lett., **201A**, 191–196 (1995)

[109] W. Garira and S. R. Bishop, *Rotating solutions of the parametrically excited pendulum*, J. Sound Vib., **263**, 233–239 (2003)

[110] B. Horton, J. Sieber, J. M. T. Thompson and M. Wiercigroch, *Dynamics of the nearly parametric pendulum*, Int J Non-linear Mech, **46**, 436–442 (2011)

[111] B. Horton, S. Lenci, E. Pavlovskaia, F. Romeo, G. Rega and M. Wiercigroch, *Stability boundaries of period-1 rotation for a pendulum under combined vertical and horizontal excitation*, J. Applied Nonlin. Dyn., **2**(2), 103–126 (2013)

[112] J. M. Schmitt and P. V. Bayly, *Bifurcations in the mean angle of a horizontally shaken pendulum: analysis and experiment*, Nonlinear Dynamics, **15**(1), 1–14 (1998)

[113] B. P. Mann and M. A. Koplow, *Symmetry breaking bifurcations of a parametrically excited pendulum*, Nonlinear Dynamics, **46**(4), 427–437 (2006)

[114] R. A. Morrison and M. Wiercigroch, *Stability of the elliptically excited pendulum using the homoclinic Melnikov function*, in IUTAM Symposium on Nonlinear Dynamics for Advanced Technologies and Engineering Design, edited by M. Wiercigroch and G. Rega, volume 32 of *IUTAM Bookseries (closed)*, pp. 87–94, Springer Netherlands (2013)

[115] T. Kapitaniak, *A property of a stochastic response with bifurcation of a nonlinear system*, J Sound Vib, **107**(1), 177–180 (1986)

[116] J. A. Blackburn, *Noise activated transitions among periodic states of a pendulum with a vertically oscillating pivot, mediated by a chaotic attractor*, Proc R Soc A, **462**(2067), 1043–1052 (2006)

[117] J. A. Blackburn, N. Grønbech-Jensen and H. Smith, *Stochastic noise and chaotic transients*, Phys Rev Lett, **74**(6), 908–911 (1995)

[118] H. Cho, D. Venturi and G. Karniadakis, *Adaptive discontinuous Galerkin method for response-excitation PDF equations*, SIAM Journal on Scientific Computing, **35**(4), B890–B911 (2013)

[119] P. S. Landa and A. A. Zaikin, *Noise-induced phase transitions in a pendulum with a randomly vibrating suspension axis*, Phys Rev E, **54**(4), 3535–3544 (1996)

[120] P. Landa and A. Zaikin, *Nonequilibrium noise-induced phase transitions in simple systems*, J Exp Theor Phys, **84**(1), 197–208 (1997)

[121] P. Landa, A. Zaikin, M. Rosenblum and J. Kurths, *Control of noise-induced oscillations of a pendulum with a randomly vibrating suspension axis*, Phys Rev E, **56**(2), 1465 (1997)

[122] E. Perkins and B. Balachandran, *Noise-influenced dynamics of a vertically excited pendulum*, in ASME 2013 IDETC/CIE, p. V07BT10A025 (8 pages), Protland, Oregon, USA (August, 4–7 2013)

[123] Z. Liu and W. Zhu, *Homoclinic bifurcation and chaos in simple pendulum under bounded noise excitation*, Chaos Soliton Fract, **20**(3), 593–607 (2004)

[124] Ü. Lepik and H. Hein, *On response of nonlinear oscillators with random frequency of excitation*, Journal of Sound and Vibration, **288**(1), 275–292 (2005)

[125] H. Hein and Ü. Lepik, *Response of nonlinear oscillators with random frequency of excitation, revisited*, Journal of Sound and Vibration, **301**(3), 1040–1049 (2007)

[126] G. Litak, M. Borowiec and M. Wiercigroch, *Phase locking and rotational motion of a parametric pendulum in noisy and chaotic conditions*, Dynamical Systems, **23**(3), 259–265 (2008)

[127] B. W. Horton and M. Wiercigroch, *Effects of heave excitation on rotations of a pendulum for wave energy extraction*, in IUTAM Symposium on fluid-structure interaction in ocean engineering, pp. 117–128, Springer (2008)

[128] M. Shinozuka and G. Deodatis, *Simulation of stochastic processes by spectral representation*, Applied Mechanics Reviews, **44**(4), 191–204 (1991)

[129] R. Haxton and A. Barr, *The autoparametric vibration absorber*, J. Manuf. Sci. Eng., **94**(1), 119–125 (1972)

[130] A. Bajaj, S. Chang and J. Johnson, *Amplitude modulated dynamics of a resonantly excited autoparametric two degree-of-freedom system*, Nonlinear dynamics, **5**(4), 433–457 (1994)

[131] M. Cartmell and J. Lawson, *Performance enhancement of an autoparametric vibration absorber by means of computer control*, Journal of Sound and Vibration, **177**(2), 173–195 (1994)

[132] Y. Song, H. Sato, Y. Iwata and T. Komtsuzaki, *The response of a dynamic vibration absorber system with a parametrically excited pendulum*, J Sound Vib, **259**(4), 747 – 759 (2003)

[133] A. Tondl, *To the analysis of autoparametric systems*, ZAMM-Journal of Applied Mathematics and Mechanics, **77**(6), 407–418 (1997)

[134] R. Nabergoj and A. Tondl, *Simulation of parametric ship rolling: Effects of hull bending and torsional elasticity*, Nonlinear Dynamics, **6**(3), 265–284 (1994)

[135] A. Tondl and R. Nabergoj, *Non-periodic and chaotic vibrations in a flow induced system*, Chaos, Solitons & Fractals, **4**(12), 2193–2202 (1994)

[136] R. Bobryk and D. Yurchenko, *Beneficial effect of noise in suppression of self-excited vibrations*, Fluctuation and Noise Letters (2014)

[137] F. Verhulst, *Parametric and autoparametric resonance*, Acta Applicandae Mathematica, **70**(1-3), 231–264 (2002)

[138] H. Hatwal, A. Mallik and A. Ghosh, *Forced nonlinear oscillations of an autoparametric system – part 1: periodic responses*, Journal of Applied Mechanics, **50**(3), 657–662 (1983)

[139] H. Hatwal, A. Mallik and A. Ghosh, *Forced nonlinear oscillations of an autoparametric system – part 2: chaotic responses*, Journal of Applied Mechanics, **50**(3), 663–668 (1983)

[140] B. Banerjee, A. K. Bajaj and P. Davies, *Resonant dynamics of an autoparametric system: A study using higher-order averaging*, International Journal of Non-Linear Mechanics, **31**(1), 21 – 39 (1996)

[141] J. Warminski and K. Kecik, *Autoparametric vibration of a nonlinear system with pendulum*, Mathematical Problems in Engineering, **2006** (2006), article ID 80705, 19 pages

[142] J. Warminski and K. Kecik, *Instabilities in the main parametric resonance area of a mechanical system with a pendulum*, Journal of Sound and Vibration, **322**(3), 612–628 (2009)

[143] K. Kecik and J. Warminski, *Dynamics of an autoparametric pendulum-like system with a nonlinear semiactive suspension*, Mathematical Problems in Engineering, **2011** (2011), article ID 451047, 15 pages

[144] P. Brzeski, P. Perlikowski, S. Yanchuk and T. Kapitaniak, *The dynamics of the pendulum suspended on the forced Duffing oscillator*, J Sound Vib, **331**(24), 5347 – 5357 (2012)

[145] A. Vyas and A. Bajaj, *Dynamics of autoparametric vibration absorbers using multiple pendulums*, Journal of Sound and Vibration, **246**(1), 115 – 135 (2001)

[146] R. Ibrahim and J. Roberts, *Broad band random excitation of a two-degree-of-freedom system with autoparametric coupling*, Journal of Sound and Vibration, **44**(3), 335–348 (1976)

[147] R. Ibrahim and J. Roberts, *Stochastic stability of the stationary response of a system with autoparametric coupling*, ZAMM-Journal of Applied Mathematics and Mechanics, **57**(11), 643–649 (1977)

[148] J. Roberts, *Random excitation of a vibratory system with autoparametric interaction*, Journal of Sound and Vibration, **69**(1), 101–116 (1980)

[149] K. Onu, N. Lingala and N. S. Namachchivaya, *Random vibration of a nonlinear autoparametric system*, in International Conference on Theory and Application in Nonlinear Dynamics (ICAND 2012), pp. 11–23, Springer (2014)

[150] M. Rosenblum and A. Pikovsky, *Synchronization: from pendulum clocks to chaotic lasers and chemical oscillators*, Contemporary Phys., **44**, 401–416 (2003)

[151] L. Marcheggiani and S. Lenci, *On a model for the pedestrians-induced lateral vibrations of footbridges*, Meccanica, **45**(4), 531–551 (2010)

[152] M. Kapitaniak, K. Czolczynski, P. Perlikowski, A. Stefanski and T. Kapitaniak, *Synchronous states of slowly rotating pendula*, Physics Reports (2014), doi:10.1016/j.physrep.2014.02.008

[153] K. Czolzynski, P. Perlikowski, A. Stefanski and T. Kapitaniak, *Synchronization of slowly rotating pendulums*, Int. J. Bifurc. Chaos, **22**(05), 1250128 (2012)

[154] K. Czolczynski, P. Perlikowski, A. Stefanski and T. Kapitaniak, *Synchronization of pendula rotating in different directions*, Communications in Nonlinear Science and Numerical Simulation, **17**(9), 3658–3672 (2012)

[155] M. Lazarek, M. Nielaczny, K. Czolczynski and T. Kapitaniak, *Synchronization of slowly rotating nonidentically driven pendula*, Journal of Computational and Nonlinear Dynamics, **9**(2), 021010 (2014)

[156] K. Czolczynski, P. Perlikowski, A. Stefanski and T. Kapitaniak, *Synchronization of the self-excited pendula suspended on the vertically displacing beam*,

Communications in Nonlinear Science and Numerical Simulation, **18**(2), 386–400 (2013)

[157] M. Kapitaniak, P. Perlikowski and T. Kapitaniak, *Synchronous motion of two vertically excited planar elastic pendula*, Communications in Nonlinear Science and Numerical Simulation, **18**(8), 2088–2096 (2013)

[158] J. Strzalko, J. Grabski, J. Wojewoda, M. Wiercigroch and T. Kapitaniak, *Synchronous rotation of the set of double pendula: Experimental observations*, Chaos, **22**(4), 047503 (2012)

[159] A. Najdecka, V. Vaziri and M. Wiercigroch, *Dynamics, synchronization and control of parametric pendulums*, in IUTAM Symposium on Nonlinear Dynamics for Advanced Technologies and Engineering Design, edited by M. Wiercigroch and G. Rega, volume 32, pp. 185–193, Springer Netherlands (2013)

[160] V. Vaziri, A. Najdecka and M. Wiercigroch, *Experimental control for initiating and maintaining rotation of parametric pendulum*, The European Physical Journal Special Topics, **223**(4), 795–812 (2014)

[161] H. Yabuno, M. Miura and N. Aoshima, *Bifurcation in an inverted pendulum with tilted high-frequency excitation: analytical and experimental investigations on the symmetry-breaking of the bifurcation*, J Sound Vib, **273**, 493–513 (2004)

[162] C. Sartorelli and W. Lacarbonara, *Parametric resonances in a base-excited double pendulum*, Nonlinear Dyn, **69**, 1679–1692 (2012)

[163] X. Xu, E. Pavlovskaia, M. Wiercigroch, F. Romeo and S. Lenci, *Dynamic interactions between parametric pendulum and electro-dynamical shaker*, ZAMM, **87**, 172–186 (2007)

[164] S. Lenci, M. Brocchini and C. Lorenzoni, *Experimental rotations of a pendulum on water waves*, J Comput Nonlinear Dyn, **7**(1), 011007 (2012)

[165] S. Lenci and G. Rega, *Experimental versus theoretical robustness of rotating solutions in a parametrically excited pendulum: a dynamical integrity perspective*, Physica D: Nonlinear Phenomena, **240**(9), 814–824 (2011)

[166] S. Lenci, *On the production of energy from sea waves by a rotating pendulum: A preliminary experimental study*, J Applied Nonlin Dyn, **3**(2), 187–201 (2014)

[167] Y. Lin, Probabilistic theory of structural dynamics, McGraw-Hill, New York (1967)

[168] Y. Lin and G. Cai, Probabilistic structural dynamics. Advanced Theory and Applications, McGraw-Hill, New York (1995)

[169] B. Øksendal, Stochastic differential equations, Springer-Verlag, Berlin (1985)

[170] L. Arnold, Stochastic differential equations: Theory and Applications, Wiley & sons, New York, USA (1974)

[171] E. Mo, Nonlinear stochastic dynamics and chaos by numerical path integration, Ph.D. thesis, Norwegian University of Science and Technology (2008)

[172] W. J. Pierson and L. Moskowitz, *A proposed spectral form for fully developed wind seas based on the similarity theory of A. Kitaigorodskii*, J. Geophysical Res., **69**, 5181–5190 (1964)

[173] K. Hasselmann, T. Barnett, E. Bouws, H. Carlson, D. Cartwright, K. Enke, J. Ewing, H. Gienapp, D. Hasselmann, P. Kruseman et al., *Measurements of wind-wave growth and swell decay during the joint north sea wave project (JONSWAP)*, J. Phys. Oceanogr., **10**, 1264–1280 (1973)

[174] I. G. Kozubovskaya and S. M. Khrisanov, *Random parametric resonance*, Ukrainian Mathematical J., **34**(4), 350–357 (1982)

[175] Y. Lin and Q. Li, *New stochastic theory for bridge stability in turbulent flow*, Journal of Engineering Mechanics, **119**(1), 113–127 (1993)

[176] M. H. Kalos and P. A. Whitlock, Monte Carlo methods. Second, revised and enlarged edition, Wiley-VCH Verlag, Wenheim, Germany (2008)

[177] N. Metropolis and S. Ulam, *The Monte Carlo method*, Journal of the American statistical association, **44**(247), 335–341 (1949)

[178] IMSL Fortran numeric library. User's guide stat/library, Visual Numerics, Houston, TX, USA, 6 edition (2007)

[179] W. Zhu, *Recent developments and applications of the stochastic averaging method in random vibration*, Applied Mechanics Reviews, **49**(10S), S72–S80 (1996)

[180] W. Zhu, Z. Huang and Y. Suzuki, *Response and stability of strongly non-linear oscillators under wide-band random excitation*, International Journal of Non-Linear Mechanics, **36**(8), 1235–1250 (2001)

[181] A. Naess and V. Moe, *Efficient path integration methods for nonlinear dynamic systems*, Probabilistic Engineering Mechanics, **15**(2), 221–231 (2000)

[182] I. Kougioumtzoglou and P. Spanos, *An analytical Wiener path integral technique for non-stationary response determination of nonlinear oscillators*, Probabilistic Engineering Mechanics, **28**(0), 125 – 131 (2012)

[183] D. Yurchenko, A. Naess and P. Alevras, *Pendulum's rotational motion governed by a stochastic Mathieu equation*, Probabilist Eng Mech, **31**, 12–18 (2013)

[184] A. Naess, F. Kolnes and E. Mo, *Stochastic spur gear dynamics by numerical path integration*, Journal of Sound and Vibration, **302**(4), 936–950 (2007)

[185] D. V. Iourtchenko, E. Mo and A. Naess, *Response probability density functions of strongly non-linear systems by the path integration method*, International Journal of Non-Linear Mechanics, **41**(5), 693–705 (2006)

[186] D. Iourtchenko, E. Mo and A. Naess, *Reliability of strongly nonlinear single degree of freedom dynamic systems by the path integration method*, Journal of Applied Mechanics, **75**(6), 061016 (2008)

[187] A. Naess, D. Iourtchenko and O. Batsevych, *Reliability of systems with randomly varying parameters by the path integration method*, Probabilistic Engineering Mechanics, **26**(1), 5–9 (2011)

[188] H. Kushner, Stochastic stability and sontrol, volume 33 of *Mathematics in Science and Engineering*, Academic Press, New York, USA (1967)

[189] V. I. Oseledec, *A multiplicative ergodic theorem. Lyapunov characteristic numbers for dynamical systems*, Trans. Moscow Math. Soc, **19**(2), 197–231 (1968)

[190] R. Khasminskii, *Stochastic stability of differential equations*, volume 66 of *Stochastic modelling and applied probability*, Springer (2011)

[191] A. Wolf, *Determining Lyapunov exponents from a time series*, Physica D: Nonlinear Phenomena, **16**, 285–317 (1985)

[192] A. Neiman, A. Silchenko, V. Anishchenko and L. Schimansky-Geier, *Stochastic resonance: Noise-enhanced phase coherence*, Phys. Rev. E, **58**, 7118–7125 (1998)

[193] P. Alevras and D. Yurchenko, *Stochastic rotational response of a parametric pendulum coupled with an SDOF system*, Probabilist Eng Mech (2013), available online

[194] D. Yurchenko and P. Alevras, *Stochastic dynamics of a parametrically base excited rotating pendulum*, Procedia IUTAM, **6**, 160–168 (2013)

[195] J. Thompson and H. Stewart, *Nonlinear dynamics and chaos: Geometrical methods for engineers and scientists*, Research supported by the DOE and SERC. Chichester, England and New York, John Wiley and Sons, 1986, 392 p., **1** (1986)

[196] M. Dimentberg and D. Iourtchenko, *Random vibrations with impacts: a review*, Nonlinear Dynamics, **36**(2-4), 229–254 (2004)

[197] R. A. Ibrahim, Vibro-impact dynamics: modeling, mapping and applications, volume 43, Springer, Berlin (2009)

[198] R. A. Ibrahim, V. I. Babitsky and M. Okuma, Vibro-impact dynamics of ocean systems and related problems, volume 44, Springer, Berlin (2009)

[199] R. Leine, *Non-smooth stability analysis of the parametrically excited impact oscillator*, International Journal of Non-Linear Mechanics, **47**(9), 1020–1032 (2012)

[200] S. Min-Bang and R. Hai-Wu, *Resonance response of a single-degree-of-freedom nonlinear vibro-impact system to a narrow-band random parametric excitation*, Chinese Physics B, **20**(6), 060501 (2011)

[201] M. Dimentberg, D. Yurchenko and O. van Ewijk, *Subharmonic response of a quasi-isochronous vibroimpact system to a randomly disordered periodic excitation*, Nonlinear Dynamics, **17**, 173–186 (1998)

[202] D. V. Iourtchenko and L. L. Song, *Numerical investigation of a response probability density function of stochastic vibroimpact systems with inelastic impacts*, International Journal of Non-Linear Mechanics, **41**(3), 447–455 (2006)

[203] D. Yurchenko and P. Alevras, *Dynamics of the N-pendulum and its application to a wave energy converter concept*, International Journal of Dynamics and Control, **1**(4), 290–299 (2013)